

**Inclusive jet production in proton-proton and copper-gold collisions at**

$$\sqrt{s_{\text{NN}}} = 200 \text{ GeV}$$

by

**Arbin Timilsina**

A dissertation submitted to the graduate faculty  
in partial fulfillment of the requirements for the degree of  
**DOCTOR OF PHILOSOPHY**

Major: Nuclear Physics

Program of Study Committee:

John Lajoie, Major Professor

Edward Yu

Patricia Thiel

Marzia Rosati

James Cochran

Iowa State University

Ames, Iowa

2016

Copyright © Arbin Timilsina, 2016. All rights reserved.

But there are men for whom the unattainable has a special attraction. Usually they are not experts: their ambitions and fantasies are strong enough to brush aside the doubts which more cautious men might have. Determination and faith are their strongest weapons. At best such men are regarded as eccentric; at worst, mad...

-Walt Unsworth  
Everest: A Mountaineering History

When you throw a rock into the water, it will speed on the fastest course to the bottom of the water. This is how it is when Siddhartha has a goal, a resolution. Siddhartha does nothing, he waits, he thinks, he fasts, but he passes through the things of the world like a rock through water, without doing anything, without stirring; he is drawn, he lets himself fall.

-Herman Hess  
Siddhartha

Dedicated to my family.

## TABLE OF CONTENTS

<b>LIST OF FIGURES . . . . .</b>	<b>xi</b>
<b>LIST OF TABLES . . . . .</b>	<b>xxii</b>
<b>ACKNOWLEDGMENTS . . . . .</b>	<b>xxiv</b>
<b>ABSTRACT . . . . .</b>	<b>xxv</b>
<b>CHAPTER 1. INTRODUCTION . . . . .</b>	<b>1</b>
<b>CHAPTER 2. BACKGROUND . . . . .</b>	<b>3</b>
2.1 Historical perspective . . . . .	3
2.1.1 The classical era . . . . .	3
2.1.2 The modern era . . . . .	5
2.1.2.1 Into the jungle . . . . .	5
2.1.2.2 The quark model . . . . .	7
2.1.2.3 The November revolution . . . . .	8
2.2 Quantum Chromodynamics . . . . .	9
2.2.1 The history . . . . .	11
2.2.1.1 Quark color . . . . .	11
2.2.1.2 Deep inelastic scattering . . . . .	13
2.2.2 The basis . . . . .	17
2.2.2.1 Renormalization . . . . .	18
2.2.2.2 Asymptotic freedom . . . . .	19
2.2.3 Experimental evidence for QCD . . . . .	21
2.3 The Standard Model . . . . .	24
2.4 The Quark-Gluon Plasma . . . . .	25

2.5	Ultra-relativistic heavy ion collisions . . . . .	28
2.5.1	Signatures of the Quark-Gluon Plasma . . . . .	32
2.5.1.1	Quarkonia suppression . . . . .	33
2.5.1.2	Energy loss of a fast parton . . . . .	33
2.6	Jets and jet quenching . . . . .	34
2.6.1	Jet reconstruction . . . . .	34
2.6.1.1	Jet reconstruction algorithms . . . . .	36
2.6.2	Framework of jet quenching . . . . .	38
2.6.2.1	Nuclear modification factor . . . . .	40
<b>CHAPTER 3. THE EXPERIMENT . . . . .</b>		44
3.1	The Relativistic Heavy Ion Collider . . . . .	44
3.1.1	Accelerator chain . . . . .	46
3.2	The PHENIX detector . . . . .	47
3.2.1	Overview . . . . .	47
3.2.2	The global detectors . . . . .	49
3.2.2.1	Beam-Beam Counter . . . . .	49
3.2.2.2	Zero-Degree Calorimeters . . . . .	50
3.2.3	The central arm . . . . .	51
3.2.3.1	The central magnet . . . . .	51
3.2.3.2	Drift Chamber . . . . .	52
3.2.3.3	Pad Chamber . . . . .	53
3.2.3.4	Ring-Imaging Cherenkov detector . . . . .	55
3.2.3.5	Electromagnetic Calorimeter . . . . .	55
3.2.4	Data Acquisition and trigger system . . . . .	57
3.2.4.1	Minimum Bias trigger . . . . .	58
3.2.4.2	EMCal/RICH trigger . . . . .	59
<b>CHAPTER 4. ANALYSIS PREAMBLE . . . . .</b>		61
4.1	Kinematic variables . . . . .	61

4.1.1	Jet-level variables . . . . .	63
4.2	Monte Carlo frameworks . . . . .	64
4.2.1	Glauber Monte Carlo . . . . .	64
4.2.2	Monte Carlo event generators . . . . .	65
4.2.2.1	PYTHIA . . . . .	66
4.2.2.2	HIJING . . . . .	67
4.3	Simulation study without detector effects . . . . .	68
4.3.1	Setup . . . . .	69
4.3.1.1	sHIJING . . . . .	69
4.3.1.2	PYTHIA . . . . .	70
4.3.2	Performance . . . . .	71
4.3.2.1	Matching efficiency . . . . .	71
4.3.2.2	Comparison of $p_{\text{T, True}}$ and $p_{\text{T, Reco}}$ . . . . .	72
4.3.2.3	“Purity” . . . . .	76
4.3.3	Conclusion . . . . .	77
<b>CHAPTER 5. DATA ANALYSIS</b>	. . . . .	79
5.1	Data selection . . . . .	79
5.1.1	Cu+Au . . . . .	79
5.1.2	$p+p$ . . . . .	80
5.2	Run quality assurance . . . . .	80
5.2.1	Cu+Au . . . . .	81
5.2.2	$p+p$ . . . . .	83
5.3	Event selection . . . . .	83
5.3.1	Offline vertex cut . . . . .	83
5.4	Track selection . . . . .	84
5.4.1	Modified quality cut . . . . .	84
5.4.2	Pair cut . . . . .	87
5.4.3	EMCal and PC3 matching . . . . .	91
5.4.4	Track cuts . . . . .	91

5.4.4.1	Secondary cuts . . . . .	92
5.5	Cluster selection . . . . .	95
5.5.1	EMCal hot/dead map . . . . .	95
5.5.2	Cluster cuts . . . . .	97
5.5.3	Cluster-track association . . . . .	100
5.6	Jet reconstruction . . . . .	100
5.6.1	Analysis of high $p_T$ background . . . . .	100
5.6.2	Analysis of fake jets . . . . .	105
5.6.2.1	Fake jet subtraction . . . . .	106
<b>CHAPTER 6. MONTE CARLO SIMULATION</b>	. . . . .	<b>109</b>
6.1	Setup . . . . .	109
6.1.1	PISA . . . . .	109
6.1.2	pisaToDST . . . . .	109
6.1.3	Binning strategy . . . . .	110
6.1.4	$p+p$ setup . . . . .	111
6.1.4.1	Vertex shifting . . . . .	111
6.1.4.2	Simulation chain . . . . .	111
6.1.5	Cu+Au setup . . . . .	112
6.1.5.1	Cu+Au data trigger . . . . .	113
6.1.5.2	Vertex matching . . . . .	113
6.1.5.3	Simulation chain . . . . .	113
6.2	Acceptance study . . . . .	115
6.2.1	For the $p+p$ setup . . . . .	115
6.2.2	For the Cu+Au setup . . . . .	117
6.3	True jet . . . . .	120
6.4	Single particle performance . . . . .	123
6.4.1	Track reconstruction efficiency . . . . .	123
6.4.2	Cluster reconstruction efficiency . . . . .	124
6.5	Jet performance . . . . .	126

6.5.1	Jet reconstruction efficiency . . . . .	126
6.5.2	Jet energy scale and jet energy resolution . . . . .	131
6.6	Fake jet simulation study . . . . .	134
<b>CHAPTER 7. PATH TO FINAL RESULTS</b>	. . . . .	<b>139</b>
7.1	Unfolding . . . . .	139
7.1.1	Unfolding methods . . . . .	140
7.1.1.1	Singular value decomposition method . . . . .	140
7.1.1.2	Iterative Bayesian method . . . . .	143
7.1.2	Unfolded spectra . . . . .	145
7.2	Trigger efficiencies, $\langle N_{\text{Coll}} \rangle$ , and $\langle T_{\text{AB}} \rangle$ . . . . .	145
7.2.1	BBC trigger efficiency . . . . .	145
7.2.2	ERT trigger efficiency . . . . .	147
7.2.3	$\langle N_{\text{Coll}} \rangle$ and $\langle T_{\text{AB}} \rangle$ for Cu+Au . . . . .	148
7.3	Constructing the per-event jet yield . . . . .	149
7.3.1	Run scalers . . . . .	149
7.3.2	Per-event jet yield for a triggered dataset . . . . .	149
7.3.3	Per-event jet yield for the Minimum Bias dataset . . . . .	150
7.3.4	Per-event jet yield for the ERT dataset . . . . .	150
7.4	Evaluation of the systematic uncertainty . . . . .	151
7.4.1	Unfolding procedure . . . . .	151
7.4.1.1	Shape of the input spectrum . . . . .	151
7.4.1.2	Unfolding method . . . . .	153
7.4.2	Energy scale . . . . .	155
7.4.2.1	DC $p_{\text{T}}$ scale . . . . .	155
7.4.2.2	EMCal energy scale . . . . .	157
7.4.3	Jet-level cuts . . . . .	159
7.4.3.1	Number of constituents . . . . .	159
7.4.3.2	Charged fraction . . . . .	159
7.4.3.3	<i>n.c.</i> and <i>c.f.</i> combined . . . . .	162

7.4.4	Acceptance . . . . .	164
7.4.4.1	Tight fiducial cut . . . . .	164
7.4.4.2	Arm . . . . .	166
7.4.5	Fake jet . . . . .	168
<b>CHAPTER 8. FINAL RESULTS . . . . .</b>		<b>170</b>
8.1	$p+p$ cross-section . . . . .	170
8.2	$R_{AA}$ and $R_{CP}$ . . . . .	173
8.3	Tabulation of the final results . . . . .	176
8.4	Conclusion . . . . .	178
<b>BIBLIOGRAPHY . . . . .</b>		<b>179</b>
<b>APPENDIX A. FAST FILTER CLASS . . . . .</b>		<b>191</b>
<b>APPENDIX B. MATCHING . . . . .</b>		<b>192</b>
<b>APPENDIX C. CROSS-CHECKS: <math>R_{AA}</math> and <math>R_{CP}</math> . . . . .</b>		<b>193</b>

## LIST OF FIGURES

<p>Figure 1.1 Measurements of the jet <math>R_{\text{AA}}</math> as a function of <math>p_{\text{T}}</math> in Pb+Pb collisions with the ATLAS detector. Each panel shows a different range in absolute rapidity <math> y </math>. Jets are found to be suppressed by approximately a factor of 2 in central collisions compared to <math>p+p</math> collisions. The <math>R_{\text{AA}}</math> shows a slight increase with <math>p_{\text{T}}</math> and no significant variation with rapidity. . . . .</p> <p>Figure 2.1 Feynman diagram for the elementary QED process. . . . .</p> <p>Figure 2.2 The ratio of the rate of hadron production to that of muon pairs, from [13]. . . . .</p> <p>Figure 2.3 Feynman diagram for <math>\pi^0</math> decay. . . . .</p> <p>Figure 2.4 Kinematics of the deeply inelastic scattering. . . . .</p> <p>Figure 2.5 The <math>F_2</math> structure function from the SLAC-MIT, BCDMS, H1, and ZEUS collaborations, from [18] . . . . .</p> <p>Figure 2.6 The ratio <math>2xF_1/F_2</math>, from [20] . . . . .</p> <p>Figure 2.7 Feynman diagrams which contribute to the <math>\beta</math> function in the one loop approximation. . . . .</p> <p>Figure 2.8 Quark polarization in QCD. . . . .</p> <p>Figure 2.10 Gluon polarization in QCD. . . . .</p> <p>Figure 2.11 Summary of measurements of <math>\alpha_s</math> as a function of the energy scale <math>Q</math>, from [26]. . . . .</p> <p>Figure 2.12 The proton structure function <math>F_2</math> measured in electromagnetic scattering of electrons and positrons on protons, from [26]. . . . .</p> <p>Figure 2.13 The particles and force carriers of the Standard Model, from [31]. . . . .</p>	<p>1</p> <p>10</p> <p>12</p> <p>13</p> <p>14</p> <p>15</p> <p>16</p> <p>20</p> <p>20</p> <p>21</p> <p>22</p> <p>23</p> <p>25</p>
--	--

Figure 2.14	Lattice QCD prediction for the dependence of the energy density $\epsilon$ on the temperature $T$ for three different quark configurations, from [38]. . . . .	27
Figure 2.15	Schematic of QCD phase diagram, from [40]. . . . .	28
Figure 2.16	Visualization of different stages of heavy ion collision, from [43]. . . . .	29
Figure 2.17	Schematic of different stages of heavy ion collision (beam axis view), from [44]. . . . .	29
Figure 2.18	A schematic of recombination and fragmentation for a meson at $p_T \approx 6$ GeV/c, from [48]. . . . .	31
Figure 2.19	Illustration of an IRC unsafe algorithm. . . . .	36
Figure 2.20	The neutral pion production cross-section as a function of $p_T$ and the results of NLO pQCD calculations, from [71]. . . . .	39
Figure 2.21	EPS09 results for the nuclear modification factor for the valence quarks, sea quarks, and gluons in Pb nucleus at $Q^2 = 1.69$ GeV $^2$ (upper panel) and $Q^2 = 200$ GeV $^2$ (lower panel), from [72]. . . . .	40
Figure 2.22	$R_{AA}$ for identified hadrons, direct photon, and non-photonic electrons measured by PHENIX in the most central Au+Au collisions at $\sqrt{s_{NN}} = 200$ GeV, from [73]. . . . .	42
Figure 2.23	The $R_{dAu}$ for $R = 0.3$ anti- $k_t$ jets. A model calculation including CNM energy-loss for the most central case is also shown. . . . .	43
Figure 3.1	Bird's-eye view of the RHIC complex, from www.google.com/maps. . . . .	45
Figure 3.2	Schematic of the RHIC complex. . . . .	45
Figure 3.3	Setup of the PHENIX detector during the 2012 RHIC running period. Top is the beam view and bottom is the side view. . . . .	48
Figure 3.4	One of the two BBCs. . . . .	49
Figure 3.5	A single BBC element consisting of a PMT and a quartz radiator. . . . .	49
Figure 3.6	Diagram of the installation location of the north and south ZDC in a view along the beam axis. . . . .	50

Figure 3.7	Magnetic field lines in PHENIX. The central magnet coils are in the combined $++$ mode. . . . .	51
Figure 3.8	Schematic of the PHENIX Drift Chamber, from [97]. . . . .	52
Figure 3.9	Layout of wire position within one sector of the PHENIX Drift Chamber in $r$ - $\phi$ plane (left). Top view of the wire orientation in $z$ - $\phi$ plane (right), from [97]. . . . .	53
Figure 3.10	Exploded view of the PHENIX Pad Chamber, from [98]. . . . .	54
Figure 3.11	A cutaway view of one arm of the PHENIX RICH detector, from [100]. . . . .	55
Figure 3.12	Schematic view of a PbSc module, from [101]. . . . .	56
Figure 3.13	Schematic view of a PbGl supermodule, from [101]. . . . .	57
Figure 3.14	Schematic of the data flow in PHENIX. . . . .	58
Figure 3.15	The conceptual diagram of the procedure to produce signals for the ERT trigger, from [102]. . . . .	59
Figure 4.1	Coordinate system used in this analysis. . . . .	62
Figure 4.2	Per-event sHIJING true jet yield with the anti- $k_t$ algorithm. . . . .	69
Figure 4.3	Per-event PYTHIA true jet yield with the anti- $k_t$ algorithm. . . . .	70
Figure 4.4	Per-event PYTHIA true jet yield with the Gaussian Filter algorithm. . . . .	70
Figure 4.5	Matching efficiency of the PYTHIA+sHIJING jets reconstructed with the anti- $k_t$ algorithm. . . . .	72
Figure 4.6	Reconstruction efficiency of the sHIJING jets reconstructed with the anti- $k_t$ algorithm. . . . .	73
Figure 4.7	Reconstruction efficiency of the PYTHIA+sHIJING jets reconstructed with the Gaussian filter algorithm. . . . .	73
Figure 4.8	Per-event yield for the PYTHIA+sHIJING true and matched jets reconstructed with the anti- $k_t$ algorithm. . . . .	74
Figure 4.9	Response matrix of the PYTHIA+sHIJING jets with $R_{\text{Anti-}k_t} = 0.2$ . . . . .	75
Figure 4.10	Response matrix of the PYTHIA+sHIJING jets with $R_{\text{Anti-}k_t} = 0.3$ . . . . .	76

Figure 4.11	"Purity" of the PYTHIA+sHIJING jets reconstructed with the anti- $k_t$ algorithm for various discriminant selections. . . . .	77
Figure 4.12	"Purity" of the PYTHIA+sHIJING jets reconstructed with the anti- $k_t$ algorithm for various centrality selections. . . . .	78
Figure 5.1	PHENIX integrated sampled luminosity vs. day for the Run-12 200 GeV Cu+Au collision period, from [110]. . . . .	79
Figure 5.2	PHENIX integrated sampled luminosity vs. day for the Run-12 200 GeV $p+p$ collision period, from [111]. . . . .	80
Figure 5.3	Example plot for the run quality assurance procedure. . . . .	81
Figure 5.4	Alpha vs. board for tracks that have the X1 quality bit. . . . .	85
Figure 5.5	Alpha vs. board showing the recorded regions of the X1 weak acceptance. . . . .	85
Figure 5.6	DC/PC acceptance for the Cu+Au dataset when the quality (63 or 31) is used. . . . .	86
Figure 5.7	DC/PC acceptance for the Cu+Au dataset when the modified quality cut is applied. . . . .	87
Figure 5.8	DC/PC acceptance for the $p+p$ dataset when the quality (63 or 31) is used. . . . .	88
Figure 5.9	DC/PC acceptance for the $p+p$ dataset when the modified quality cut is applied. . . . .	88
Figure 5.10	$\Delta\phi$ vs $\Delta z$ for all pairs, same charge pairs, and opposite charge pairs. . . . .	89
Figure 5.11	$\Delta\phi$ vs. $\Delta z$ distribution and the projections for the same charge track pairs. . . . .	90
Figure 5.12	$\Delta\phi$ vs $\Delta z$ distribution and the projections for the opposite charge track pairs. . . . .	90
Figure 5.13	$z$ vs. $\phi_0$ for the low- $p_T$ conversions. . . . .	93
Figure 5.14	Selected $\phi_0$ regions. . . . .	93
Figure 5.15	Ecore for the low- $p_T$ conversions. . . . .	93
Figure 5.17	Cu+Au dataset. . . . .	94

Figure 5.18	$p+p$ dataset. . . . .	94
Figure 5.19	Ecore for the hadron tracks that match to the EMCAL in the Cu+Au dataset (left) and in the $p+p$ dataset (right) . . . . .	94
Figure 5.21	Cu+Au dataset. . . . .	95
Figure 5.22	$p+p$ dataset. . . . .	95
Figure 5.23	E/p for the electron candidates in the Cu+Au dataset (left) and the $p+p$ dataset (right) . . . . .	95
Figure 5.24	R-vertex <sub>true</sub> vs. Z-vertex <sub>true</sub> for the conversion electrons. . . . .	96
Figure 5.25	Hit distribution for sector 0. . . . .	97
Figure 5.27	Map for the west arm. . . . .	98
Figure 5.28	Map for the east arm. . . . .	98
Figure 5.29	Hot/dead map for the Cu+Au dataset. Red represents the hot towers, black the dead, and cyan the uncalibrated. Gray represents the towers that are around the hot or dead or uncalibrated towers. . . . .	98
Figure 5.31	Map for the west arm. . . . .	99
Figure 5.32	Map for the east arm. . . . .	99
Figure 5.33	Hot/dead map for the $p+p$ dataset. Red represents the hot towers, black the dead, and cyan the uncalibrated. Gray represents the towers that are around the hot or dead or uncalibrated towers. . . . .	99
Figure 5.34	Charged fraction distribution for the Cu+Au dataset. . . . .	100
Figure 5.35	Charged fraction distribution for the $p+p$ dataset. . . . .	100
Figure 5.36	Per-event yield of the anti- $k_t$ jets for the Cu+Au dataset with various charged fraction selections. . . . .	101
Figure 5.37	Per-event yield of the anti- $k_t$ jets for the $p+p$ dataset with the various charged fraction selections. . . . .	102
Figure 5.38	Charged constituents spectra. . . . .	103
Figure 5.39	Neutral constituents spectra. . . . .	103
Figure 5.40	Charged to neutral constituents ratio for the Cu+Au dataset. . . . .	104
Figure 5.41	Charged to neutral constituents ratio for the $p+p$ dataset. . . . .	104

Figure 5.42	Discriminant distribution for the Cu+Au dataset. . . . .	105
Figure 5.43	Discriminant distribution for the $p+p$ dataset. . . . .	105
Figure 5.44	Per-event yield of the anti- $k_t$ jets for the Cu+Au dataset. . . . .	106
Figure 5.45	Per-event yield of the anti- $k_t$ jets for the $p+p$ datasets. . . . .	106
Figure 5.46	"Fake" jet subtraction for the $p+p$ dataset. . . . .	107
Figure 5.47	"Fake" jet subtraction for the different centrality selections in the Cu+Au collisions. . . . .	107
Figure 6.1	$Z$ -vertex distribution for the $\sqrt{s_{\text{NN}}} = 200$ GeV $p+p$ Minimum Bias dataset.	111
Figure 6.2	Simulation chain for the $p+p$ setup. . . . .	112
Figure 6.3	Simulation chain for the Cu+Au setup. . . . .	114
Figure 6.5	Data: West arm . . . . .	115
Figure 6.6	Simulation: West arm . . . . .	115
Figure 6.7	DC/PC acceptance comparison between the data and the simulation for the west arm. . . . .	115
Figure 6.9	Data: East arm . . . . .	116
Figure 6.10	Simulation: East arm . . . . .	116
Figure 6.11	DC/PC acceptance comparison between the data and the simulation for the east arm. . . . .	116
Figure 6.12	Per-event $dN/d\phi$ distribution of the good tracks for both data (black line) and simulation (red line). The distributions are normalized from $\phi = 2.2$ to $2.4$ . . . . .	116
Figure 6.14	Data: Sectors 0 to 3 . . . . .	118
Figure 6.15	Simulation: Sectors 0 to 3 . . . . .	118
Figure 6.16	Data: Sectors 4 to 7 . . . . .	118
Figure 6.17	Simulation: Sectors 4 to 7 . . . . .	118
Figure 6.18	EMCal acceptance comparison between the data and the simulation for sector 0 to 7. . . . .	118
Figure 6.20	Data: West arm . . . . .	119

Figure 6.21	Simulation: West arm . . . . .	119
Figure 6.22	DC/PC acceptance comparison between the data and the simulation for the west arm. . . . .	119
Figure 6.24	Data: East arm . . . . .	119
Figure 6.25	Simulation: East arm . . . . .	119
Figure 6.26	DC/PC acceptance comparison between the data and the simulation for the east arm. . . . .	119
Figure 6.27	Per-event $dN/d\phi$ distribution of the good tracks for both data (black line) and simulation (red line). The distributions are normalized from $\phi = 2.2$ to $2.4$ . . . . .	120
Figure 6.29	Data: Sectors 0 to 3 . . . . .	121
Figure 6.30	Simulation: Sectors 0 to 3 . . . . .	121
Figure 6.31	Data: Sectors 4 to 7 . . . . .	121
Figure 6.32	Simulation: Sectors 4 to 7 . . . . .	121
Figure 6.33	EMCal acceptance comparison between the data and the simulation for sector 0 to 7. . . . .	121
Figure 6.34	Per-event PYTHIA true jet yield for the $p+p$ and Cu+Au setups. . . . .	122
Figure 6.35	Average contribution of the true jet constituent particles to the true jet's $p_T$ . . . . .	122
Figure 6.36	$\Delta R$ distribution between the charged hadrons or electrons and the closest tracks. . . . .	123
Figure 6.37	Response matrix between the charged hadrons or electrons and the matched tracks. . . . .	123
Figure 6.38	Reconstruction efficiency for the charged hadrons or electrons. . . . .	124
Figure 6.39	Reconstruction efficiency for the charged hadrons or electrons for the perfect DC/PC. . . . .	125
Figure 6.40	$\Delta R$ distribution between the photons and the closest clusters. . . . .	125
Figure 6.41	Response matrix between the photons and the matched clusters. . . . .	125
Figure 6.42	Reconstruction efficiency for the photons. . . . .	126

Figure 6.43	$\Delta R$ distribution for the Cu+Au 0–20% centrality. . . . .	127
Figure 6.44	Reconstruction efficiency as a function of $\phi_{\text{True}}$ . . . . .	128
Figure 6.45	Reconstruction efficiency as a function of $\eta_{\text{True}}$ . . . . .	128
Figure 6.46	Reconstruction efficiency as a function of $\eta_{\text{True}}$ for four different $z_{\text{vertex}}$ ranges. . . . .	129
Figure 6.47	Jet reconstruction efficiency for the $p+p$ and different centrality selections of the Cu+Au collisions. . . . .	130
Figure 6.48	Jet reconstruction efficiency for the different centralities of the Cu+Au collisions subtracted from that of the $p+p$ collisions. . . . .	130
Figure 6.49	Response matrix for the $p+p$ collisions. . . . .	131
Figure 6.50	Response matrices for the different centralities of the Cu+Au collisions. . . . .	132
Figure 6.51	$p_{\text{T, Reco}}/p_{\text{T, True}}$ distribution for $p_{\text{T, True}} \in 16.6\text{--}19.9 \text{ GeV}/c$ . . . . .	133
Figure 6.52	$p_{\text{T, Reco}}/p_{\text{T, True}}$ distribution for $p_{\text{T, True}} \in 34.6\text{--}41.6 \text{ GeV}/c$ . . . . .	133
Figure 6.53	JES for the $p+p$ and different centrality selections of the Cu+Au collisions. . . . .	133
Figure 6.54	JES for the different centralities of the Cu+Au collisions subtracted from that of the $p+p$ collisions. . . . .	134
Figure 6.55	JER for the $p+p$ and the different centrality selections of the Cu+Au collisions. . . . .	135
Figure 6.56	JER for the different centralities of the Cu+Au collisions subtracted from that of the $p+p$ collisions. . . . .	135
Figure 6.57	Simulation chain for the fake jet study. . . . .	136
Figure 6.58	Fake jet simulation study for the different centralities of the Cu+Au collisions. . . . .	137
Figure 7.1	Distribution of $d_i$ for the $p+p$ and different centrality selections of the Cu+Au collisions. Red vertical lines show the choice of regularization parameter. . . . .	142
Figure 7.2	$p+p$ jet spectra with the default value of the regularization parameter and with the variations $\pm 1$ . . . . .	143

Figure 7.3	Different centrality selected Cu+Au jet spectra with the default value of the regularization parameter and with the variations $\pm 1$ . . . . .	144
Figure 7.4	“Fake” jet subtracted, the SVD method unfolded and the Bayesian method unfolded per-event jet yield for the $p+p$ collisions. . . . .	146
Figure 7.5	“Fake” jet subtracted, the SVD method unfolded and the Bayesian method unfolded per-event jet yield for the different centrality selections of the Cu+Au collisions. . . . .	146
Figure 7.6	ERT 4x4c efficiency. . . . .	148
Figure 7.7	Effect for the $p+p$ spectrum due to the variation in the shape of the input spectrum. . . . .	151
Figure 7.8	Effect for the different centrality selected Cu+Au spectrum due to the variation in the shape of the input spectrum. . . . .	152
Figure 7.9	Double ratio for the variation in the shape of the input spectrum. . . .	152
Figure 7.10	Effect for the $p+p$ spectrum due to the variation in the unfolding method. .	153
Figure 7.11	Effect for the different centrality selected Cu+Au spectrum due to the variation in the unfolding method . . . . .	154
Figure 7.12	Double ratio for the variation in the unfolding method. . . . .	154
Figure 7.13	Effect for the $p+p$ spectrum due to the variation in the DC $p_T$ scale. .	155
Figure 7.14	Effect for the different centrality selected Cu+Au spectrum due to the variation in the DC $p_T$ scale. . . . .	156
Figure 7.15	Double ratio for the variation in the DC $p_T$ scale. . . . .	156
Figure 7.16	Effect for the $p+p$ spectrum due to the variation in the EMCAL energy scale. . . . .	157
Figure 7.17	Effect for the different centrality selected Cu+Au spectrum due to the variation in the EMCAL energy scale. . . . .	158
Figure 7.18	Double ratio for the variation in the EMCAL energy scale. . . . .	158
Figure 7.19	Effect for the $p+p$ spectrum due to the variation in the <i>n.c.</i> selection. .	159
Figure 7.20	Effect for the different centrality selected Cu+Au spectrum due to the variation in the <i>n.c.</i> selection. . . . .	160

Figure 7.21	Effect for the $p+p$ spectrum due to the variation in the <i>c.f.</i> selection. . . . .	160
Figure 7.22	Effect for the different centrality selected Cu+Au spectrum due to the variation in the <i>c.f.</i> selection. . . . .	161
Figure 7.23	Effect for the $p+p$ spectrum due to the variation in <i>n.c.</i> and <i>c.f.</i> combined selection. . . . .	162
Figure 7.24	Effect for the different centrality selected Cu+Au spectrum due to the variation in the <i>n.c.</i> and <i>c.f.</i> combined selection. . . . .	163
Figure 7.25	Double ratio for the variation in the <i>n.c.</i> and <i>c.f.</i> combined selection. . . . .	163
Figure 7.26	Effect for the $p+p$ spectrum due to the variation in the fiducial requirement. . . . .	164
Figure 7.27	Effect for the different centrality selected Cu+Au spectrum due to the variation in the fiducial requirement. . . . .	165
Figure 7.28	Double ratio for the variation in the fiducial requirement. . . . .	165
Figure 7.29	Effect for the $p+p$ spectrum when the east and the west arm yield are unfolded separately. . . . .	166
Figure 7.30	Effect for the different centrality selected Cu+Au spectrum when the east and the west arm yield are unfolded separately. . . . .	167
Figure 7.31	Double ratio for the east and the west arm yield unfolded separately. . . . .	167
Figure 7.32	Effect for the $p+p$ spectrum due to the variation in the minimum cluster energy and track $p_T$ requirements. . . . .	168
Figure 7.33	Effect for the different centrality selected Cu+Au spectrum due to the variation in the minimum cluster energy and track $p_T$ requirements. . . . .	169
Figure 7.34	Double ratio for the variation in the minimum cluster energy and track $p_T$ requirements. . . . .	169
Figure 8.1	Measured anti- $k_t$ , $R=0.2$ jet yield in the $p+p$ and Cu+Au collisions with an arbitrary normalization. The vertical bars in the measurement indicate the statistical uncertainties and the shaded bands indicate the total systematic uncertainties. . . . .	170

- Figure 8.2 Measured and calculated anti- $k_t$ , R=0.2 jet cross-section in the  $p+p$  collisions. The vertical bars in the measurement indicate the statistical uncertainties and the shaded bands indicate the total systematic uncertainties(which includes the overall normalization uncertainties). The lines are the theoretical values and the bands are the theoretical scale uncertainty; the green color lines and bands are NLO calculations and the red color lines and bands are NLO calculations corrected for hadronization. The lower panel shows the ratio of NLO + Hadronization calculation to data. . . . . 172
- Figure 8.3  $R_{AA}$  for four different centrality selections of the Cu+Au collisions a function of jet transverse momentum  $p_T$ . The vertical bars indicate the statistical uncertainties and the shaded bands indicate the systematic uncertainties. The overall normalization uncertainties are shown as the vertical bands on the left side at  $R_{AA} = 1$  mark. . . . . 173
- Figure 8.4  $R_{AA}$  as a function of the number of participating nucleons  $N_{\text{Part}}$  for two different  $p_T$  ranges: 17–20 GeV/c and 29–35 GeV/c. . . . . 174
- Figure 8.5 Jet  $R_{AA}$  for the most central case compared to theory calculations for two different couplings between the jet and the QGP medium:  $g = 2.0$  and  $g = 2.2$ . The calculations are done for small cold nuclear matter (CNM) effect. . . . . 175
- Figure 8.6  $R_{CP}$  for three different centrality selections of the Cu+Au collisions as a function of jet transverse momentum  $p_T$ . The vertical bars indicate the statistical uncertainties and the shaded bands indicate the systematic uncertainties. The overall normalization uncertainties are shown as vertical band on the left side at  $R_{CP} = 1$  mark. . . . . 175
- Figure C.1 Comparison of  $R_{AA}$  constructed from the uncorrected reco-level, the SVD method unfolded and the Bayes method unfolded yields. . . . . 193

Figure C.2 Comparison of $R_{CP}$ for uncorrected reco-level yield and SVD and Bayes method unfolded yield. . . . .	194
--	-----

## LIST OF TABLES

Table 4.1	Centrality selection for the HIJING Cu+Au events. . . . .	68
Table 5.1	Excluded runs for the Cu+Au dataset. . . . .	82
Table 5.2	Excluded runs for the $p+p$ dataset. . . . .	83
Table 5.3	“Fake” jet contribution for the $p+p$ and different centralities of the Cu+Au collisions. . . . .	108
Table 7.1	Default regularization parameter selection for the SVD method. . . .	142
Table 7.2	$\langle N_{\text{Coll}} \rangle$ and $\langle T_{\text{AB}} \rangle$ for the Cu+Au collisions. . . . .	149
Table 8.1	Tabulation of the overall normalization uncertainties for the observables in this analysis. The uncertainties are added in quadrature to obtain the total. . . . .	176
Table 8.2	Tabulation of the $R_{\text{AA}}$ results. The quantities in parentheses are the absolute statistical and systematic uncertainties. The normalization uncertainties from Table 8.1 are not shown here. . . . .	177
Table 8.3	Tabulation of $R_{\text{CP}}$ results. The quantities in parentheses are the absolute statistical and systematic uncertainties. The normalization uncertainties from Table 8.1 are not shown here. . . . .	177

## ACKNOWLEDGMENTS

I would like to thank my advisor, John Lajoie, for providing the unprecedented freedom to nurture my scientific curiosities. Thanks John for giving me time to think, struggle, and grow on my own; and also for always being there to guide whenever my steps had faltered. John leads by example and I can only hope that I have been able to absorb some of his intuition, integrity, and rigor for the scientific enterprise.

I would like to thank all the members of my program of study committee, Edward Yu, Patricia Thiel, Marzia Rosati, and James Cochran, for their support. Also, big thanks to the past committee member Kevin de Laplante. Special thanks to Marzia for her endless guidance; whenever things fell apart, she was always there to pick up the pieces and rebuild.

Head bowed, hands folded, I would like to thank all the members of the PHENIX collaboration. From 1008 to PWG meetings, from ‘what is Root’ phase to ‘soon to graduate’ phase, I have received nothing but support and encouragement. Thank you!

I am very grateful to my friends at Iowa State University; thank you guys for making graduate school fun! Also, heartfelt thanks to Josh, Sarah, and the stupid cat Bindi for making Manorville lively.

I offer my sincere gratitude to Chadani, Big Sir, and friends and family of the Kumudini Homes; you all have been a big inspiration and motivation for whatever I do. Thank you!

Mum, Didi, Bhena, Dai, Bhauju, Motu and my better half, thanks for always being there through my endeavors; this thesis is a testimony of your unconditional love and support.

## ABSTRACT

Jets are a dominant feature of high energy particle interactions and can be interpreted in terms of the fragmentation of quarks and gluons produced in a hard scattering process. Jets provide important tools for studying hot and dense Quantum Chromodynamics (QCD) matter that is created in high energy collisions of heavy nuclei. In heavy ion collisions, such as Cu+Au, large transverse momentum partons traverse the colored Quark-Gluon Plasma (QGP) medium and lose energy which modifies the jet structure relative to jets generated in the vacuum.

Jet production in relativistic heavy ion collisions is investigated using the Cu+Au collisions at  $\sqrt{s_{\text{NN}}} = 200 \text{ GeV}$ . The measurements reported here utilize 200 GeV Cu+Au and  $p+p$  data recorded by the PHENIX detector at the Relativistic Heavy Ion Collider (RHIC) in 2012 RHIC running period. Jets are reconstructed from charged particles and electromagnetic calorimeter clusters using the anti- $k_t$  algorithm with  $R = 0.2$ .

Inclusive, centrality-dependent jet yields within  $|\eta| < 0.35$  and  $12.0 < p_T < 42.0 \text{ GeV}/c$  are presented. The jet yield in Cu+Au collisions relative to the geometric expectation is found to be suppressed by approximately a factor of two in the most central events, nearly independent of the jet  $p_T$ . These results are compared with theoretical calculations with implications for sensitivity to the parton energy loss models in heavy ion collisions.

## CHAPTER 1. INTRODUCTION

Relativistic heavy ion collisions produce an evanescent hot, dense medium of strongly interacting nuclear matter composed of deconfined color charges, called Quark-Gluon Plasma. Hard scattering processes occurring early in these collisions produce high transverse momentum ( $p_T$ ) partons that propagate through the medium and eventually fragment into jets of hadrons. Due to the interactions of the high- $p_T$  partons with the medium, jet production rate in heavy ion collisions is expected to be modified relative to proton-proton collisions. This modification of jet rate in heavy ion collisions is attributed to the energy loss of the high- $p_T$  partons in the medium and is studied through measurements of the jet suppression relative to proton-proton collisions, where there are no energy loss effects.

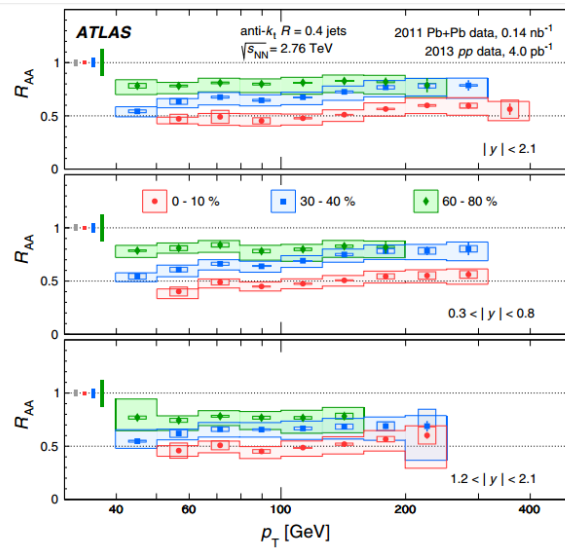


Figure 1.1: Measurements of the jet  $R_{AA}$  as a function of  $p_T$  in Pb+Pb collisions with the ATLAS detector. Each panel shows a different range in absolute rapidity  $|y|$ . Jets are found to be suppressed by approximately a factor of 2 in central collisions compared to  $p+p$  collisions. The  $R_{AA}$  shows a slight increase with  $p_T$  and no significant variation with rapidity.

Jet suppression can be explored in a systematic way through measurements of fully reconstructed jets. The subject of this dissertation is the centrality-dependent measurement of jet yield in the Cu+Au collisions at RHIC. Ratios of jet yield in different centrality intervals relative to  $p+p$  collision is constructed to quantify the effects of jet suppression in the presence of the QGP. The suppression is measured as a function of jet  $p_T$  and collision centrality.

This dissertation is organized as follows. Chapter 2 provides the theoretical and experimental background on the QCD, QGP, jets and jet quenching. Chapter 3 describes the experimental apparatuses, the RHIC and the PHENIX detector. Chapter 4 introduces important concepts that are used in the analysis. Chapter 5 discusses data, event, track, cluster, and reconstructed jet selection criteria. Monte Carlo simulation setup is discussed in Chapter 6. The path to the final result is discussed in Chapter 7, including unfolding techniques, construction of per-event jet yield, and estimation of systematic uncertainties. The final results of this analysis, as well as the conclusion, are presented in Chapter 8.

## CHAPTER 2. BACKGROUND

### 2.1 Historical perspective

One can speculate that when ancient humans looked at the stars in a clear sky and asked questions like “What?”, “How?”, and “Why?”, ideas that would ultimately result in nuclear physics were already germinating. By the time Greek atomists were theorizing the concepts of atom and void, the germinating seed had its radicle fully emerged. In 1897, with J. J. Thomson’s discovery of the electron, the first leaves had unfolded from the young stem. Today, nuclear physics has grown into a majestic tree with numerous branches. Each branch, marked by sporadic scars of miscalculations, misconceptions, and frustrations, bears fruits of unyielding dedication, unique insights, and unprecedented triumphs. The tree is at its prime and is still growing mighty and tall. In this chapter, we will explore some of its roots and climb to few of its branches.

#### 2.1.1 The classical era

The scale of energy achievable in the lab has changed, but when we peek at the core foundation of experimental nuclear physics, we still use magnets to steer charged particles into collision, similar to the physicists in the early 1900s. Faraday’s discovery of electromagnetic induction in 1831, the principle that changing magnetic field causes the electric current, has become the fundamental operating principle of electrical motors, generators, and transformers. Using an apparatus built upon this very principle, in 1897, J. J. Thomson deflected cathode rays, and after analyzing the deflection curvature, concluded that the cathode rays were, in fact, a negatively charged stream of particles. Using the same setup, Thomson determined the velocity of the particles and also established the ratio of electric charge to mass. To his and

everyone's surprise, the ratio turned out to be strikingly large. The ratio was also determined to be independent of the cathode material, and the cathode rays were subsequently given a name, electrons. In 1909, through a series of oil-drop experiments, Robert Millikan determined the elementary electric charge (the charge of the electron). By combining this value with the value of the charge-to-mass ratio for the electron, the mass of the electron was calculated to be extremely small<sup>i</sup>.

Establishment of the electron as a fundamental particle of matter generated many speculations on the nature of the atom. As atoms are electrically neutral and much heavier than electrons, it became an interesting puzzle how charge (both negative and compensating positive) and mass were distributed throughout them. Thompson postulated a model, now popularly known as the plum-pudding model, where electrons floated in a cloud (or pudding) of positive charge. In 1909, Ernest Rutherford studied the distribution of electrons in an atom by bombarding very thin foils of gold with a beam of alpha particles and analyzing their scattering patterns. The outcome of the experiment is summarized below:

- The majority of alpha particles penetrated through the foil undeflected
- Some alpha particles experienced slight deflections and few experienced serious deflections
- Very few even bounced back right to the source

Rutherford had expected that most of the alpha particles would pass straight through the foil undeflected, and only a few would be slightly scattered whenever they encountered electrons. The large angle scattering greatly puzzled Rutherford and gave him an impression that alpha particles had rather encountered something small, hard, and heavy. In his words, "It was almost as incredible as if you fired a 15-inch shell at a piece of tissue paper and it came back and hit you" [1]. The nature of his observations led Rutherford to postulate the concept of 'nucleus' and develop a model of atom [2].

Rutherford's postulate of the nucleus in an atom suggested the existence of a positively charged fundamental particle of matter, proton. In 1919, while studying the scattering of alpha particles by nitrogen in the air, Rutherford discovered the proton. He had deduced that protons were freed during the collision of alpha particles with the nuclei of nitrogen atoms. The discovery

---

<sup>i</sup>The mass of the electron is approximately  $9.109 \times 10^{-31}$  kg.

of the proton created a dilemma; the mass of heavier atoms (i.e., other than Hydrogen) was more than the mass of the total number of protons in the nucleus. As the mass of the electron was relatively negligible, Rutherford predicted that electrically neutral fundamental particle, called neutron, was contributing to the mass of the atom.

In 1930, it was discovered that when Beryllium was bombarded with alpha particles, it emitted an energetic stream of radiation. As this radiation was not deflected by magnetic fields and was extremely penetrating, it was initially thought to be a gamma radiation. However, upon further investigation, it was discovered that this radiation was non-ionizing, unlike gamma rays. It was also discovered that when this radiation hit substance rich in protons, like paraffin, the substance would eject protons. Calculations revealed that, for energy and momentum to be conserved, the bombarding radiation needed to be something other than gamma rays. In 1932, James Chadwick used scattering data to calculate the mass of this neutral particle and suggested that this particle was Rutherford's neutron. With the discovery of the neutron by Chadwick, the age-old question "What is matter made of?" had a simple answer: protons, neutrons, and electrons, and brought what we like to call 'the classical era' to an end.

## 2.1.2 The modern era

### 2.1.2.1 Into the jungle

When one question is answered, another begins: if positively charged protons are tightly packed in the nucleus with neutral neutrons, what holds the nucleus together? After all, electromagnetic repulsion between tightly bound protons is strong enough to tear the nucleus apart. A stronger attractive force was postulated to explain this phenomenon, and for lack of a better name, physicists called it the strong force. It was hypothesized that this fundamental force was much stronger than the electromagnetic repulsion and held protons (and neutrons) together in an atom. It was assumed that the strong force was of short range, i.e., the influence of the force dropped rapidly to zero beyond certain short distances; nevertheless, a lack of evidence for such force in everyday life was unsettling.

In 1934, Hideki Yukawa proposed a new theory of the strong force in which protons and neutrons were attracted to one another by the U-field. Just as the electromagnetic field is accompanied by the photon (the exchange particle for the electromagnetic interaction), he assumed that this U-field is accompanied by a new quantum (the particle whose exchange would account for the known properties of the strong force) [3]. Yukawa calculated that the mass of such quantum to be 300 times that of the electron (or about six times lighter than the proton). As its mass was in-between the proton's and electron's, it was later called a ‘meson’<sup>ii</sup>.

In 1937, Neddermeyer and Anderson provided evidence indicating the existence of particles of a new type based on curvature and ionization relations; these particles curved less sharply than electrons but more sharply than protons for particles of the same velocity, and were less massive than protons [4] . In the ‘letter to the editor’ titled “New evidence for the existence of a particle of a mass intermediate between the proton and electron” by Street and Stevenson, the existence of new particle was confirmed [5]. Right away it was thought to be Yukawa’s meson because its mass matched the one predicted by Yukawa. Once again, the universe seems to be back in order; the atom was made of protons, neutrons, and electrons, and Yukawa’s meson glued protons and neutrons together in the nucleus.

A detailed study showed that the properties of the recently discovered particle did not match those predicted by Yukawa; they had the wrong lifetime, and they seemed to be slightly lighter than his prediction. Also, in 1946, it was demonstrated that they reacted very weakly with atomic nuclei. If these particles were the carrier of the strong force, the interaction would have been very strong. It was obvious that they were not Yukawa’s meson, but what were they? In 1947, Powell and his collaborators revealed that they were, in fact, composed of two particles: the pion ( $\pi$ ) and the muon ( $\mu$ ) [6]. Further investigation showed that the pion was Yukawa’s meson, the transmitter of the strong force, and the muon was just a heavier version of the electron that had no role in the nuclear interaction. When looking for one particle (carrier of the strong force), physicists ended up with two on their hands, and no one knew how muons fitted in the grand scheme of nature. Upon the sudden and un-welcomed appearance of the

---

<sup>ii</sup>Meson is a Greek word for the middle. In the similar fashion, electrons are called leptons (light), and protons and neutrons are called baryons (heavy).

muon on the table, everyone was puzzled and whispers of ‘Who ordered that?’ could be heard around physics cafeterias<sup>iii</sup>.

Who had guessed that the unexpected appearance of the muon was the first of many strangers entering into the small particle garden? In December of 1947, Rochester and Butler published ‘Evidence for the Existence of New Unstable Elementary Particles’ that showed a new neutral particle, the kaon  $K^0$ , decaying into a  $\pi^+$  and a  $\pi^-$  [7]. In due course of time, many more mesons were discovered; the  $K^+$ , the  $\eta$ , the  $\omega$ , and the  $\rho$ ’s. In 1950, a particle substantially heavier than the proton, the lambda  $\Lambda$ , was discovered decaying into a  $p^+$  and a  $\pi^-$ . The lambda was classified into the baryon family along with the proton and the neutron. Over the next few years, many more baryons were discovered: the  $\Sigma$ ’s, the  $\Xi$ ’s, and the  $\Delta$ ’s. All the newly discovered mesons and baryons were collectively called ‘strange’ particles; they were strange in the sense that they were produced abundantly but decayed relatively slowly. By early 1960s, physicists were desperately struggling to find the rhyme and the reason in what had grown into a particle jungle and were hoping to find an underlying order in the chaos.

### 2.1.2.2 The quark model

In 1964, Gell-Mann and Zweig independently proposed that all hadrons (mesons and baryons) were composed of elementary constituents, which Gell-Mann called quarks [8]. The proposed quark model had three flavors of quarks: the up quark  $u$  with the charge of  $2/3$ , the down quark  $d$  with the charge of  $-1/3$ , and the strange quark  $s$  with the charge of  $-1/3$ . For each quark  $q$ , there existed corresponding anti-quark  $\bar{q}$  with opposite charge. All mesons and baryons could then be constructed from quarks and anti-quarks by using simple combination rules:

- Mesons were constructed from a quark and an anti-quark; for example,  $\pi^+$  was a combination of a  $u$  quark and a  $\bar{d}$  quark.
- Baryons were constructed from three quarks, and anti-baryons were constructed from three anti-quarks; for example,  $\Delta^+$  was a combination of two  $u$  quarks and a  $d$  quark.

---

<sup>iii</sup>It is, in fact, Nobel laureate I. I. Rabi who famously jokes, "Who ordered that?" in regards to the discovery of the muon.

The quark model was a beautiful piece of theory that had eventually brought order to a rather chaotic particle jungle. However, it suffered from an undeniable flaw: no one had discovered individual quark despite rigorous searches. Theoretically, quarks were easy to produce as they were the building blocks of all hadrons, and they were easy to detect as they had the unique signature of fractional charge. The quark model also had another challenge built within. It had been established that the Pauli exclusion principle applies not only to electrons but also to all particle of half-integer spin. As quarks carried 1/2 spin, the quark model appeared to violate the Pauli exclusion principle by allowing quarks of the same flavor to occupy the same state (for example,  $\Delta^{++}$  was postulated to consist of three  $u$  quarks in the same state). O. W. Greenberg proposed a way around this dilemma by introducing the concept of quark color; quarks not only came in three flavors ( $u$ ,  $d$ , and  $s$ ) but also came in three colors (red, green, and blue)<sup>iv</sup>; then in the example above, the three  $u$  quarks would have three different colors and thus be in three different states.

Although deep inelastic scattering experiments at Stanford Linear Accelerator Center (SLAC) and European Organization for Nuclear Research (CERN) had established that the charge of the proton is concentrated in small lumps, it was not the ‘knight in shining armor’ that physicists at that time were waiting for. The lumps were addressed as partons (not quarks) mostly for the reason that free quarks had yet to be detected, and for many the concept of color seemed like a forced idea. By the early 1970s, the skeptics had started looking for a different model, and the supporter of the quark model has postulated a concept of confinement, an idea that quarks were confined within hadrons.

### 2.1.2.3 The November revolution

By 1974, four leptons ( $e$ ,  $\nu_e$ ,  $\mu$ , and  $\nu_\mu$ ) and their anti-particles had been experimentally detected in laboratories. Although the quark model had incorporated only three quarks ( $d$ ,  $u$ ,  $s$ ), an idea of a fourth quark, called the charm quark  $c$ , had been introduced in 1964 by Bjorken and Glashow [9]. A symmetric universe with four leptons and four quarks as fundamental particles was a gratifying picture, but it was regarded as another desperate attempt of speculations.

---

<sup>iv</sup>The term color is a new property of quarks (like charge) and not the color we experience in our daily life.

What eventually rescued the quark model was not the detection of a free quark or the confirmation of color hypothesis or confinement, but the discovery of the  $J/\psi$  meson in the November of 1974. The  $J/\psi$  was independently discovered by two research groups, one at SLAC, headed by Burton Richter, and one at Brookhaven National Laboratory (BNL), led by Samuel Ting of the Massachusetts Institute of Technology (MIT), for which both shared the Nobel prize in 1976. The  $J/\psi$  was electrically neutral and had two surprising features: it was extremely heavy (more than three times the mass of a proton) and had an unprecedented long lifetime (about 1000 times longer than the lifetime of a particle with comparable mass).

Ten days after the discovery of the  $J/\psi$ , the psi-prime  $\psi'$  was discovered, and soon, three more mesons between the  $J/\psi$  and  $\psi'$  were discovered. The nature of the  $J/\psi$  meson was a subject of enormous theoretical speculations and vigorous experimental activities. The most convincing explanation, in the months following November 1974, was eventually provided by the quark model: the  $J/\psi$  was explained as a bound state of charm and anti-charm quarks,  $J/\psi = (c\bar{c})$ . All other recently discovered mesons were explained as the various states of the charmonium ( $c\bar{c}$ ). The quark model was back in the map, and the universe had regained its symmetric vibe with four leptons and four quarks. However, in 1975, a heavy partner of the electron and muon, the tau lepton  $\tau$ , was discovered [10]. The tau lepton has its own neutrino, so the total count changed to six leptons and four quarks. Even the persistent cynics of the quark model had quietly come to an understanding that more leptons meant more quarks, and surely enough, in 1977, a new heavy meson, named upsilon, was discovered [11]. The upsilon was quickly recognized as the bound state of a new quark, bottom  $b$ ,  $\Upsilon = (b\bar{b})$ . By this time, everyone was anticipating the discovery of the sixth quark, top  $t$ , but the top quark turned out to be extraordinarily heavy (over 40 times the weight of the bottom quark) and too short-lived. The existence of the top quark was finally established by Tevatron in 1995 [12].

## 2.2 Quantum Chromodynamics

Elementary particles interact with each other through four fundamental forces: the strong, electromagnetic, weak, and gravitational. Each force is mediated by the exchange of the mediator particles and is described by physical theories. Quantum electrodynamics, commonly

referred to as QED, is a quantum field theory of the electromagnetic force. Although electromagnetic interactions are complex in nature, they can be reduced to simple symbolic representations of mathematical expressions through Feynman diagrams. For example, all electromagnetic interactions are ultimately reduced to the elementary process shown in Figure 2.1. This Figure is interpreted as: a charged particle  $p$  enters, emits (or absorbs) a photon  $\gamma$ , and exits. It is essential to note that Feynman diagrams enforce the conservation of energy and momentum at each vertex, and reversing a line's direction is equivalent to replacing a particle by its anti-particle.

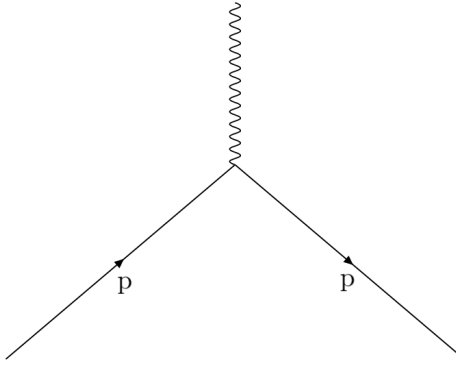


Figure 2.1: Feynman diagram for the elementary QED process.

How can such simple diagrams be useful in calculating complex quantities? Elementary particle interactions boil down to the calculation of decay rates and scattering cross-sections, and the recipe for calculating such transitions is known as Fermi's golden rule. Fermi's golden rule says that a transition rate is given by the product of the phase space and the absolute square of the amplitude. The phase space depends on the mass, energy, and momentum of the participating particles and is purely kinematic. The amplitude, also known as the matrix element, contains dynamical information and is calculated by evaluating relevant Feynman diagrams. To get the amplitude, in layman's terms, one multiplies together a propagator factor for each line and an interaction factor for each vertex of a Feynman diagram.

Quantum chromodynamics (QCD) is a quantum field theory of the strong force. When QCD was in its childhood, during the 1960s, QED was mature enough to be its role model. There are

many similarities between QCD and QED and few crucial differences which will be discussed in due course. Meanwhile, let's step back and peek at the birth of the chromodynamics.

### 2.2.1 The history

#### 2.2.1.1 Quark color

In Section 2.1.2.2 the concept of quark color was briefly mentioned as a solution that respected Pauli exclusion principle. Besides being an elegant solution to this statistical dilemma, introduction of color had solved other problems as well, the most notable two are discussed below.

At a particular collision energy, the ratio of the rate of hadron production to that of muon pairs production,

$$R \equiv \frac{\sigma(e^+e^- \rightarrow \text{hadrons})}{\sigma(e^+e^- \rightarrow \mu^+\mu^-)}, \quad (2.1)$$

is simply given by

$$R(E) = \sum e_q^2, \quad (2.2)$$

where the sum is over all quark species with thresholds below  $E$ . At low energy where only the  $u$ ,  $d$ , and  $s$  quarks contribute<sup>v</sup>, we expect

$$\begin{aligned} R &= e_u^2 + e_d^2 + e_s^2 \\ &= \left(\frac{2}{3}\right)^2 + \left(-\frac{1}{3}\right)^2 + \left(-\frac{1}{3}\right)^2 \\ &= \frac{2}{3}, \end{aligned} \quad (2.3)$$

but if each quark flavor exists in three colors, we expect

$$\begin{aligned} R &= 3(e_u^2 + e_d^2 + e_s^2) \\ &= 3 \left[ \left(\frac{2}{3}\right)^2 + \left(-\frac{1}{3}\right)^2 + \left(-\frac{1}{3}\right)^2 \right] \\ &= 2, \end{aligned} \quad (2.4)$$

Experiment favors the color triplet hypothesis, as shown in Figure 2.2. The factor of three in Equation 2.4 is, in fact, a necessity, and without it, the theory would be far off from data. For

---

<sup>v</sup>For  $\sqrt{s} \leq 3.6 \text{ GeV}$ , only pairs of  $u$ ,  $d$ , and  $s$  quarks are kinematically accessible.

center-of-mass energies  $\sqrt{s} \geq 10$  GeV, one is above the threshold for the production of pairs of  $c$  and  $b$  quarks, and so

$$\begin{aligned} R &= 3(e_u^2 + e_d^2 + e_s^2 + e_c^2 + e_b^2) \\ &= 3 \left[ \left(\frac{2}{3}\right)^2 + \left(-\frac{1}{3}\right)^2 + \left(-\frac{1}{3}\right)^2 + \left(\frac{2}{3}\right)^2 + \left(-\frac{1}{3}\right)^2 \right] \\ &= \frac{11}{3}, \end{aligned} \quad (2.5)$$

which is in excellent agreement with data as shown in Figure 2.2. The factor of 3 counts the number of colors and the ratio in Figure 2.2 provides the compelling experimental evidence that there are three colors for each flavor of quark.

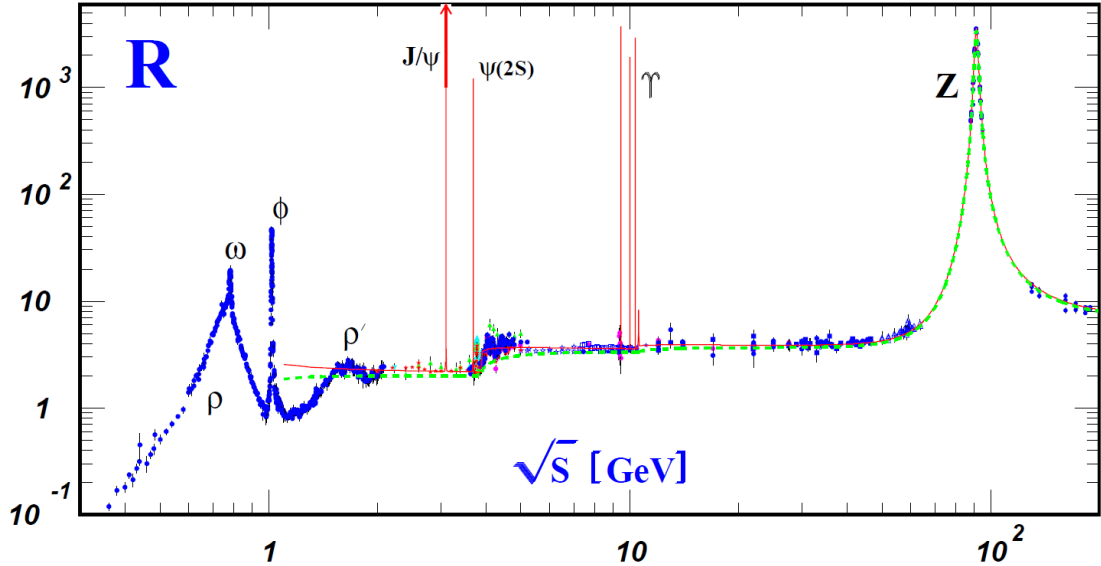


Figure 2.2: The ratio of the rate of hadron production to that of muon pairs, from [13].

The other important measurement to support the quark color hypothesis is the  $\pi^0 \rightarrow \gamma\gamma$  decay rate. The decay  $\pi^0 \rightarrow \gamma\gamma$  proceeds by coupling of the pion to a quark anti-quark loop, as shown in Figure 2.3. This leads to the prediction of the decay rate,

$$\Gamma(\pi^0 \rightarrow \gamma\gamma) = \left(\frac{\alpha}{2\pi}\right)^2 [N_c(e_u^2 - e_d^2)]^2 \frac{M_\pi^3}{8\pi f_\pi}, \quad (2.6)$$

where  $f_\pi \simeq 130$  MeV is the pion decay constant and  $N_c$  is the number of colors. The experimentally measured decay rate is  $7.86 \pm 0.54$  eV. The predicted rate from Equation 2.6 is

$$\Gamma(\pi^0 \rightarrow \gamma\gamma) = \begin{cases} 0.86 \text{ eV}, N_c = 1 \\ 7.75 \text{ eV}, N_c = 3 \end{cases} \quad (2.7)$$

Hence, the measured decay rate supports the existence of three colors of fractionally charged quarks.

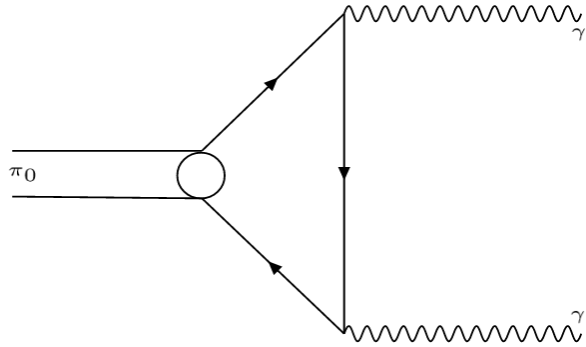


Figure 2.3: Feynman diagram for  $\pi^0$  decay.

### 2.2.1.2 Deep inelastic scattering

Section 2.1.2.2 had briefly mentioned about the deep inelastic scattering experiments performed at SLAC. The surprising feature of the measurement was that the cross-section did not fall off exponentially as the inelasticity of the reaction had increased. Rather, they had a scaling behavior which was indicative of point-like structure inside the target nucleons [14, 15, 16]. Feynman had named these point-like constituents partons.

Let's consider scattering of a high energy charged lepton  $l$  off a hadron target  $N$ ,

$$l + N \rightarrow l' + X, \quad (2.8)$$

for which the kinematic notations are indicated in Figure 2.4. If  $l^\mu$ ,  $l'^\mu$ , and  $p^\mu$  are four-momenta of the incoming lepton, outgoing lepton, and target hadron, respectively, useful variables are: the four-momentum transfer,

$$q^\mu = l^\mu - l'^\mu, \quad (2.9)$$

the four-momentum transfer squared,

$$Q^2 \equiv -q_\mu q^\mu = -q^2, \quad (2.10)$$

the energy loss variable,

$$\nu = q.p = M(E - E'), \quad (2.11)$$

the fraction of hadron's momentum carried by the parton,

$$x = \frac{Q^2}{2\nu} = \frac{Q^2}{2M(E - E')}, \text{ and} \quad (2.12)$$

the fraction of the lepton's energy lost,

$$y = \frac{q.p}{l.p} = 1 - \frac{E}{E'}, \quad (2.13)$$

where  $M$  is the target mass, and the energy variables are in the target rest frame. If the lepton is the electron or muon and the scattering is mediated by the exchange of virtual photon, the inclusive differential lepton scattering cross-section is

$$\frac{d^2\sigma}{dxdy} = \frac{2\pi\alpha^2}{MEx^2y^2} \left[ xy^2F_1 + \left( 1 - y - \frac{M}{2E}xy \right) F_2 \right]. \quad (2.14)$$

The internal hadron structure is encoded in the structure functions  $F_i(x, Q^2)$ , which parametrize the structure of the target as seen by the virtual photon.

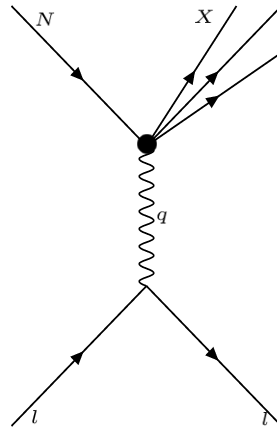


Figure 2.4: Kinematics of the deeply inelastic scattering.

The Bjorken limit is defined as

$$Q^2 \rightarrow \infty \text{ and } \nu \rightarrow \infty, \text{ with } x \text{ fixed.}$$

In 1969, J. Bjorken proposed that in the Bjorken limit, the structure functions should obey the approximate scaling law [17], i.e., they should largely be independent of  $Q^2$ , such that

$$F_i(x, Q^2) \rightarrow F_i(x). \quad (2.15)$$

What Bjorken scaling postulates is that the virtual photon scatters off point-like constituents without substructure; else, changing the energy of the probe should resolve more details about the structure of the proton<sup>vi</sup>. Figure 2.5 shows the  $F_2$  structure function from the SLAC-MIT, BCDMS, H1, and ZEUS collaborations, validating the Bjorken scaling (and hence, the parton model). The data is collected over two decades and the  $Q^2$  value vary by three order of magnitude.

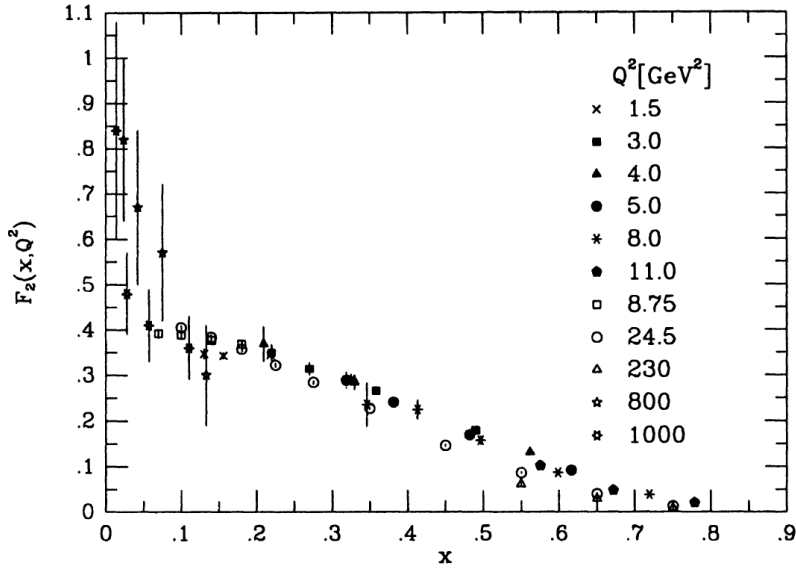


Figure 2.5: The  $F_2$  structure function from the SLAC-MIT, BCDMS, H1, and ZEUS collaborations, from [18]

Once the scaling behavior of the structure functions was understood as due to the lepton scattering off charged point-like particles in the proton, the parton model picture of deep inelastic scattering was formulated in the ‘infinite momentum frame’ in which the proton has a very large momentum. In this frame, the partons have mostly collinear momentum with the proton and carry a fraction of its momentum. Neglecting the proton mass  $M$ , Equation 2.14 is then written as

$$\frac{d^2\sigma}{dxdQ^2} = \frac{4\pi\alpha^2}{Q^4} \left[ [1 + (1 - y)^2]F_1 + \frac{(1 - y)}{x}(F_2 - 2xF_1) \right]. \quad (2.16)$$

---

<sup>vi</sup>The resolving power of a probe is approximately  $\lambda \sim \sqrt{Q^2}$  and the regime  $Q^2 \geq 1 \text{ GeV}^2$  is referred to as deep inelastic regime

Two terms in the square brackets on the right-hand side of Equation 2.16 correspond to the absorption of transversely polarized ( $F_1$ ) and longitudinally polarized ( $F_2 - 2xF_1$ ) virtual photons. If partons were spin-0, they could not absorb transversely polarized vector bosons and would have  $F_1 = 0$ . Instead, if partons were spin-1/2, they could not absorb longitudinally polarized vector bosons and would have  $F_2 = 2xF_1$ . The last relation ( $F_2 = 2xF_1$ ) is called the Callan-Gross relation and was suggested by Callan and Gross in 1969 [19]. This relation was later confirmed experimentally, as shown in Figure 2.6.

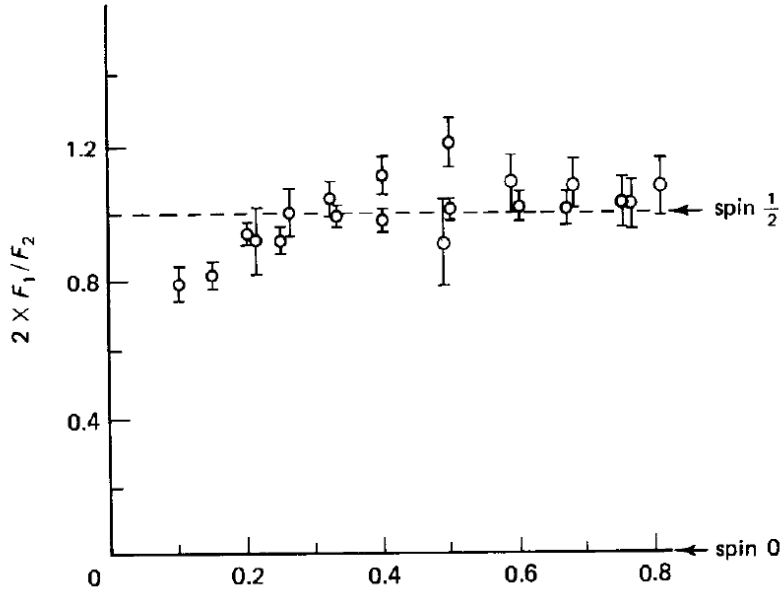


Figure 2.6: The ratio  $2xF_1/F_2$ , from [20]

The importance of the Bjorken scaling and Callan-Gross formula lies in the fact that they provide clear experimental tests for the parton model. What we can conclude from these tests is that protons do have charged constituents, and those constituents behave as point-like spin-1/2 particles.

The structure functions can be constructed at a more basic level from the probability density,  $p_i(x)$ , the probability of finding a parton of type  $i$  with momentum fraction  $x$  via

$$F_2(x) = \sum_i e_i^2 x p_i(x). \quad (2.17)$$

Equation 2.17 can be written as

$$\int_0^1 F_2(x) dx = \int_0^1 \sum_i e_i^2 x p_i(x) dx. \quad (2.18)$$

As the proton consists of two up quarks and one down quark, the average momentum carried by up quarks is twice the average momentum carried by the down quark, such that

$$\int_0^1 x p_u(x) dx = 2 \int_0^1 x p_d(x) dx. \quad (2.19)$$

Equation 2.18 can then be written as

$$\begin{aligned} \int_0^1 F_2(x) dx &= \int_0^1 \left(\frac{2}{3}\right)^2 x p_u(x) dx + \int_0^1 \left(-\frac{1}{3}\right)^2 x p_d(x) dx \\ &= \int_0^1 2 \left(\frac{2}{3}\right)^2 x p_d(x) dx + \int_0^1 \left(-\frac{1}{3}\right)^2 x p_d(x) dx \\ &= \int_0^1 x p_d(x) dx \end{aligned} \quad (2.20)$$

From [20], the area under  $F_2$  distribution is 0.18, hence

$$\int_0^1 x p_d(x) dx = 0.18 \text{ and } \int_0^1 x p_u(x) dx = 0.36. \quad (2.21)$$

The average total momentum carried by the quarks is then

$$\int_0^1 x p_u(x) p dx + \int_0^1 x p_d(x) p dx = (0.18 + 0.36) p = 0.54 p. \quad (2.22)$$

So, on average, the quarks carry only 54% of the proton's momentum. The question that immediately follows is "Who has the rest of it?" The rest, in fact, is attributed to gluon constituents. As gluons are neutral, they are not directly measured in the deep inelastic lepton-hadron scattering. The structure functions allow us to determine the momentum carried by charged partons, whatever left is attributed to uncharged partons. Thus, in an indirect way, the deep inelastic scattering experiments provide an early evidence for the existence of gluons, the mediators of the strong force.

### 2.2.2 The basis

The strong interaction that binds quarks and gluons inside hadrons is the strongest of the four fundamental forces of nature. A theoretical description of the strong interaction by a

quantum field theory, called Quantum Chromodynamics (QCD), was presented by Fritzsch and Gell-Mann in 1973 [21].

Constructing a Lagrangian  $\mathcal{L}$  based on some underlying symmetries is the starting point of any quantum field theory. QCD is the gauge field that describes the strong interactions of colored quarks and gluons for which the Lagrangian density,

$$\mathcal{L} = \sum_q \bar{\psi}_{q,a} (i\gamma^\mu \partial_\mu \delta_{ab} - g_s \gamma^\mu t_{ab}^C \mathcal{A}_\mu^C - m_q \delta_{ab}) \psi_{q,b} - \frac{1}{4} F_{\mu\nu}^A F^{A\mu\nu}, \quad (2.23)$$

where repeated indices are summed over. The  $\psi_{q,b}$  are quark-field spinors for a quark of flavor  $q$  and mass  $m_q$ , with a color index  $a$  that runs from  $a = 1$  to  $N_c = 3$  (quarks comes in three colors). The  $\gamma^\mu$  are the Dirac  $\gamma$ -matrices which express the vector nature of the strong interaction. The  $\mathcal{A}_\mu^C$  correspond to the gluon fields, with  $C$  running from 1 to  $N_C^2 - 1 = 8$  (there are eight kinds of gluons). The  $t_{ab}^C$  correspond to eight  $3 \times 3$  matrices and are the generators of the SU(3) color group. They encode the fact that a gluon's interaction with a quark rotates the quark's color in SU(3) space. The quantity  $g_s$  (or  $\alpha_s = g_s/4\pi$ ) is the QCD coupling constant. The field tensor  $F_{\mu\nu}^A$  is given by

$$F_{\mu\nu}^A = \partial_\mu \mathcal{A}_\nu^A - \partial_\nu \mathcal{A}_\mu^A - g_s f_{ABC} \mathcal{A}_\mu^B \mathcal{A}_\nu^C, \quad (2.24)$$

where  $f_{ABC}$  are the structure constants of the SU(3) group defined by  $[t_A, t_B] = i f_{ABC} t_C$  for the eight  $3 \times 3$  generators  $t_A$ . Note that in this description of QCD Lagrangian, for simplicity, we have omitted ghost fields and possible gauge fixing terms, which are introduced during the quantization of the theory [22].

### 2.2.2.1 Renormalization

In quantum field theories like QCD, physical quantities such as cross-section, decay rates, jet production rates, etc., can be expressed in a perturbation series in powers of the coupling parameter  $\alpha_s$ . Let one of such physical quantities be  $\mathcal{R}$ , which is dimensionless and depends on  $\alpha_s$  and energy scale  $Q$ . Let the scale  $Q$  be much larger than all other dimensional parameters, such as quark masses, and also, let the quark masses be set to zero.

When calculating  $\mathcal{R}$  as a perturbation series in  $\alpha_s$ , ultraviolet divergences occur, and the series require renormalization to remove these divergences. Renormalization procedure introduces a renormalization scale  $\mu$ , and hence,  $\mathcal{R}$  becomes a function of  $Q^2/\mu^2$ .

The fundamental parameters of QCD are the coupling  $\alpha_s$  and the quark masses. As the choice of  $\mu$  is arbitrary and the Lagrangian of QCD makes no mention of this scale,  $\mathcal{R}$  cannot depend on the choice made for  $\mu$  such that

$$\mu^2 \frac{d}{d\mu^2} \mathcal{R}(Q^2/\mu^2, \alpha_s) = \left( \mu^2 \frac{\partial}{\partial \mu^2} + \mu^2 \frac{\partial \alpha_s}{\partial \mu^2} \frac{\partial}{\partial \alpha_s} \right) \mathcal{R} = 0, \quad (2.25)$$

where the derivative is multiplied with  $\mu^2$  in order to keep the expression dimensionless. Equation 2.25 implies that any dependence of  $\mathcal{R}$  on  $\mu$  must be canceled by an appropriate  $\mu$ -dependence of  $\alpha_s$  to all orders. In a case where  $\mu^2 = Q^2$ ,  $\alpha_s$  transforms to the ‘running coupling constant’  $\alpha_s(Q^2)$  and the energy scale dependence of  $\mathcal{R}$  enters through the energy dependence of  $\alpha_s(Q^2)$  [23].

The running of the coupling constant  $\alpha_s$  is determined by the renormalization group equation,

$$Q^2 \frac{\partial \alpha_s}{\partial Q^2} = \beta(\alpha_s) \quad (2.26)$$

In QCD, the  $\beta$  function has the perturbation expansion [24, 25]

$$\beta(\alpha_s) = -b\alpha_s^2(1 + b'\alpha_s + b''\alpha_s^2 + O(\alpha_s^3)), \quad (2.27)$$

where  $b = (11n - 2f)/12\pi$ ,  $n$  is the number of colors, and  $f$  is the number of active quark flavors at the energy scale  $Q$ .

### 2.2.2.2 Asymptotic freedom

A solution of Equation 2.26 in the one-loop approximation, i.e., neglecting  $b'$  and higher order terms, is

$$\alpha_s(Q^2) = \alpha_s(\mu^2) \frac{1}{1 + \alpha_s(\mu^2) b \ln(\frac{Q^2}{\mu^2})} \quad (2.28)$$

Figure 2.7 shows some of the diagrams which contribute to the  $\beta$  function of QCD in one-loop approximation. Equation 2.28 gives the relation between  $\alpha_s(Q^2)$  and  $\alpha_s(\mu^2)$  if both are in



Figure 2.7: Feynman diagrams which contribute to the  $\beta$  function in the one loop approximation.

the perturbative region. It also highlights the property of asymptotic freedom: if  $Q^2$  becomes large and  $b$  is positive (i.e., if  $f < 17$ ),  $\alpha_s(Q^2)$  will asymptotically decrease to zero. With negative  $b$ , the coupling would increase at large  $Q^2$ .

What is the physical origin of asymptotic freedom? The loop diagram, as in Figure 2.8, makes the effective color charge of the quark a function of the momentum transfer. The coupling strength increases as quarks get closer together because the quark anti-quark bubbles partially screen the quark color charge. As QCD can have direct gluon-gluon vertices, gluon loop diagrams, like in Figure 2.10, are also included. It turns out that the gluon contribution works in the opposite direction, producing the anti-screening effect: while the quark polarization drives  $\alpha_s$  up at short distances, the gluon polarization drives it down. Since quark polarization depends on the number of quark flavors  $f$  and gluon polarization depends on the number of colors  $n$ , like mentioned earlier, the critical parameter turns out to be  $b \approx 11n - 2f$ . As in the Standard Model,  $n = 3$ ,  $f = 6$ , and so,  $b = 21$ , the QCD coupling decreases at short distances, leading to asymptotic freedom.

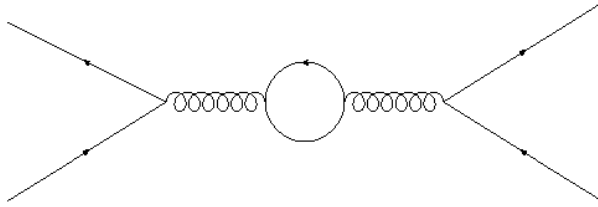


Figure 2.8: Quark polarization in QCD.

Equation 2.28 tells how the coupling constant varies with the energy scale, but does not provide the absolute value itself. The absolute value of coupling constant is obtained from

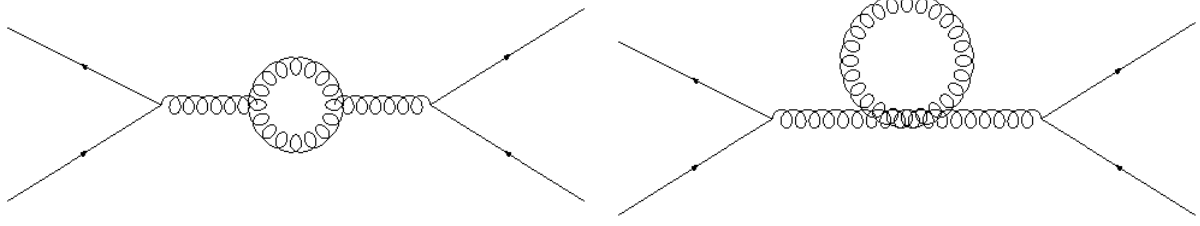


Figure 2.10: Gluon polarization in QCD.

experiments by a convenient reference scale, like the mass of the  $Z^0$  boson ( $\mu = M_Z$ ), which is large enough to be in the perturbative domain. If we define a scale  $\Lambda^2$  by

$$1 = \alpha_s(\mu^2) b \ln(\mu^2/\Lambda^2),$$

Equation 2.28 can be written as

$$\alpha_s(Q^2) = \frac{1}{b \ln(Q^2/\Lambda^2)}. \quad (2.29)$$

Hence, the  $\Lambda$  parameter is technically identical to the energy scale  $Q$  where  $\alpha_s(Q^2)$  diverges to infinity,  $\alpha_s(Q^2) \rightarrow \infty$ , for  $Q^2 \rightarrow \Lambda^2$ . The parametrization of the running coupling  $\alpha_s(Q^2)$  with  $\Lambda$  instead of  $\alpha_s(\mu^2)$  has become a standard. A summary of the  $Q^2$  dependence of  $\alpha_s$  from experiments is shown in Figure 2.11. The world average for the value of the strong coupling constant at the  $Z$  boson mass scale is [26]

$$\alpha_s(M_Z) = 0.1184 \pm 0.0007. \quad (2.30)$$

### 2.2.3 Experimental evidence for QCD

One of the first experimental signatures proposed to test QCD was the violation of approximate scaling of the proton structure function [27]. In Section 2.2.1.2, it was noted that the deep inelastic lepton-nucleon scattering process depends on two kinematic parameters: the momentum transfer  $Q^2$  between the lepton and the struck quark, and the fraction of the proton's momentum  $x$  that is carried by the struck quark. The structure function  $F_2$  of the proton parametrizes the population of quarks with momentum  $x$  as a function of  $Q^2$ . QCD predicts that as  $Q^2$  grows, the structure functions undergo a characteristic evolution. At large values of  $x$

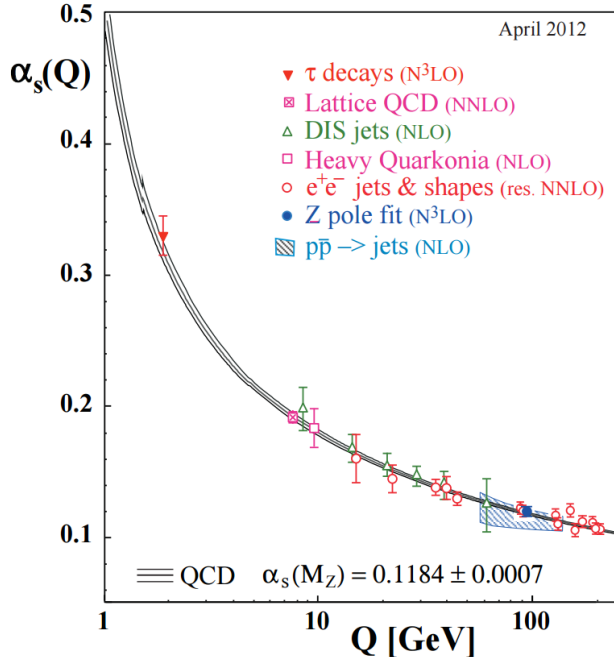


Figure 2.11: Summary of measurements of  $\alpha_s$  as a function of the energy scale  $Q$ , from [26].

( $0.3 \lesssim x < 1$ ), the uncertainty principle makes it increasingly likely that a quark with momentum fraction  $x$  will be caught in mid-dissociation into a quark and a gluon. For small values of  $x$ , the population of both quarks and anti-quarks will be enhanced by the virtual dissociation of a gluon into a quark and an anti-quark. What this means is that as  $Q^2$  increases, the structure function should fall at large values of  $x$  and rise at small values of  $x$ .

Historically, the limited range of fixed-target lepton-nucleon scattering experiments in  $x$  and  $Q^2$  had prevented unambiguous tests of QCD scaling violations [28]. However, this changed dramatically when the HERA electron-proton and positron-proton collider started operation in 1991, with lepton beam energy of 30 GeV and protons of 920 GeV.

A recent summary of measurements of the proton structure function  $F_2$  is given in Figure 2.12. The measurements cover a large parameter space in both  $x$  and  $Q^2$ . The scaling violation predicted by QCD, mainly a strong increase in  $F_2$  with increasing  $Q^2$  at small  $x$ , and a decrease in  $F_2$  at  $x > 0.1$ , is clearly in strong agreement with the data.

Another important evidence of QCD was provided by the angular distribution of hadron jets in electron-positron annihilation. As quarks are confined in hadrons and cannot be detected in

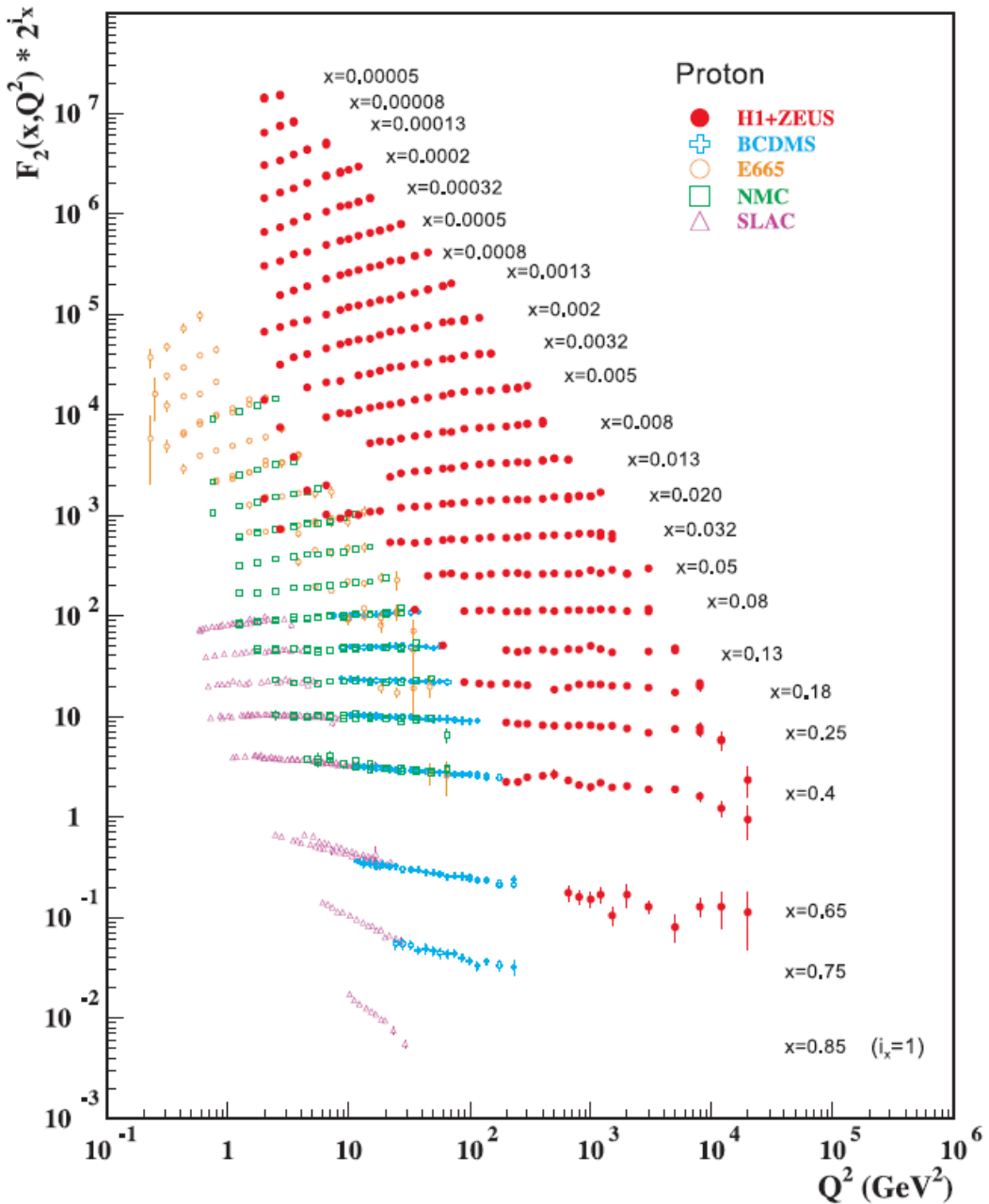


Figure 2.12: The proton structure function  $F_2$  measured in electromagnetic scattering of electrons and positrons on protons, from [26].

experiments as free particles, observing the jet of hadrons into which quarks fragments is the nearest approach to observing a free isolated quark. One of the earliest evidence for jets was found in  $e^+e^-$  annihilation at high energies, in which jets emerged back-to-back with total jet production cross-section and angular distribution identical to that for the production of point-like quark anti-quark pairs[29, 30]. When electrons and protons collide at sufficiently high energy, they can produce a pair of quarks:  $e^+ + e^- \rightarrow q + \bar{q}$ . Initially, these quarks fly apart as free particles, but once they reach a separation distance of  $\approx 10 \times 10^{-15}$  m, they subsequently fragment into hadrons, producing the two distinct jets.

The three-jet event observed in these  $e^+e^-$  annihilations were interpreted as evidence for the process

$$e^+ + e^- \rightarrow q\bar{q} + \text{gluon}, \quad (2.31)$$

in which the gluon is radiated from the outgoing quark in a QCD analogy of the QED bremsstrahlung. Observation of these three-jet events was quantitative confirmation of the hard gluon bremsstrahlung predicted by the leading order QCD, and one of the first experimental evidence for the existence of the gluon.

### 2.3 The Standard Model

The current understanding of the constituents of matter and their interactions is established in a theoretical framework called the Standard Model (SM). According to the SM, the matter is made out of three kinds of elementary particles: quarks, leptons, and mediators. Figure 2.13 summarizes the particles and force carriers of the SM. It shows the quarks and leptons classified into three generations and also some of their physical properties. Note that all charge signs would be reversed for anti-quarks and anti-leptons. There are six leptons and six anti-leptons, making 12 total leptons. There are six flavors of quarks, and as each quark and anti-quark come in three colors, there are 36 of quarks in total. Finally, every interaction has its mediator: eight gluons for the strong force, the photon for the electromagnetic force, two  $W$ 's and a  $Z$  for the weak force, and presumably the graviton for the gravity<sup>vii</sup>.

---

<sup>vii</sup>Gravity is not included in the Standard Model.

The Higgs boson is the quantum of the scalar Higgs field. At a seminar held on 4 July 2012, the ATLAS and CMS experiments at the LHC announced that they had observed a new particle, a boson consistent with the Higgs boson. In March 2013, CERN officially announced that the new particle was indeed a Higgs boson.

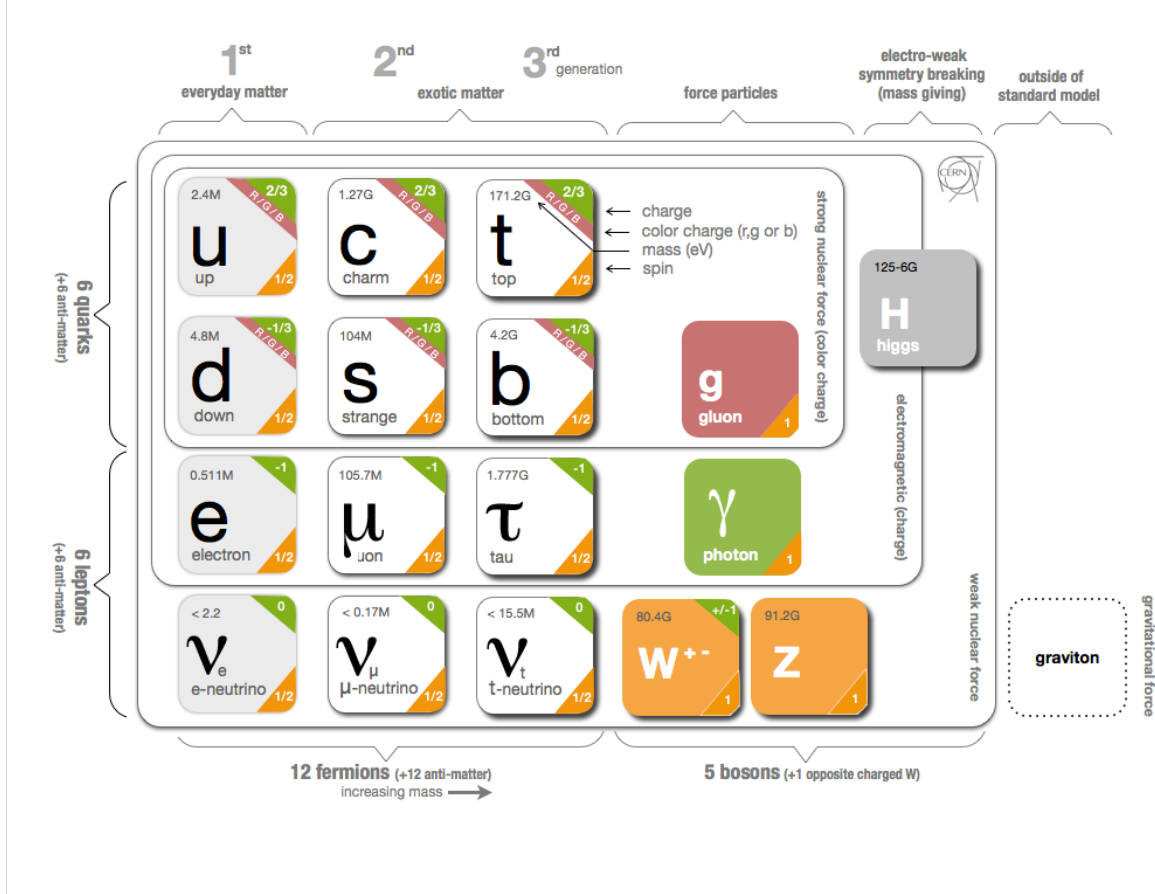


Figure 2.13: The particles and force carriers of the Standard Model, from [31].

## 2.4 The Quark-Gluon Plasma

The other side of asymptotic freedom, the property that the interaction between colored particles becomes weaker at shorter distances (as discussed in Section 2.2.2.2), is color confinement [32], the property that the interaction between colored particles becomes stronger at larger distances. As a consequence of color confinement, isolated free quarks and gluons cannot exist in nature. The concept of confinement can be illustrated with the phenomenological potential

for the strong interaction,

$$V_s = -\frac{4}{3} \frac{\alpha_s}{r} + kr, \quad (2.32)$$

where the first term dominates at the small distance  $r$  and is similar to the Coulomb potential. The second term increases indefinitely at large distance and is associated with the confinement of quarks and gluons inside a hadron.

Suppose, for example, someone is trying to separate a quark from a quark anti-quark pair in a color singlet state. As the quark is pulled apart from the anti-quark, the distance between them gets larger, and hence, the interaction between them becomes stronger. Analogues to a spring breaking into two springs when stretched beyond its elastic limit, in the case of quark anti-quark pair, it becomes energetically more favorable to form a new quark anti-quark pair when pulled beyond a certain distance. Part of the stored energy  $kr$  goes into the creation of a new pair and as a consequence, rather than having isolated quarks and anti-quarks, new color neutral particles are produced.

If quarks are bound within hadrons, what happens to them when the hadronic density is dramatically increased such that hadrons begin to overlap, and each quark finds within its immediate proximity a considerable number of other quarks? After the discovery of asymptotic freedom property of QCD, the existence of a deconfined state of quarks and gluons was predicted at high pressure and high temperature [33, 34, 35]. At sufficiently high pressure or temperature, quarks and gluons were predicted to interact weakly and the system to behave as an ideal ultra-relativistic gas. This ultra-dense form of matter with deconfined quarks and gluons was later called the Quark-Gluon Plasma (QGP) [36, 37].

At low temperature or pressure, quarks are confined within hadrons and at high temperature or pressure, quarks are deconfined. Although the prediction of a QGP state is based on perturbative QCD, its properties cannot be predicted perturbatively. However, the treatment of the non-perturbative regime of QCD can be made in a fundamental way by lattice QCD (LQCD) calculations, where the space-time continuum is discretized into a finite number of points in which the theory of QCD is formulated. A LQCD calculation is shown in Figure 2.14. It shows a sudden rise of the energy density  $\epsilon/T^4$  at a critical temperature  $T_c \approx 170$  MeV ( $\approx 10 \times 10^{12}$  K) for different numbers of quark flavors. The sudden rise of the energy density is

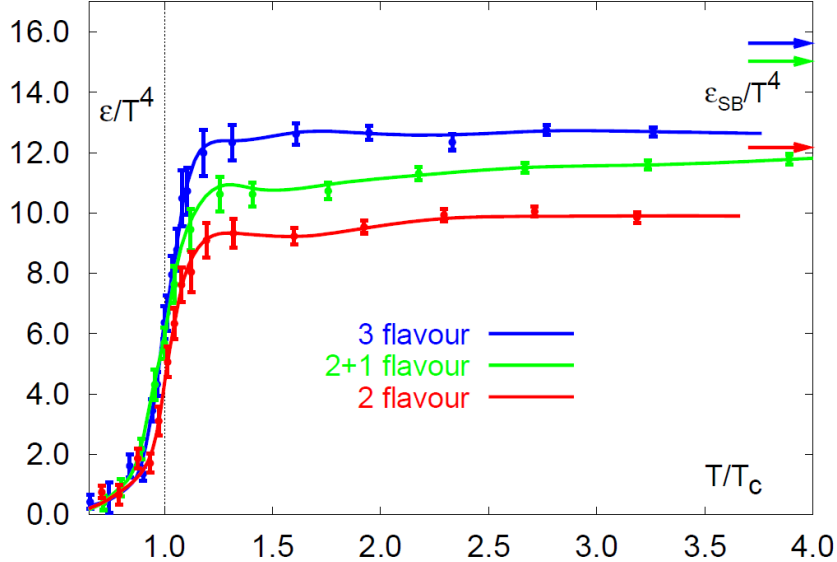


Figure 2.14: Lattice QCD prediction for the dependence of the energy density  $\epsilon$  on the temperature  $T$  for three different quark configurations, from [38].

interpreted as the phase transition from the hadronic state into the deconfined QGP phase. This transition temperature corresponds to an energy density  $\epsilon \approx 1 \text{ GeV/fm}^3$ , nearly an order of magnitude larger than that of a normal nuclear matter. The value of  $\epsilon/T^4$  is shown to plateau at  $\sim 80\%$  of the Stephan-Boltzmann limit (indicated by arrows), which describes the expectation for an ideal gas with quarks and gluons. The deviation from this limit suggests that the QGP is rather strongly coupled and not a free gas of weakly interacting quarks and gluons as originally suggested.

Does the transition from the hadron gas to the QGP take place smoothly or via a phase transition? This is one of the most important but difficult questions for non-perturbative QCD. Recent developments in LQCD indicate that the equation of state shows a critical point at a finite baryo-chemical potential  $\mu_B$ , where the crossover becomes a second order phase transition, and beyond it, the transition becomes a first order phase transition [39]. Figure 2.15 shows a schematic of the current understanding of the phase diagram for the transition from a hadron gas to the QGP. For small  $T$  and  $\mu_B$  the system is in the hadronic phase, for large  $T$  it is in QGP phase, and for small  $T$  and large  $\mu_B$  color superconductivity is conjectured. The small

$\mu_B$  region indicates the crossover transition and this transition is connected to the first order phase transition at larger  $\mu_B$  by a critical point.

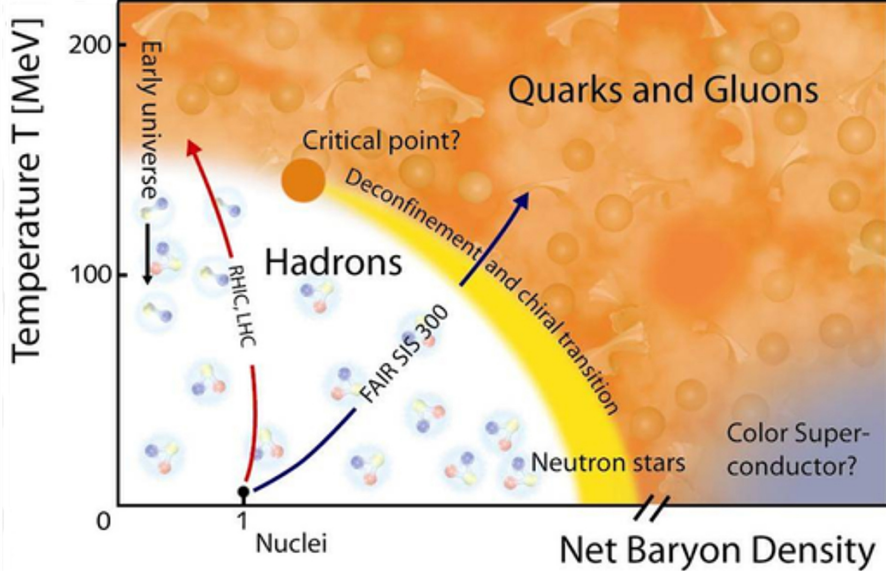


Figure 2.15: Schematic of QCD phase diagram, from [40].

## 2.5 Ultra-relativistic heavy ion collisions

To create the QGP in a laboratory, an energy density of about  $1 \text{ GeV/fm}^3$  has to be reached, which is accessible in collisions of heavy ions at ultra-relativistic energies. The formation of the QGP in the relativistic nucleus-nucleus collision can be explained following the scenario originally outlined by J.D. Bjorken [41]. If the system is formed after some formation time  $t_f$ , the energy density in the overlap region can be estimated as

$$\epsilon = \frac{1}{\pi R^2 t_f} \frac{dE_T}{dy}, \quad (2.33)$$

where  $R(\sim 1.18A^{1/3} \text{ fm})$  is the nuclear radius and  $\frac{dE_T}{dy}$  is the transverse energy produced per unit of rapidity. For Au+Au collisions at RHIC,  $\frac{dE_T}{dy}$  measured by PHENIX at  $\sqrt{s_{NN}} = 130 \text{ GeV}$  is 688 GeV [42]. If the formation time is in the order of  $0.1 \text{ fm/c}$ , the energy density is estimated to be  $\epsilon = 4.6 \text{ GeV/fm}^3$ . The Stefan-Boltzmann equation of state gives the temperature of the

medium as

$$T \simeq \left[ \frac{\epsilon (\hbar c)^3}{\alpha} \right]^{1/4}, \quad (2.34)$$

where  $\alpha$  is a constant of proportionality determined by the effective number of degree of freedom. Since the lattice results indicate that Stefan-Boltzmann limit is not reached (as shown in Figure 2.14), the estimated value just above the transition region is taken such that  $\alpha = \epsilon/T^4 \simeq 13$ . The temperature of the medium is then estimated to be 225 MeV from Equation 2.34.

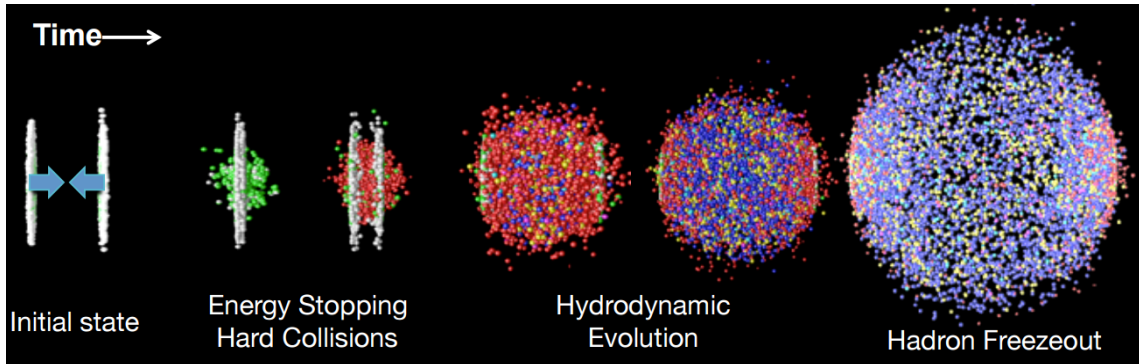


Figure 2.16: Visualization of different stages of heavy ion collision, from [43].

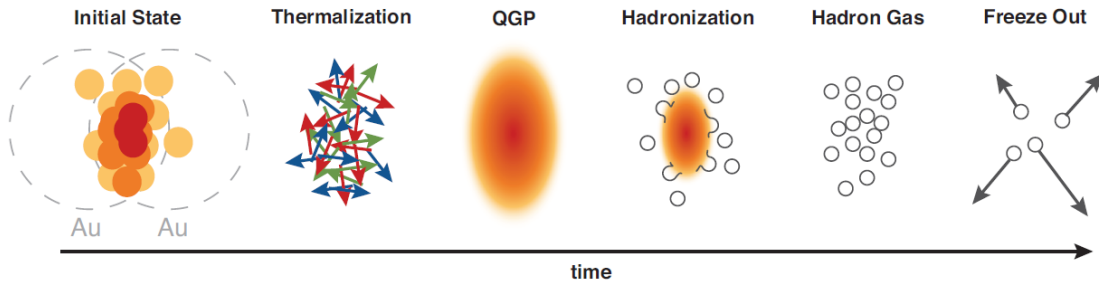


Figure 2.17: Schematic of different stages of heavy ion collision (beam axis view), from [44].

Figure 2.16 gives a visualization and Figure 2.17 gives a schematic of different stages of heavy ion collision. Note that at ultra-relativistic energies, nuclei appear as pancakes in the center-of-mass frame due to Lorentz contraction, and the system go through the different stages in a course of just  $\sim 10 \times 10^{-23}$  s (or  $\sim 10$  fm/c). Below is a brief description of each stage summarized from [44]:

1. **Initial state:** The initial state plays an important role in the creation of initial energy that later evolves and dissipates. There are many descriptions of the initial state, including hard sphere, Wood-Saxon, Glauber, and Color Glass. The Glauber model is one of the models that is relevant to this dissertation and will be discussed in detail later.
2. **Thermalization:** The nuclei move through each other on a time scale of  $\sim 0.1 \text{ fm}/c$  in the center-of-mass reference frame, during which a large energy is deposited in the collision zone. The deposited energy is dense and localized but not thermal. One of the suggested processes for thermalization in the framework of perturbative QCD is ‘bottom-up’ [45]. In the limit  $Q_s \gg \Lambda_{\text{QCD}}$ <sup>viii</sup>, where the scale  $Q_s$  is the saturation scale, thermalization occurs relatively fast while the system is still undergoing one-dimensional expansion. Formation of the QGP starts at  $\tau \sim Q_s^{-1}$  dominated by hard gluons freed from the nuclei with momenta  $p \sim Q_s$ . At time  $\tau \sim \alpha^{-5/2} Q_s^{-1}$ , the emission of soft gluons overwhelm (in terms of number) the primary hard gluons. These soft gluons then quickly equilibrate and form a thermal bath, which initially carries only a small fraction of the total energy. The thermal bath then draws energy from the hard gluons. At  $\tau \sim \alpha^{-13/5} Q_s^{-1}$ , full thermalization is achieved when the primary hard gluons have lost all their energy. At this time, the temperature of the system achieves its maximal value of  $\alpha^{2/5} Q_s$ . Hydrodynamic descriptions, which describe heavy ion measurements very well, suggest rapid thermalization in a remarkably short timescale (about 0.6 fm), but most theories, including bottom-up, have not been able to explain the fast thermalization process. Also, the bottom-up scenario overlooks the possibility that collective processes (as opposed to sequences of individual collisions) can play a significant role in the equilibration of the plasma. Plasma instabilities in the QGP have been suggested as one of the possibilities for a mechanism that speeds the arrival of thermalization [46]. A plasma instability results from the rapid growth of a particular spatial mode of charge or current, and the collective effect of these within the soft gluon plasma allows hard gluons to begin scattering at earlier times than otherwise suggested in other scenarios.

---

<sup>viii</sup>This corresponds to a very large nuclei or a very high collision energy.

3. **QGP:** After the thermalization of the deconfined matter, if the temperature and lifetime are sufficient, the QGP phase follows. Some of the key signatures of the QGP will be discussed in Section 2.5.1.
4. **Hadronization:** As the QGP cools through physical expansion and photon radiation, its decreasing energy density becomes unable to sustain deconfinement, and the hadronization process begins. The hadronization process takes the deconfined matter in the QGP and repackages it into color neutral particles. Hadronization in heavy ion environment is divided into two mechanisms: fragmentation and recombination [47].

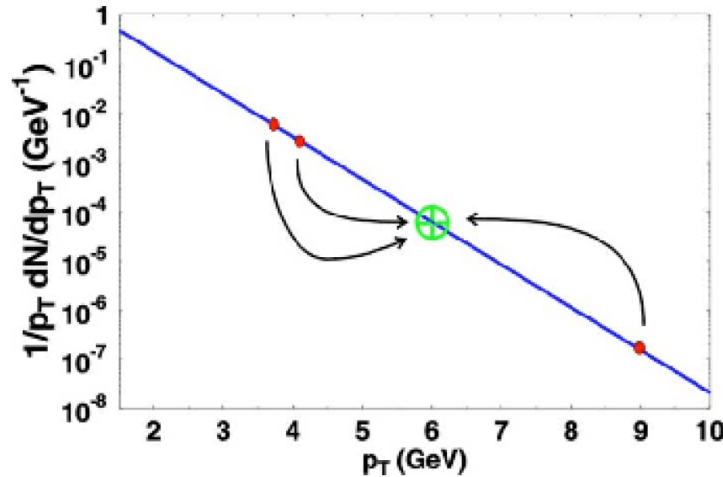


Figure 2.18: A schematic of recombination and fragmentation for a meson at  $p_T \approx 6$  GeV/c, from [48].

In the fragmentation mechanism of hadronization, an outgoing high energy parton initiates the creation of quark anti-quark pairs until there is a jet of partons, which finally turn into hadrons. As multiple final state hadrons come from each fragmenting parton, hadrons' momentum must be less than the parent parton's momentum. Recombination is the idea that the color neutral final state hadrons are produced from valence quarks of the deconfined medium. Recombination involves adding quark momenta together; each valence quark adds its momentum to the final hadron's momentum. Figure 2.18 shows the recombination and fragmentation for a meson at  $p_T \approx 6$  GeV/c. The fragmentation mechanism requires a single parton with  $p_T$  larger than 6 GeV/c to start with while the

recombination is possible with two partons of roughly  $3\text{ GeV}/c$  each. Hence, recombination is expected to dominate as long as the parton's  $p_T$  spectrum is of exponential form and the fragmentation is expected to become more significant for power-law spectrum due to the enhancement of high  $p_T$  partons [49].

5. **Hadron gas:** If hadrons are produced at sufficient density, hadron gas phase follows, and hadrons collide at a high rate and start behaving in a collective manner. However, if the density of the hadronization phase is too small or the radial expansion too rapid, this stage may exist only briefly (or not at all), and its effects on final state measurement may be small or negligible.
6. **Freeze out:** Freeze out is the final stage of the collision and comes in two varieties: chemical and kinetic. Chemical freeze out describes the point where inelastic processes, which convert one kind of hadronic species into a different one, cease. Kinetic freeze out end even the elastic collisions, momenta of particles stop changing, and free flight of the final state particles to the detector begins.

### 2.5.1 Signatures of the Quark-Gluon Plasma

Observing the formation of the QGP and studying its properties is an enormous experimental challenge as the volume of QGP formed in laboratories is expected to be small, at most a few femtometers in diameter, and its lifetime is expected to be between  $5\text{ fm}/c$  and  $10\text{ fm}/c$ . Additionally, all signals emerging from the plasma have to compete with the background from the hot hadronic gas phase. Nevertheless, identification and investigation of the short-lived QGP have been a vital topic of discussion, and a lot of experimental tools have been developed in the last two decades. Signatures (or signals) of the QGP can be classified in the following way [50]:

- Signals sensitive to the equation of state
- Signals of chiral symmetry restoration
  - Strangeness Enhancement, disoriented chiral condensates
- Probes of the electromagnetic response function
  - Lepton pairs, direct photon

- Probes of the color response function
  - Quarkonium suppression, energy loss of a fast parton
- Various other signatures

As it is not the intention of this dissertation to present an exhaustive review of signatures of the QGP, only two key signatures are discussed in the sections below.

### 2.5.1.1 Quarkonia suppression

Quarkonia are bound states of two heavy quarks:  $c\bar{c}$  for the family  $J/\psi$ ,  $\psi(2S)$ ,  $\chi_c$ , etc, and the states  $b\bar{b}$  for the family  $\Upsilon$ 's and  $\chi_b$ . It should be noted that the bound state  $t\bar{t}$  is predicted not to exist due to the short lifetime of the top quark. Quarkonia are produced early in the heavy ion collisions, and if they evolve through the deconfined medium, the yields should be suppressed in comparison with those in  $p+p$  collisions. The first such measurement was the  $J/\psi$  suppression discovered at the SPS, which was considered to be a hint of QGP formation. The PHENIX measurement later showed the same suppression at a much higher energy[51]. These observations were consistent with the scenario that at higher collision energies, the expected greater suppression is compensated by  $J/\psi$  regeneration through recombination of two independently produced charm quarks [52]. Since the first Pb+Pb collisions at the LHC, a wealth of quarkonia results has become available [53, 54]. The suppression of quarkonia in the QGP is understood in terms of color screening models [55], and alternatively in terms of quarkonium dissociation by collisions with gluons [56].

### 2.5.1.2 Energy loss of a fast parton

Another possible way of probing the color structure of QCD matter is by investigating the energy loss of a fast parton. Bjorken had predicted that the energy loss would proceed by elastic scattering of quarks in the QGP. It was later realized that induced gluon bremsstrahlung should dominate energy loss [57]; however, with an exception of heavy quarks in which elastic collisional energy loss could prevail [58]. It was also recognized that if the characteristic time of gluon emission was long enough, then one needed to consider coherence. This coherence, known as the Landau-Pomeranchuk-Migdal (LPM) effect, further enhances the significance of

energy loss through radiation. LMP effect predicts that the energy loss for the static medium depends on the path-length squared, and the dependence may reduce to linear for an expanding medium [59].

Many competing models of energy loss have been developed since the beginning of QCD, and GLV [60] and BDMPS [59] are often considered as limits. In the GLV model, the parton experience a finite number of scatterings and the energy loss is evaluated as an expansion in the opacity. The number of scattering centers per unit length is considered the relevant medium property. The BDMPS model treats the energy loss as a smooth process, and the energy loss is commonly reported as a function of transport coefficient  $\hat{q}$ , which is the average momentum transfer per unit length in the medium.

The energy loss is also expected to depend on the nature of parton. The gluon is expected to exhibit larger energy loss per unit length than quarks. As for quarks, heavy quarks are expected to lose less energy than light quarks due to the absence of gluon radiation at forward angles. This phenomenon is called dead-cone effect and is expected to be relatively large for beauty quarks than for charm quarks.

In the vacuum, the hard scattered parton creates a shower of partons that eventually form a jet of hadrons. In the QGP, the low energy portion of the shower may eventually be equilibrated into the medium leading to modifications in the jet of hadrons. The measurement of jet probes is thus fundamental to understanding various aspects of the medium. In the next section, jets and jet quenching (the significant loss of energy by fast parton traversing the QGP) will be discussed in detail.

## 2.6 Jets and jet quenching

### 2.6.1 Jet reconstruction

A jet is an experimental observable that can be related to theory predictions. The goal of jet reconstruction is to associate the kinematic properties ( $p_T$ ,  $\eta$ ,  $\phi$ ) of the collimated shower of particles to the kinematic properties of the original patrons produced from the hard scattering process. As there is no one-to-one correspondence between the short distance physics and the

final hadronization, no definition of the jet is absolute. Despite the non-absolute interpretation of the jet, there are many definitions and reconstruction algorithms that are consistent with theory predictions and experimental measurements.

In December 1990, a list of fundamental requirements was prepared with a goal of standardizing jet definitions in what is now known as Snowmass accords. Following five properties were recommended to be met by jet definitions [61]:

1. Simple to implement in an experimental analysis
2. Simple to implement in the theoretical calculations
3. Defined at any order of perturbation theory
4. Yields finite cross-section at any order of perturbation theory
5. Yields a cross-section that is relatively insensitive to hadronization

The requirement that the cross-section should be finite at any order of perturbation theory implies that the jet definition should be infrared and collinear (IRC) safe. Also, the requirement that the cross-section should be relatively insensitive to hadronization requires that it should be insensitive to the underlying event. As the algorithm should work both in experimental analyses (at particle level) and theoretical calculations (at parton level), satisfying all five requirements is a challenge.

To date, IRC safety has been a key guiding principle in benchmarking jet reconstruction algorithms. IRC safety is the property that neither collinear splitting nor soft emissions in an event should change the set of jets that are found in that event. In a QCD event, both perturbative and non-perturbative effects lead to the emission of soft particles. Also, a hard parton can go through collinear splitting through non-perturbative dynamics or during fragmentation process. In an event with just two hard partons, two jets are reconstructed, as illustrated in Figure 2.19(a). However, in a case like in Figure 2.19(b), where an extra soft gluon has been emitted, an IRC unsafe algorithm can end up reconstructing just one jet. IRC unsafe algorithms can lead to different sets of jet depending on the presence or absence of a soft gluon, and perturbative QCD calculations can result in infinite cross-section, violating the point no. 4 of the Snowmass accords.

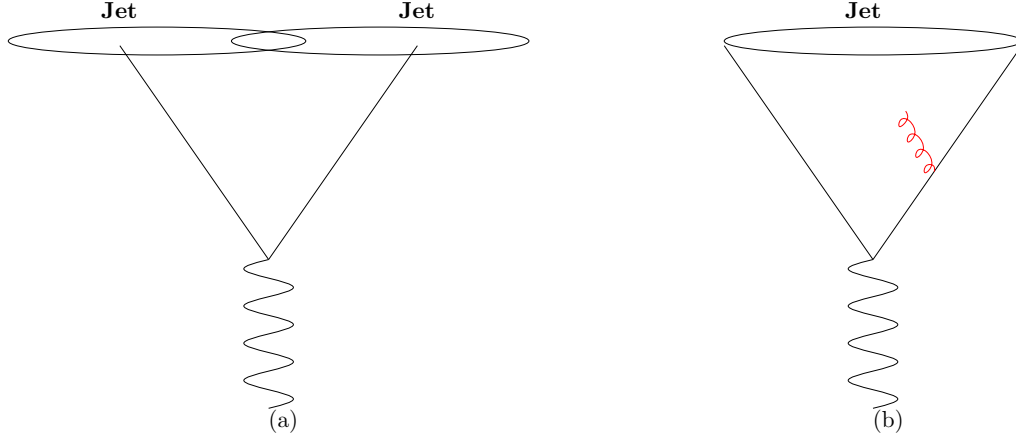


Figure 2.19: Illustration of an IRC unsafe algorithm.

### 2.6.1.1 Jet reconstruction algorithms

There are many jet reconstruction algorithms available and most can be divided into two categories [62]: cone and sequential recombination algorithms. The cone algorithms seek to find stable regions of energy by defining a jet as an angular cone around some direction of dominant energy flow. While widely used in the past, the traditional cone algorithms, like the mid-point algorithms, were found not to be infrared safe [63]. The sequential recombination algorithms implement the knowledge that the final state particles in a shower are collinear in nature and seek to find clusters of particles which are close in momentum space. The sequential recombination family of algorithms is implemented in the FastJet package [64]. Following two algorithms are relevant to this analysis:

1. The anti- $k_t$  algorithm [65], which is widely used in the most of the heavy ion analyses.
2. The Gaussian filter algorithm [66], which is intended for detectors like PHENIX with limited acceptance.

The anti- $k_t$  algorithm, which is infrared safe [65], is a sequential recombination algorithm that takes four-momenta of particles as input, iteratively combines pairs of them until the procedure terminates, and returns one or more jet four-momenta. The essential working mechanism of the anti- $k_t$  algorithm is summarized below:

0. Choose a resolution parameter  $R$  for the jet reconstruction

**At every iteration,**

1. Define the anti- $k_t$  distance  $d_{ij}$  between each pair of particles  $i$  and  $j$ :

$$d_{ij} = \min\left(\frac{1}{k_{T,i}^2}, \frac{1}{k_{T,j}^2}\right) \frac{(\Delta\phi_{ij}^2 + \Delta\eta_{ij}^2)}{R^2} \quad (2.35)$$

2. Define the distance between any particle  $i$  and the beam:

$$d_{ib} = \frac{1}{k_{T,i}^2} \quad (2.36)$$

3. Compute all distances, find the minimum  $d_{\min}$  of all the  $d_{ij}$  and  $d_{ib}$

Note that as  $p_T$  appears in the denominator, the smallest  $d_{ij}$  tends to involve the highest  $p_T$  particle in the event.

4. If  $d_{\min}$  is a  $d_{ij}$ , merge particles  $i$  and  $j$  into a single particle, summing their four-momenta

5. Repeat the steps 1 to 4:

- Compute all distances:  $d_{ij}$  and  $d_{ib}$
- Find the minimum  $d_{\min}$  of all the distances
- If  $d_{\min}$  is a  $d_{ij}$ , merge particles  $i$  and  $j$  into a single particle

6. Eventually, there will be nothing within a distance less than  $R$ , so,  $d_{ib}$  will be the smallest anti- $k_t$  distance. Remove the particle  $i$  from the list and call it a jet.

One key advantage of the anti- $k_t$  algorithm is that it is easily adaptable to PHENIX, which has limited  $\eta$  and incomplete  $\phi$  acceptance. As the anti- $k_t$  algorithm starts combining the leading particles of the jet first and then the auxiliaries, in a case where a jet lies partially within the PHENIX acceptance (i.e., the leading particles are just inside the acceptance), the bias towards mis-reconstructing the jet energy is minimized.

Gaussian filter is an infrared safe algorithm that, unlike traditional jet reconstruction algorithms, reconstructs jet by looking for local maxima in the  $p_T$  density of an event. The essential working mechanism of the Gaussian filter algorithm is summarized below:

1. A set of particles ( $p_T, i$ ) generate rectangularly binned  $p_T$  density of the event,

$$p_T(\eta, \phi) = \sum_i p_{T,i} \delta(\eta - \eta_i) \delta(\phi - \phi_i). \quad (2.37)$$

2. The filtered  $p_T$  density is calculated as

$$\tilde{p}_T(\eta, \phi) = \iint d\eta' d\phi' p_T(\eta', \phi') e^{-\frac{(\Delta\eta^2 + \Delta\phi^2)}{2R_{\text{Filter}}^2}}. \quad (2.38)$$

The discrete filtering provide an efficient mean to calculate  $\tilde{p}_T(\eta, \phi)$  for a large number of sample points; thus one could find every possible maximum.

3. The  $p_T$  of the jet is given by

$$p_T^{\text{jet}}(\eta, \phi) = \max \left\{ \tilde{p}_T(\eta^{\text{jet}}, \phi^{\text{jet}}) \right\}, \quad (2.39)$$

where  $\eta^{\text{jet}}$  and  $\phi^{\text{jet}}$  are the  $\eta$  and  $\phi$  of the final jet axis.

The Gaussian filter algorithm has been successfully used in PHENIX in 200 GeV Cu+Cu collisions [67] and 200 GeV  $d$ +Au collisions [68].

### 2.6.2 Framework of jet quenching

With the notion of jet definition in place, let's explore the production of jets and their interaction with the dense nuclear matter within the framework of perturbative QCD. The cross-section of inclusive hadron production at high  $p_T$  in  $p+p$  collisions can be obtained under the factorization scheme<sup>ix</sup> as:

$$\begin{aligned} d\sigma_{pp \rightarrow hX} \approx & \sum_{ab \rightarrow j} \int dx_a \int dx_b \\ & \int dz_j f_{a/p}(x_a, \mu_f) \otimes f_{b/p}(x_b, \mu_f) \\ & \otimes d\sigma_{ab \rightarrow jd}(\mu_f, \mu_F, \mu_R) \\ & \otimes D_{j/h}(z_j, \mu_F), \end{aligned} \quad (2.40)$$

where  $x_a = p_a/P_A$ ,  $x_b = p_b/P_B$  are the initial momentum fractions carried by the interacting partons,  $x_j = p_h/p_j$  is the momentum fraction carried by the final observed hadron.  $f_{a/p}(x_a, \mu_f)$  and  $f_{b/p}(x_b, \mu_f)$  are two parton distribution functions (PDFs),  $d\sigma_{ab \rightarrow jd}(\mu_f, \mu_F, \mu_R)$  is the differential cross-section for parton scattering process, and  $D_{j/h}(z_j, \mu_F)$  is the fragmentation function (FF) for parton  $j$  to  $h$ . There are three different scales involved in the calculation:  $\mu_f$  and  $\mu_F$  are the factorization scales and  $\mu_R$  is the renormalization scale. These scales are usually taken to be the same ( $\mu_f = \mu_F = \mu_R$ ) and equal to a typical hard scale  $Q$  involved in the process (such as the hadron  $p_T$ ).

---

<sup>ix</sup>Factorization [69] is the separation of hadronic cross-section into short-scale partonic processes and long-scale processes such as hadronization. It sets a link between the calculable partonic cross-section and the measurable hadronic cross-section.

Equation 2.40 is written at the leading order (LO) perturbative QCD. At the next-to-leading order (NLO), calculations of real  $2 \rightarrow 3$  diagrams and  $2 \rightarrow 2$  one-loop virtual diagrams for hard scattering cross-sections are also needed [70]. Figure 2.20 shows the production cross-section for high  $p_T$  neutral pions in  $p+p$  collisions at  $\sqrt{s_{NN}} = 200$  GeV, compared to NLO perturbative QCD calculations. The comparison verifies that the NLO pQCD can describe the production of single inclusive hadrons at high  $p_T$  very well.

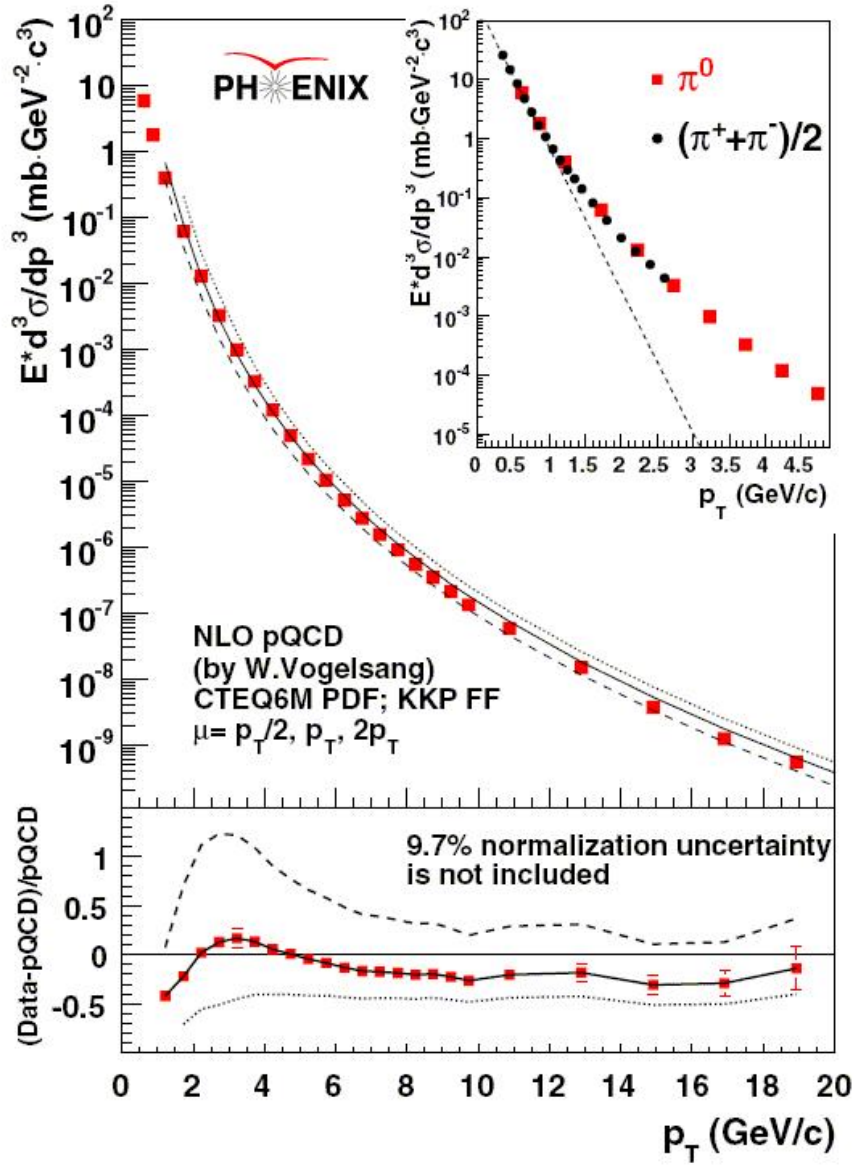


Figure 2.20: The neutral pion production cross-section as a function of  $p_T$  and the results of NLO pQCD calculations, from [71].

### 2.6.2.1 Nuclear modification factor

When studying jet energy loss in the ultra-relativistic heavy ion collisions, two types of nuclear effects need to be taken into account: cold and hot nuclear matter effects. First, the PDF in an ion nucleus  $f_{a/A}$  is different from the free proton PDF  $f_{a/p}$  used in  $p+p$  collisions (as in Equation 2.40). Such effect is called the cold nuclear matter (CNM) effect, and to take this into account, the PDF nuclear modification factor is defined as:

$$R_a^A(x, Q^2) = \frac{f_{a/A}(x, Q^2)}{f_{a/p}(x, Q^2)}. \quad (2.41)$$

Figure 2.21 shows the EPS09 results for the nuclear modification factor for the valence quarks, sea quarks, and gluons in Pb nucleus at  $Q^2 = 1.69 \text{ GeV}^2$  (upper panel) and  $Q^2 = 200 \text{ GeV}^2$  (lower panel).

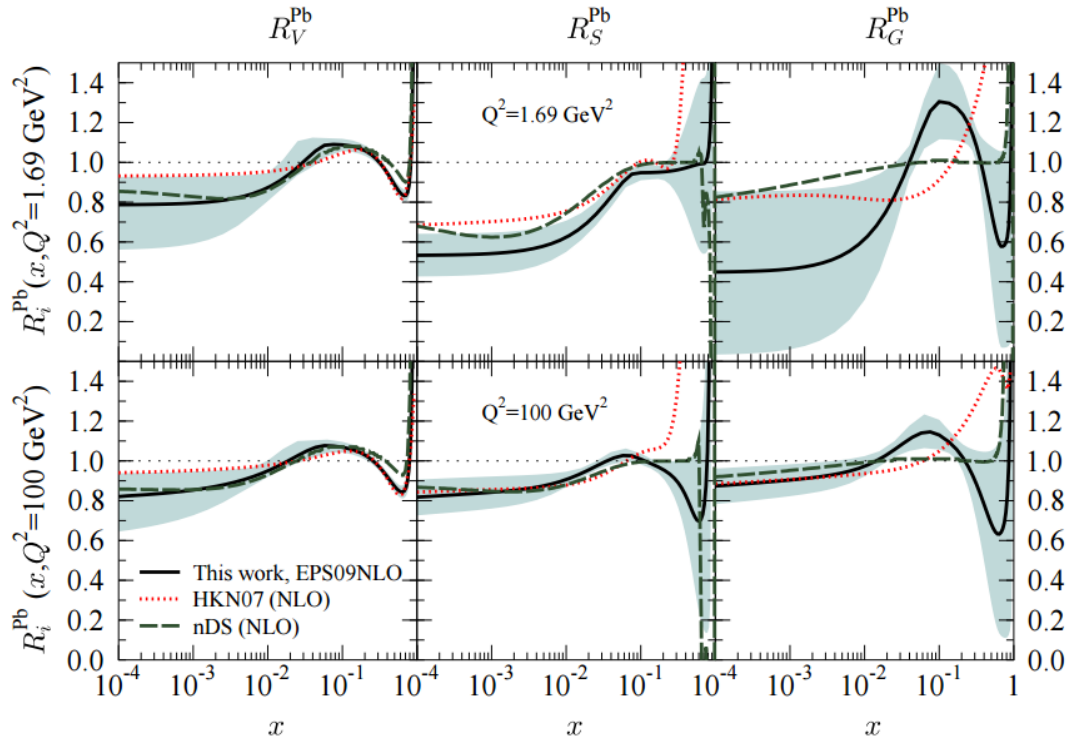


Figure 2.21: EPS09 results for the nuclear modification factor for the valence quarks, sea quarks, and gluons in Pb nucleus at  $Q^2 = 1.69 \text{ GeV}^2$  (upper panel) and  $Q^2 = 200 \text{ GeV}^2$  (lower panel), from [72].

The second effect that needs to be taken into account is the production of the QGP and is called the hot nuclear matter effect. Like discussed earlier, partonic jets which are produced from the initial hard scattering processes have to travel through and interact with the hot and dense nuclear matter before hadronizing into the final state hadrons. After considering both the cold and hot nuclear matter effects, Equation 2.40 can then be modified as

$$\begin{aligned} d\sigma_{AB \rightarrow hX} &\approx f_{a/A}(x_a) \otimes f_{b/B}(x_b) \\ &\otimes d\sigma_{ab \rightarrow jd} \otimes P_{j \rightarrow j'} \otimes D_{j'/h}(z_{j'}), \end{aligned} \quad (2.42)$$

where the additional term  $P_{j \rightarrow j'}$  describes the effects of the hard parton  $j$  interacting with the colored medium before fragmenting into hadrons. It must be noted that Equation 2.42, which is a fundamental basis for phenomenological studies of jet quenching in the ultra-relativistic heavy ion collisions, has not been explicitly written for brevity.

One of the most important observables in studying jet energy loss in the medium is the nuclear modification factor,

$$R_{AB} = \frac{dN_{AB}^h}{\langle T_{AB} \rangle d\sigma_{pp}^h}, \quad (2.43)$$

where  $\langle T_{AB} \rangle$  is the mean value of the nuclear thickness function. Generally,  $R_{AB} < 1$  is referred to as suppression, indicating fewer final state particles at a given  $(p_T, \eta)$  than expected. This expectation is made in comparison to a naive geometric-scaled cross-section in  $p+p$  collisions.  $R_{AB} > 1$  is referred to as enhancement and indicates particle production in excess of expectations.

Figure 2.22 shows the nuclear modification factor  $R_{AA}$  as a function of  $p_T$  for identified hadrons, direct photon, and non-photonic electrons measured by PHENIX in the most central Au+Au collisions at  $\sqrt{s_{NN}} = 200$  GeV. It can be noted that the yields of high  $p_T$  hadrons are strongly suppressed in nucleus-nucleus collisions as compared to  $p+p$  collisions; whereas, the nuclear modification factor  $R_{AA}$  is consistent with unity for high  $p_T$  photons. Since photons carry no color charge, they only interact with the QGP medium electromagnetically, and hence, don't get suppressed. High  $p_T$  hadrons, however, get suppressed due to the fact that partonic jets interact with the medium and lose fraction of their energy before hadronizing.

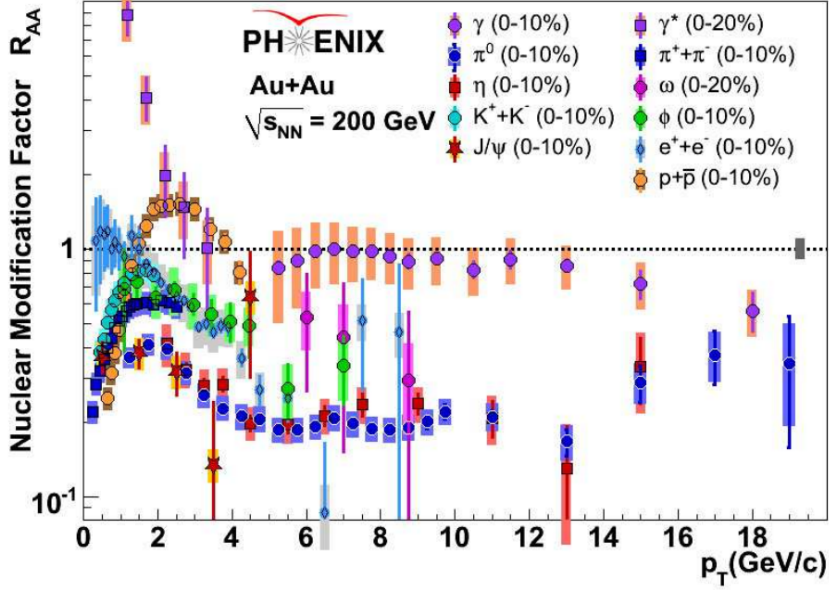


Figure 2.22:  $R_{AA}$  for identified hadrons, direct photon, and non-photonic electrons measured by PHENIX in the most central Au+Au collisions at  $\sqrt{s_{NN}} = 200$  GeV, from [73].

Jet quenching was discovered at RHIC through the measurement of suppression of single hadron yields compared to expectations from  $p+p$  collisions [74, 75]. Since then, the mechanism for energy loss of the leading parton in the medium has been studied through full jet reconstruction, jet-hadron correlation, and  $\gamma$ -jet correlation observables.

To quantify the amount and the spatial distribution of the lost energy, studying the modification of jet production rates is crucial. The nuclear modification factor measured by ATLAS for jets in Pb+Pb collisions [76] indicates a suppression by approximately a factor of two in central collisions. The  $R_{AA}$  shows a slight increase with  $p_T$  and no significant variation with rapidity. In the 0-10% central collisions, ALICE has observed a strong jet suppression,  $0.3 < R_{CP} < 0.5$ , for jets reconstructed with  $R = 0.2$  and requiring a leading track with  $p_T > 5$  GeV/c [77]. In another jet suppression measurement made by ALICE,  $R_{AA}$  is found to be 0.28 and independent of  $p_T$  in central collision, for jets reconstructed from charged and neutral particles with  $R = 0.2$  [78]. These measurements imply a strong interaction of partons with the medium up to very high transverse momentum. Within uncertainties, the observed suppressions are in good agreement with expectations from different jet quenching model calculations.

PHENIX has recently published results on fully reconstructed  $R = 0.3$  anti- $k_t$  jets measured in  $p+p$  and  $d+\text{Au}$  collisions at  $\sqrt{s_{\text{NN}}} = 200 \text{ GeV}$  [79]. The results are shown in Figure 2.23. A strong centrality dependence is seen, with slight suppression in the most central case and a strong enhancement for larger centralities. These modifications also show a slight  $p_T$  dependence, getting stronger with higher  $p_T$ . The suppression in the most central case is comparable to models including initial-state energy loss effects, but enhancement in peripheral is very challenging to understand within these models.

In small system collisions, such as  $d+\text{Au}$ , measurements of jet production rates benchmark the effects of the cold nuclear matter environment as they are expected to be sensitive to the modification of the parton densities in the initial state. In heavy ion collisions, such as Cu+Au, large transverse momentum partons traverse the colored medium and lose energy which modifies the jet structure relative to jets generated in vacuum. As the underlying event in Cu+Au event is smaller when compared to that in the largest heavy ion event, the Cu+Au collision system offers an intermediate testing ground for heavy ion jet reconstruction between small systems and those with the largest heavy ions.

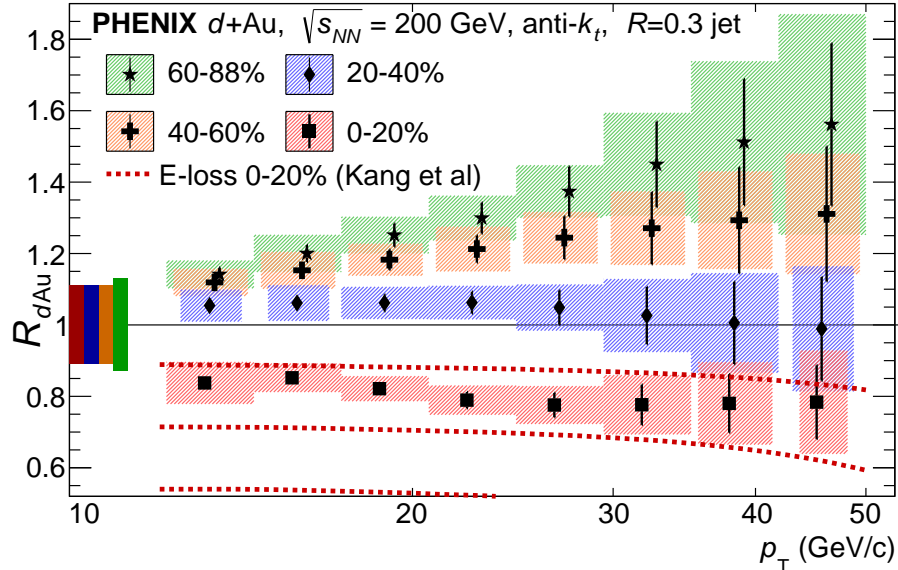


Figure 2.23: The  $R_{dAu}$  for  $R = 0.3$  anti- $k_t$  jets. A model calculation including CNM energy-loss for the most central case is also shown.

## CHAPTER 3. THE EXPERIMENT

### 3.1 The Relativistic Heavy Ion Collider

The Relativistic Heavy Ion Collider (RHIC) [80, 81, 82] at Brookhaven National Laboratory (BNL) is one of the two operating heavy-ion colliders in the world, the other being the Large Hadron Collider (LHC) at European Organization for Nuclear Research (CERN). RHIC is also the only spin-polarized proton collider in operation [83].

RHIC started its operation in 2000 with four detectors: the smaller detectors PHOBOS and BRAHMS<sup>i</sup>, and the larger detectors STAR<sup>ii</sup> and PHENIX<sup>iii</sup>. The PHOBOS detector was designed to study particle production in a broad kinematic region of the colliding nuclei. BRAHMS, which included a forward spectrometer, was designed to measure charged hadrons over a wider rapidity range. PHOBOS and BRAHMS completed data taking in 2005 and 2006, respectively, after finishing their scientific mission, while the larger detectors, STAR and PHENIX, continue to operate.

The STAR detector was designed with the primary purpose of measuring charged and neutral hadrons, photons, and electrons over a large region in phase space [84]. The main subsystem in STAR, the Time Projection Chamber (TPC), provides charged particle tracking over  $2\pi$  in azimuth and a large spread in pseudorapidity ( $|\eta| < 1$ ). The Barrel Electromagnetic Calorimeter (BEMC) is used for detecting neutral energy in the same phase space as well as for triggering. The Forward Time Projection Chambers (FTPCs) are used for detecting charged tracks at forward rapidities as well as to determine event plane. With recent upgrades, including the

---

<sup>i</sup>Broad RAnge Hadron Magnetic Spectrometers

<sup>ii</sup>Solenoidal Tracker at RHIC

<sup>iii</sup>Pioneering High Energy Nuclear Interaction eXperiment

installation of Time-Of-Flight (TOF), Muon Telescope Detector (MTD), and Heavy Flavor Tracker (HFT), the capabilities of the STAR detector have been significantly extended.

One of the goals of the four RHIC experiments was to verify the formation of the QGP and study its properties. In 2005, the four experiments published review articles highlighting their experimental evaluation and perspective on the QGP [85, 86, 87, 88]. A short survey of the PHENIX detector will be given in Section 3.2.

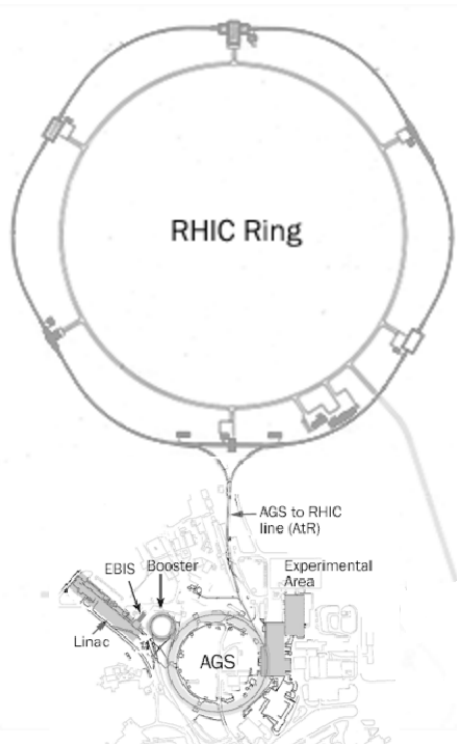


Figure 3.2: Schematic of the RHIC complex.

Figure 3.1: Bird's-eye view of the RHIC complex, from [www.google.com/maps](http://www.google.com/maps).

RHIC is a very versatile machine and provides a wide variety of species and energies for collision. Collision species include  $\uparrow p + \uparrow p$ <sup>iv</sup>, Au+Au, d+Au, Cu+Cu, U+U, Cu+Au, h+Au<sup>v</sup>, and more recently  $\uparrow p + \text{Au}$  and  $\uparrow p + \text{Al}$ . Collision energies vary from maximum  $\sqrt{s_{\text{NN}}} = 510 \text{ GeV}$  in  $p+p$  running to minimum  $\sqrt{s_{\text{NN}}} = 7.7 \text{ GeV}$  in Au+Au running (for the beam energy scan program).

<sup>iv</sup>The symbol  $\uparrow$  indicates spin polarized beam.

<sup>v</sup>h is the nucleus of the  $^3\text{He}$  atom.

A bird's-eye view of the RHIC complex is shown in Figure 3.1. RHIC operates as an accelerator, as a storage ring, and as a collider. It consists of two concentric rings of superconducting magnets, called blue for clockwise and yellow for counter-clockwise beams, each 3.8 km in circumference. The main components of the magnet system are 288 arc dipoles, 108 insertion dipoles, 276 arc quadrupoles, and 216 insertion quadrupoles. In total, each ring consists of six arc sections and six insertion sections with a collision point at their center. In the arc sections, the counter-rotating beams are horizontally separated by 90 cm. In the insertion sections, a pair of dipole magnets, DX and D0 located at  $\sim 10$  m and  $\sim 23$  m from the collision point, respectively, steer beams to a co-linear path for head-on collisions.

### 3.1.1 Accelerator chain

While the acceleration sequence for protons is

$$\text{Linac} \rightarrow \text{Booster} \rightarrow \text{AGS} \xrightarrow{\text{ATR}} \text{RHIC},$$

the acceleration sequence for ions is

$$\text{EBIS} \rightarrow \text{Booster} \rightarrow \text{AGS} \xrightarrow{\text{ATR}} \text{RHIC}.$$

The RHIC acceleration scenario for ion beams is shown in Figure 3.2, with three accelerators in the injection chain: the Electron-Beam Ion Source (EBIS), the Booster, and the Alternating Gradient Synchrotron (AGS). Until 2012, ions were delivered by the Tandem Van de Graaff and associated 840 m transport line. In 2012, a new pre-injector, the EBIS, was commissioned. The EBIS has a 5 T superconducting solenoid which compresses an electron beam into a 1.5 m long trap region. Ions of the desired species are injected, held in the trap, and stepwise ionized by the electron beam [89]. When the desired charge state is reached (+32 for Au), they are released from the trap and injected into the Booster at 2 MeV/u (for ions with  $q/m > 0.16$ ). In the case of Au ions, the Booster Synchrotron accelerates the ions to 95 MeV/u. The Au ions are stripped again at the exit from the Booster to reach a charge state of +77. They are then injected to the AGS for acceleration to the RHIC injection energy of 10.8 GeV/u. Gold ions are fully stripped to a charge state of +79 at the exit from the AGS and are transferred to the RHIC yellow and blue rings through the AGS-to-RHIC (AtR) beam transfer line.

## 3.2 The PHENIX detector

### 3.2.1 Overview

The Pioneering High Energy Nuclear Interaction eXperiment (PHENIX) [90] is a detector designed for two purposes: to investigate the nuclear matter under the extreme condition and to study the spin structure of the nucleon in polarized  $p+p$  collisions. The PHENIX detector, designed and built through 2001 and continuously upgraded through 2015, is comprised of a number of global detectors close to the beam pipe and four separate spectrometers (or arms): the east and the west central arm at mid-rapidity, and the north and the south muon arm at forward and backward rapidity. Figure 3.3 shows the setup of the PHENIX detector during the 2012 RHIC running period.

The muon arms, which are not used in this analysis, are dedicated to the detection of muons. Each muon spectrometer consists of the Muon Tracker (MuTr) inside a radial magnetic field followed by the Muon Identifier (MuId), both with full azimuthal acceptance. The pseudorapidity coverage is  $-2.2 \leq \eta \leq -1.15$  for the south arm and  $1.15 \leq \eta \leq 2.44$  for the north arm. The MuTr, used for precision tracking, consists of three stations of multi-plane drift chambers. The MuId, used for muon identification, consists of alternating layers of steel absorbers and low resolution tracking layers of streamer tubes of the Iarocci type [90].

The muon arms have received a significant number of upgrades in the recent years. As MuId based trigger has a rejection power of only  $\sim 100$ , for an efficient acquisition of  $W$ -candidates, a new trigger was developed for the  $W$  detection, which provides rejection power of at least 5000 [91]. The  $W$  trigger consists of two components: upgraded front-end electronics for the MuTr to process fast trigger signals and Resistive Plate Chambers (RPCs) which provide momentum-sensitive position information with good timing resolution. RPC3 was installed in 2009 and RPC1 in 2011. Most recently, the Forward Vertex Detector (FVTX), a silicon detector developed to provide precision in tracking charged particles before they interact with hadron absorber, was installed in 2012 [92].

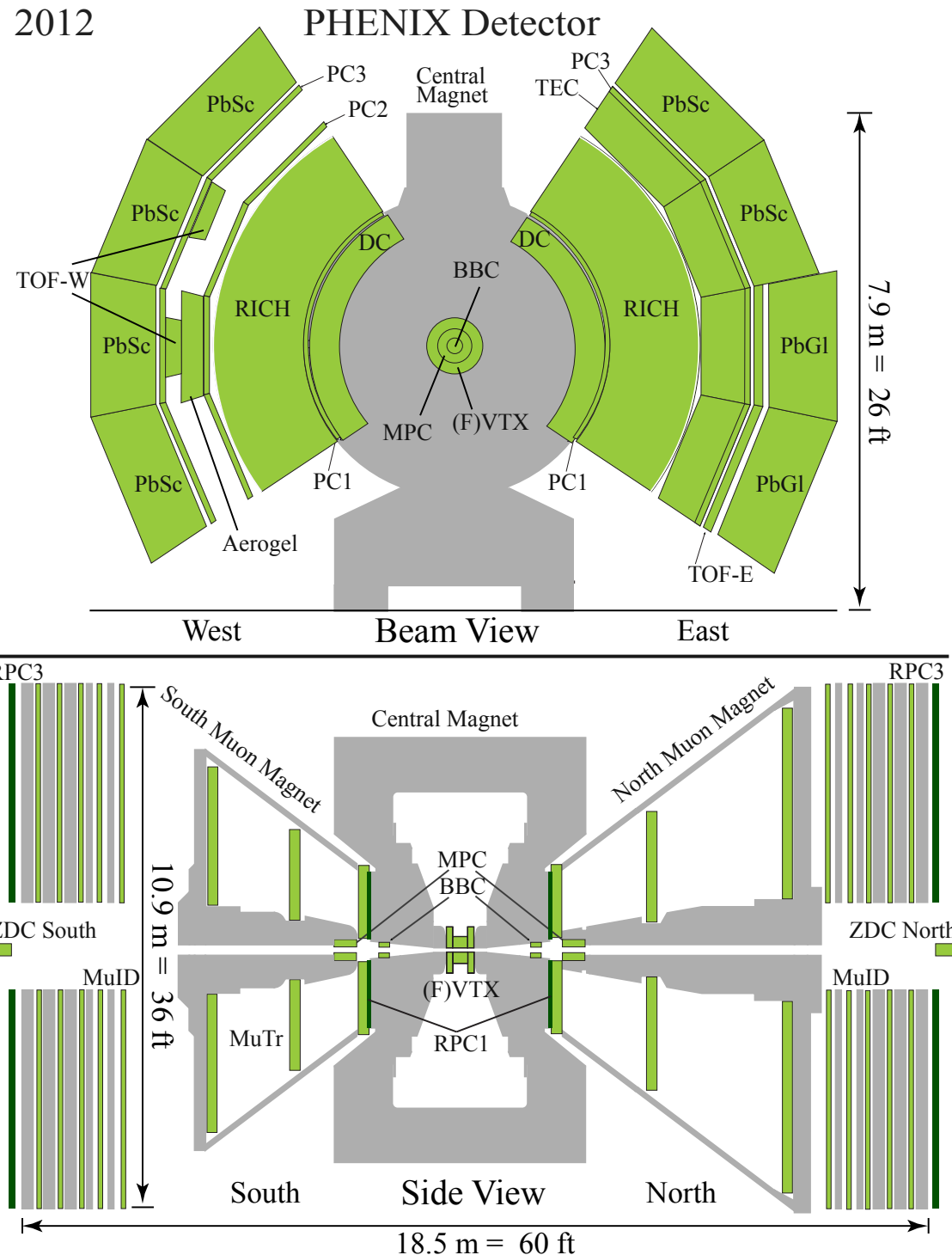


Figure 3.3: Setup of the PHENIX detector during the 2012 RHIC running period. Top is the beam view and bottom is the side view.

### 3.2.2 The global detectors

Timing, location, and particle multiplicity of a PHENIX collision are determined by the Beam-Beam Counters (BBCs) and the Zero-Degree Calorimeters (ZDCs). The BBCs provide both the time and position of a collision while the ZDCs provide information on the most grazing collisions [93].

#### 3.2.2.1 Beam-Beam Counter

The BBCs consist of two identical counters installed on both sides of the collision point along the beam axis. They are located  $\pm 144$  cm from the nominal collision vertex, and cover  $2\pi$  in azimuth and  $3.0 < |\eta| < 3.9$  in pseudorapidity. Each BBC counter, shown in Figure 3.4, has 64 one-inch mesh dynode photomultiplier tubes (PMTs). Each PMT is equipped with 3 cm quartz on the head as a Cherenkov radiator (Figure 3.5) and has a dynamic range spanning 1 to  $\approx 30$  minimum ionizing particles (MIPs) per PMT.



Figure 3.4: One of the two BBCs.



Figure 3.5: A single BBC element consisting of a PMT and a quartz radiator.

The collision time  $T_0$  and the collision vertex  $z_{\text{vertex}}$  are calculated using the average of the arrival times ( $T_n$  for the north array and  $T_s$  for the south array) of the leading charged particles from a collision into the BBC array. The collision time  $T_0$  is calculated as

$$T_0 = \frac{T_n + T_s}{2} - \frac{z_{\text{BBC}}}{c} + t_{\text{offset}}, \quad (3.1)$$

where  $z_{BBC} = 144\text{ cm}$  and  $t_{\text{offset}}$  is the intrinsic time offset. The collision vertex is calculated as

$$z_{\text{vertex}} = \frac{T_n - T_s}{2} c + z_{\text{offset}}, \quad (3.2)$$

where  $z_{\text{offset}}$  is the intrinsic  $z$ -position offset.

One of the most important features of the BBC detectors is their excellent timing resolution. The timing resolution of a single BBC element is  $52 \pm 4\text{ ps}$  under real experimental conditions [93]. The  $z_{\text{vertex}}$  resolution is  $\sim 2.0\text{ cm}$  in  $p+p$  and peripheral Au+Au collisions, and  $\sim 0.5\text{ cm}$  in the central Au+Au events. Furthermore, signals from the BBCs serve as the basis for the Local Level 1 trigger to determine the occurrence of an inelastic collision, and BBC, in combination with ZDC, serves a significant role in determining centrality class of heavy-ion collisions.

### 3.2.2.2 Zero-Degree Calorimeters

The ZDCs are a pair of hadronic calorimeters located 18 m from the interaction point along the beam axis. They are designed to measure neutron fragments at extremely forward direction ( $|\eta| \sim 6$ ). Since ZDCs sit behind the dipole magnets (as shown in Figure 3.6), charged particles are bent out of the ZDC acceptance.

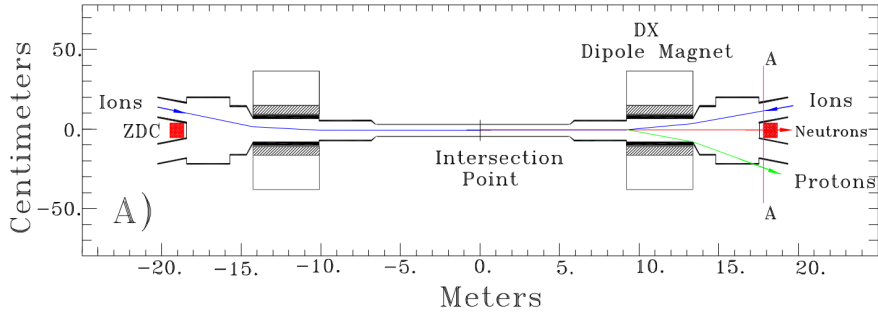


Figure 3.6: Diagram of the installation location of the north and south ZDC in a view along the beam axis.

Each ZDC consists of 3 modules, and each module is composed of tungsten plates and optical fiber ribbons. The Cherenkov lights from neutrons are transferred to PMTs via optical fibers. The Shower Maximum Detector (SMD), a position sensitive hodoscope, is located between the

first and the second ZDC modules. The SMD provides the position of a hadronic shower in  $x$ - $y$  coordinates through seven vertical scintillator strips (that provide  $x$ -coordinates) and eight horizontal scintillator strips (that provide  $y$ -coordinates).

The ZDC, in combination with the SMD, is used as the PHENIX local polarimeter that monitors the beam polarization direction at the PHENIX interaction region. Since there is a strong correlation between the neutron multiplicity and the collision geometry [94], as mentioned earlier, the ZDC is also used in centrality determination.

### 3.2.3 The central arm

#### 3.2.3.1 The central magnet

There are three magnets in PHENIX: the central magnet, the south muon magnet, and the north muon magnet. Details of the PHENIX magnet system can be found in [95]. The muon magnets use solenoid coils to produce a radial magnetic field for muon analysis. The central magnet is energized by two pairs of concentric coils and provides a field around the interaction vertex that is parallel to the beam axis. The axially symmetric field is used to bend the charged particles into the central arm acceptance. The concentric coils of the central magnet can be run separately (+ or -), together (++) or in opposition (+-). Figure 3.7 shows the magnetic field lines in PHENIX. The field configuration for 2012  $p+p$  and Cu+Au running was ++.

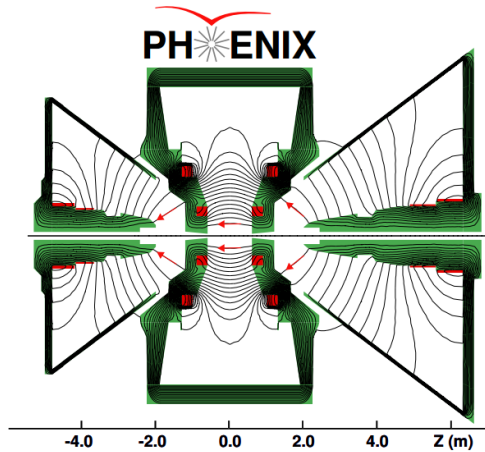


Figure 3.7: Magnetic field lines in PHENIX. The central magnet coils are in the combined ++ mode.

The central magnet is 9 m tall, weighs approximately 500 tons, and provides a total field integral ranging from 0.43 T m to 1.15 T m depending on the trajectory of the charged particle. The field is minimal ( $\sim 100$  G m) for the region  $R > 2.0$  m, the beginning point of the Drift Chamber detector.

### 3.2.3.2 Drift Chamber

The PHENIX Drift Chamber (DC) [96] is the innermost subsystem in the central arm and consists of two gas wire chambers, one in each arm. The chambers are cylindrical titanium frames with mylar windows on the front and back surfaces, which lie at the radial distance of 2 m and 2.46 m from the beam axis, respectively. Each of the chambers covers an active area of  $\pm 0.35$  in pseudorapidity,  $\pm 1.25$  m in the  $z$  direction, and  $90^\circ$  in azimuthal angle  $\phi$ , and contains 20 equal keystones covering  $4.5^\circ$  in  $\phi$  (as shown in Figure 3.8).

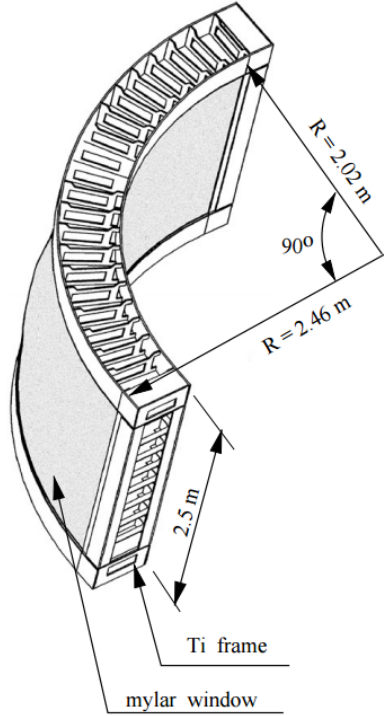


Figure 3.8: Schematic of the PHENIX Drift Chamber, from [97].

Each keystone contains six wire modules stacked radially: X1, U1, V1, X2, U2, and V2. Each module contains four anode planes and four cathode planes forming cells with a 2 cm

to 2.5 cm drift space in the  $\phi$  direction. The layout of wires within one DC sector is shown in Figure 3.9. The X wire cells run in parallel to the beam axis and perform precise track measurement in  $r\text{-}\phi$  plane. The U and V wires cells are placed at an angle of  $6^\circ$  with respect to the X wires in order to measure the  $z$ -coordinate of the track. In total, the DC, filled with 50% argon and 50% ethane mixture, consists of 6500 anode wires leading to 13,000 readout channels. Each wire provides a resolution in  $r\text{-}\phi$  of 165  $\mu\text{m}$  and a spatial resolution in  $z$ -direction of 2 mm.

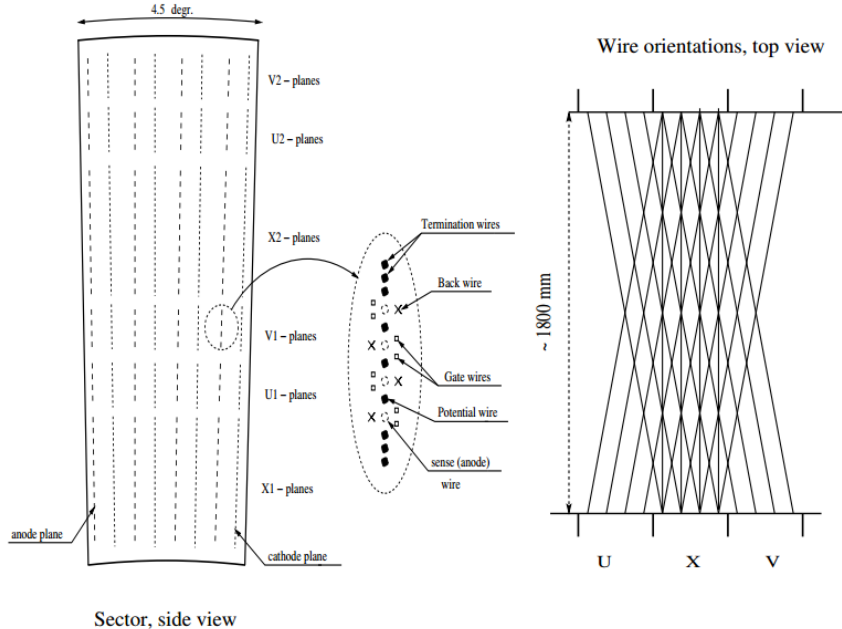


Figure 3.9: Layout of wire position within one sector of the PHENIX Drift Chamber in  $r\text{-}\phi$  plane (left). Top view of the wire orientation in  $z\text{-}\phi$  plane (right), from [97].

### 3.2.3.3 Pad Chamber

The Pad Chambers (PCs) [98], also called PC1, PC2, and PC3, are layers of multiwire proportional chambers filled with an argon-ethane gas mixture, located at different radii from the beam axis (Figure 3.3). The innermost layer, PC1, is located 2.5 m from the interaction region and is sandwiched between DC and Ring-Imaging Cherenkov (RICH) in both the east and west arms. The second layer, PC2, is located behind RICH in the west arm only. The outermost layer, PC3, is located 4.9 m from the beam axis and lies just inside EMCal in both arms. Only PC1 and PC3 are used in this analysis.

Each PC consists of sectors containing a cathode plane, an anode wire plane, and a pixel pad plane, as shown in Figure 3.10. Three pixels are tied together into a cell, where each pixel is used to determine a valid hit. In PC1, these cells are segmented into  $8.4 \times 8.4 \text{ mm}^2$  yielding a  $z$ -position resolution of  $\pm 1.7 \text{ mm}$ .

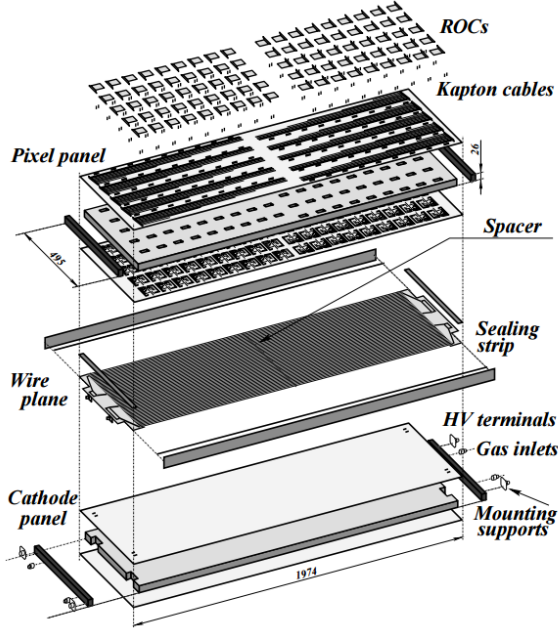


Figure 3.10: Exploded view of the PHENIX Pad Chamber, from [98].

The DC and PC1 information,  $\phi$ - and  $z$ -position from the DC and  $z$ -position confirmation from the PC1, provide direction vectors through the RICH during the central arm track reconstruction. The momentum resolution of the combined tracking system is

$$\frac{\delta p}{p} = 0.7\% \oplus 1.0\% p \text{ (GeV/c)}, \quad (3.3)$$

where the first term is the contribution from multiple scattering and the second term is the contribution from the intrinsic angular resolution of the DC [99]. PC3 is used to resolve ambiguities in the EMCAL, where approximately 30% of the particles are produced either by secondary interactions or particles decays.

### 3.2.3.4 Ring-Imaging Cherenkov detector

The Ring-Imaging Cherenkov (RICH) [100] detector lies in both arms between a radius of 2.6 and 4.1 m from the beam axis and is a principle detector used for identifying electrons. A cutaway view of one arm of the RICH detector is shown in Figure 3.11. Each RICH detector has a volume of  $40\text{ m}^3$ , with an entrance window area of  $8.9\text{ m}^2$  and an exit window area of  $21.6\text{ m}^2$ . Each detector contains 48 composite mirror panels, forming two intersecting spherical surfaces, with a total reflecting area of  $20\text{ m}^2$ .

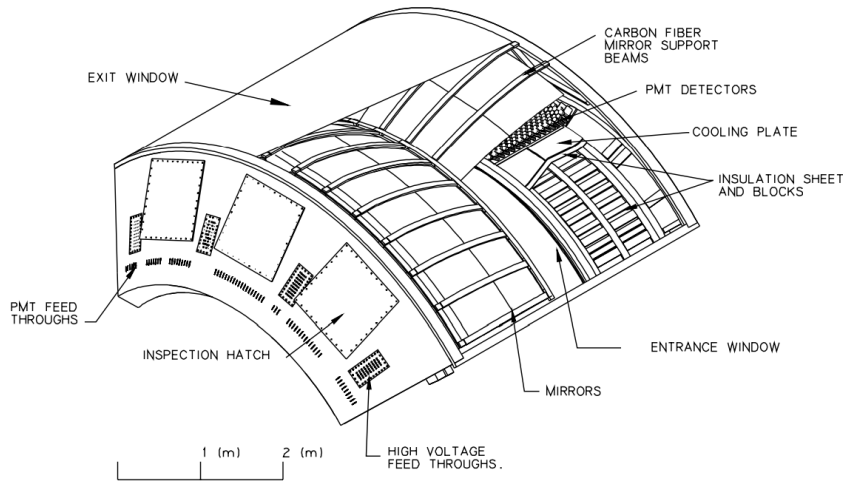


Figure 3.11: A cutaway view of one arm of the PHENIX RICH detector, from [100].

The RICH is filled with carbon dioxide ( $\text{CO}_2$ ) gas at 1 atm.  $\text{CO}_2$  has a Cherenkov threshold of  $18\text{ MeV}/c$  for electrons and  $4.65\text{ GeV}/c$  for pions. A particle with  $\beta = 1$  will radiate 12 Cherenkov photons into a ring of about 11.8 cm in diameter during a 1.2 m transit of the  $\text{CO}_2$  gas. The spherical mirrors focus Cherenkov light onto arrays of 1280 PMTs, each located on either side of the RICH entrance window. Thus, searching for PMTs within the nominal radius of a charged tracks can distinguish electrons from other hadrons below  $\approx 4.65\text{ GeV}/c$ .

### 3.2.3.5 Electromagnetic Calorimeter

The PHENIX Electromagnetic Calorimeter (EMCal) [101] is comprised of separate lead-scintillator (PbSc) and lead-glass (PbGl) calorimeters. The EMCal consists of eight sectors, six of which are PbSc and two, in the bottom half of the east arm, are PbGl. As PbGl has a

better energy resolution and PbSc has better linearity and timing, these two designs serve as an important internal cross-check for PHENIX analyses. All eight sectors are situated just outside the PC3 at approximately 5 m away from the interaction region, as shown in Figure 3.3.

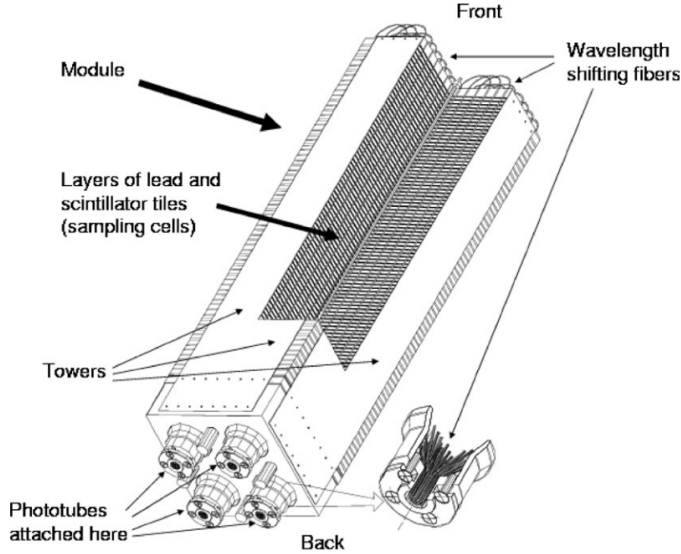


Figure 3.12: Schematic view of a PbSc module, from [101].

The PbSc is a sampling calorimeter made of alternating tiles of Pb and scintillator. The basic building block of the PbSc is a module consisting of four optically isolated towers that are read out individually, as shown in Figure 3.12. Thirty-six modules are further grouped together into a supermodule (SM), and 18 SMs are grouped into a  $2 \times 4 \text{ m}^2$  sector. In total, PbSc consists of 15,552 individual towers and covers an area of approximately  $48 \text{ m}^2$ .

A tower consists of 66 sampling layers containing 0.15 cm of Pb and 0.4 cm of scintillator. These layers are optically connected by 36 wavelength shifting fibers for light collection. Light is read out by PMTs mounted to the back of the tower. Each tower is 18 radiation lengths long with nominal energy resolution,

$$\frac{\sigma_E^{\text{PbSc}}}{E} = \frac{8.1\%}{\sqrt{E(\text{GeV}/)}} \oplus 2.1\%, \quad (3.4)$$

where the first value is the stochastic term and the second value is the constant term (contributed mainly by intrinsic non-uniformities).

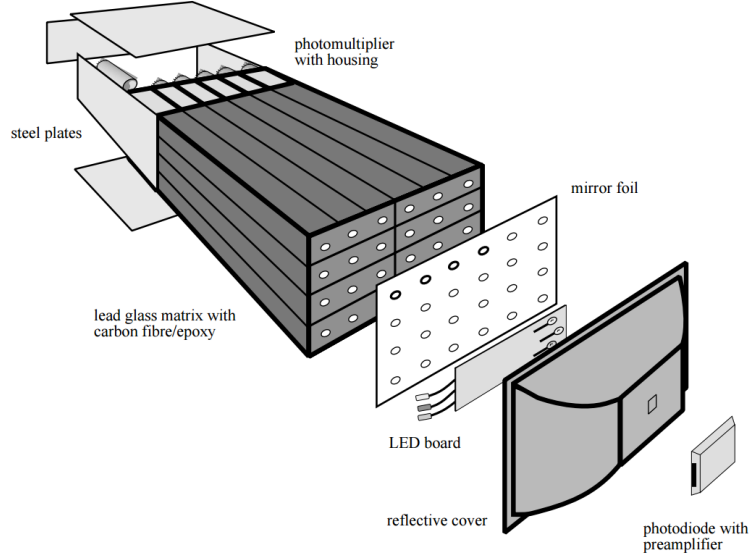


Figure 3.13: Schematic view of a PbGl supermodule, from [101].

The PbGl is a Cherenkov calorimeter composed of a lead, glass, and lead-oxide homogeneous medium. It serves as both the Cherenkov radiator and secondary particle generator (or absorber). Each of the two PbGl sectors contains 192 SMs. Each SM contains a  $6 \times 4$  array of PbGl towers, as shown in Figure 3.13. Each tower is  $4\text{ cm} \times 4\text{ cm} \times 40\text{ cm}$  in size and 14.4 radiation lengths long with nominal energy resolution,

$$\frac{\sigma_E^{\text{PbGl}}}{E} = \frac{5.9\%}{\sqrt{E(\text{GeV})}} \oplus 0.8\%. \quad (3.5)$$

### 3.2.4 Data Acquisition and trigger system

The PHENIX data acquisition (DAQ) system, at peak running, writes data at an event rate of 6 kHz to 7 kHz. Figure 3.14 shows a schematic of the data flow in PHENIX. Data flow starts from each detector's Front-End Module (FEM) in the interaction region. Each FEM digitizes the detector's signals and sends it via fiber optic cables to the Data Collection Modules (DCMs), located outside the interaction region. The DCMs receive the data, package them, and send them to the Sub Event Buffers (SEBs) which then pass the data to the Assembly and Trigger Processors (ATPs). The ATPs assemble the event fragments from the individual detectors into a whole event and pass the data to one of the buffer boxes for archiving.

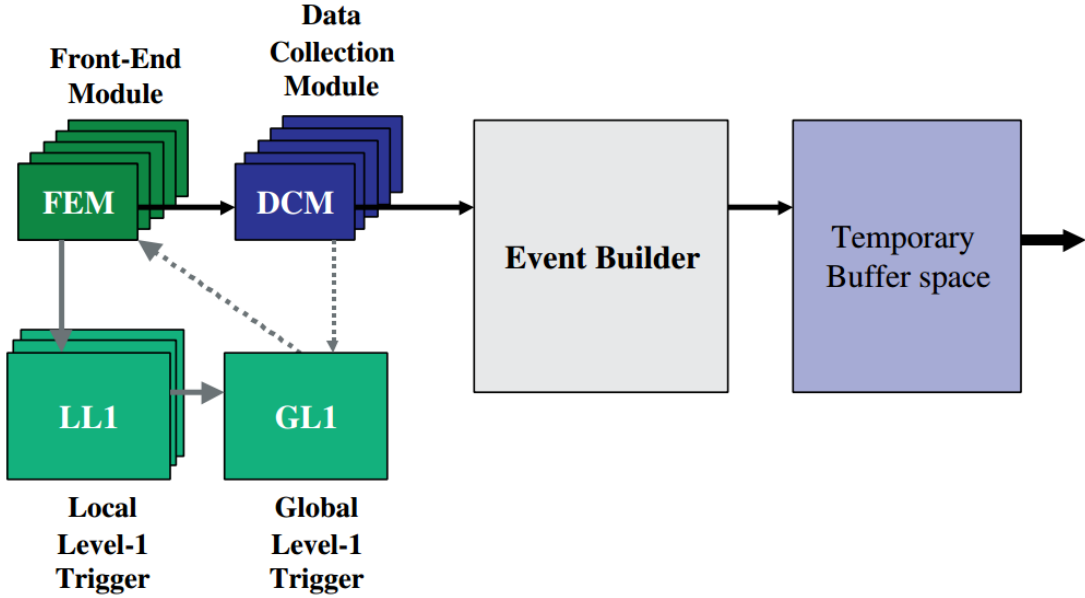


Figure 3.14: Schematic of the data flow in PHENIX.

BBC firing rates have reached as large as  $\sim 10$  MHz during the highest luminosity  $p+p$  fills. Due to the limited rate of PHENIX DAQ, recording every collision is not possible. To select which events to read out in real time, PHENIX uses several Local Level 1 (LL1) online triggers combined into one Global Level 1 (GL1) trigger. LL1 triggers are typically specific to a single subsystem, and the GL1 trigger combines trigger decisions from separate LL1 triggers. For the purposes of this analysis, there are two triggers of interest: the Minimum Bias trigger and the EMCAL/RICH trigger (ERT).

#### 3.2.4.1 Minimum Bias trigger

As mentioned before, the BBCs are the main global detectors in PHENIX to determine the timing and location of a collision. As such, they also provide the minimum requirement for the DAQ system to register a collision as an event. By having at least one tube fired in the both the BBCs, the collision vertex can be determined, and a trigger decision can then be sent to the DAQ. Based on this minimum requirement, there are three types of Minimum Bias triggers:

1. a normal trigger accepting events that have a  $z_{\text{vertex}}$  between  $\pm 30$  cm from the nominal collision point,
2. a narrow vertex trigger accepting events that have a  $z_{\text{vertex}}$  between  $\pm 10$  cm from the nominal collision point, and
3. a no vertex trigger accepting any coincidence between the BBCs.

### 3.2.4.2 EMCal/RICH trigger

The EMCal/RICH trigger (ERT) is designed to select events with high- $p_{\text{T}}$  electromagnetic probes or the presence of heavy flavor decays. It is implemented by considering the energy in  $2 \times 2$  tiles of calorimeter towers and in sliding  $4 \times 4$  windows of four adjacent  $2 \times 2$  tiles.

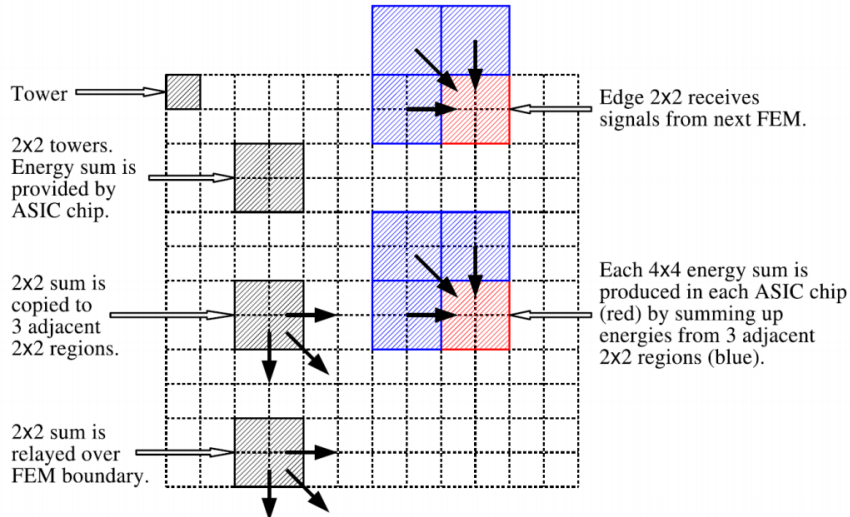


Figure 3.15: The conceptual diagram of the procedure to produce signals for the ERT trigger, from [102].

The conceptual diagram of the procedure to select an ERT event is shown in Figure 3.15. As the shower generated by a particle hitting the EMCal usually spreads over several towers<sup>vi</sup>, summing of energy deposits on the neighboring towers is important. The energies of  $2 \times 2$  tower is summed by an ASIC chip. The information of  $6 \times 6$  ASIC chips (from  $12 \times 12$  towers) are then read out by one FEM. Hence, 36 energy sums of  $2 \times 2$  towers are produced per FEM.

<sup>vi</sup>When a particle hits the center of a tower, the typical energy deposited in that tower is  $\approx 80\%$  of the total energy, but it is only  $\approx 20\%$  if it hits the corner.

To eliminate the inefficiency in the case of a particle hitting the border of the  $2 \times 2$  block, the energy sum of  $4 \times 4$  towers is formed from the four  $2 \times 2$  energy sum. In total, 36 signals of  $4 \times 4$  energy sum are obtained for one FEM. Each  $4 \times 4$  energy sum as well as  $2 \times 2$  energy sum is compared to certain energy threshold for a trigger decision. In order of increasing threshold, the  $4 \times 4$  energy sum triggers are called ERT\_4x4c, ERT\_4x4a, and ERT\_4x4b. ERT\_2x2 trigger considers just the energy in  $2 \times 2$  window, and ERT\_Electron trigger, in addition to the energy in  $2 \times 2$  window, also accounts for a minimum number of photoelectron hits in the RICH.

## CHAPTER 4. ANALYSIS PREAMBLE

### 4.1 Kinematic variables

This section follows the natural units convention, such that  $c = 1$  and  $\hbar = 1$ , and defines the kinematic variables that are used throughout this analysis.

The energy  $E$  and three-momentum  $\vec{p}$  of a particle of mass  $m$  form the momentum four-vector (or four-momentum),

$$p^\mu = (E, p_x, p_y, p_z). \quad (4.1)$$

Although the four-momentum transforms under Lorentz transformation, the absolute value of the four-momentum is frame independent (or invariant under Lorentz transformation), and is called the invariant mass  $m_{\text{inv}}$ , such that

$$m_{\text{inv}}^2 = p^\mu p_\mu = E^2 - \vec{p} \cdot \vec{p}. \quad (4.2)$$

When the system is at rest, Equation 4.2 converts to the famous energy-momentum relation,  $E = mc^2$ .

The sum of the four-momentum of two colliding particles is a Mandelstam variable,

$$s = (p_1 + p_2)^2, \quad (4.3)$$

where  $p_1$  and  $p_2$  are the four-momentum of the incoming particles. The center-of-mass energy of the collision is determined with  $\sqrt{s}$ .

The coordinate system used in this analysis is shown in Figure 4.1, where the  $z$ -axis lies along the beam direction,  $\phi$  is the azimuthal angle, and  $\theta$  is the scattering angle. In this coordinate system, the transverse momentum  $p_T$  and the longitudinal momentum  $p_L$  are defined as

$$p_T = |\vec{p}| \sin(\theta), \text{ and} \quad (4.4)$$

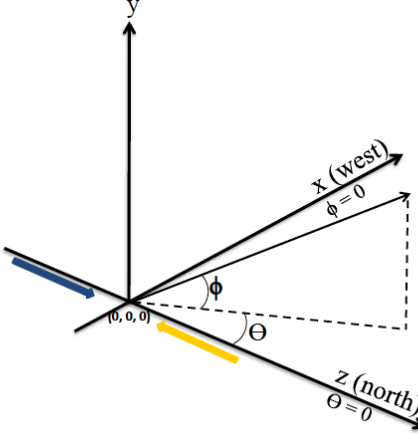


Figure 4.1: Coordinate system used in this analysis.

$$p_L = |\vec{p}| \cos(\theta). \quad (4.5)$$

The transverse momentum is invariant under Lorentz transformation in the  $z$ -direction, while the longitudinal momentum is not.

The rapidity  $y$  is related to the particle's longitudinal momentum and energy as

$$y = \frac{1}{2} \ln \left( \frac{E + p_L}{E - p_L} \right). \quad (4.6)$$

In the limit  $E \gg m_0$ , the rapidity can be approximated by pseudorapidity  $\eta$ , such that

$$\begin{aligned} \eta &= \frac{1}{2} \ln \left( \frac{p + p_L}{p - p_L} \right) \\ &\equiv -\ln \left[ \tan \left( \frac{\theta}{2} \right) \right]. \end{aligned} \quad (4.7)$$

Pseudorapidity is widely used in the nuclear physics experiments because it can be determined directly from the (measurable) scattering angle  $\theta$ . Also, relevant kinematic variables such as the energy and longitudinal momentum of a particle can be written in terms of the pseudorapidity as

$$E = p_T \cosh(\eta) \text{ and} \quad (4.8)$$

$$p_L = p_T \sinh(\eta). \quad (4.9)$$

### 4.1.1 Jet-level variables

As the properties of a jet are strongly related to the properties of its constituents, several jet-level variables are used in this analysis; primarily to reject jets reconstructed from combinatoric particles and to reduce contamination from the high- $p_T$  background.

**Number of constituents:** The number of constituents n.c. of a anti- $k_t$  jet is defined as:

$$n.c. = \sum_{\text{particles}} \Theta \left( R_{\text{Anti-}k_t} - \sqrt{\Delta\eta_{\text{jet, particle}}^2 + \Delta\phi_{\text{jet, particle}}^2} \right). \quad (4.10)$$

The number of constituents of a Gaussian filter jet is the Gaussian weighted number of particles associated with it, such that

$$\text{the total Gaussian weight} = \sum_{\text{particles}} \exp \left( -\frac{\Delta\eta_{\text{jet, particle}}^2 + \Delta\phi_{\text{jet, particle}}^2}{2R_{\text{Filter}}^2} \right). \quad (4.11)$$

Since each particle contributes less than one to the total Gaussian weight, three or more particles are required to produce the total Gaussian weight of 2.5. Therefore, for the Gaussian filter algorithm, the number of constituents n.c.  $\geq 3$  implies the total Gaussian weight  $> 2.5$ .

The default number of constituents requirement used in this analysis is n.c.  $\geq 3$ . Requiring three or more constituents in a reconstructed jet helps reject jets that were reconstructed from the combinatoric particles (and not from the harder fragmentation kinematics).

**Charged fraction:** The charged fraction *c.f.* of a jet is the fraction of the jet's  $p_T$  that comes from the charged constituents. For a anti- $k_t$  jet, the charged fraction,

$$c.f. = \frac{1}{p_T^{\text{jet}}} \sum_i p_T^i, \quad (4.12)$$

where  $i =$  the charged constituents.

**Discriminant:** The discriminant *d* is used for the fake jet identification and rejection (jet-by-jet) and is defined as

$$d = \sum_{\text{particle}} (p_T^{\text{particle}})^2 \exp \left( -\frac{\Delta\eta_{\text{jet, particle}}^2 + \Delta\phi_{\text{jet, particle}}^2}{2R_{\text{dis}}^2} \right). \quad (4.13)$$

In the PHENIX Cu+Cu jet reconstruction analysis [67], it was concluded that the  $p_T^1$  weighing in the discriminant results in a behavior that the fake rate changes slowly and the  $p_T^3$  weighing offers little gain in rejection vs. efficiency trade-off over the  $p_T^2$  weighing. The  $p_T^2$  weighing results in a high value of the discriminant for jets with a harder fragmentation kinematics. Also, the choice of  $R_{\text{dis}} = 0.1$  results in a high value of the discriminant for jets with a tighter core of particles.

## 4.2 Monte Carlo frameworks

### 4.2.1 Glauber Monte Carlo

The Glauber model [103] is a geometric model that uses information about the size and shape of the colliding nuclei to calculate geometric quantities such as the impact parameter  $b$ , the number of participating nucleons  $N_{\text{Part}}$ , and the number of binary nucleon-nucleon collisions  $N_{\text{Coll}}$ . In this model, the nuclei view each other as a collection of nucleons, and the nucleons are assumed to travel on straight line trajectories in parallel with the beam axis. Also, the inelastic nucleon-nucleon cross-section  $\sigma_{\text{ine}}^{\text{NN}}$  is assumed to be the same as in the vacuum. To estimate a realistic density profile of the nuclei, the Woods-Saxon density profile is used, such that

$$\rho(r) = \rho_0 \frac{1}{1 + \exp(\frac{r-R}{a})}, \quad (4.14)$$

where  $\rho_0$  is the nucleon density in the center of the nucleus,  $R$  is the nuclear radius<sup>i</sup>, and  $a$  is the ‘skin depth’ of the nucleus.

In the Glauber Monte Carlo framework, nucleons of the two nuclei are distributed in space according to the nucleon density profile, and the impact parameter of the two nuclei is chosen randomly. A nucleon-nucleon collision is considered to have taken place if their distance  $d$  in the plane orthogonal to the beam axis satisfies

$$d \leq \sqrt{\frac{\sigma_{\text{ine}}^{\text{NN}}}{\pi}}. \quad (4.15)$$

As the inelastic nucleon-nucleon cross-section involves the processes with low momentum transfer, it is not possible to calculate this cross-section using perturbative QCD. Thus, the measured

---

<sup>i</sup> $R = r_0 A^{1/3}$ , where  $r_0 = 1.25$  fm and  $A$  is the atomic mass number.

$\sigma_{\text{ine}}^{\text{NN}}$  is used as an input. The baseline Glauber calculation in PHENIX uses  $\sigma_{\text{ine}}^{\text{NN}}$  of 42 mb for  $\sqrt{s_{\text{NN}}} = 200 \text{ GeV}$ .

Experimental results are usually presented as a function of the geometric quantities such as  $b$ ,  $N_{\text{Part}}$ , and  $N_{\text{Coll}}$ . As these quantities cannot be directly measured in an experiment, their mean values are extracted via a mapping procedure involving the definition of centrality classes in both the measured and the calculated distribution. For the Cu+Au collisions at  $\sqrt{s_{\text{NN}}} = 200 \text{ GeV}$ , PHENIX uses the total charge deposited in the Beam-Beam Counters to determine the centrality classes, as explained in [104].

The basic assumption underlying the centrality class is that the impact parameter  $b$  is monotonically related to the particle multiplicity. For large  $b$  (peripheral) events, a low multiplicity at the mid-rapidity and a large number of spectator nucleons at the beam-rapidity is expected, whereas for small  $b$  (central) events, a large multiplicity at the mid-rapidity and a small number of spectator nucleons at the beam-rapidity is expected. Once the total integral of this charge distribution is known, the distribution is fitted with the Negative Binomial Distribution (NBD), and the centrality classes are defined by binning the distribution based on the fraction of the total integral. The same procedure is then applied to the Glauber-based distribution obtained by matching the input NBD parameters to the parameters obtained from the fit to the data. For each centrality class, the mean value of the geometric quantities (e.g.,  $\langle N_{\text{Part}} \rangle$ ,  $\langle N_{\text{Coll}} \rangle$ ) are calculated from the Glauber distribution.

#### 4.2.2 Monte Carlo event generators

Monte Carlo event generators provide the simulation of high energy particle collisions and are used in almost all experimental nuclear physics analyses. They are designed to simulate high energy collisions in full detail, and when these generators are combined with the detector simulation, they provide an estimate of the detector response to the collisions. The underlying mechanism of a general event generator can be summarized in the following stages [105]:

1. **Hard process:** Outgoing partons (quarks and gluons) are produced when the partons of the colliding particles interact at a high momentum scale. The PDFs describe partons

coming into the process, and the lowest order perturbation theory gives a probabilistic distribution of the outgoing partons.

2. **Parton shower:** As hard processes involve large momentum transfer, the partons involved, as well as any new particles with color, radiate gluons. These gluons can further radiate gluons or produce quark anti-quark pairs, leading to an extended shower and fill the phase space with mostly soft gluons.
3. **Multiple parton interactions:** In hadron-hadron collisions, other constituent partons of the incoming hadrons, which do not directly participate in the hard process, undergo secondary interactions and produce the underlying event (of soft hadrons).
4. **Hadronization:** During the parton showering (and the multiple parton interactions), when the interaction scale falls, the system of partons confines into hadrons.
5. **Decay of unstable particles:** Many of the produced hadrons are unstable; so, the final stage of the event generation is the sequential decay of these hadrons.

Two Monte Carlo event generators used in this analysis and their nominal settings are discussed in the sections below.

#### 4.2.2.1 PYTHIA

PYTHIA [106] is a general purpose event generator and contains theories and models for many physics aspects, including hard and soft interactions, parton distributions, initial-state and final-state parton showers, multiple interactions, fragmentations, and decays. It provides the simulation of high energy collisions between particles, such as electrons, positrons, protons, and anti-protons, in various combinations.

This analysis uses PHPYTHIA, which generates events using the Fortan version of PYTHIA 6 within the PHENIX's Fun4All framework. The following nominal settings are used to generate the PYTHIA events<sup>ii</sup>

- The  $p+p$  collisions at  $\sqrt{s_{NN}} = 200 \text{ GeV}$
- PYTHIA tune "A"
- In addition, only the following  $2 \rightarrow 2$  (tree-level) QCD processes are selected:

---

<sup>ii</sup>The PHPYTHIA configuration is set in the PHENIX pythia.cfg file.

- $q_i + q_j \rightarrow q_i + q_j$  (msub 11)
- $q_i + \bar{q}_i \rightarrow q_k + \bar{q}_k$  (msub 12)
- $q_i + \bar{q}_i \rightarrow g + g$  (msub 13)
- $q_i + g \rightarrow q_i + g$  (msub 28)
- $g + g \rightarrow q_k + \bar{q}_k$  (msub 53)
- $g + g \rightarrow g + g$  (msub 68)

The choice of the minimum parton  $p_T$  (PYTHIA ckin 3) will be mentioned whenever relevant.

#### 4.2.2.2 HIJING

With an expectation that hard or semi-hard parton scatterings dominate high energy heavy ion collisions, Heavy Ion Jet INteraction Generator (HIJING) [107] was developed with special emphasis on the role of mini-jets in  $p+p$ ,  $p+A$ , and  $A+A$  collisions.

To identify ‘true jets’ from the HIJING event generator, the HIJING code has been augmented as sHIJING so that every time the fragmentation routine (HIJFRG) is called, the final state hadrons that result from that fragmentation are recorded. The anti- $k_t$  algorithm is run on those final state hadrons for each  $R_{\text{Anti-}k_t}$  under consideration, and the resulting ‘true jet’ information is added to the sHIJING output [108].

This analysis uses PHHIJING and sHIJING, which generate events using HIJING within the PHENIX’s Fun4All framework. The following nominal settings are used to generate HIJING events<sup>iii</sup>:

- Minimum Bias events for Cu+Au at  $\sqrt{s_{\text{NN}}} = 200 \text{ GeV}$
- Jet quenching turned off

The choice (or choices) of  $R_{\text{Anti-}k_t}$  while running sHIJING will be mentioned whenever relevant. Centrality classes for the HIJING Cu+Au events are selected by using the estimated Glauber model impact parameter  $b$  from [104] and are summarized in Table 4.1.

---

<sup>iii</sup>The PHHIJING configuration is set in the PHENIX phhijing.cfg file and the sHIJING configuration is set in the PHENIX sHijing.xml file.

Table 4.1: Centrality selection for the HIJING Cu+Au events.

Centrality	$b$ (fm)
0–20%	0.0–5.63
20–40%	5.63–8.09
40–60%	8.09–10.04
60–90%	10.04–12.95

### 4.3 Simulation study without detector effects

The underlying event in the heavy ion collisions affects the performance of jet reconstruction. An addition of even a moderately high- $p_T$  particle in an event can cause the jet energy to be misreconstructed. For Au+Au collisions at  $\sqrt{s_{\text{NN}}} = 200 \text{ GeV}$  in RHIC, the transverse momentum density  $\rho$  of the final state particles is about  $100 \text{ GeV}$  per unit area (in the  $\eta$ - $\phi$  plane) [109]. Thus, for  $R = 0.4$ , the reconstructed jet in the Au+Au collisions will contain background contamination in the order of

$$\pi R^2 \rho = 50 \text{ GeV}.$$

The Cu+Au collision system offers an intermediate testing ground for the heavy ion jet reconstruction as the underlying event in the Cu+Au collisions is smaller when compared to that in the larger heavy ion systems.

As a preamble to the data analysis and to examine the dependence of observables on the jet reconstruction algorithms and the  $R$ -parameters, a simple simulation study without detector effects is discussed in this section. As the background contamination grows with  $R^2$ , as shown above, four different  $R$ -parameters are used, and the jets are reconstructed separately with the anti- $k_t$  and Gaussian filter algorithms. Overall, the following three sets of jets are discussed here:

1. sHIJING jets reconstructed with the anti- $k_t$  algorithm.
2. PYTHIA+sHIJING jets reconstructed with the anti- $k_t$  algorithm.
3. PYTHIA+sHIJING jets reconstructed with the Gaussian filter algorithm.

### 4.3.1 Setup

#### 4.3.1.1 sHIJING

In addition to the nominal settings mentioned in Section 4.2.2.2,  $R_{\text{Anti-}k_t} = 0.15, 0.2, 0.25,$  and  $0.3$  are used to generate the sHIJING Cu+Au events. Two sets of output are obtained from sHIJING: true jets and final state particles. The following requirements are imposed on the sHIJING true jets:

- $p_{\text{T, True}} > 5.0 \text{ GeV}/c$
- Jet axis in the PHENIX acceptance

Figure 4.2 is the per-event sHIJING true jet yield for the various  $R_{\text{Anti-}k_t}$  parameters.

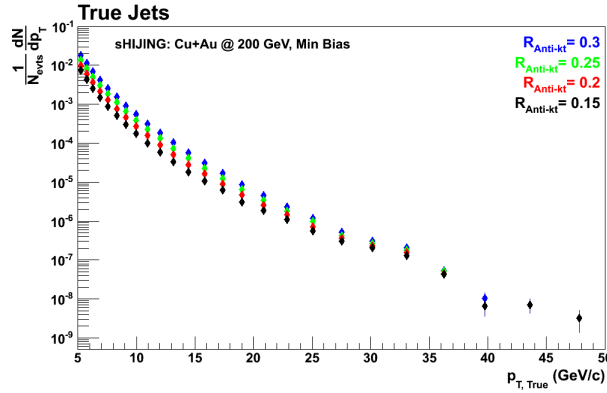


Figure 4.2: Per-event sHIJING true jet yield with the anti- $k_t$  algorithm.

The final state particles are passed through the PHENIX acceptance in the 2012 PHENIX magnetic field configuration using the fast-filter class (which is explained in Appendix A). The anti- $k_t$  algorithm is run on these final state particles<sup>iv</sup> with  $R_{\text{Anti-}k_t} = 0.15, 0.2, 0.25,$  and  $0.3$  to obtain the inclusive sHIJING jets. The following requirements are imposed on the sHIJING inclusive jets:

- $p_{\text{T, Reco}} > 5.0 \text{ GeV}/c$
- $n.c. >= 3$

---

<sup>iv</sup>Muons and neutrinos are excluded.

When the sHIJING inclusive jets are uniquely matched to the sHIJING true jets, the constituents of these matched jets are saved. To obtain the soft background of sHIJING, the constituents of the sHIJING matched jets are subtracted from the sHIJING final particle list.

#### 4.3.1.2 PYTHIA

In addition to the nominal settings mentioned in Section 4.2.2.1, the minimum parton  $p_T$  (ckin 3) of 5.0 GeV/c is used to generate the PYTHIA  $p+p$  events. As with sHIJING, the final state particles of PYTHIA are required to pass through the PHENIX acceptance in the 2012 PHENIX magnetic field configuration using the fast-filter class. The anti- $k_t$  algorithm with  $R_{\text{Anti-}k_t} = 0.15, 0.2, 0.25$ , and  $0.3$  and the Gaussian filter algorithm with  $R_{\text{Filter}} = 0.106, 0.141, 0.177$ , and  $0.212$  are run on these final state particles<sup>v</sup> to obtain two sets of PYTHIA true jets.

The following requirements are imposed on the PYTHIA true jets:

- $p_{T,\text{True}} > 5.0 \text{ GeV}/c$

Note that, unlike for the sHIJING true jets, there is no acceptance requirement for the PYTHIA true jets as the final state particles of PYTHIA (and hence, the constituents of the PYTHIA true jets) are already required to fall in the PHENIX acceptance.

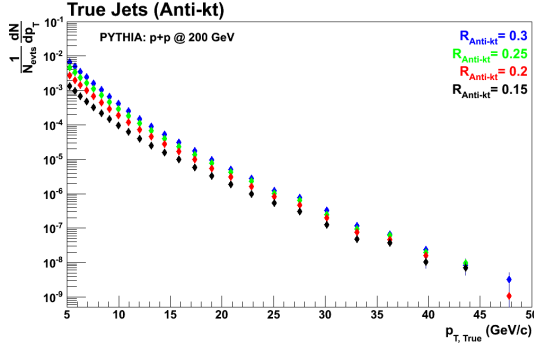


Figure 4.3: Per-event PYTHIA true jet yield with the anti- $k_t$  algorithm.

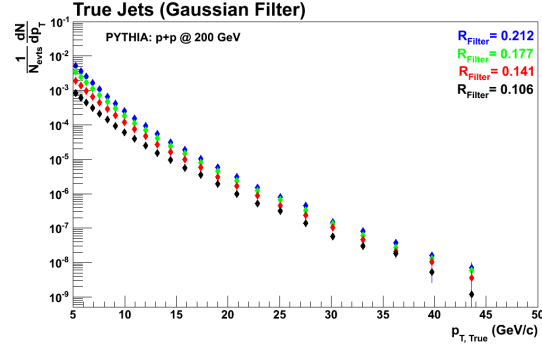


Figure 4.4: Per-event PYTHIA true jet yield with the Gaussian Filter algorithm.

---

<sup>v</sup>Muons and neutrinos are excluded.

Figure 4.3 and Figure 4.4 are the per-event PYTHIA true jet yield for the various  $R_{\text{Anti-}k_t}$  and  $R_{\text{Filter}}$  parameters, respectively. When comparing Figure 4.2 and Figure 4.4, no obvious difference in the anti- $k_t$  algorithm and the Gaussian filter algorithm is observed.

The constituents of the PYTHIA true jets are saved to be embedded in the soft background of sHIJING. For the anti- $k_t$  algorithm, the kinematics of the constituents of a jet are readily accessible. For the Gaussian filter algorithm, as the number of constituents of a jet is the Gaussian weighted number of particles associated with it, only particles with the Gaussian weight  $> 0.4$  are recorded as its constituents. For the process of embedding, the constituents of the PYTHIA true jets are added to the soft background of sHIJING. Two sets of embedded particle lists are saved, and the anti- $k_t$  and Gaussian filter algorithms are run on them. The following requirements are imposed on the PYTHIA+sHIJING inclusive jets:

- $p_{\text{T, Reco}} > 5.0 \text{ GeV}/c$
- $n.c. \geq 3$

### 4.3.2 Performance

#### 4.3.2.1 Matching efficiency

The inclusive jets are uniquely matched to the true jets, and the matching efficiency is defined as

$$\text{matching efficiency} = \frac{\text{no. of matched jets (with discriminant cut)}}{\text{no. of true jets}}. \quad (4.16)$$

The procedure that performs the one-to-one matching is described in Appendix B, and in this case, minimum  $\Delta R_{\min}$  is chosen such that  $\Delta R_{\min} = R$ -parameter being used<sup>vi</sup>. Figure 4.5 shows the matching efficiency of the PYTHIA+sHIJING jets reconstructed with the anti- $k_t$  algorithm for four different  $R$ -parameters; the top-left plot is for  $R_{\text{Anti-}k_t} = 0.15$ , top-right for  $R_{\text{Anti-}k_t} = 0.2$ , bottom-left for  $R_{\text{Anti-}k_t} = 0.25$ , and bottom-right for  $R_{\text{Anti-}k_t} = 0.3$ . Various discriminant cuts are shown in the legend of each plot. With no discriminant cut, the reconstruction efficiency is  $\sim 1$  across all  $p_{\text{T, True}}$  for all  $R$ -parameters. For the discriminant  $> 10 (\text{GeV}/c)^2$ , the reconstruction efficiency saturates at  $\sim 10 \text{ GeV}/c$  for  $R_{\text{Anti-}k_t} = 0.2$  and at

---

<sup>vi</sup>  $\Delta R = \sqrt{\Delta\eta^2 + \Delta\phi^2}$  is the distance between the true jet axis and the closest reconstructed jet axis.

$\sim 15 \text{ GeV}/c$  for  $R_{\text{Anti-}k_t} = 0.3$ , while for the discriminant  $> 25 (\text{GeV}/c)^2$ , the reconstruction efficiency saturates at  $\sim 15 \text{ GeV}/c$  for  $R_{\text{Anti-}k_t} = 0.2$  and at  $\sim 20 \text{ GeV}/c$  for  $R_{\text{Anti-}k_t} = 0.3$ .

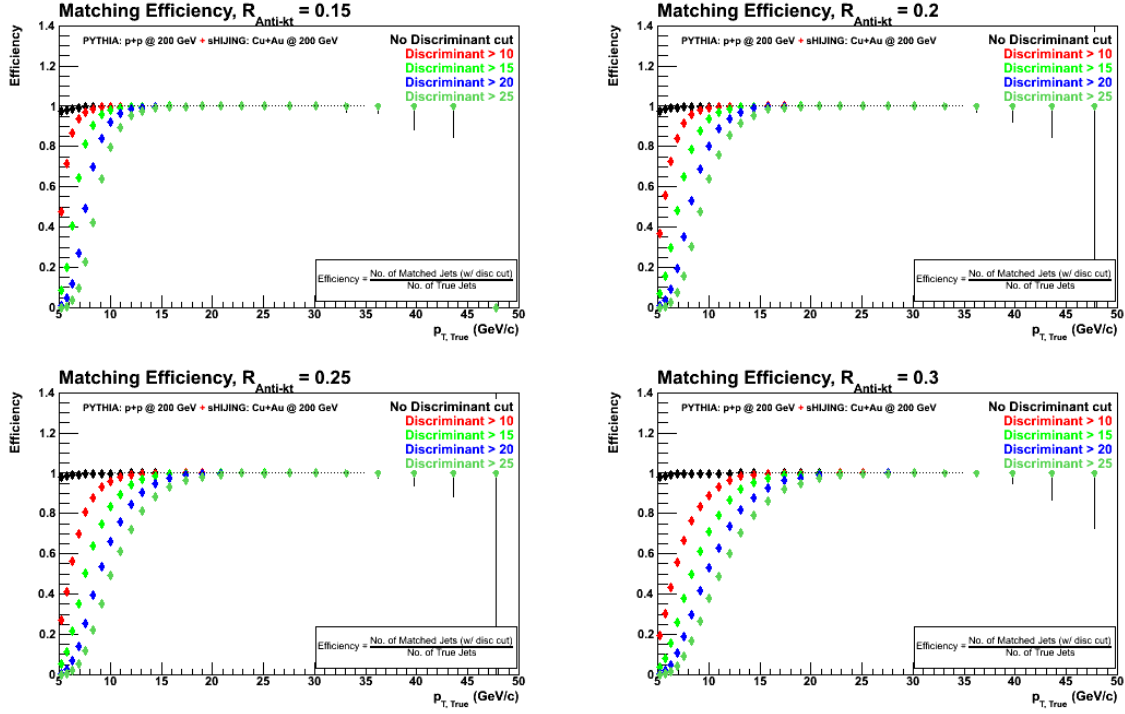


Figure 4.5: Matching efficiency of the PYTHIA+sHIJING jets reconstructed with the anti- $k_t$  algorithm.

Similar behavior is observed in the other two sets of jets; Figure 4.6 and Figure 4.7 are the matching efficiency of the sHIJING jets reconstructed with the anti- $k_t$  algorithm and the PYTHIA+sHIJING jets reconstructed with the Gaussian filter algorithm, respectively. Although the saturation behavior is similar to that of the PYTHIA+sHIJING jets, the sHIJING jets do not reach the saturation of  $\sim 1$  (especially for small  $R_{\text{Anti-}k_t}$ ); the reason for which can be attributed to the difference in the definition of the true jet.

#### 4.3.2.2 Comparison of $p_T, \text{True}$ and $p_T, \text{Reco}$

The effect of the underlying event and its dependence on the choice of  $R$ -parameter can be examined directly by comparing  $p_T, \text{True}$  and  $p_T, \text{Reco}$ . Figure 4.8 is the per-event yield of the true jets (red markers) and the matched jets (black markers) overlaid in the same plot

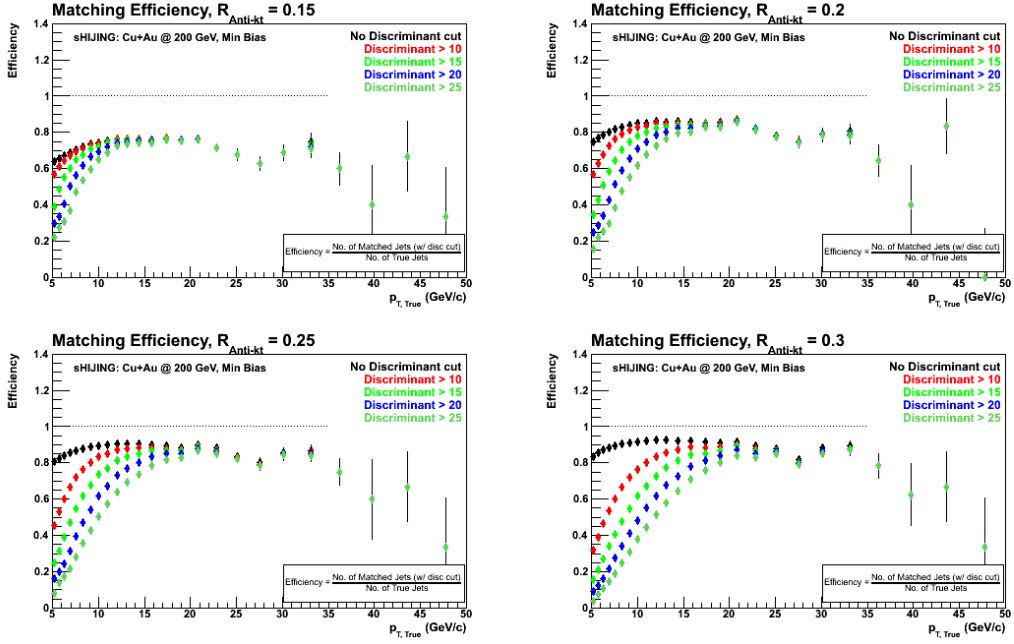


Figure 4.6: Reconstruction efficiency of the sHIJING jets reconstructed with the anti- $k_t$  algorithm.

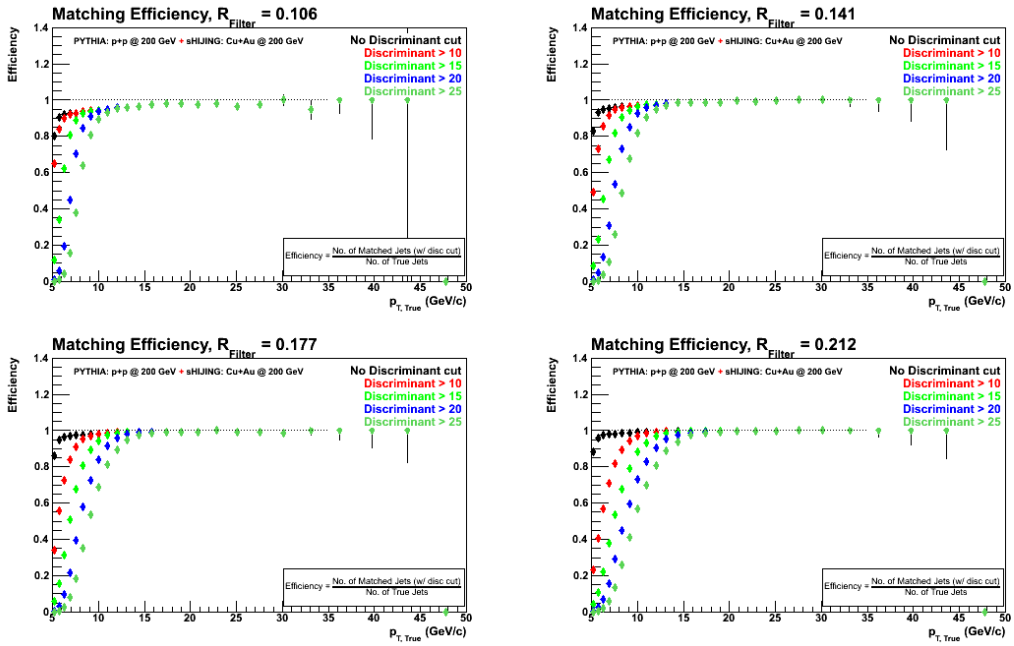


Figure 4.7: Reconstruction efficiency of the PYTHIA+sHIJING jets reconstructed with the Gaussian filter algorithm.

for the PYTHIA+sHIJING jets reconstructed with the anti- $k_t$  algorithm; the top-left plot is for  $R_{\text{Anti-}k_t} = 0.15$ , top-right for  $R_{\text{Anti-}k_t} = 0.2$ , bottom-left for  $R_{\text{Anti-}k_t} = 0.25$ , and bottom-right for  $R_{\text{Anti-}k_t} = 0.3$ . It can be realized from Figure 4.8 that for smaller  $R$ -parameters, like  $R_{\text{Anti-}k_t} = 0.15$ , the contribution of the underlying event is minimal, and the reconstructed spectrum is very similar to the true spectrum. With increasing  $R_{\text{Anti-}k_t}$ , the difference between  $p_{T,\text{True}}$  and  $p_{T,\text{Reco}}$  increases on average across all  $p_{T,\text{True}}$ . A similar observation can be made from the other two sets of the jets.

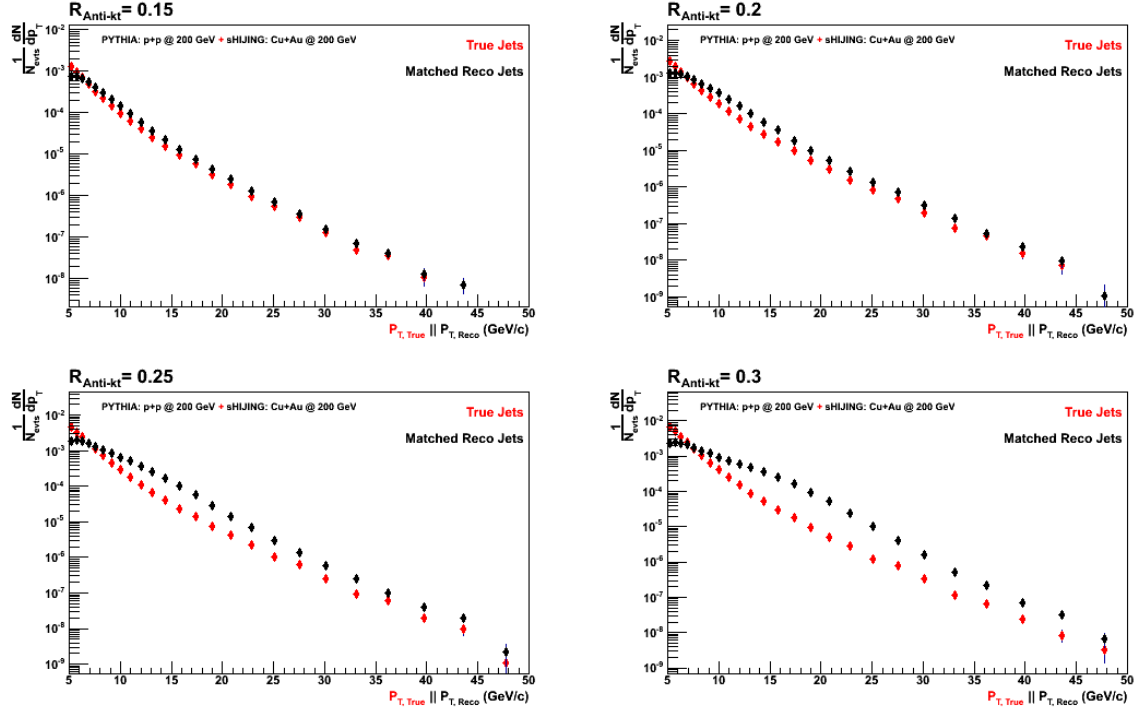


Figure 4.8: Per-event yield for the PYTHIA+sHIJING true and matched jets reconstructed with the anti- $k_t$  algorithm.

While only considering the effects of the underlying event, a choice of smaller  $R$ -parameter, like  $R_{\text{Anti-}k_t} = 0.2$ , seems to minimize the contribution of the underlying event. Although we want to minimize the effects of the underlying event, we also aim to capture most of the energy produced from the hard scattering, and a choice of too small  $R$ -parameter, like  $R_{\text{Anti-}k_t} = 0.15$ , puts us at the risk of not being able to do so.

The centrality dependence of the underlying event contribution can be examined by a simple analysis of the response matrix. Figure 4.9 and Figure 4.10 show the response matrix<sup>vii</sup> of the PYTHIA+sHIJING jets reconstructed with the anti- $k_t$  algorithm for different centralities. Figure 4.9 is for  $R_{\text{Anti-}k_t} = 0.2$  and Figure 4.10 is for  $R_{\text{Anti-}k_t} = 0.3$ , and the following observations can be made by analyzing them:

- For both  $R_{\text{Anti-}k_t}$ , the contribution of the underlying event is more severe in the central collisions than the peripheral. For the 60–90% centrality, the matrix is almost diagonal for both  $R_{\text{Anti-}k_t}$ 's, and on average,  $p_{T,\text{Reco}}$  is very much similar to  $p_{T,\text{True}}$ . For the 0–20%, a strong influence of the underlying event can be observed, and on average,  $p_{T,\text{Reco}}$  is greater than  $p_{T,\text{True}}$ .
- The contribution of the underlying event is more severe for  $R_{\text{Anti-}k_t} = 0.3$  than  $R_{\text{Anti-}k_t} = 0.2$ . For example, for the 0–20%, between two  $R_{\text{Anti-}k_t}$ 's,  $R_{\text{Anti-}k_t} = 0.3$  has  $p_{T,\text{Reco}}$  relatively greater than  $p_{T,\text{True}}$  (due to the  $p_T$  feeding effect).

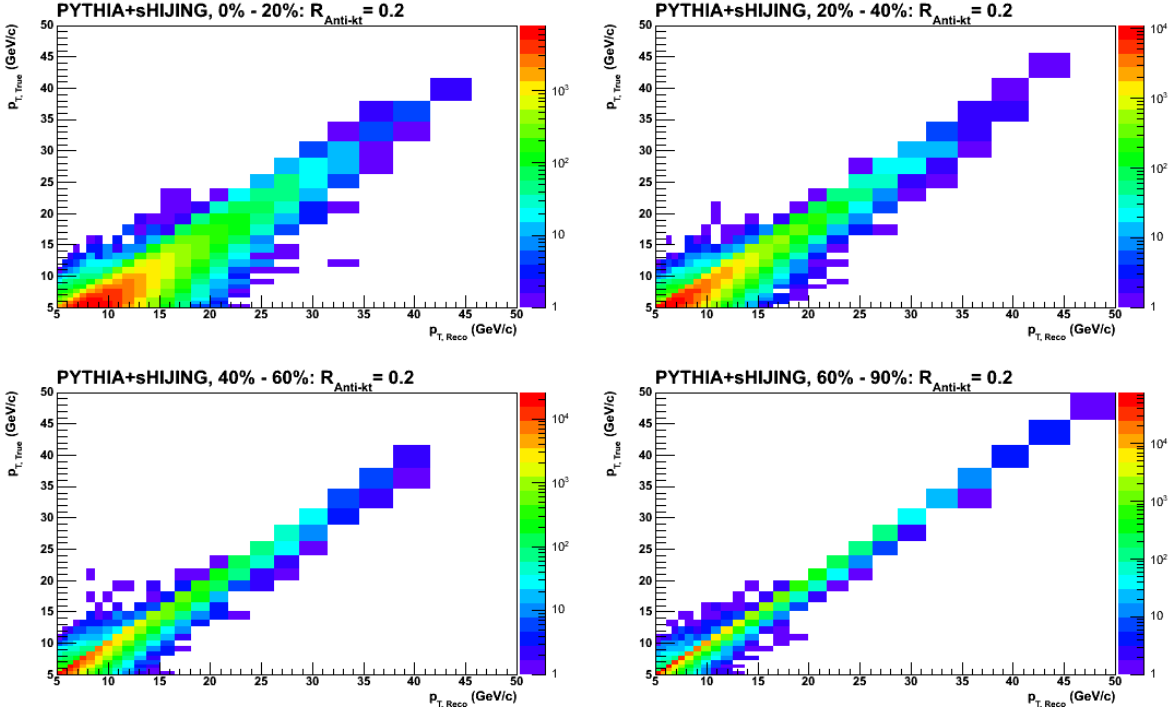


Figure 4.9: Response matrix of the PYTHIA+sHIJING jets with  $R_{\text{Anti-}k_t} = 0.2$ .

---

<sup>vii</sup> $p_{T,\text{True}}$  is on the  $y$ -axis and  $p_{T,\text{Reco}}$  is on the  $x$ -axis.

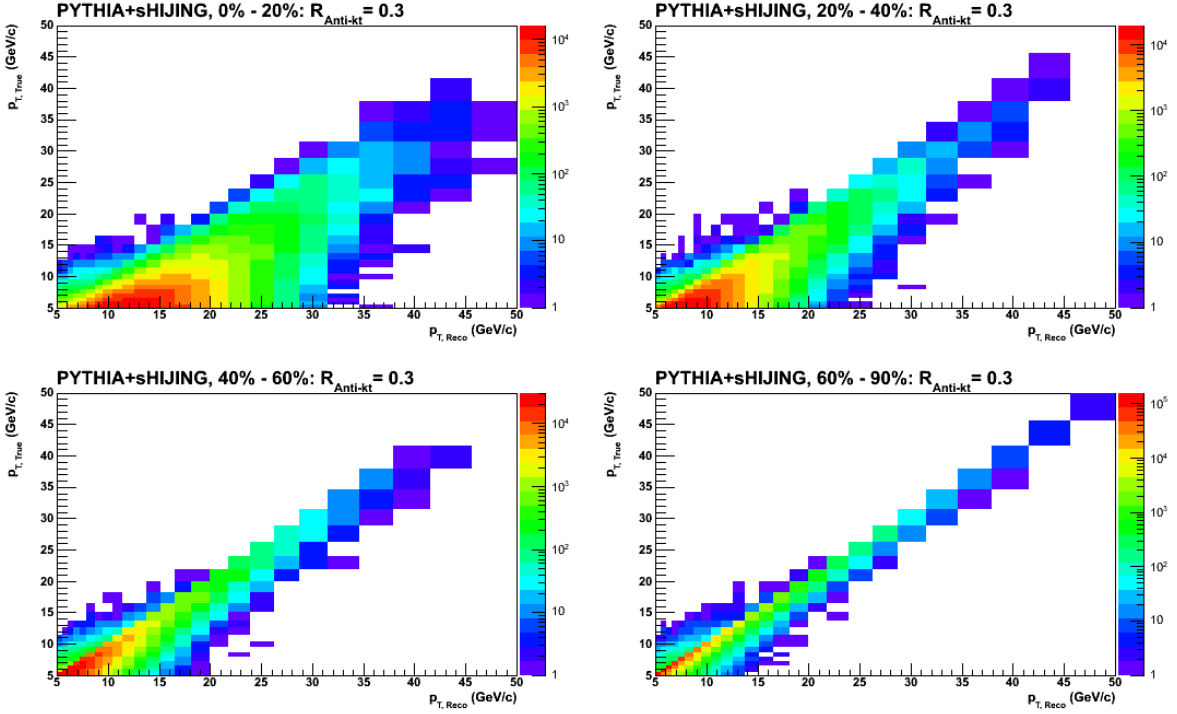


Figure 4.10: Response matrix of the PYTHIA+sHIJING jets with  $R_{\text{Anti-}k_t} = 0.3$ .

#### 4.3.2.3 “Purity”

The “purity” for various discriminant cuts is defined as<sup>viii</sup>

$$\text{“purity”} = \frac{\text{no. of matched jets}}{\text{no. of inclusive jets}} \text{ (with discriminant cut).} \quad (4.17)$$

Figure 4.11 shows the “purity” of the PYTHIA+sHIJING jets reconstructed with the anti- $k_t$  algorithm; the top-left plot is for  $R_{\text{Anti-}k_t} = 0.15$ , top-right for  $R_{\text{Anti-}k_t} = 0.2$ , bottom-left for  $R_{\text{Anti-}k_t} = 0.25$ , and bottom-right for  $R_{\text{Anti-}k_t} = 0.3$ . The various discriminant cuts are shown in the legend of each plot. For all the discriminant cuts, the “purity” saturates at  $\sim 20 \text{ GeV}/c$  for  $R_{\text{Anti-}k_t} = 0.2$  and at  $\sim 35 \text{ GeV}/c$  for  $R_{\text{Anti-}k_t} = 0.3$ . In both the cases, the saturation happens slowly for no discriminant selection and the rate of the saturation increases with larger discriminant selection. What this suggests is that the fake jet rate is severe below  $\sim 20 \text{ GeV}/c$  for  $R_{\text{Anti-}k_t} = 0.2$  and below  $\sim 35 \text{ GeV}/c$  for  $R_{\text{Anti-}k_t} = 0.3$ , and to measure spectra below the

---

<sup>viii</sup>The “purity” is put on quotes as it differs from the purity defined in the literature ( $S/(S+B)$ ).

mentioned  $p_T$ 's for respective  $R_{\text{Anti-}k_t}$ , some form of the fake jet rejection/subtraction method is essential. Similar behavior is also observed for the other two sets of jets.

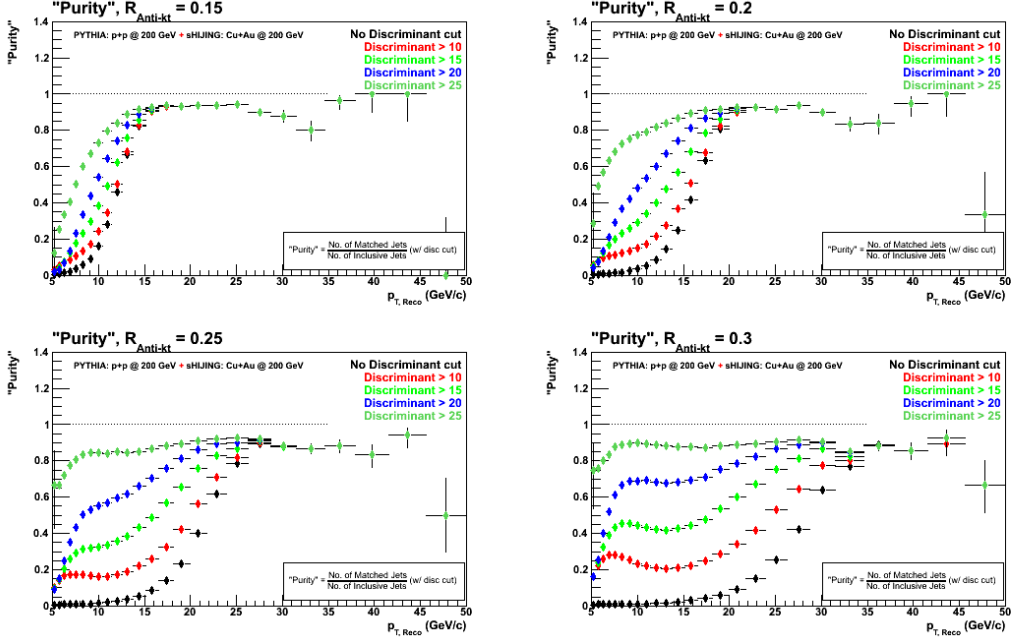


Figure 4.11: “Purity” of the PYTHIA+sHIJING jets reconstructed with the anti- $k_t$  algorithm for various discriminant selections.

Dependence of the “purity” on different centrality selection with a moderate fake jet rejection (discriminant  $> 15 (\text{GeV}/c)^2$ ) is also studied here. Figure 4.12 shows the “purity” for the PYTHIA+sHIJING jets reconstructed with the anti- $k_t$  algorithm; the top-left plot is for  $R_{\text{Anti-}k_t} = 0.15$ , top-right for  $R_{\text{Anti-}k_t} = 0.2$ , bottom-left for  $R_{\text{Anti-}k_t} = 0.25$ , and bottom-right for  $R_{\text{Anti-}k_t} = 0.3$ . Various centrality selections are shown in the legend of each plot. For the most peripheral centrality bin (60–90%), the “purity” is  $\sim 1$  for all  $p_T, \text{True}$ . As expected, the “purity” is worse for more central events due to higher multiplicity and stronger contribution of the underlying event. The most central distribution shows a strong  $R_{\text{Anti-}k_t}$  dependence too.

### 4.3.3 Conclusion

The following conclusions can be drawn from the observations made in this section:

- For smaller  $R$ -parameter, the contribution of the underlying event is moderate, and the reconstructed spectrum is relatively similar to the true spectrum.

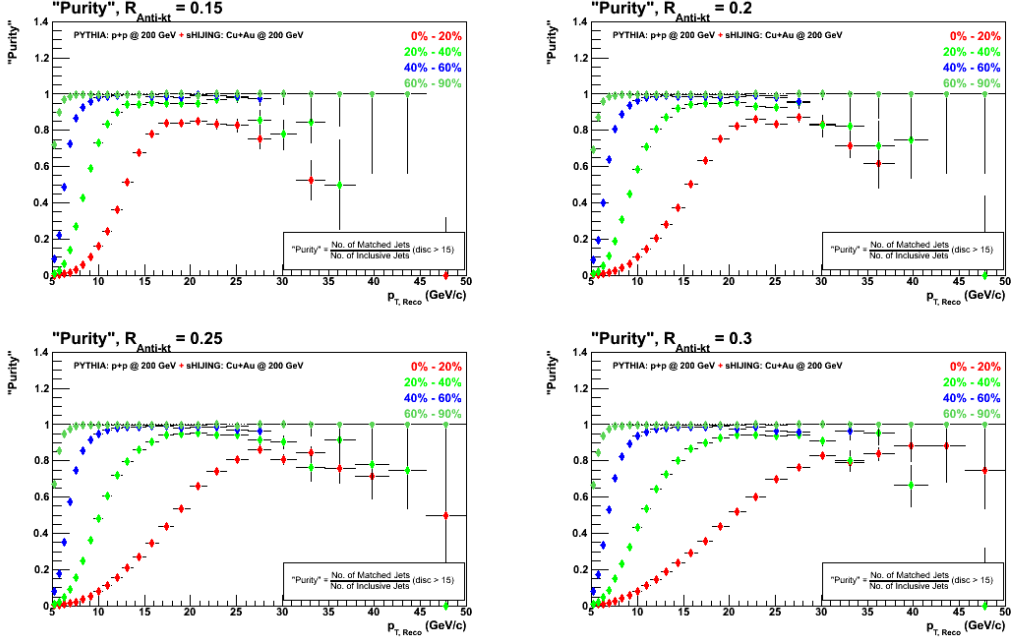


Figure 4.12: “Purity” of the PYTHIA+sHIJING jets reconstructed with the anti- $k_t$  algorithm for various centrality selections.

- The fake jet contribution is less sever for smaller  $R$ -parameters.
- There is no significant difference in the observables obtained by using the anti- $k_t$  algorithm or the Gaussian filter algorithm.

After weighing-in the above mentioned conclusions, this analysis will hereafter continue by using anti- $k_t$  algorithm with  $R_{\text{Anti-}k_t} = 0.2$ .

## CHAPTER 5. DATA ANALYSIS

### 5.1 Data selection

#### 5.1.1 Cu+Au

The first physics run for the Run-12<sup>i</sup> 200 GeV Cu+Au collisions was taken on May 18, 2012, with the run number 372402, and the last physics run was taken on June 25, 2012, with the run number 377310. During that time, the total integrated sampled luminosity of  $2.96 \text{ nb}^{-1}$  for the 12 cm vertex was collected, as shown in Figure 5.1.

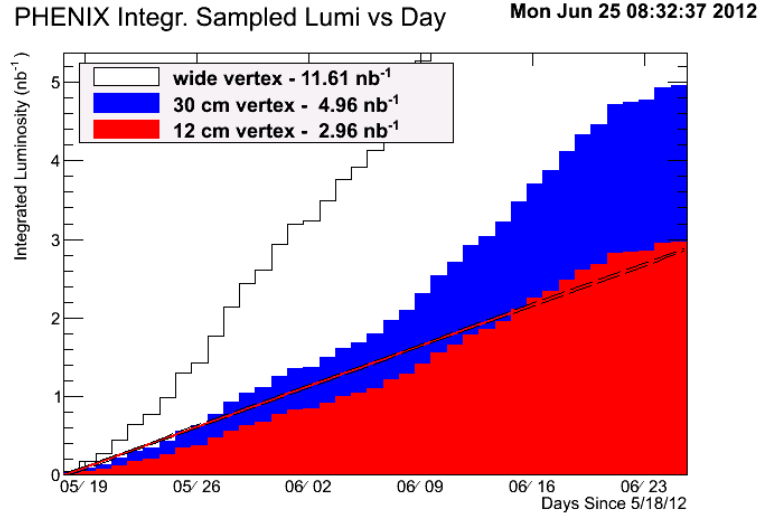


Figure 5.1: PHENIX integrated sampled luminosity vs. day for the Run-12 200 GeV Cu+Au collision period, from [110].

For the Cu+Au dataset, the following trigger is selected:

- Minimum Bias: BBCLL1(> 1 tubes) narrowvtx

---

<sup>i</sup>2012 RHIC running period.

### 5.1.2 $p+p$

The first physics run for the Run-12 200 GeV  $p+p$  collisions was taken on February 10, 2012, with the run number 358513, and the last physics run was taken on March 12, 2012, with the run number 363228. During that time, the total integrated sampled luminosity of  $4.34 \text{ pb}^{-1}$  for the 15 cm vertex was collected, as shown in Figure 5.2.

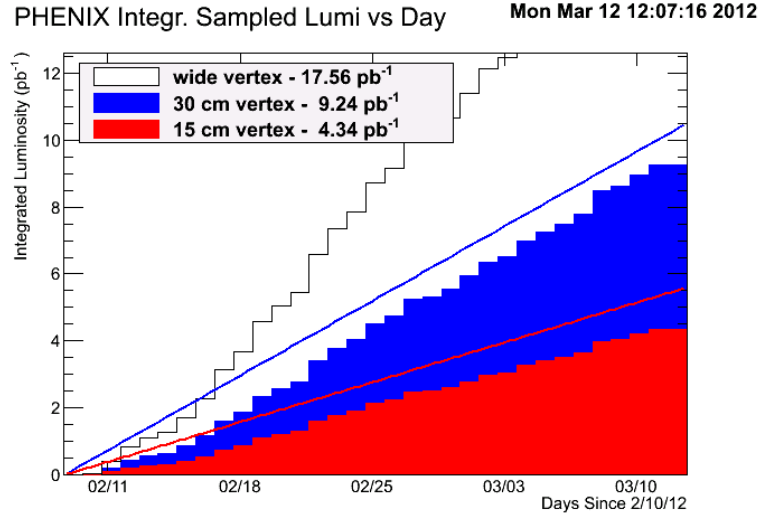


Figure 5.2: PHENIX integrated sampled luminosity vs. day for the Run-12 200 GeV  $p+p$  collision period, from [111].

For the  $p+p$  dataset, the following triggers are selected:

- ERT: ERT\\_4x4c&BBCLL1(narrow)
- Minimum Bias: BBCLL1(>0 tubes) narrowvtx. This trigger selection is used to determine the ERT trigger efficiency as well as to calculate the effective number of Minimum Bias events for the ERT dataset, both of which will be discussed in Chapter 7.

## 5.2 Run quality assurance

Bad runs were determined by scanning for problems in the DC/PC and the individual sectors of EMCAL. To isolate runs with problems in the DC/PC, the total tracks and total quality (63 or 31) tracks per event distributions were analyzed. The track yields were analyzed for the east arm and the west arm separately as well as for the arms combined. To isolate runs with the

problem in the EMCal, the total cluster per event distribution (for each sector) was analyzed. For the purpose of run quality assurance (QA), only tracks with  $p_T > 500 \text{ MeV}/c$  and clusters with energy  $> 500 \text{ MeV}$  were considered.

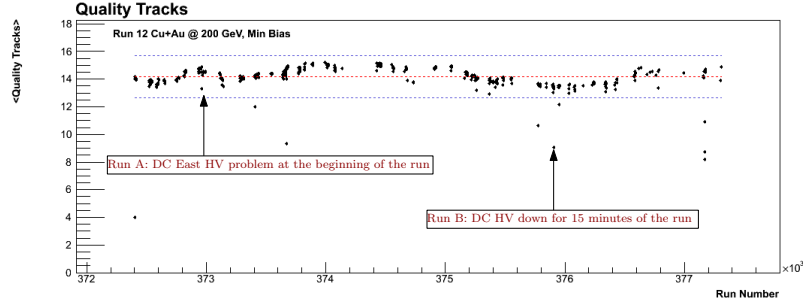


Figure 5.3: Example plot for the run quality assurance procedure.

Figure 5.3 shows an example of the process; the  $y$ -axis is the mean number of quality tracks and the  $x$ -axis is the run number. The red line in Figure 5.3 is the mean of the distribution, and the blue lines are at  $\pm 3 \sigma$ . If a run falls outside the  $3 \sigma$  limit, it is considered to be an outlier and is excluded from the analysis (for example, the run B in Figure 5.3). Occasionally, even when a run falls within the  $3 \sigma$  limit, when compared with its neighbors, it can seem suspicious. For such runs, the Run-12 logbook and shift leader comments were consulted, and if some problems were discovered, such runs were also excluded. For example, although the run A in Figure 5.3 was within the  $3 \sigma$  limit, it was suspicious in regards to its neighbors and was excluded after consulting the run logbook (there was a DC high voltage (HV) problem at the beginning of the run).

### 5.2.1 Cu+Au

Out of the 451 runs available in the train for the Run-12 Cu+Au Minimum Bias dataset<sup>ii</sup>, 30 runs were identified with problems. Table 5.1 lists the excluded runs and the reason (or reasons) for the exclusion.

---

<sup>ii</sup>Train registration name: Run-12 200 GeV Cu+Au MinBias Trigger Pro99(CNT)+Pro100(MWG\_MU)

Table 5.1: Excluded runs for the Cu+Au dataset.

Excluded run	Reason
372402	The first physics run for the Cu+Au collisions, DC HVs were not fully turned on
372524	Problems with the DCW X1 and UV1 channels
372525	Problems with the DCW X1 and UV1 channels
372531	PbGl problems seen in the QA plots but none mentioned in the log
372533	PbSc trips at the beginning and the middle of the run
372536	Two PbSc trips during the run
372647	PbSc problems seen in the QA plots but none mentioned in the log
372648	PbGl problems seen in the QA plots but none mentioned in the log
372959	DCE HV problems at the beginning of the run
372961	Unexpected beam dump and then massive trips
373407	DC/PC problems seen in QA plots but none mentioned in the log
373655	Noisy channels in the DCW
373672	Problem with a DC mainframe (MF), the run was stopped after the DC HV went off
374428	PbSc MF troubles
375773	Miscommunication with MF in the X2 sector of the DC
375774	Miscommunication with MF in the X2 sector of the DC
375906	Various problems with DC MF, DC HV down for 15 minutes of the run
375953	Problems recovering DC channels during the run
375957	Problems with PbSc HV MF
376433	PbGl removed from readout due to LV problems
376434	PbGl removed from readout due to LV problems
376435	PbGl removed from readout due to LV problems
376620	PbGl not included in the run
377155	Lots of PbSc dead channels during the run
377156	Lots of PbSc dead channels during the run
377157	Lots of PbSc dead channels during the run
377167	PbSc problems seen in the QA plots but none mentioned in the log
377171	Problem with the PbSc E2, the MF83 was out of access
377172	Too many DCE X2 channels were in disabled state
377173	Too many DCE X2 channels were in disabled state

### 5.2.2 $p+p$

Out of the 327 runs available in the train for the Run-12  $p+p$  ERT dataset<sup>iii</sup>, 49 runs were identified with problems. Sector 6 and Sector 2 of the PbSc were identified to be dead for the beginning 27 and later 17 runs, respectively. Table 5.2 lists the excluded runs and the reason (or reasons) for the exclusion.

Table 5.2: Excluded runs for the  $p+p$  dataset.

Excluded run	Reason
358717 to 359062 <b>(27 runs)</b>	PbSc (sector 6) problem
359520	PbSc (Sector 3) problem seen in the QA plots but none mentioned in the log
360075 to 360141 <b>(17 runs)</b>	PbSc (sector 2) problem
361244	PbSc (Sector 3) problem seen in the QA plots but none mentioned in the log
361640	1/3 of PC1 was accidentally disabled
361641	1/3 of PC1 was accidentally disabled
362214	PbSc HV problems

## 5.3 Event selection

### 5.3.1 Offline vertex cut

For the event selection, the following offline vertex cut is applied to both the Cu+Au and  $p+p$  datasets:

- $z_{\text{vertex}} < \pm 10 \text{ cm}$

After the trigger selection from Section 5.1.1 and excluding the bad runs from Section 5.2.1, for the Cu+Au Minimum Bias dataset, of  $5.81 \times 10^9$  events available in the train,  $4.13 \times 10^9$  events pass the offline vertex cut and are analyzed in this analysis. For the  $p+p$  ERT dataset, after the trigger selection from Section 5.1.2 and excluding the bad runs from Section 5.2.2, of  $3.34 \times 10^8$

---

<sup>iii</sup>Train registration name: Run-12 200 GeV  $p+p$  (ERT) Pro101

events available in the train,  $1.96 \times 10^8$  events pass the offline vertex cut and are analyzed in this analysis.

## 5.4 Track selection

### 5.4.1 Modified quality cut

During the track reconstruction, the bit pattern assigned for the DC X1 wire, X2 wire, UV wire, and PC1 is:

- X1 used: 1
- X2 used: 2
- UV found: 4
- UV unique: 8
- PC1 found: 16
- PC1 unique: 32

From the track model, the highest quality tracks are the ones with the X1 used bit, X2 used bit, UV unique bit, and PC unique bit; i.e., the ones with the quality 63. The second best tracks are the ones with the quality 31, where the PC1 may be ambiguous [112]. Due to the presence of broken or inefficient X1, X2, and UV wires in the DC, just selecting tracks with the quality (63 or 31) results in a non-uniform DC/PC1 acceptance. In order to obtain more uniform acceptance, which is very crucial for jet reconstruction analyses, the quality requirement in the areas of these broken wires are loosen by creating quality masks. The quality masks are created by plotting ‘alpha vs. board’. The board<sup>iv</sup> is defined as [113]:

$$\text{for the east arm, board} = \frac{3.72402 - \phi_{\text{DC}} + 0.008047 \times \cos(\phi_{\text{DC}} + 0.87851)}{0.01963496} \text{ and} \quad (5.1)$$

$$\text{for the west arm, board} = \frac{0.573231 + \phi_{\text{DC}} - 0.0046 \times \cos(\phi_{\text{DC}} + 0.05721)}{0.01963496}. \quad (5.2)$$

Figure 5.4 is an example of the alpha vs. board plot for tracks that have the X1 quality bit, and hence, the X1 broken or inefficient areas are visible in the plot. These regions of weak acceptance are recorded for each wire (X1, X2, and UV) and are later used to create the modified quality cut. Figure 5.5 is an example of the alpha vs. board plot showing the recorded regions of the X1 weak acceptance. Both Figure 5.4 and Figure 5.5 are for the Cu+Au dataset and show the southeast region in the top-left plot, the northeast region in the top-right plot,

---

<sup>iv</sup>The board is used instead of the azimuthal angle  $\phi$  as it is also related to the DC/PC hardware.

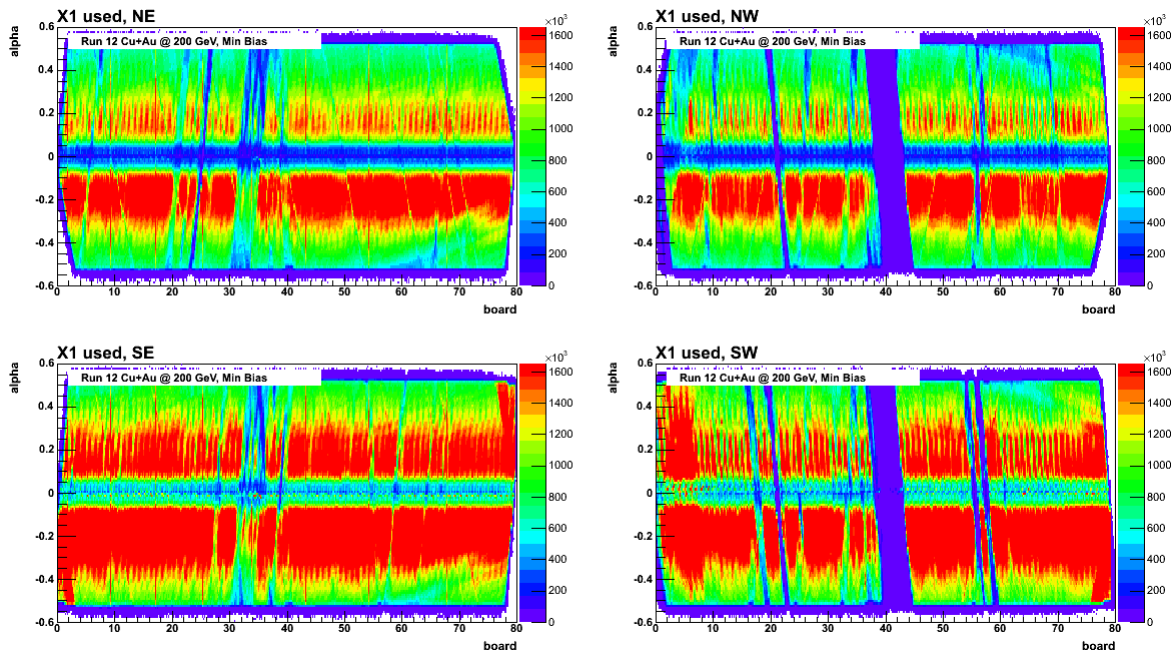


Figure 5.4: Alpha vs. board for tracks that have the X1 quality bit.

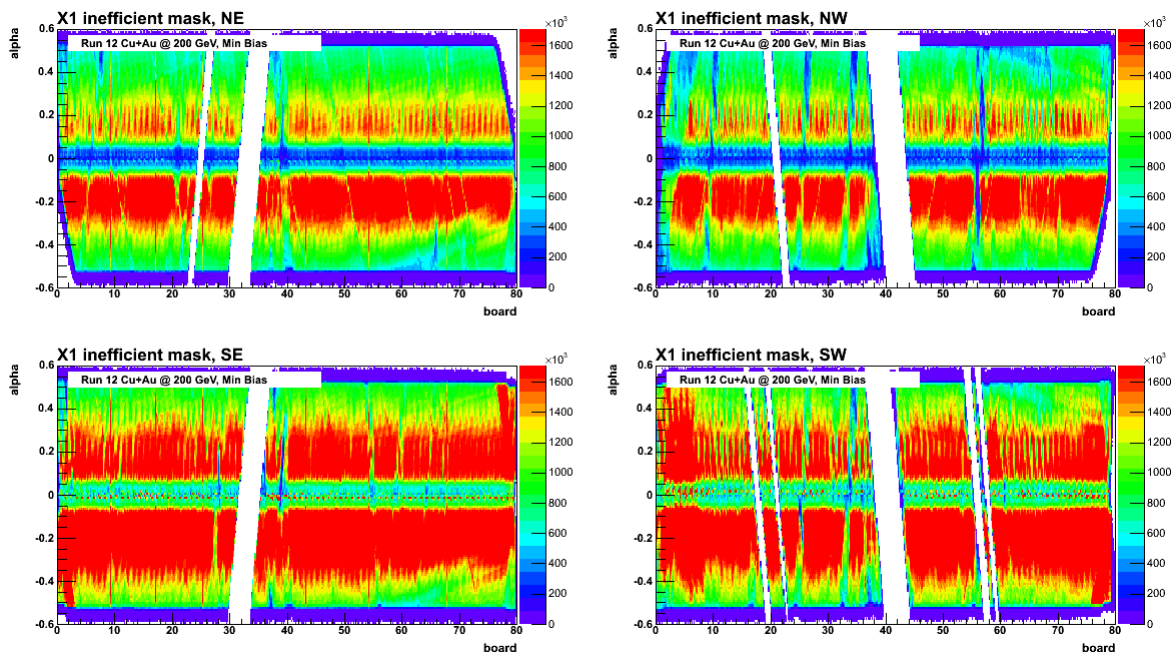


Figure 5.5: Alpha vs. board showing the recorded regions of the X1 weak acceptance.

the southwest region in the bottom-left plot, and the southwest region in the bottom-right plot. The modified quality cut is then created such that a track is rejected if any of the following conditions are not satisfied:

- no (X1 used bit) and no (X2 used bit),  
i.e.  $((\text{quality} \& 1) == 0 \text{ and } (\text{quality} \& 2) == 0)$
- no (X1 used bit) and not (in the region of weak X1 acceptance):
- no (X2 used bit) and not (in the region of weak X2 acceptance)
- no (PC1 found bit),  
i.e.  $((\text{quality} \& 16) == 0)$
- no (PC1 unique bit) and no (UV unique bit),  
i.e.  $((\text{quality} \& 32) == 0 \text{ and } (\text{quality} \& 12) == 0)$
- no (UV unique bit) and not (in the region of weak UV acceptance)

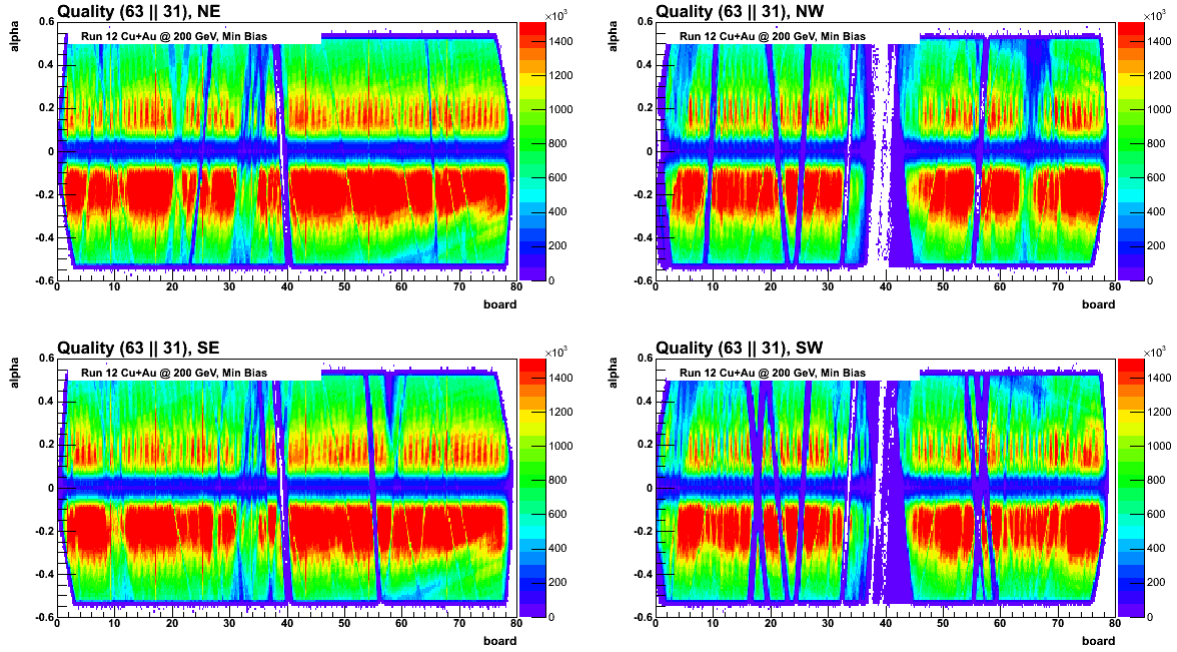


Figure 5.6: DC/PC acceptance for the Cu+Au dataset when the quality (63 or 31) is used.

To demonstrate the improvement in the acceptance, Figure 5.6 shows the DC/PC acceptance when the quality (63||31) is used, while Figure 5.7 shows the acceptance when the modified

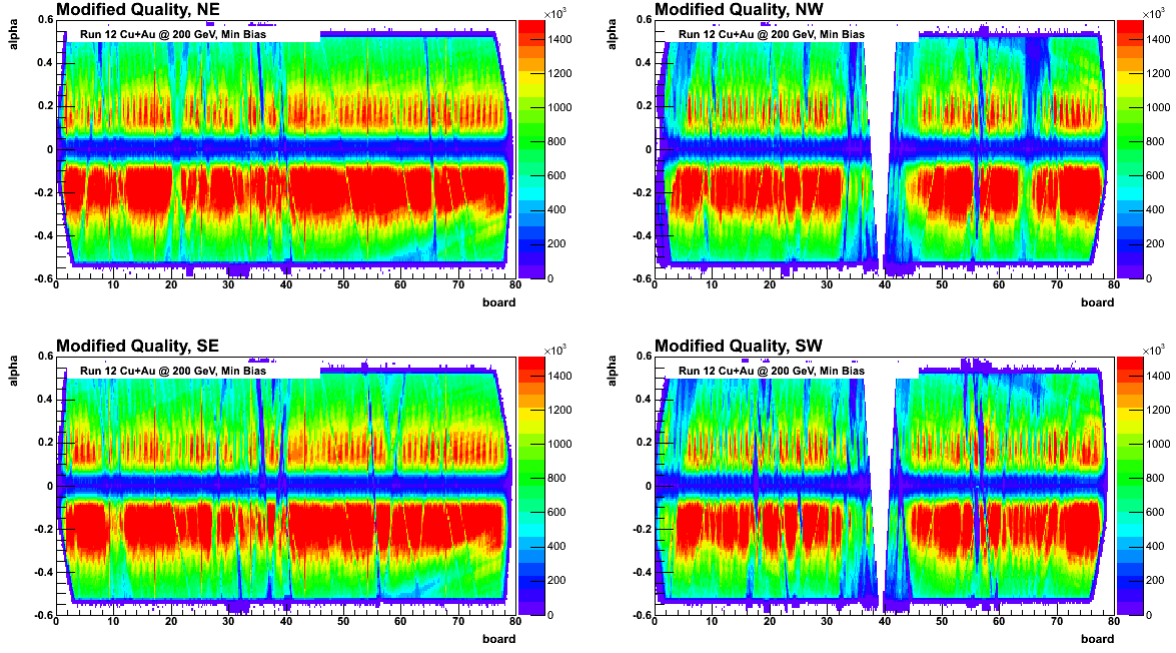


Figure 5.7: DC/PC acceptance for the Cu+Au dataset when the modified quality cut is applied.

quality cut is applied to the Cu+Au dataset. Significant improvement can be observed by comparing these figures side by side.

As the regions of weak acceptance differ between the Cu+Au and  $p+p$  datasets, separate modified quality cuts are developed and applied for each. Figure 5.8 shows the acceptance when the quality (63 or 31) is used while Figure 5.9 shows the acceptance when the modified quality cut is applied for the  $p+p$  dataset.

#### 5.4.2 Pair cut

Track pairs extremely close together in the  $\phi_{DC}$ - $z_{DC}$  space can be a result of the ghosting phenomena during the track reconstruction or the photon conversion at the front face of the DC. Figure 5.10 shows the  $\Delta\phi$  vs.  $\Delta z$  distribution for all track pairs, same charge track pairs, and opposite charge track pairs.

The ghosting phenomena arise during the charged track reconstruction when a single track is reconstructed as two different tracks close in the  $\phi_{DC}$ - $z_{DC}$  space. The ghost cut is developed

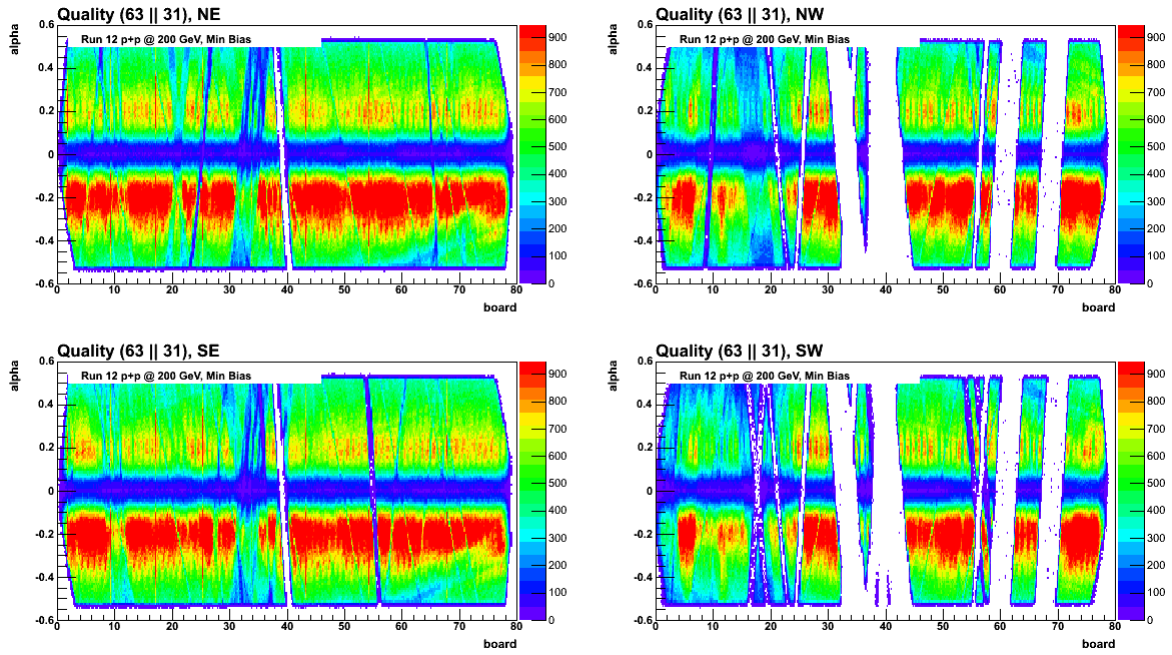


Figure 5.8: DC/PC acceptance for the  $p+p$  dataset when the quality (63 or 31) is used.

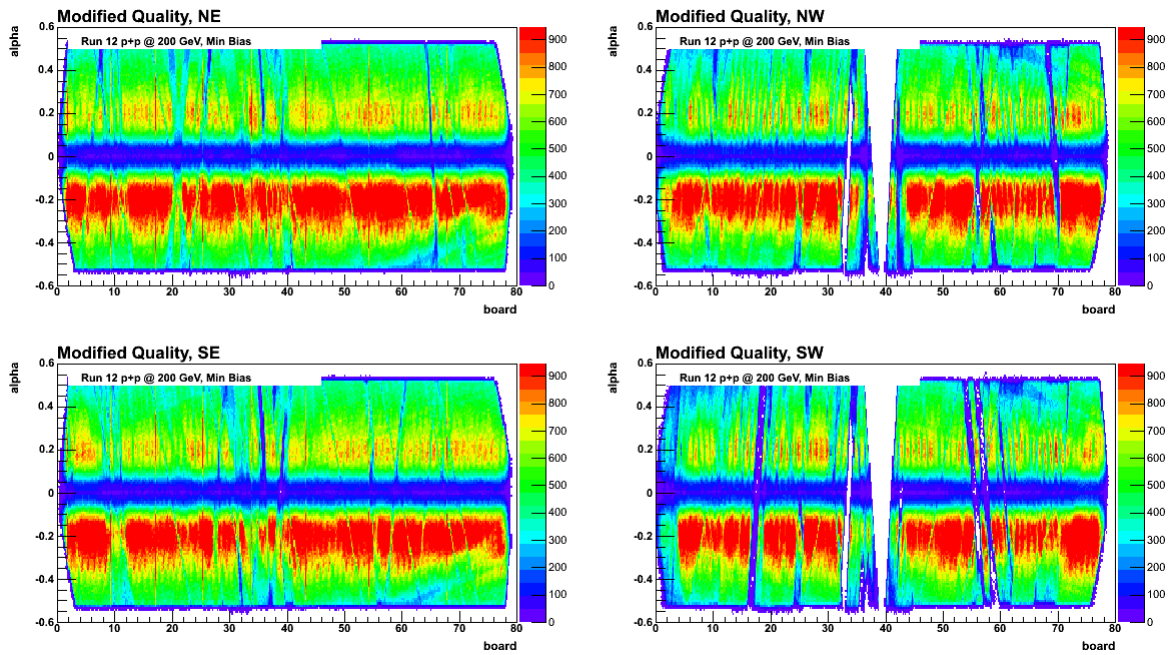


Figure 5.9: DC/PC acceptance for the  $p+p$  dataset when the modified quality cut is applied.

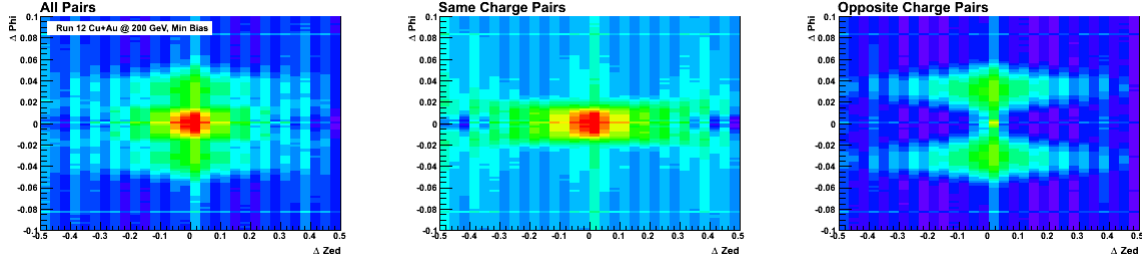


Figure 5.10:  $\Delta\phi$  vs  $\Delta z$  for all pairs, same charge pairs, and opposite charge pairs.

by projecting the  $\Delta\phi$  vs.  $\Delta z$  distribution for the same charge track pairs into the  $x$ -axis and the  $y$ -axis and fitting the projected distribution with a Gaussian function. Figure 5.11 shows the  $\Delta\phi$  vs.  $\Delta z$  distribution, the projections, and the mean and sigma of the fit. The ghost cut used for both the Cu+Au and  $p+p$  datasets is:

For the same charge track pair,

- if  $|\Delta\phi| < 0.024 \text{ rad}$  and  $|\Delta z| < 0.105 \text{ cm}$ 
  - if the asymmetry  $< 0.3$ , reject one track; else, reject both tracks

The asymmetry is defined as

$$\text{asymmetry} = \frac{p_T^{\text{track1}} - p_T^{\text{track2}}}{p_T^{\text{track1}} + p_T^{\text{track2}}}$$

Since the ghost track pairs correspond to the reconstruction of a real charged hadron into multiple tracks by the reconstruction algorithm, this cut keeps one track of the two only if the asymmetry in the  $p_T$  of the two reconstructed tracks is not more than 30%.

The phenomena of conversions arises when photon conversion occurs in the face of the DC. The DC conversion cut is developed by projecting the  $\Delta\phi$  vs.  $\Delta z$  distribution for the opposite charge track pairs into the  $x$ -axis and the  $y$ -axis and fitting the distribution with a Gaussian function. Figure 5.12 shows the  $\Delta\phi$  vs.  $\Delta z$  distribution, the projection into the  $y$ -axis, and the mean and the sigma of the fit for the different  $\Delta\phi$  ranges. The conversion cut used for both the Cu+Au and  $p+p$  datasets is:

For different charge track pair,

- if  $|\Delta\phi| < 0.07 \text{ rad}$  and  $|\Delta z| < 0.105 \text{ cm}$ , reject both tracks

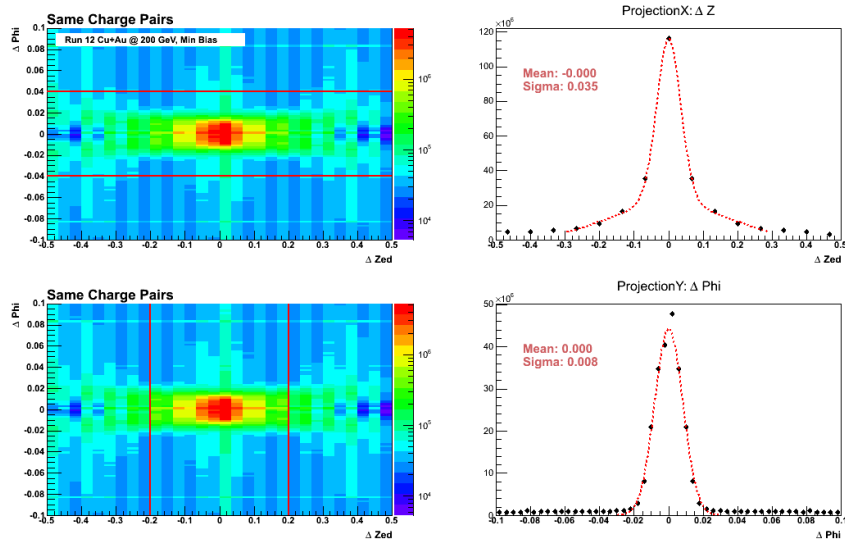


Figure 5.11:  $\Delta\phi$  vs.  $\Delta z$  distribution and the projections for the same charge track pairs.

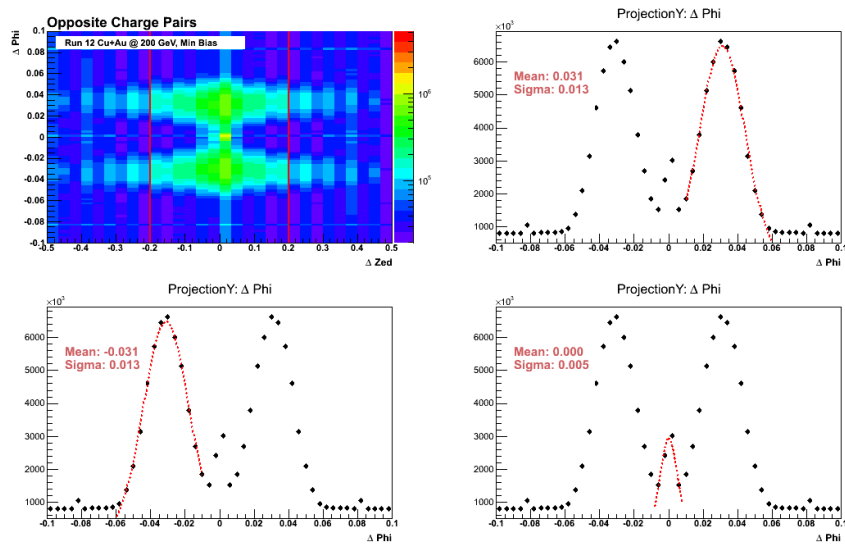


Figure 5.12:  $\Delta\phi$  vs  $\Delta z$  distribution and the projections for the opposite charge track pairs.

### 5.4.3 EMCAL and PC3 matching

To reject tracks originating from conversion electrons<sup>v</sup> and hadronic backgrounds, the charged tracks in the central arms are required to be matched to a hit in the EMCAL or the PC3. Such requirements also help reject fake tracks reconstructed from the combinatorial; for example, three random hits in the DC can lineup and get mis-reconstructed as a track.

The differences between the DC track model projections and the hits in the EMCAL are stored as *emcdphi* (rad) and *emcdz* (cm). The differences with the hits in the PC3 are stored as *pc3dphi* (radian) and *pc3dz* (cm). Ideally, these distributions are expected to have a mean of zero and a width of one, independent of the particle's momentum and charge. As, in reality, the mean and sigma deviate from the expectation, these variables are recalibrated such that the mean becomes zero and the width one, independent of the particle's momentum and charge. The following PHENIX analysis notes give the details and results of such recalibrations that are used in this analysis:

- PHENIX analysis note 1074 [114]: Recalibration of the PC3 matching variables for the Run-12 Cu+Au dataset.
- PHENIX analysis note 1105 [115]: Recalibration of the EMCAL matching variables for the Run-12 Cu+Au dataset.
- PHENIX analysis note 1117 [116]: Recalibration of the EMCAL and PC3 matching variables for the Run-12  $p+p$  dataset.

### 5.4.4 Track cuts

Tracks cuts are designed to select the well reconstructed charged hadrons to be used in the jet reconstruction. Summary of the track cuts (primary) for both the Cu+Au and  $p+p$  datasets are given below:

- $p_T > 500 \text{ MeV}/c$
- Modified quality cut
- Pair cuts

---

<sup>v</sup>The conversion cut in Section 5.4.2 is very specific to the conversions occurring at the face of DC.

- Matching: PC3 or EMCal

$$\text{PC3: } \sqrt{sdp\phi i_{\text{pc3}}^2 + sdz_{\text{pc3}}^2} < 3.0, \text{ EMC: } \sqrt{sdp\phi i_{\text{emc}}^2 + sdz_{\text{emc}}^2} < 3.0$$

One thing to notice here is that no maximum  $p_T$  cut is made on the tracks. Although tracks with  $p_T > 20 \text{ GeV}/c$  are likely to be mis-reconstructed conversions, we intend to obtain control on these high- $p_T$  background through the jet-level cuts instead. This way, no restrictions are forced on the phase space of the parton fragmentation function.

#### 5.4.4.1 Secondary cuts

After the tracks pass all primary cuts, they are then required to pass the secondary cuts. The secondary cuts are developed specifically to reject conversion (or mis-reconstructed) electrons, and are studied in the Monte Carlo<sup>vi</sup> with the following settings:

- Events produced with the Run-13 simulation setup. Two  $\pi_0$ 's with flat  $p_T$  from 1 to  $11 \text{ GeV}/c$  per event.
- Events with Dalitz decays excluded.

#### Edges of central arm

Figure 5.13 shows the  $z$  vs.  $\phi_0$  distribution for the low- $p_T$  conversions ( $p_{T, \text{True}} < 0.1 \text{ GeV}/c$  and  $p_{T, \text{Reco}} > 4.0 \text{ GeV}/c$ ). The  $\phi_0$  is the track's  $\phi$  direction at the vertex. Figure 5.13 shows that the low- $p_T$  conversions get reconstructed as the high- $p_T$  tracks at the top and bottom edges of the central arm. Therefore, a track is discarded if it falls in the following  $\phi_0$  region:

$$(\phi_0 > -0.65 \text{ and } \phi_0 < -0.49) \text{ or } (\phi_0 > 0.89 \text{ and } \phi_0 < 1.05) \text{ or } (\phi_0 > 2.10 \text{ and } \phi_0 < 2.26) \text{ or} \\ (\phi_0 > 3.62 \text{ and } \phi_0 < 3.78)$$

Figure 5.14 shows the selected  $\phi_0$  regions.

#### Ecore

Figure 5.15 shows the ecore (EMCal cluster energy) distribution for the low- $p_T$  conversions ( $p_{T, \text{True}} < 0.1 \text{ GeV}/c$  and  $p_{T, \text{Reco}} > 4.0 \text{ GeV}/c$ ). It shows that the low  $p_T$  conversions that get reconstructed as the high- $p_T$  tracks deposit a small amount or no energy in the EMCal.

---

<sup>vi</sup>The Monte Carlo events are courtesy of Alex Lebedev.

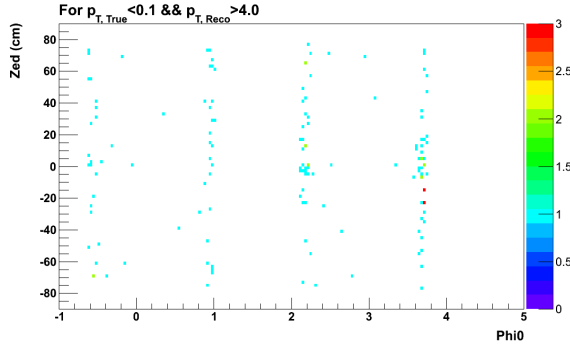


Figure 5.13:  $z$  vs.  $\phi_0$  for the low- $p_T$  conversions.

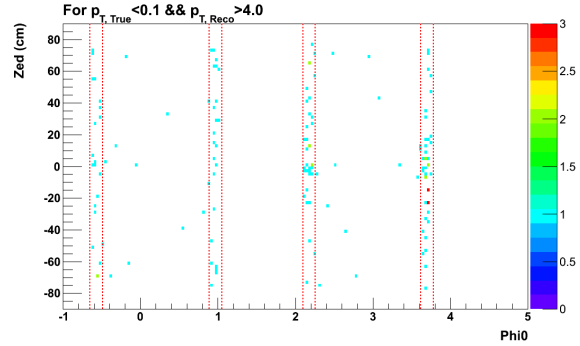


Figure 5.14: Selected  $\phi_0$  regions.

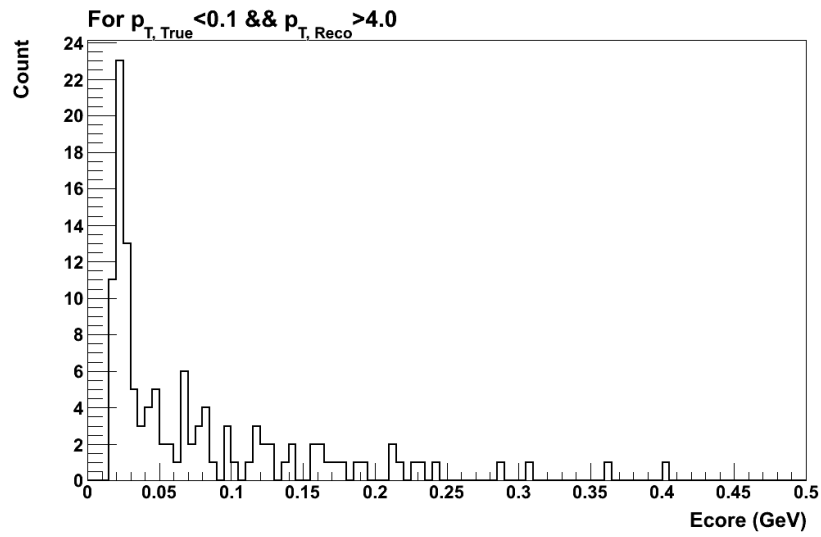


Figure 5.15:  $E_{core}$  for the low- $p_T$  conversions.

In the data, it is found that the hadron tracks ( $n_0 \leq 0$ )<sup>vii</sup> that match to the EMCAL ( $\sqrt{sd\phi_{emc}^2 + sdz_{emc}^2} < 3.0$ ) have a MIP peak at  $\approx 300$  MeV, as shown in Figure 5.17 and Figure 5.18 for the Cu+Au dataset and the  $p+p$  dataset, respectively. Therefore, a track is discarded if:

- $\sqrt{sd\phi_{emc}^2 + sdz_{emc}^2} < 3.0$  and  $ecore < 200$  MeV

Note that this cut does not cut off the hadrons as they have a MIP peak at  $\approx 300$  MeV.

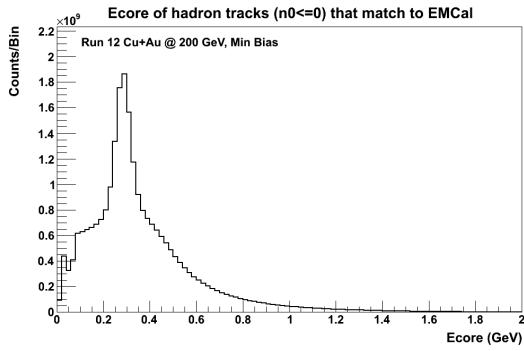


Figure 5.17 Cu+Au dataset.

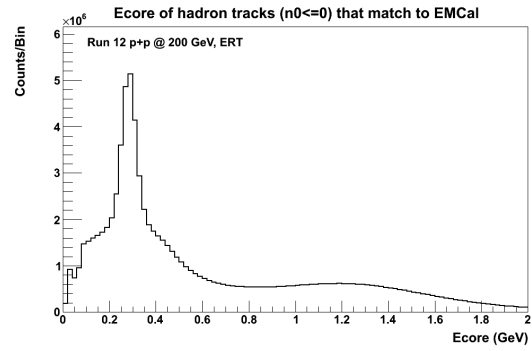


Figure 5.18  $p+p$  dataset.

Figure 5.19: Ecore for the hadron tracks that match to the EMCAL in the Cu+Au dataset (left) and in the  $p+p$  dataset (right)

## Electrons

If a track has  $p_T < 4.5$  GeV/c and  $n_0 \geq 2$ , it is most likely to be an electron. If, for that track,  $(ecore/\text{momentum}) < 0.6$ , the  $p_T$  of that track is mis-reconstructed; therefore, a track is discarded if it satisfies the following condition:

- $p_T < 4.5$  GeV/c and  $n_0 \geq 2$  and  $(ecore / \text{momentum}) < 0.6$

Figure 5.21 and Figure 5.22 show the ecore/momentum distribution for the electron candidates in the Cu+Au dataset and the  $p+p$  dataset, respectively.

---

<sup>vii</sup> $n_0$  is the number of RICH phototubes fired in the normally sized ring area.

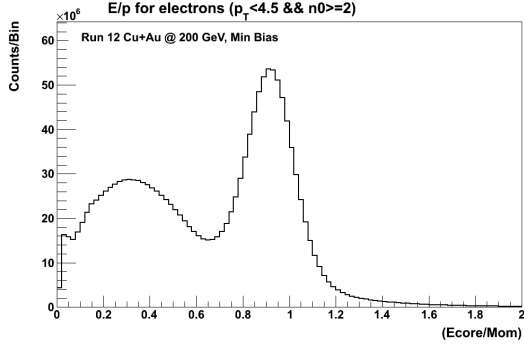
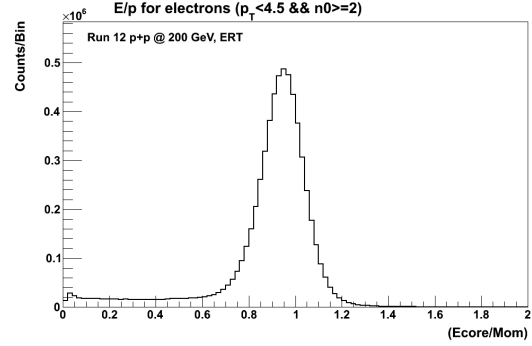


Figure 5.21 Cu+Au dataset.

Figure 5.22  $p+p$  dataset.Figure 5.23: E/p for the electron candidates in the Cu+Au dataset (left) and the  $p+p$  dataset (right)

### Note on the conversion electrons from the VTX detector

Figure 5.24 shows the  $R$ -vertex<sub>true</sub> vs.  $Z$ -vertex<sub>true</sub> distribution for the conversion electrons. As the dimensions of the VTX outer layer are  $R = 17\text{ cm}$  and  $-19\text{ cm} < Z < 19\text{ cm}$ , it can be concluded that most of the conversion electrons do not originate from the VTX detector. Also, as the conversion electrons originating from the VTX travel the similar magnetic field integral as  $e^+/e^-$  originating from the vertex, the reconstructed momentum of these conversions can be close to their actual momentum. Hence, no additional cuts are implemented to reject conversion electrons coming from the VTX detector in this analysis.

## 5.5 Cluster selection

Cluster cuts are designed to select the good EMCal clusters, originating from photons, decaying neutral pions, and neutral hadrons, to be used in the jet reconstruction.

### 5.5.1 EMCal hot/dead map

To avoid the EMCal clusters associated with the towers with pathological bad behavior, a hot/dead map is implemented during the cluster selection. The hot/dead map is prepared by plotting the total hit distribution of towers for each sector with eight different energy cuts.

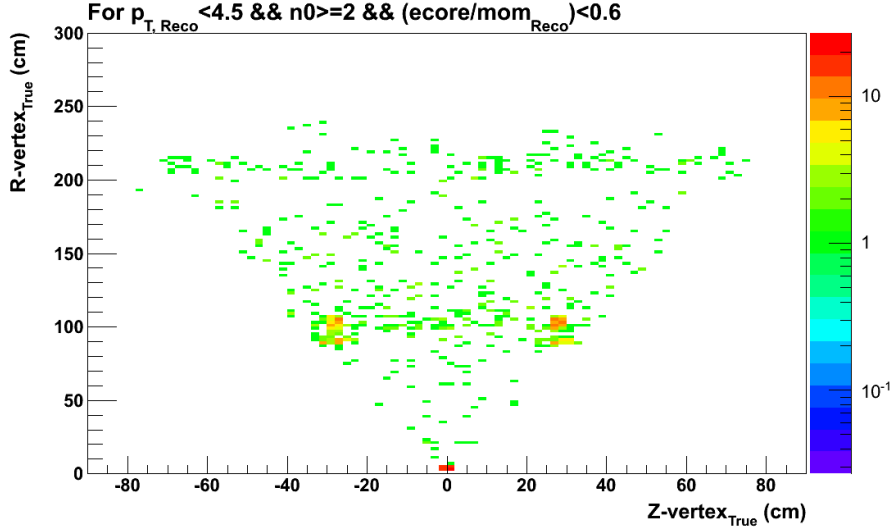


Figure 5.24:  $R\text{-vertex}_{\text{true}}$  vs.  $Z\text{-vertex}_{\text{true}}$  for the conversion electrons.

The energy cuts used are 0.5 GeV, 0.7 GeV, 1.0 GeV, 1.5 GeV, 2.0 GeV, 3.0 GeV, 5.0 GeV, and 7.0 GeV. Figure 5.25 shows the hit distribution for EMCAL sector 0. The distribution is fitted with a double Gaussian function; the background is shown in light green, and the signal is shown in cyan. A tower is considered to be ‘hot’ if the total hits for the tower is  $3.5 \sigma$  above the average for that sector. Similarly, a tower is considered to be ‘dead’ if the total hits for the tower is  $3.5 \sigma$  below the average for that sector. Since a tower can only be hot at higher energies, the hot tower tagging process is repeated for all eight energy cuts. The uncalibrated towers are also tagged as ‘uncalibrated’ by using the uncalibrated tower list prepared by the EMCAL calibration experts.

The EMCAL sector definitions used in this analysis are:

- Sector 0: West 0 (PbSc)
- Sector 1: West 1 (PbSc)
- Sector 2: West 2 (PbSc)
- Sector 3: West 3 (PbSc)
- Sector 4: East 0 (PbGl)
- Sector 5: East 1 (PbGl)
- Sector 6: East 2 (PbSc)
- Sector 7: East 3 (PbSc)

The details of the map prepared for the Cu+Au dataset are given below:

- 409 out of 24768 towers are uncalibrated
- 981 towers are hot [131 towers are hot and uncalibrated]
- 1009 towers are dead [142 towers are dead and uncalibrated]

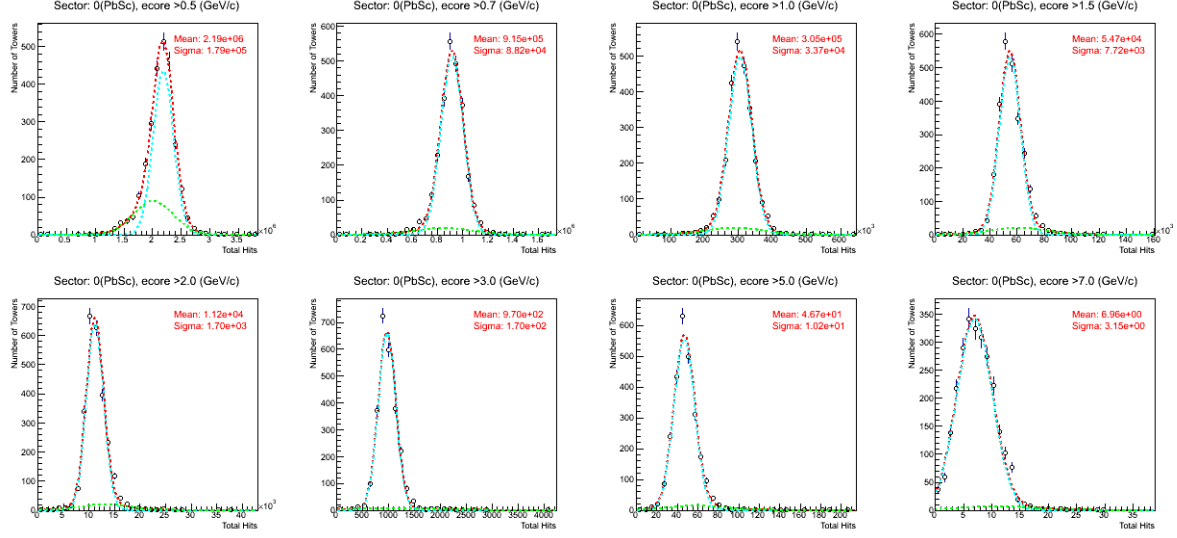


Figure 5.25: Hit distribution for sector 0.

Overall, 2079 out of 24768 towers (8.39%) are hot or dead or uncalibrated. Figure 5.29 shows the map used for the Cu+Au dataset.

The details of the map prepared for the  $p+p$  dataset are given below<sup>viii</sup>:

- 24 out of 24768 towers are uncalibrated
- 793 towers are hot [6 towers are hot and uncalibrated]
- 1380 towers are dead [6 towers are dead and uncalibrated]

Overall, 2184 out of 24768 towers (8.82%) are hot or dead or uncalibrated. Figure 5.33 shows the map used for the  $p+p$  dataset.

### 5.5.2 Cluster cuts

The following cluster selections are made for both the Cu+Au and  $p+p$  datasets:

- Energy  $> 500 \text{ MeV}$
- As a cluster spreads over  $3 \times 3$  towers, exclude clusters whose center is:
  - hot or dead or uncalibrated or at the edge
  - around hot or around dead or around uncalibrated

---

<sup>viii</sup>Map for the  $p+p$  dataset was prepared by Josh Perry using the similar method; details can be found in [117].

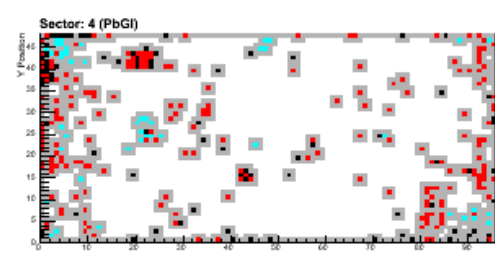
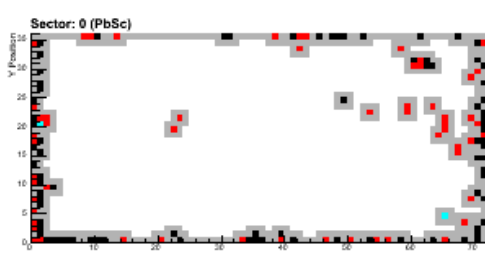
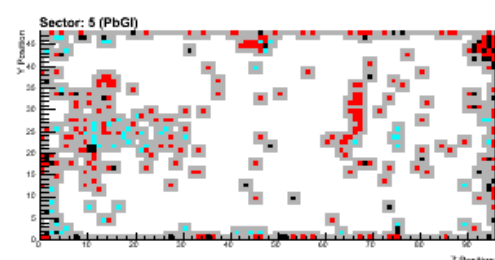
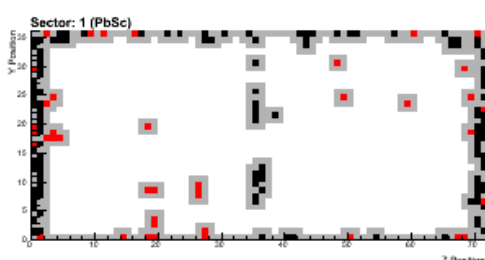
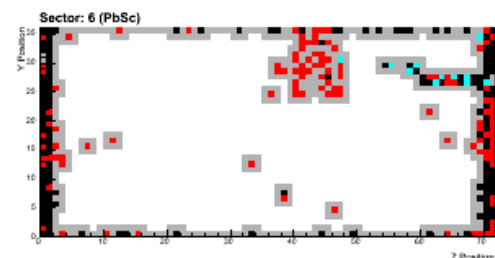
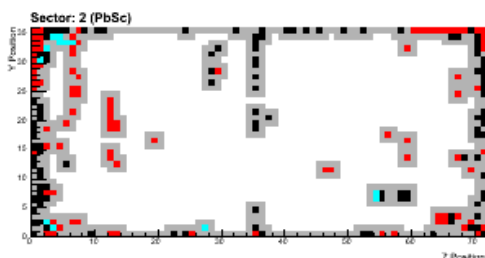
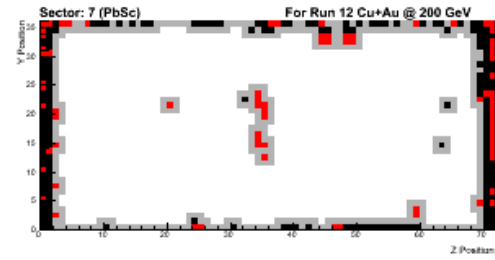
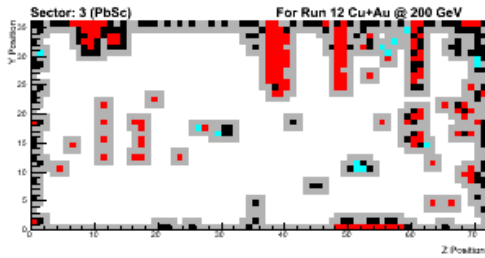


Figure 5.27 Map for the west arm.

Figure 5.28 Map for the east arm.

Figure 5.29: Hot/dead map for the Cu+Au dataset. Red represents the hot towers, black the dead, and cyan the uncalibrated. Gray represents the towers that are around the hot or dead or uncalibrated towers.

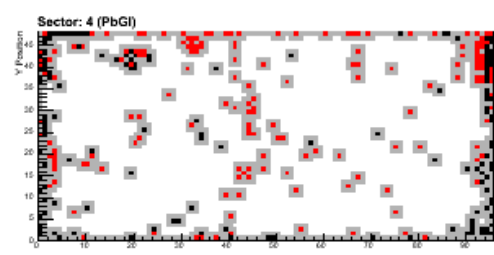
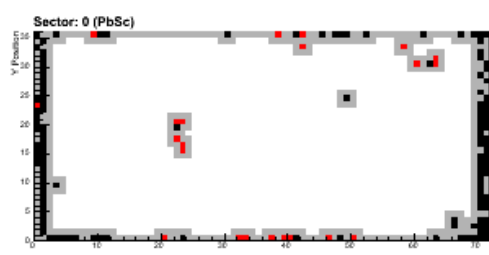
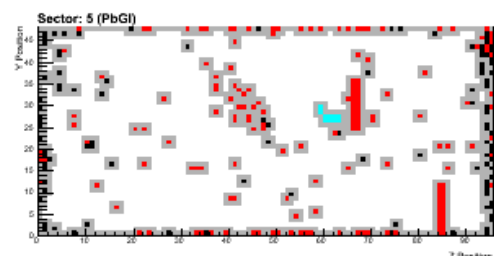
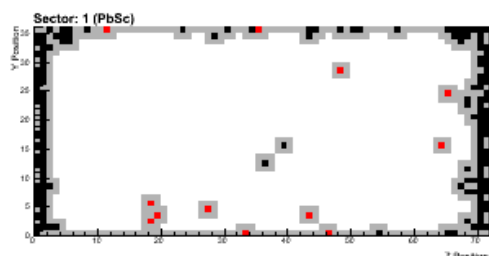
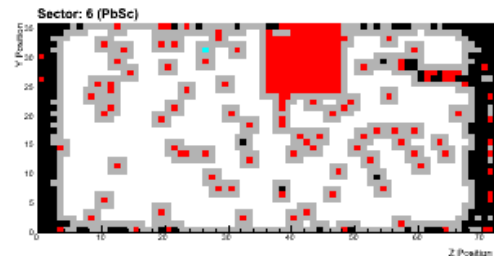
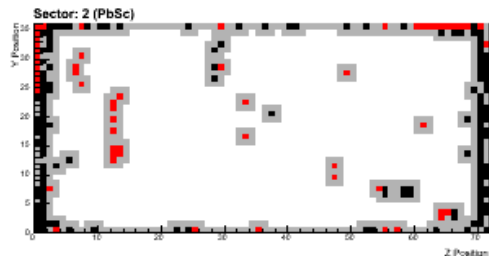
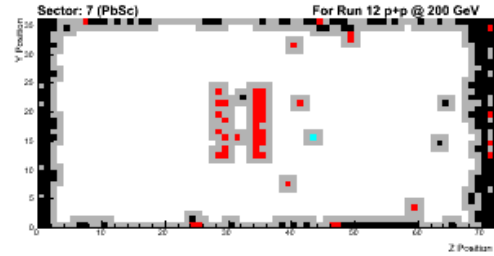
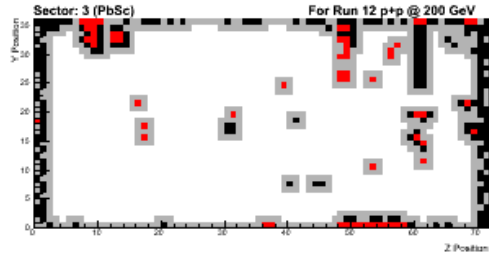


Figure 5.31 Map for the west arm.

Figure 5.32 Map for the east arm.

Figure 5.33: Hot/dead map for the  $p+p$  dataset. Red represents the hot towers, black the dead, and cyan the uncalibrated. Gray represents the towers that are around the hot or dead or uncalibrated towers.

### 5.5.3 Cluster-track association

Charged hadrons and electrons deposit energy in the EMCAL in addition to being reconstructed as charged tracks. The cluster-track association is performed such that the good clusters, which pass the selection from Section 5.5.2, are discarded if they are associated with the well reconstructed tracks. The following conditions are required to be satisfied by the well reconstructed tracks:

- $p_T > 500 \text{ MeV}/c$
- Pass modified quality cut
- $\sqrt{sdp\phi i_{\text{emc}}^2 + sdz_{\text{emc}}^2} < 3.0$

## 5.6 Jet reconstruction

### 5.6.1 Analysis of high $p_T$ background

Although requiring three or more constituents in a reconstructed jet helps reject jets that were reconstructed from the combinatoric particles and not from the harder fragmentation kinematics, this requirement solely is not enough to reject high- $p_T$  jets reconstructed due the presence of a high- $p_T$  background (for e.g., jets that gets reconstructed when a single high- $p_T$  conversion track gets combined with combinatoric tracks and clusters).

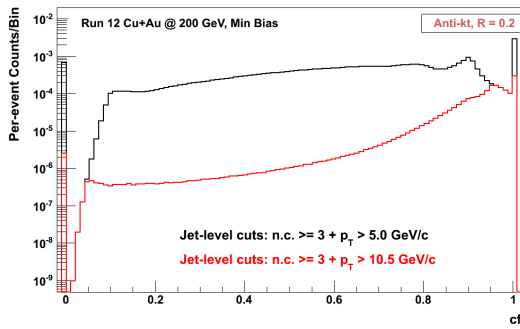


Figure 5.34: Charged fraction distribution for the Cu+Au dataset.

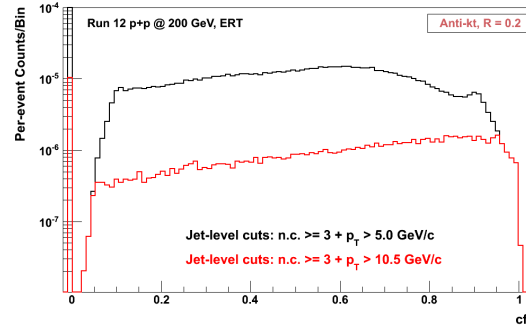


Figure 5.35: Charged fraction distribution for the  $p+p$  dataset.

The charged fraction of a anti- $k_t$  jet is defined in Section 4.1.1 as:

$$c.f. = \frac{1}{p_T^{\text{jet}}} \sum p_T^{\text{track constituents}}. \quad (5.3)$$

Figure 5.34 and Figure 5.35 show the *c.f.* distribution of the anti- $k_t$  jets for the Cu+Au dataset and the  $p+p$  dataset, respectively. The black distribution is for jets with (*c.f.*  $\geq 3$  and  $p_T > 5 \text{ GeV}/c$ ), while the red distribution is for jets with (*n.c.*  $\geq 3$  and  $p_T > 10.5 \text{ GeV}/c$ ). The peak at zero for the *c.f.* distribution occurs when all the jet constituents are the EMCAL clusters, whereas the peak at one occurs when all the jet constituents are the tracks. The charged fraction distribution of the high- $p_T$  jets (red distributions) have a shape that sharply increases towards the value of one, hinting the severity for contamination from conversion tracks. In the  $p+p$  collisions, where the contamination from the high- $p_T$  background is relatively minimal, the slope of the *c.f.* distribution is almost linear (in the log scale) relative to the Cu+Au collisions.

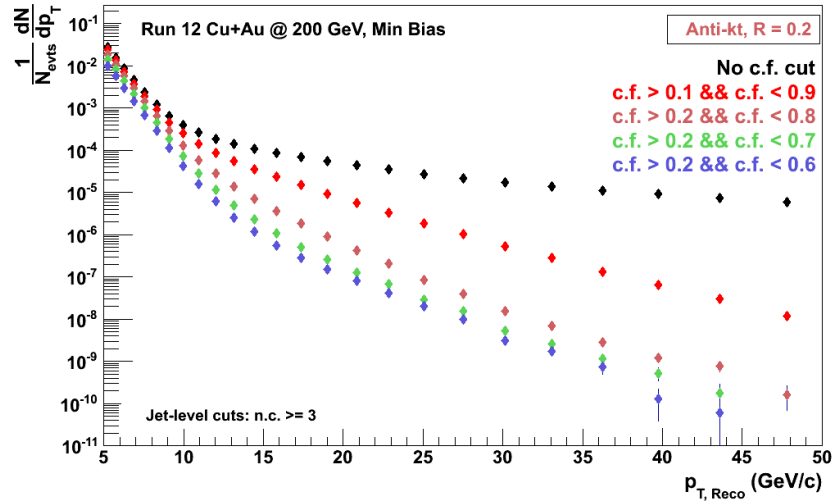


Figure 5.36: Per-event yield of the anti- $k_t$  jets for the Cu+Au dataset with various charged fraction selections.

Figure 5.36 shows the per-event yield of the anti- $k_t$  jets for the Cu+Au dataset with the different *c.f.* selections as shown in the legend. The only additional cut in the yield is *n.c.*  $\geq 3$ . As evident from Figure 5.36, without any *c.f.* selection, the  $p_T$  spectra is dominated by the high- $p_T$  background and a tighter *c.f.* selection changes the shape of the spectrum. Going

from the *c.f.* selection of (*c.f.* > 0.2 and *c.f.* < 0.7) to (*c.f.* > 0.2 and *c.f.* < 0.6), the effect is mostly the reduction in the yield with minimal impact on the shape. Figure 5.37 shows the per-event yield of the anti- $k_t$  jets for the  $p+p$  dataset. As before, the only additional selection in the yield is *n.c.*  $\geq 3$ . Comparing Figure 5.37 and Figure 5.36, it can be concluded that the high- $p_T$  background contamination for the  $p+p$  dataset is relatively milder than for the Cu+Au dataset.

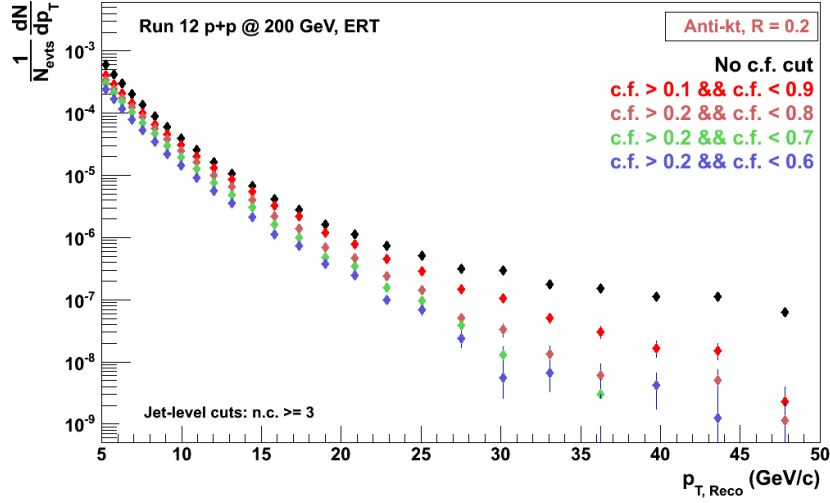


Figure 5.37: Per-event yield of the anti- $k_t$  jets for the  $p+p$  dataset with the various charged fraction selections.

The effect of the *c.f.* selection on the high- $p_T$  background can also be demonstrated by investigating its influence on the jet constituent spectra. Figure 5.38 shows the spectra of the charged constituents of the anti- $k_t$  jets with (*n.c.*  $\geq 3$  and  $p_T > 10.5 \text{ GeV}/c$ ). The kink in the shape of the spectra is due to the requirement of  $p_T > 10.5 \text{ GeV}/c$  on the reconstructed jets. Figure 5.39 is the similar spectra for the neutral constituents of the anti- $k_t$  jets.

The effect of the *c.f.* selection on the high- $p_T$  background becomes more distinct after taking the ratio of these two spectra. If the neutral constituents spectra is considered to be a baseline with no high- $p_T$  cluster contamination, the ratio of the charged to neutral spectra is expected to be a flat distribution as a function of  $p_T$  in absence of the high- $p_T$  track contamination. Figure 5.40 shows the ratio of the charged to neutral constituents spectra for the Cu+Au dataset. For the *c.f.* selection of (*c.f.* > 0.2 and *c.f.* < 0.7), the ratio is flat and stays flat up

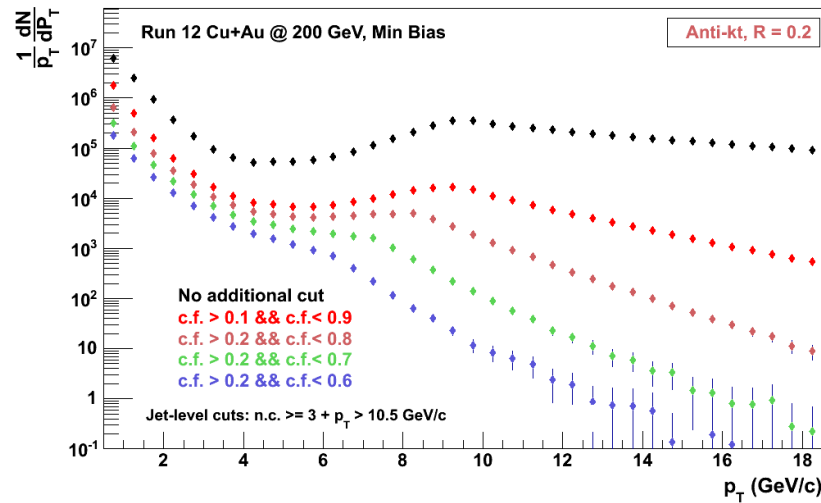


Figure 5.38: Charged constituents spectra.

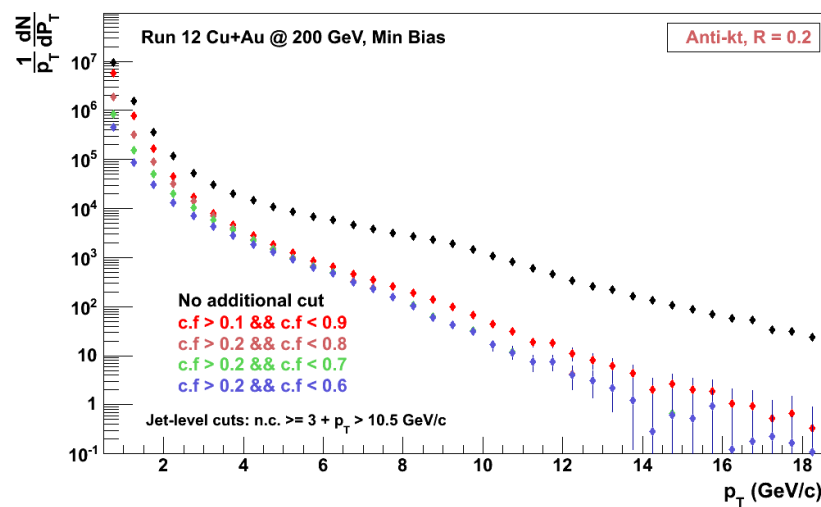


Figure 5.39: Neutral constituents spectra.

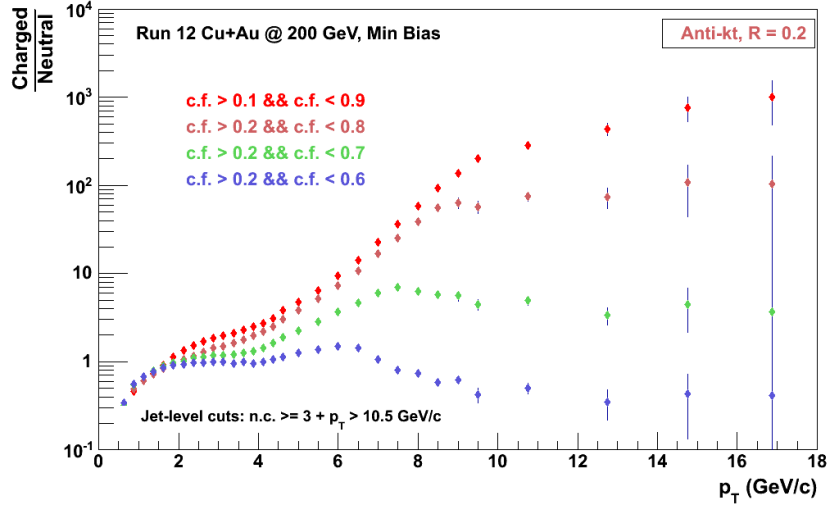


Figure 5.40: Charged to neutral constituents ratio for the Cu+Au dataset.

to high- $p_T$ . For comparison, Figure 5.41 shows the similar ratio for the  $p+p$  dataset. As with the Cu+Au dataset, for the  $c.f.$  selection of ( $c.f. > 0.2$  and  $c.f. < 0.7$ ), the ratio is flat as a function of  $p_T$ . The default  $c.f.$  selection used in this analysis hereafter is ( $c.f. > 0.2$  and  $c.f. < 0.7$ ).

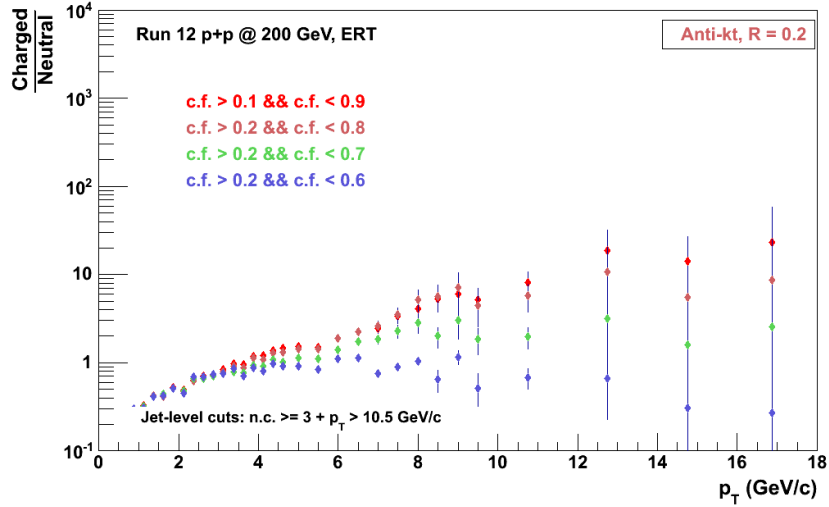


Figure 5.41: Charged to neutral constituents ratio for the  $p+p$  dataset.

### 5.6.2 Analysis of fake jets

Fake jets are reconstructed from a random association of the uncorrelated soft particles. As most of these jets are reconstructed from fluctuations in the underlying event (that are not associated with hard scattering), requiring a hard scattering signature in a jet can help reject this background. The discriminant, which is useful in identifying and rejecting fake jets, is defined in Section 4.1.1. Figure 5.42 and Figure 5.43 show the discriminant distribution of the anti- $k_t$  jets with ( $n.c. \geq 3$  and  $p_T > 5 \text{ GeV}/c$ ) for the Cu+Au dataset and the  $p+p$  dataset, respectively.

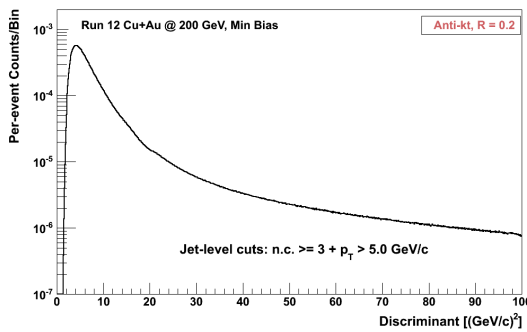


Figure 5.42: Discriminant distribution for the Cu+Au dataset.

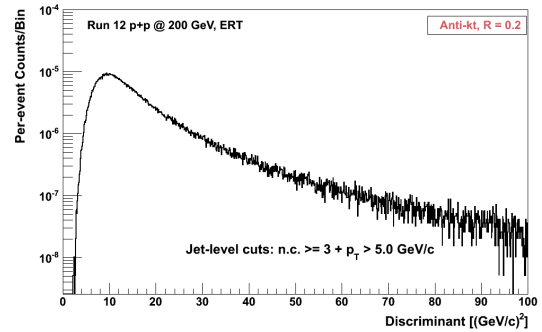


Figure 5.43: Discriminant distribution for the  $p+p$  dataset.

Figure 5.44 and Figure 5.45 show the per-event anti- $k_t$  jet yield for the Cu+Au dataset and the  $p+p$  dataset, respectively, with the different discriminant selections as shown in the legend. Additional cuts on the yield are ( $n.c. \geq 3$  and  $c.f. > 0.2$  and  $c.f. < 0.7$ ). As fake jets are more likely to reconstruct as low- $p_T$  jets, the discriminant cut essentially acts as a lower  $p_T$  limit on the spectrum. As evident from Figure 5.44 and Figure 5.45, the fake jet contribution is severe for the  $p_{T, \text{Reco}} < 10.5 \text{ GeV}/c$  part of the spectrum. For this analysis, only the  $p_{T, \text{Reco}} > 10.5 \text{ GeV}/c$  part of the spectrum is analyzed, and the fake jet contribution for this range is statistically subtracted, which will be discussed in the next section.

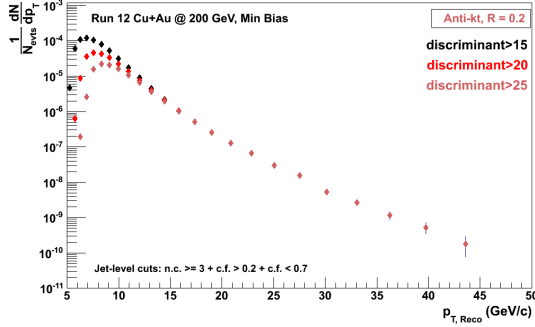


Figure 5.44: Per-event yield of the anti- $k_t$  jets for the Cu+Au dataset.

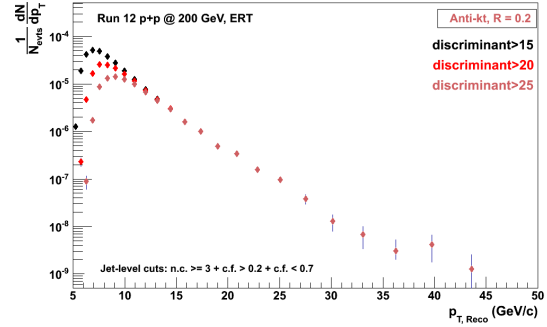


Figure 5.45: Per-event yield of the anti- $k_t$  jets for the  $p+p$  datasets.

### 5.6.2.1 Fake jet subtraction

There is no unique way to separate the jets reconstructed from the soft background and the jets reconstructed from the hard scattering. This section discusses a new data driven method to statistically subtract the fake jet contribution from the raw jet yield. The procedure for such fake jet subtraction is explained below:

1. For events where no jet is reconstructed, the position  $(\eta, \phi)$  of the tracks and the position  $(\eta, \phi)$  of the clusters are randomly shuffled. The positions of the tracks and the clusters are shuffled independently to ensure that they do not fall in the dead or inefficient areas of the central arm. Also, the random shuffling is performed for the east arm and the west arm separately.
2. The anti- $k_t$  algorithm with  $R_{\text{Anti-}k_t} = 0.2$  is run on these shuffled tracks and clusters, and then all the jet-level cuts are applied to the reconstructed jets.
3. The resulting yield is the “fake” jet yield.
4. For the  $p+p$  ERT dataset, at least one cluster with the ERT bit is required as a constituent of the reconstructed “fake” jet.

Figure 5.46 shows the result of the procedure for the  $p+p$  dataset. The black distribution is the raw yield, and the blue distribution is the “fake” jet yield obtained from this procedure. The raw jet per-event yield is constructed using the total events that were analyzed, and the “fake” jet per-event yield is constructed from the total events without the reconstructed jet.

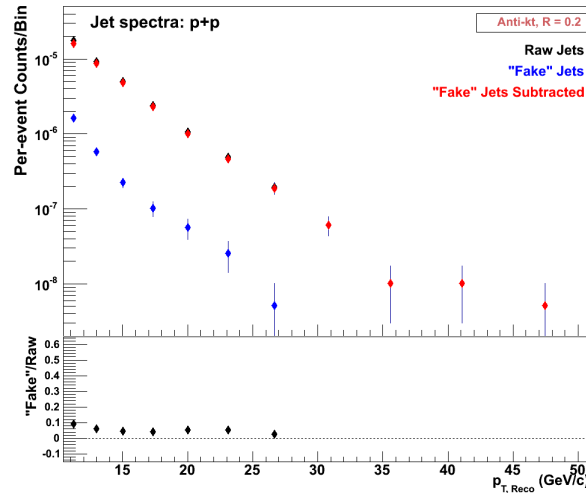


Figure 5.46: "Fake" jet subtraction for the  $p+p$  dataset.

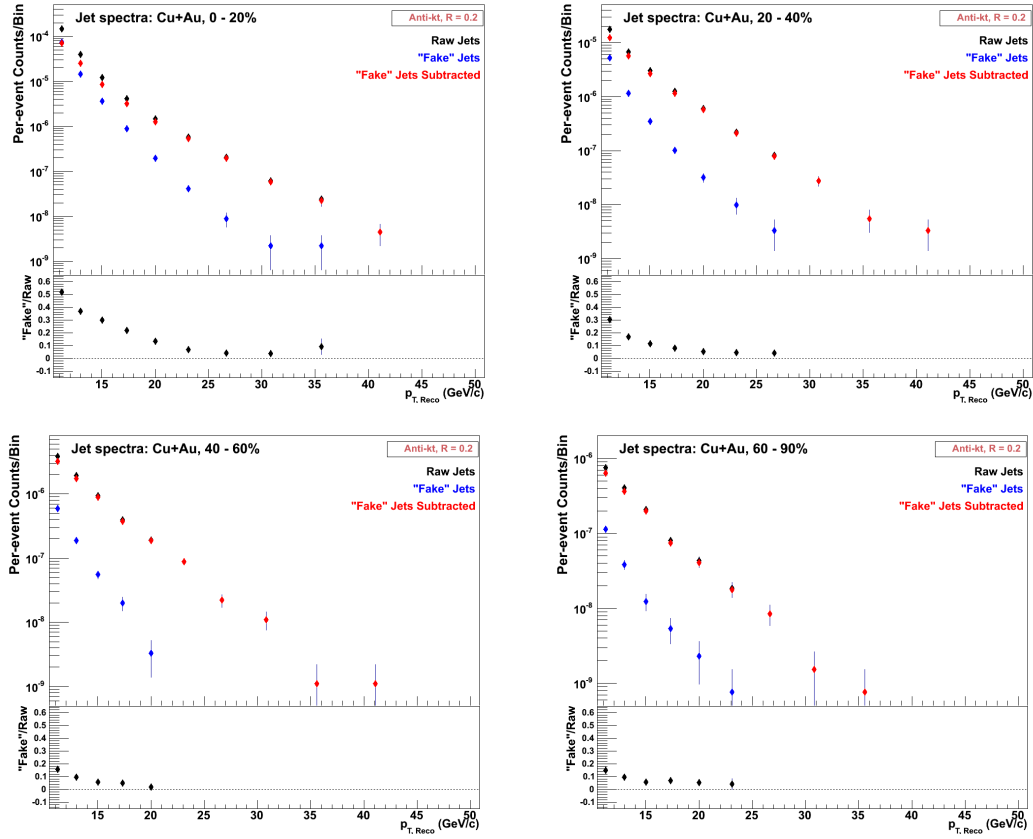


Figure 5.47: "Fake" jet subtraction for the different centrality selections in the Cu+Au collisions.

The red distribution is what is obtained after the statistical subtraction of the “fake” jet yield from the raw jet yield. The bottom panel shows the “fake” to raw ratio. Figure 5.47 shows the result for the different centrality selections of the Cu+Au collisions; the top-left plot is for the 0–20% centrality, top-right for 20–40%, bottom-left for 40–60%, and bottom-right for 60–90%.

Table 5.3 summarizes the fake jet contribution for the  $p+p$  and different centralities of the Cu+Au collisions (for the three  $p_{\text{T, Reco}}$  ranges). As expected, the contribution is both  $p_{\text{T, Reco}}$  and centrality-dependent. The fake jet contribution is the highest at low- $p_{\text{T}}$  and the minimal at high- $p_{\text{T}}$ . Also, for a given  $p_{\text{T, Reco}}$  range, the contribution is the highest for the central collisions than for the peripheral or  $p+p$  collisions.

Table 5.3: “Fake” jet contribution for the  $p+p$  and different centralities of the Cu+Au collisions.

$p_{\text{T, Reco}}$ range (GeV/c)	$p+p$	Cu+Au: 0–20%	20–40%	40–60%	60–90%
10.5–12.1	9.1%	51.7%	30.1%	15.5%	15.1%
13.9–16.1	4.5%	29.9%	11.6%	5.9%	5.9%
18.6–21.5	5.3%	13.4%	5.3%	1.7%	5.3%

## CHAPTER 6. MONTE CARLO SIMULATION

### 6.1 Setup

#### 6.1.1 PISA

PHENIX Integrated Simulation Application (PISA) is the PHENIX simulation software package based on the GEANT-3 [118] libraries. PISA tracks particles produced by the event generators until they are stopped or escape the PHENIX detector volume. The main inputs to PISA are the tracking criteria, the magnetic field criteria, and the detector geometry setup for the active and passive volumes. Any of the detector subsystems can be turned ON or OFF in the pisa.kumac setup file. For this analysis, all of the central arm detectors that were ON during the Run-12 were turned ON in PISA. The magnetic field through which particles swim via GEANT in PISA is also set in the pisa.kumac file. For the Run-12 setup, the 3D++ tag was used. The ++ sign corresponds to the current sign in the inner and outer coils of the central arm magnets. PISA outputs a collection of event-by-event data known as ‘hits file’.

#### 6.1.2 pisaToDST

The information obtained from the GEANT particle tracking through each detector subsystem is converted into the simulated detector signal. These simulated detector signals are similar in format to the real detector signals and are processed by the same software which reconstructs the real data files. The procedure, processed by the piasToDST macro, generates a simulated data summary tape (DST) file, which is similar to the real DST files and contains useful information needed by the analysis code.

When running the pisaToDST macro, a reference run number is needed to get the relevant calibrations, list of dead channels, thresholds, etc., by the subsystems. The reference run numbers used in this analysis are:

- 372524 for the Cu+Au setup
- 360934 for the  $p+p$  setup

PISA assumes a perfect PHENIX detector without any dead or inefficient channels in the subsystems. To match the simulation setup to the real detector in the Run-12 period, the following dead or inefficient channel files are used during the pisaToDST phase of the simulation.

- For the Drift Chamber, the DchAlwaysDead.dat and DchEfficiency.Real files are used for the channel deadmap and channel efficiencies, respectively. These files were created specifically for the Run-12 period using the reference run number 372524 by the DC experts. The same files are used for both the Cu+Au and  $p+p$  setups.
- For the Pad Chamber, the pad\_deadroc.dat and pad\_deadch.dat files are used for the dead read out cards (ROCs) and dead channels, respectively. The dead ROCs file was generated from the calibration database, and the dead channels file was generated from the online calibration (OnCal) histograms for the Pad Chamber. Two different set of files were generated for the Cu+Au and  $p+p$  setups by using the respective reference run numbers mentioned above.
- For the EMCAL, the hot/dead map was implemented during the analysis rather than in the pisaToDST phase.

### 6.1.3 Binning strategy

To ensure the measurement of  $p_T$  dependence with good statistics, the jet spectra are binned with the exponentially growing bin sizes. The bin sizes and ranges are different for the truth-level yield and the reco-level yield as summarized below:

- Reco-level: Finely binned from 10.4 to 50 GeV/c such that the bin width is 14.37% of the bin center (the ratio of the adjacent bin edges is 1.15).

- Truth-level: Loosely binned from 6.6 to 50 GeV/c such that the bin width is 18.37% of the bin center (the ratio of the adjacent bin edges is 1.2). The choice of this specific truth-level binning is motivated by the evaluation of the jet energy resolution in Section 6.5.2.

#### 6.1.4 $p+p$ setup

##### 6.1.4.1 Vertex shifting

Figure 6.1 shows the  $z_{\text{vertex}}$  distribution for the  $\sqrt{s_{\text{NN}}} = 200$  GeV Minimum Bias  $p+p$  dataset. The distribution has a Gaussian width of 15 cm. As the  $z_{\text{vertex}}$  cut of 10.0 cm is applied during the data analysis (see Section 5.3), the same vertex cut is implemented in the simulation. A Gaussian vertex distribution with mean 0 cm and width 15 cm is generated, and if  $|z_{\text{vertex}}| < 10$  cm, the vertex is fed into the triggered PYTHIA event by using the PHPyVertexShift class.

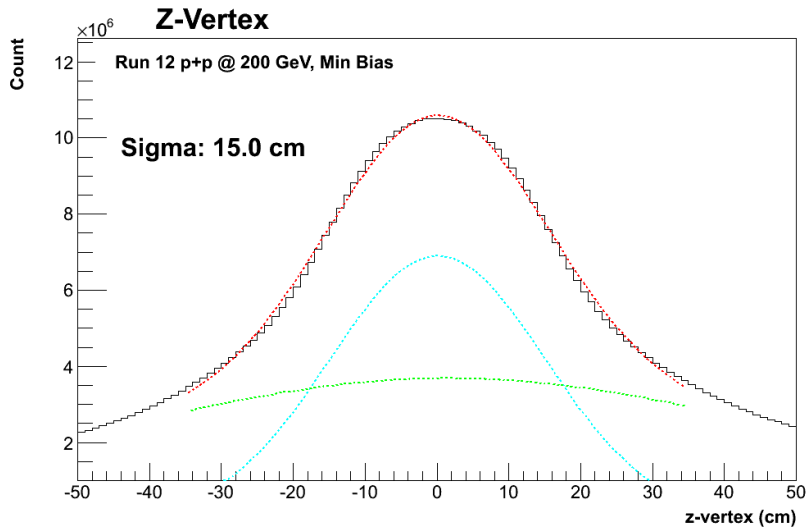


Figure 6.1:  $Z$ -vertex distribution for the  $\sqrt{s_{\text{NN}}} = 200$  GeV  $p+p$  Minimum Bias dataset.

##### 6.1.4.2 Simulation chain

Figure 6.2 summarizes the simulation chain for the  $p+p$  setup. As we are interested in the events with jets in the PHENIX acceptance, only PYTHIA events with a true jet are selected. The requirement for the true jet is explained in Section 6.3. The vertices of all the final particles

of the triggered events are shifted as explained in Section 6.1.4.1. The final state particles are then fed through PISA, and the output of PISA is passed through the pisaToDST macro. The reconstructed tracks and clusters from the simulated DST are required to pass all the track and clusters cuts as in the real data. The anti- $k_t$  algorithm is run on these tracks and clusters, and the reconstructed jets are then required to pass all the jet-level cuts.

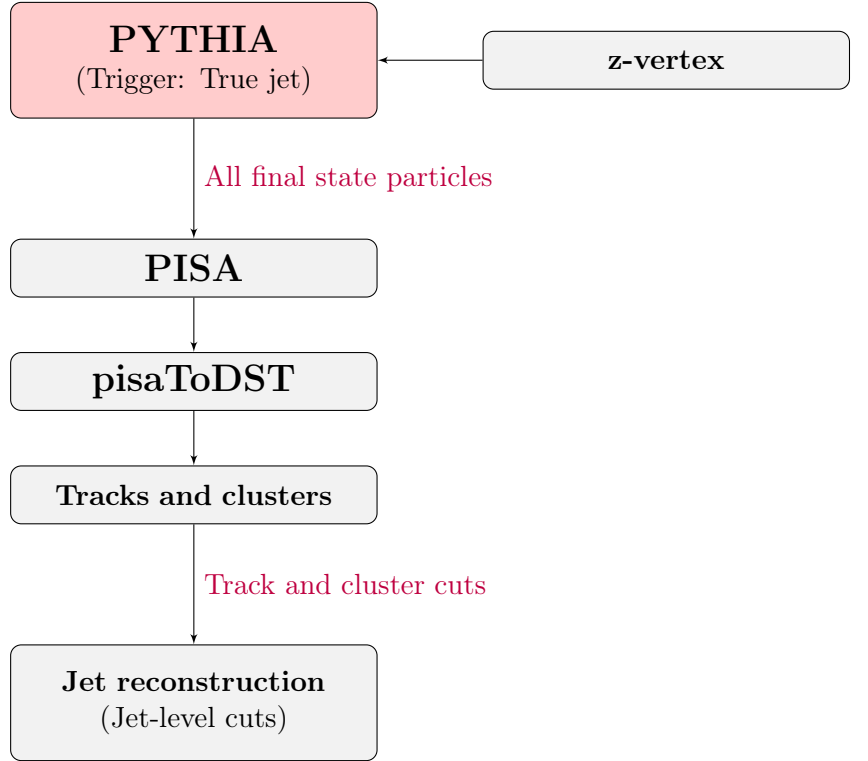


Figure 6.2: Simulation chain for the  $p+p$  setup.

### 6.1.5 Cu+Au setup

To understand and correct the effects of the soft Cu+Au underlying event, the PYTHIA  $p+p$  events are embedded into the real Cu+Au events. The embedding is performed at the tracks and clusters level; meaning, the reconstructed tracks and clusters from the PYTHIA  $p+p$  events are merged with the tracks and clusters from the real Cu+Au events. Jet reconstruction is then performed on the total embedded tracks and clusters.

### 6.1.5.1 Cu+Au data trigger

The Cu+Au events used for embedding are drawn from dCache at the RHIC computing facility (RCF). The following 18 different runs (40 segments each) expanding over the entire Run-12 Cu+Au collision period are selected for the purpose of embedding:

1. 373777	4. 373889	7. 374080	10. 375176	13. 375429	16. 376083
2. 373780	5. 374072	8. 374565	11. 375225	14. 375954	17. 377175
3. 373828	6. 374074	9. 375047	12. 375428	15. 376034	18. 377176

The process and requirements for selecting an event for embedding are given below:

1. Apply the event, track, and cluster selection cuts.
2. Perform the jet reconstruction using  $R_{\text{Anti-}k_t} = 0.2$ .
3. Keep the event if no jet is reconstructed that pass the following jet-level cuts:  
 $n.c. \geq 3$  and  $p_T > 6.6 \text{ GeV}/c$  and  $c.f. > 0.2$  and  $c.f. < 0.7$
4. For such events, store the  $z_{\text{vertex}}$  information.

### 6.1.5.2 Vertex matching

For the purpose of the vertex matching, the vertex from the data is fed into PYTHIA event-by-event by using the PHPyVertexShift class.

### 6.1.5.3 Simulation chain

Figure 6.3 summarizes the simulation chain for the Cu+Au setup. Data events are selected when no reconstructed jet is not found in the event. For each selected event, the  $z_{\text{vertex}}$  information is stored and later fed into the triggered PYTHIA event by using the PHPyVertexShift class. The final state PYTHIA particles are passed through PISA and then through the pisaToDST macro. Tracks and clusters from both the data and PYTHIA are required to pass all the track and cluster cuts and then are combined. The anti- $k_t$  algorithm is run on these combined tracks and clusters, and the reconstructed jets are required to pass all the jet-level cuts.

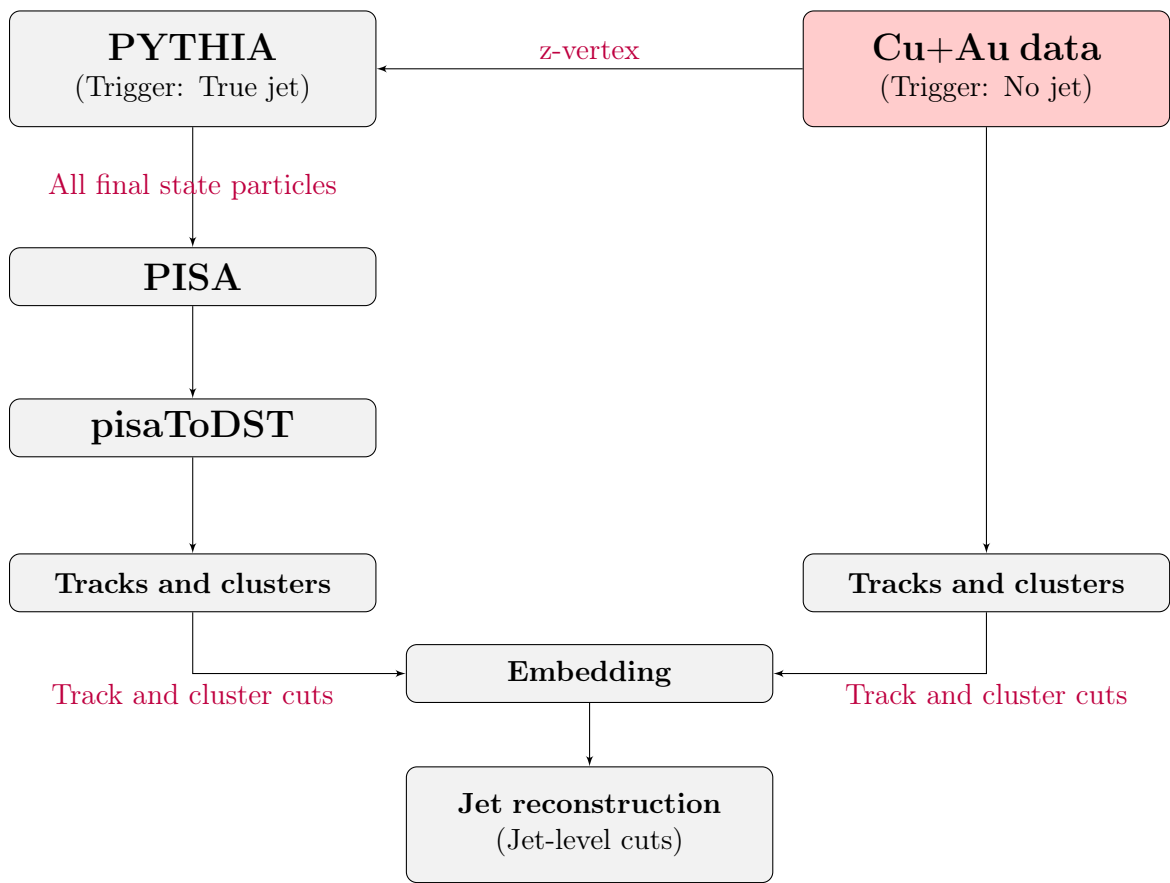


Figure 6.3: Simulation chain for the Cu+Au setup.

## 6.2 Acceptance study

For any analysis, it is critical that the simulation setup matches the actual detector. For the purpose of comparing the acceptance between the data and the simulation, the PYTHIA  $p+p$  Minimum Bias events are passed through the  $p+p$  setup and the HIJING Cu+Au Minimum Bias events through the Cu+Au setup.

### 6.2.1 For the $p+p$ setup

Figure 6.7 and Figure 6.11 show the alpha vs. board plots for the  $p+p$  Minimum Bias data (left) and the  $p+p$  simulation setup (right) for the west arm and the east arm, respectively. For both arms, the simulation setup matches the data reasonably.

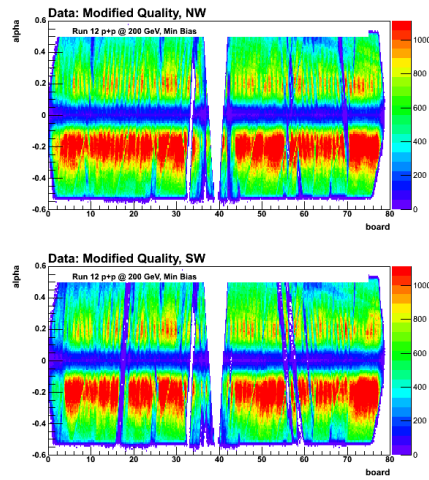


Figure 6.5 Data: West arm

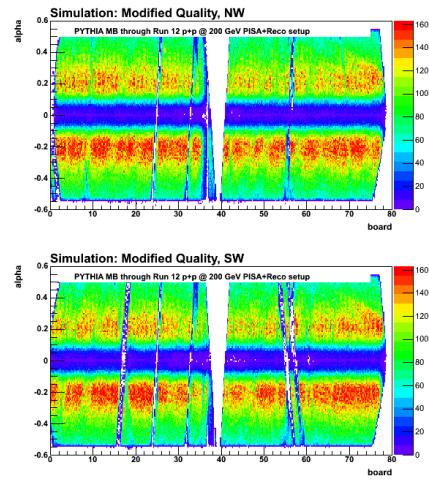


Figure 6.6 Simulation: West arm

Figure 6.7: DC/PC acceptance comparison between the data and the simulation for the west arm.

Figure 6.12 shows the per-event  $dN/d\phi$  distribution of the good tracks going into the jet reconstruction for both data (black line) and simulation (red line). The distributions are normalized from  $\phi = 2.2$  to  $2.4$ .

For the EMCAL, the number of hits for each tower in each sector are compared. In order to do so, 2D histograms are plotted with the  $z$ -position on the  $x$ -axis and the  $y$ -position on the  $y$ -axis, where the  $z$ - and  $y$ -positions are the local variables to the sector. Figure 6.18 shows

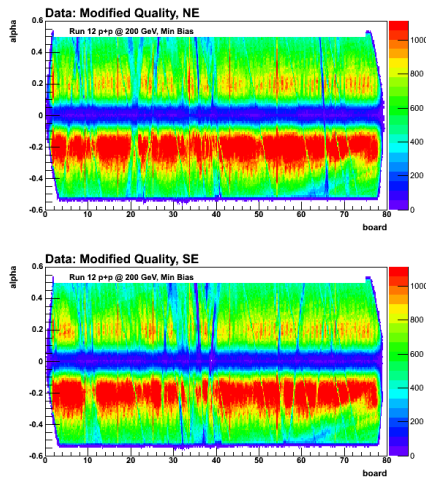


Figure 6.9 Data: East arm

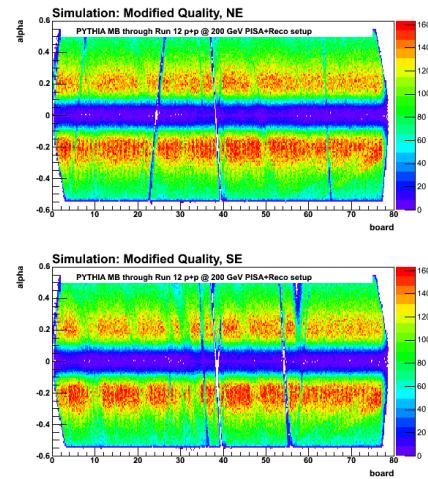
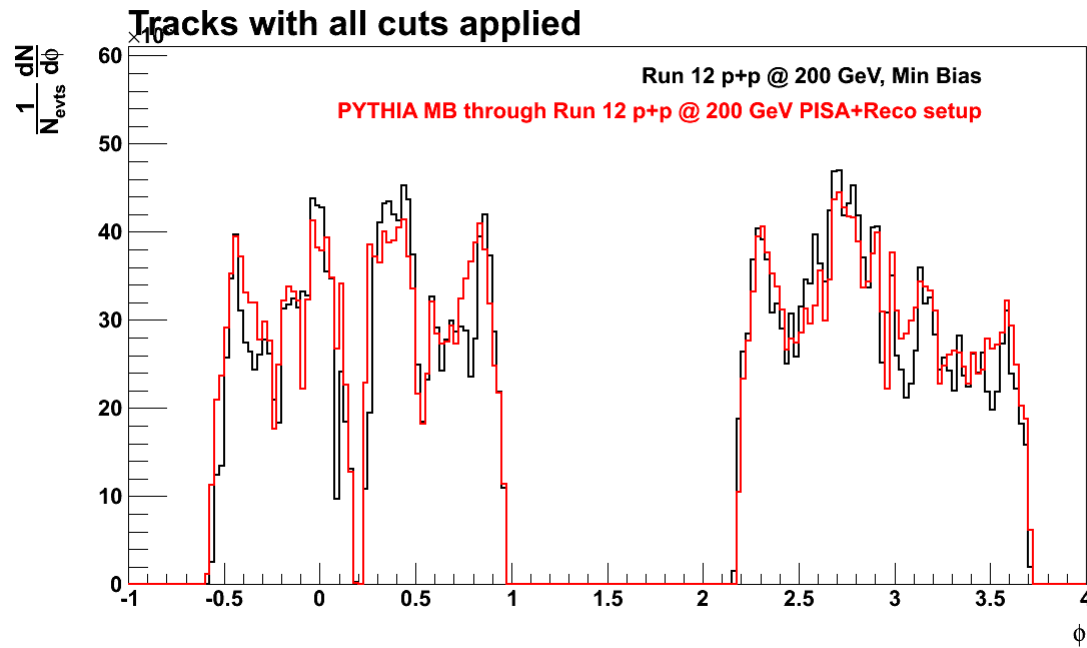


Figure 6.10 Simulation: East arm

Figure 6.11: DC/PC acceptance comparison between the data and the simulation for the east arm.

Figure 6.12: Per-event  $dN/d\phi$  distribution of the good tracks for both data (black line) and simulation (red line). The distributions are normalized from  $\phi = 2.2$  to  $2.4$ .

the EMCal acceptance comparison between the  $p+p$  Minimum Bias data (left) and the Cu+Au simulation setup (right) for sectors 0 to 7. The  $z$ -scale is setup such that for

$$\text{average} = \langle \text{hits/event} \rangle \text{ for that sector,}$$

red is  $(2.0 \text{ to } 1.5) \times \text{average}$ , green is  $(1.5 \text{ to } 1.3) \times \text{average}$ , dark gray is  $(1.3 \text{ to } 1.0) \times \text{average}$ , brown is  $(1.0 \text{ to } 0.8) \times \text{average}$ , light gray is  $(0.8 \text{ to } 0.5) \times \text{average}$ , and cyan is  $(0.5 \text{ to } 0.1) \times \text{average}$ . For all the sectors, the simulation setup matches the data reasonably.

### 6.2.2 For the Cu+Au setup

Figure 6.22 and Figure 6.26 show the alpha vs. board plots for the Cu+Au Minimum Bias data (left) and the Cu+Au simulation setup (right) for the west arm and the east arm, respectively. For both arms, the simulation setup matches the data reasonably.

Figure 6.27 shows the per-event  $dN/d\phi$  distribution of the good tracks going into the jet reconstruction for both data (black line) and simulation (red line). The distributions are normalized from  $\phi = 2.2$  to 2.4.

Figure 6.33 shows the EMCal acceptance comparison between the Cu+Au Minimum Bias data (left) and the Cu+Au simulation setup (right) for sectors 0 to 7. Like before, the  $z$ -scale is setup such that for

$$\text{average} = \langle \text{hits/event} \rangle \text{ for that sector,}$$

red is  $(2.0 \text{ to } 1.5) \times \text{average}$ , green is  $(1.5 \text{ to } 1.3) \times \text{average}$ , dark gray is  $(1.3 \text{ to } 1.0) \times \text{average}$ , brown is  $(1.0 \text{ to } 0.8) \times \text{average}$ , light gray is  $(0.8 \text{ to } 0.5) \times \text{average}$ , and cyan is  $(0.5 \text{ to } 0.1) \times \text{average}$ . For all the sectors, the simulation setup matches the data reasonably.

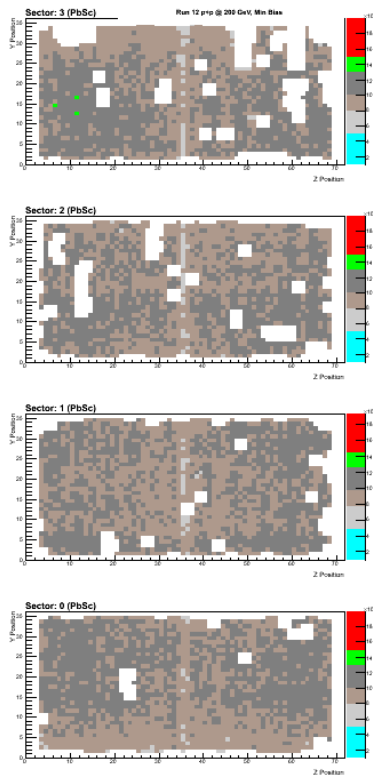


Figure 6.14 Data: Sectors 0 to 3

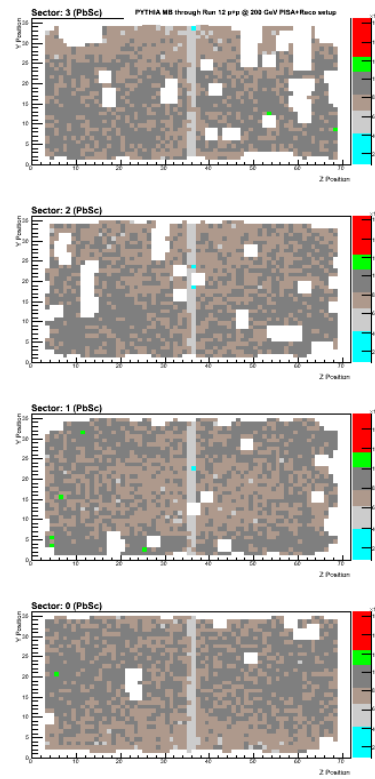


Figure 6.15 Simulation: Sectors 0 to 3

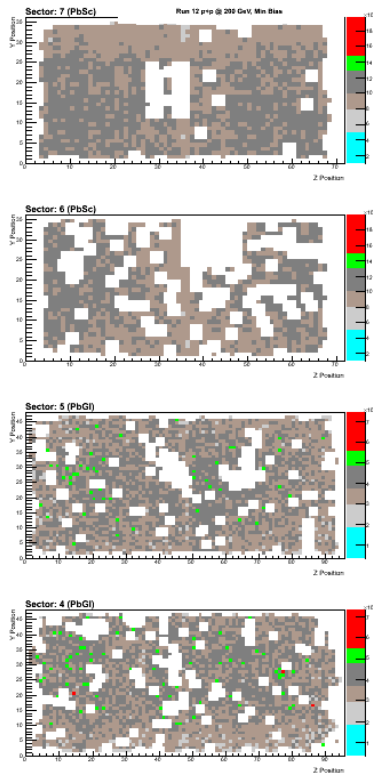


Figure 6.16 Data: Sectors 4 to 7

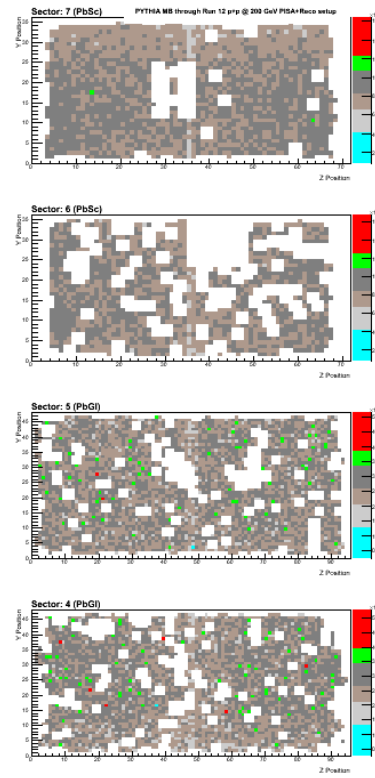


Figure 6.17 Simulation: Sectors 4 to 7

Figure 6.18: EMCAL acceptance comparison between the data and the simulation for sector 0 to 7.

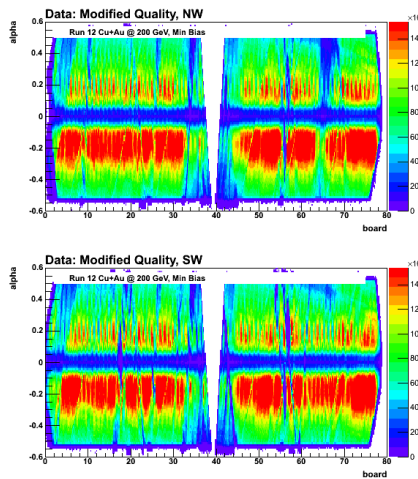


Figure 6.20 Data: West arm

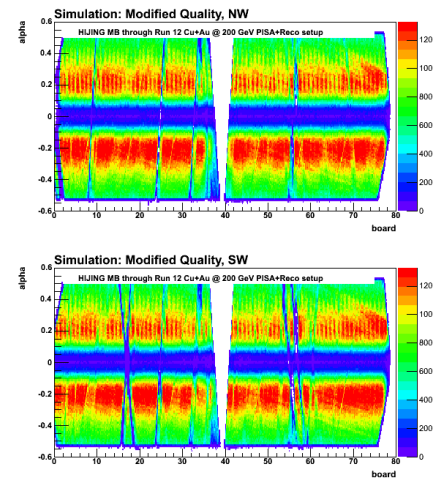


Figure 6.21 Simulation: West arm

Figure 6.22: DC/PC acceptance comparison between the data and the simulation for the west arm.

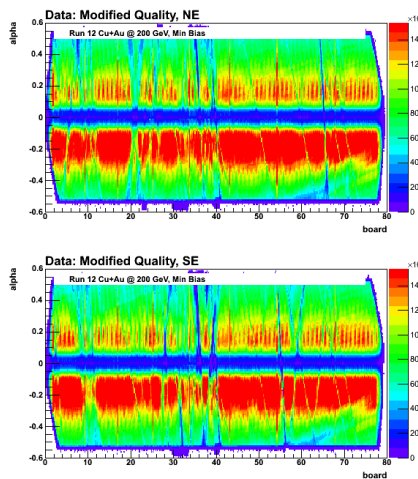


Figure 6.24 Data: East arm

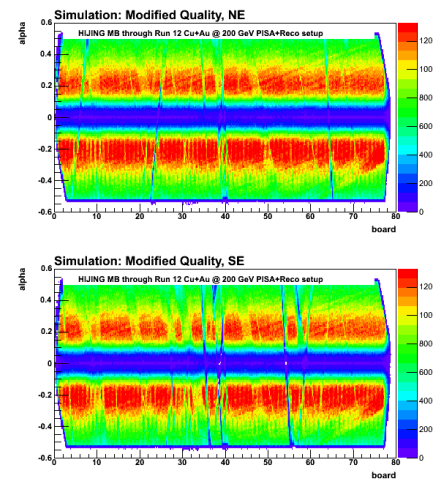


Figure 6.25 Simulation: East arm

Figure 6.26: DC/PC acceptance comparison between the data and the simulation for the east arm.

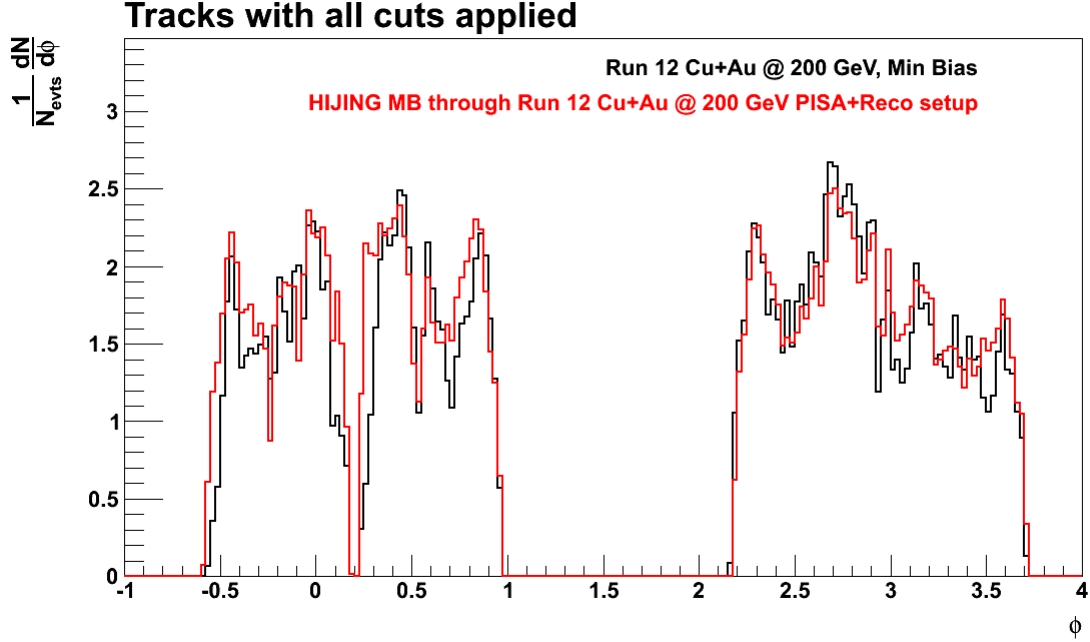


Figure 6.27: Per-event  $dN/d\phi$  distribution of the good tracks for both data (black line) and simulation (red line). The distributions are normalized from  $\phi = 2.2$  to  $2.4$ .

### 6.3 True jet

In addition to the nominal settings mentioned in Section 4.2.2.1, the minimum parton  $p_T$  (ckin 3) of  $6.6 \text{ GeV}/c$  is used to generate the  $p+p$  PYTHIA events. The following requirements are imposed on the PYTHIA true jets:

- The jet reconstruction is performed using the anti- $k_t$  algorithm with  $R_{\text{Anti-}k_t} = 0.2$  on the final state particles<sup>i</sup> of PYTHIA.
- The jet axis is required to pass  $|\eta_{\text{True}}| < 0.35$ .
- The only jet-level requirement is  $p_{T,\text{True}} > 6.6 \text{ GeV}/c$ . Note that neither the *n.c.* nor the *c.f.* requirements are imposed on the true jets.

Figure 6.34 shows the per-event PYTHIA true jet yield for the  $p+p$  and Cu+Au setups. As expected, there is no significant difference in the yield at the truth level.

It is beneficial to have a rough understanding of how much jet energy is captured by the PHENIX detector for our definition of the true jet. Figure 6.35 shows the average contribution

<sup>i</sup>Muons and neutrinos are excluded

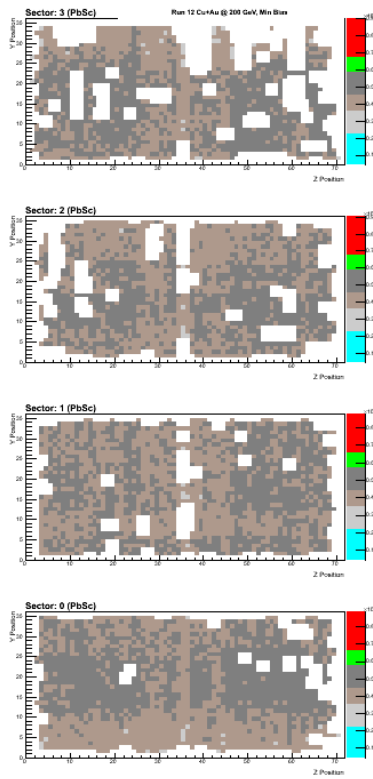


Figure 6.29 Data: Sectors 0 to 3

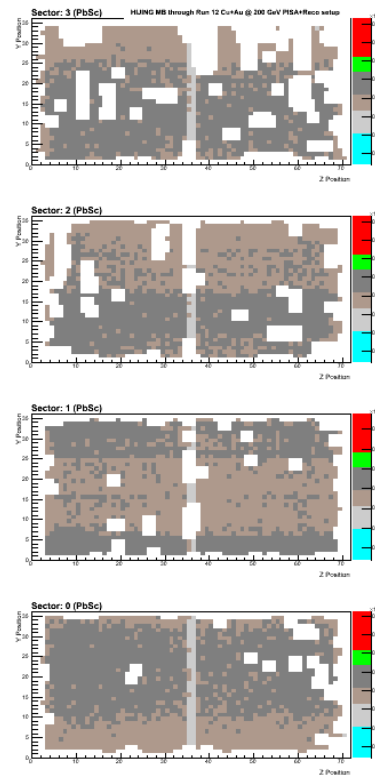


Figure 6.30 Simulation: Sectors 0 to 3

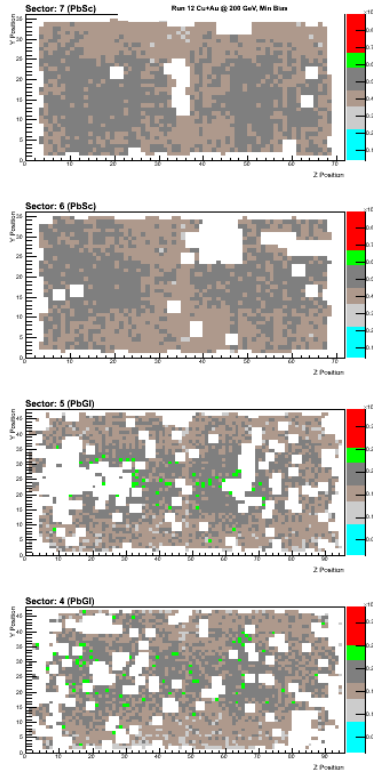


Figure 6.31 Data: Sectors 4 to 7

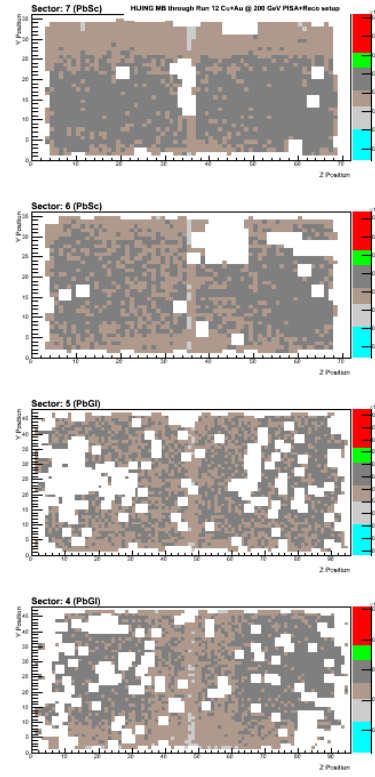


Figure 6.32 Simulation: Sectors 4 to 7

Figure 6.33: EMCAL acceptance comparison between the data and the simulation for sector 0 to 7.

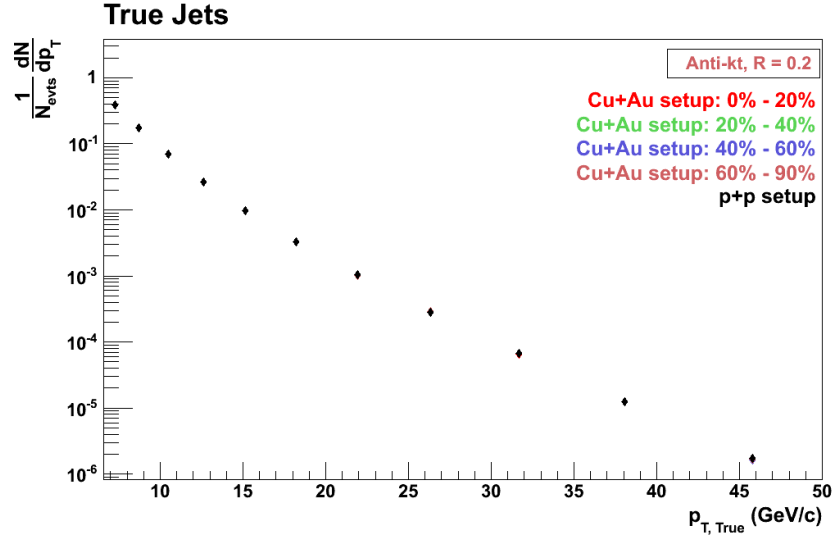


Figure 6.34: Per-event PYTHIA true jet yield for the  $p+p$  and Cu+Au setups.

of the true jet constituent particles to the true jet's  $p_T$  as a function of  $p_{T, \text{True}}$ . The biggest contribution ( $\approx 40\%$ ) comes from the  $\pi^\pm$ . Photons, which include direct as well as decays from  $\pi^0$ 's,  $\eta$ 's, and other short-lived neutral mesons, contribute  $\approx 30\%$ . The  $k^\pm$  and  $p/\bar{p}$  contribute  $\approx 9\%$  each. The neutral hadrons  $n/\bar{n}$  and  $K_L^0$  contribute  $\approx 9\%$  and  $\approx 5\%$ , respectively.

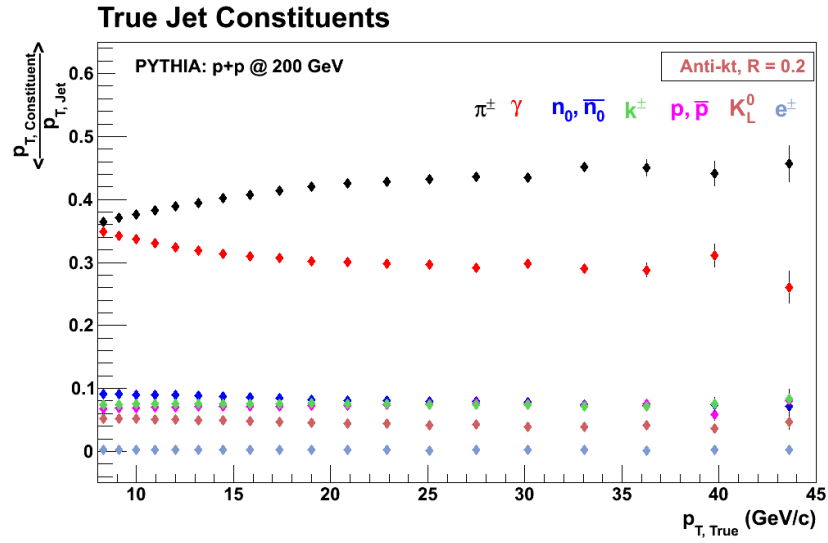


Figure 6.35: Average contribution of the true jet constituent particles to the true jet's  $p_T$ .

## 6.4 Single particle performance

### 6.4.1 Track reconstruction efficiency

To evaluate the track reconstruction efficiency, each charged hadron or electron constituent of the true jet is associated with the closest reconstructed track. Figure 6.36 is the  $\Delta R$  distribution in the  $\eta$ - $\phi$  space (defined as  $\Delta R = \sqrt{\Delta\eta^2 + \Delta\phi^2}$ ) between the charged hadrons or electron and the closest tracks. If a track is found within  $\Delta R < 0.09$ , the charged hadron or electrons is determined to have been reconstructed. Figure 6.37 is the response matrix between the charged hadrons or electrons and the matched tracks. The strong correlation between  $p_{T,\text{True}}$  and  $p_{T,\text{Reco}}$  is an indication that  $p_T$  of the charged hadrons or electrons is well reconstructed for all  $p_{T,\text{True}}$ .

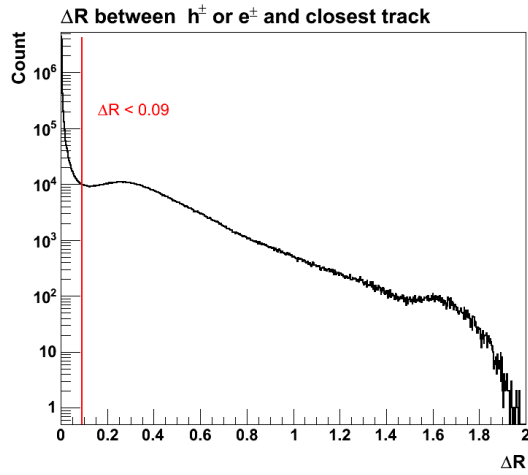


Figure 6.36:  $\Delta R$  distribution between the charged hadrons or electrons and the closest tracks.

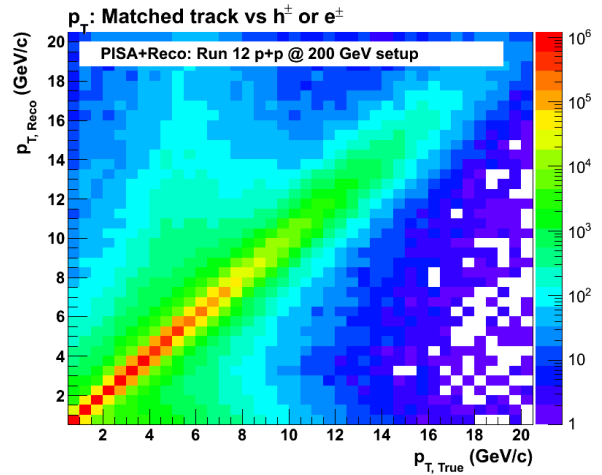


Figure 6.37: Response matrix between the charged hadrons or electrons and the matched tracks.

Figure 6.38 shows the reconstruction efficiency for the charged hadrons or electrons as a function of  $p_{T,\text{True}}$  for the different track-level cuts. Without any additional cuts (except for  $\Delta R < 0.09$ ), the reconstruction efficiency is  $\sim 84\%$  at high- $p_T$ . With the addition of the modified quality cut, the reconstruction efficiency becomes  $\sim 78\%$ . With the modified quality and the matching cuts, the efficiency is  $\sim 74\%$ , whereas with the addition of the secondary cuts

(as summarized in Section 5.4.4.1), the efficiency saturates at  $\sim 63\%$  at high- $p_T$  (a decrease of  $\approx 11\%$ ). The three secondary cuts, which were designed to reject the low- $p_T$  conversions that get reconstructed as the high- $p_T$  tracks, are the biggest contribution to the loss of the track reconstruction efficiency.

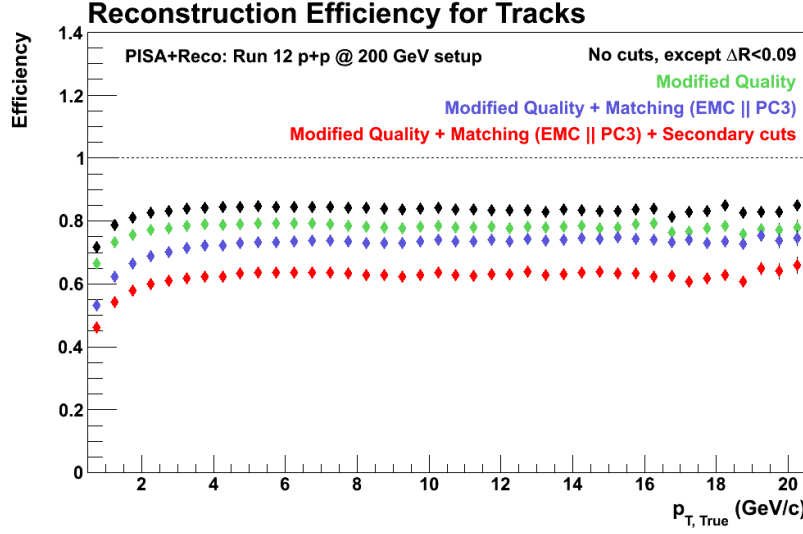


Figure 6.38: Reconstruction efficiency for the charged hadrons or electrons.

To examine the contribution of the dead and inefficient areas in the DC/PC, the same plot (Figure 6.38) is remade with the perfect DC/PC settings in the pisaToDST macro (i.e., no dead channels or ROCs are added). Figure 6.39 shows the reconstruction efficiency for the charged hadrons or electrons as a function of  $p_{T, \text{True}}$  for the perfect DC/PC. The efficiency saturates at  $\sim 71\%$  at high- $p_T$  for all track level-cuts. It can be concluded that there is a loss of overall  $\approx 7\%$  due to the dead and inefficient areas in the DC/PC during the Run-12 period.

#### 6.4.2 Cluster reconstruction efficiency

To evaluate the cluster reconstruction efficiency, each photon constituent of the true jet is associated with the closest reconstructed cluster. Figure 6.40 is the  $\Delta R$  distribution between the photons and the closest clusters. If a cluster is found within  $\Delta R < 0.04$ , the photon is determined to have been reconstructed. Figure 6.41 is the response matrix between the photons and the matched clusters.

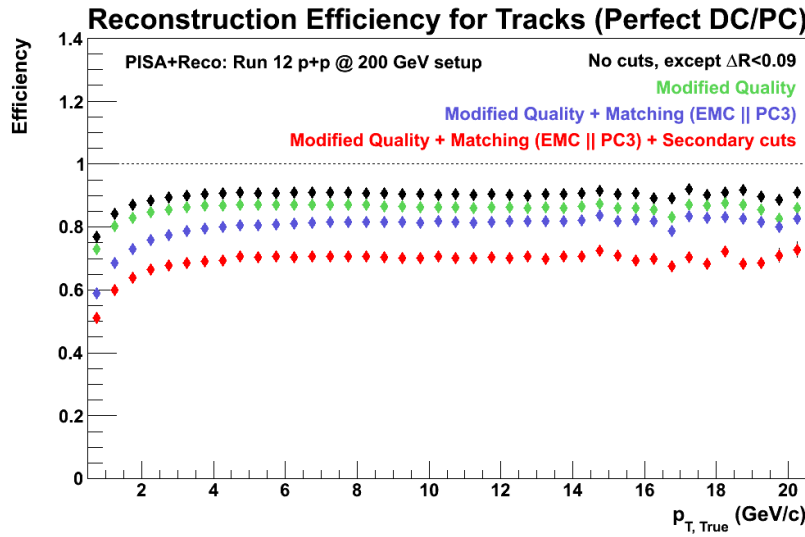


Figure 6.39: Reconstruction efficiency for the charged hadrons or electrons for the perfect DC/PC.

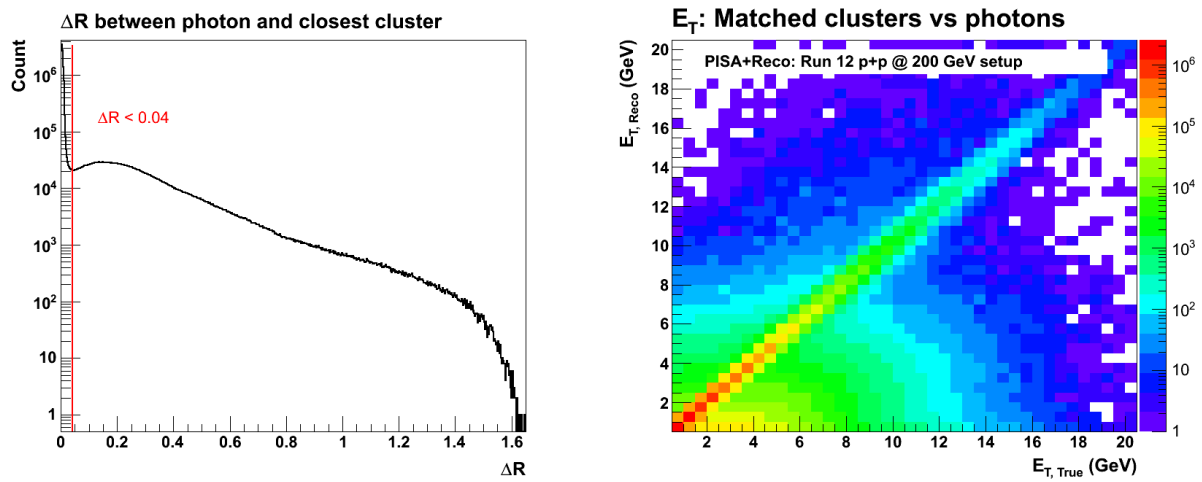


Figure 6.40:  $\Delta R$  distribution between the photons and the closest clusters.

Figure 6.41: Response matrix between the photons and the matched clusters.

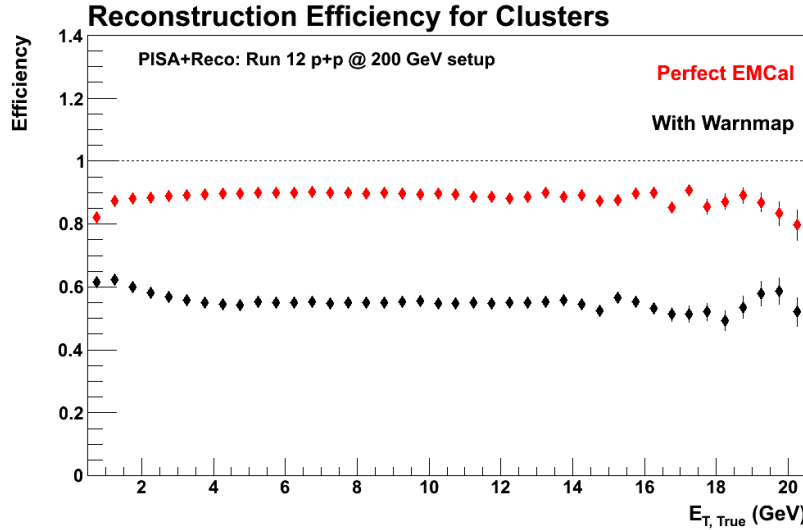


Figure 6.42: Reconstruction efficiency for the photons.

Figure 6.42 shows the reconstruction efficiency for the photons as a function of  $E_{T,\text{True}}$ . The reconstruction efficiency for the perfect EMCAL (red markers) saturates at  $\sim 90\%$ . The inefficiency of 10% can be related to the loss of photons in the cracks between the EMCAL sectors and the  $\Delta R$  cut. The reconstruction efficiency for the EMCAL with hot/dead map (black markers) saturates at  $\sim 65\%$ . This loss in the efficiency of  $\approx 25\%$  is attributed to the hot or dead or uncalibrated EMCAL towers.

## 6.5 Jet performance

### 6.5.1 Jet reconstruction efficiency

True jets are reconstructed from the final state particles of PYTHIA as explained in Section 6.3. If a reconstructed jet axis<sup>ii</sup> is within  $\Delta R < 0.2$  of the true jet axis, it is considered to be reconstructed. The one-to-one matching between the true jet and the reconstructed jet is imposed as explained in Appendix B. Figure 6.43 shows the  $\Delta R$  distribution (left) and the  $\Delta R$  vs.  $p_{T,\text{True}}$  distribution (right) for the Cu+Au 0–20% centrality.

<sup>ii</sup>The reconstructed jets are required to pass all the jet-level cuts.

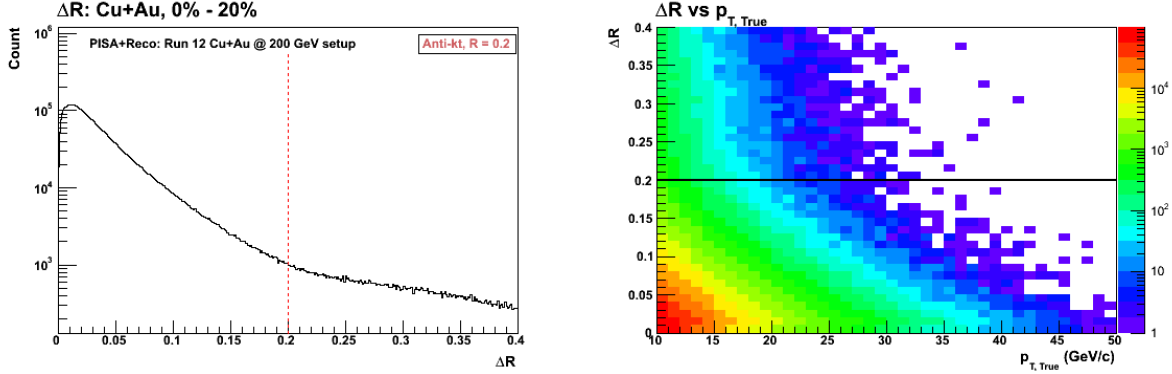


Figure 6.43:  $\Delta R$  distribution for the Cu+Au 0–20% centrality.

Figure 6.44 shows the reconstruction efficiency as a function of  $\phi_{\text{True}}$ . The red lines trace the edge of the PHENIX acceptance in azimuth. The periodic drop in the efficiency is due to the combination of the following three factors:

- Choice of small  $R_{\text{Anti-}k_t}$  ( $= 0.2$ ).
- Neutral constituent falling in the cracks between the EMCAL sectors.
- Requirement of  $n.c. \geq 3$  for the reconstructed jet.

As the reconstruction efficiency for jets near the edge of the PHENIX acceptance falls rapidly, the reconstructed jet axis will be restricted to 0.12 in  $\phi$  from the edge. The selected fiducial  $\phi$  cut is traced in blue in Figure 6.44 and is implemented in both the data and the simulation for the reconstructed jets.

Figure 6.45 shows the reconstruction efficiency as a function of  $\eta_{\text{True}}$  for  $|z_{\text{vertex}}| < 10$  cm. As the pseudorapidity is dependent on the  $z_{\text{vertex}}$ , the pseudorapidity range as a function of  $z_{\text{vertex}}$  is calculated as

$$\eta \in \left[ \log \tan \left( \frac{1}{2} \arctan \left( -\frac{246}{90 - z_{\text{vertex}}} \right) \right), \log \tan \left( \frac{1}{2} \arctan \left( \frac{246}{90 - z_{\text{vertex}}} \right) \right) \right]. \quad (6.1)$$

To understand the  $z_{\text{vertex}}$  dependence, Figure 6.46 shows the reconstruction efficiency as a function of  $\eta$  for four different  $z_{\text{vertex}}$  (and hence  $\eta$ ) ranges. The top-left plot is for the  $|z_{\text{vertex}}| < 8$  cm, top-right for  $|z_{\text{vertex}}| < 6$  cm, bottom-left for  $|z_{\text{vertex}}| < 4$  cm, and bottom-right for  $|z_{\text{vertex}}| < 2$  cm. As the reconstruction efficiency for jets near the edge falls rapidly for all the

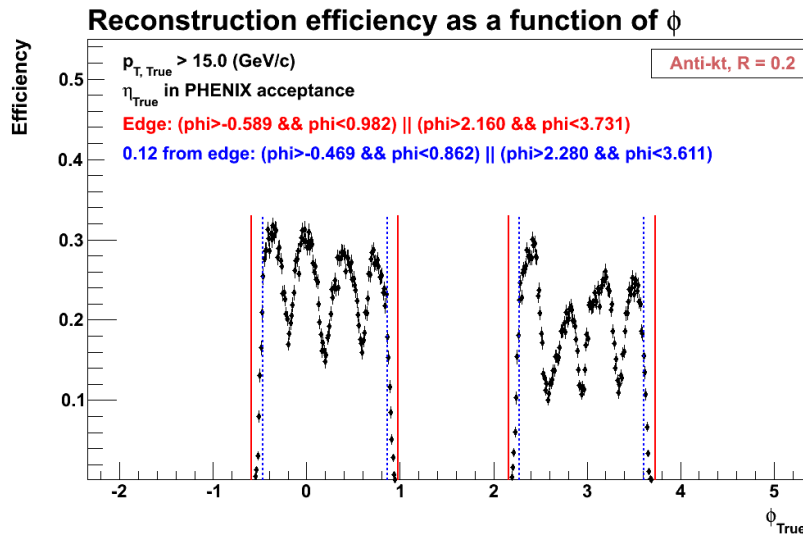


Figure 6.44: Reconstruction efficiency as a function of  $\phi_{\text{True}}$ .

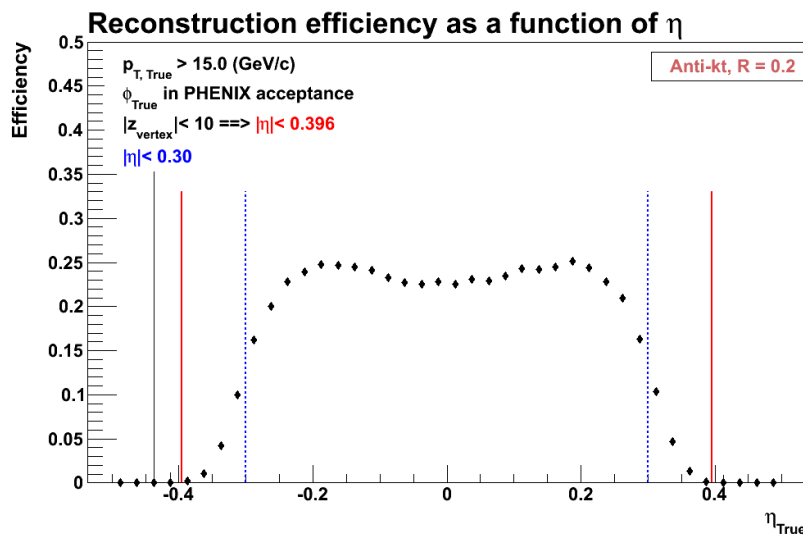


Figure 6.45: Reconstruction efficiency as a function of  $\eta_{\text{True}}$ .

ranges within  $|z_{\text{vertex}}| < 10 \text{ cm}$ , the reconstructed jet axis is restricted to  $|\eta| < 0.3$ . The selected fiducial  $\eta$  cut is traced in blue in both Figure 6.45 and Figure 6.46.

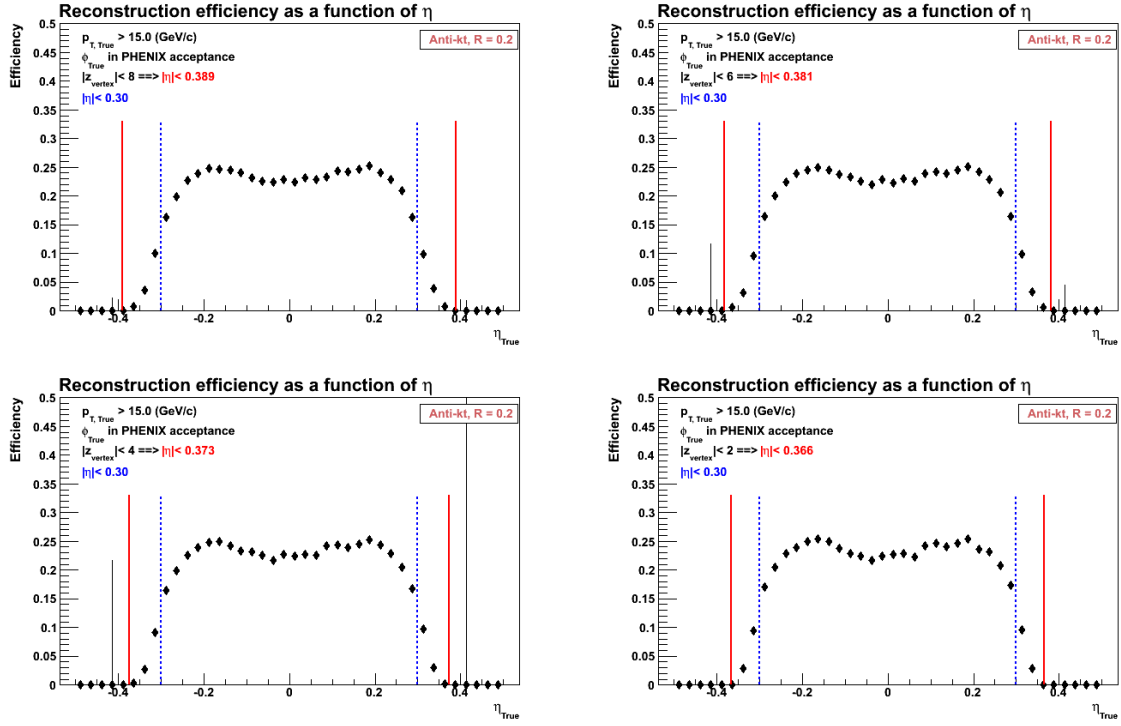


Figure 6.46: Reconstruction efficiency as a function of  $\eta_{\text{True}}$  for four different  $z_{\text{vertex}}$  ranges.

To summarize, the reconstructed jets are required to fall within the following phase space in both the data and the simulation:

- $\eta \in (-0.30, 0.30)$
- $\phi \in (-0.469, 0.862)$  in the west arm
- $\phi \in (2.280, 3.611)$  in the east arm

Hence, the total phase space for the reconstructed jet is:

$$\Delta\eta \times \Delta\phi = 0.6 \times (2 \times 1.331) = 0.6 \times 2.662 \quad (6.2)$$

Figure 6.47 shows the jet reconstruction efficiency ( $\epsilon/\epsilon_{\text{geo}}$ ) for the  $p+p$  and different centrality selections of the Cu+Au collisions. At a fixed  $p_{\text{T, True}}$ , the reconstruction efficiency for the  $p+p$  and Cu+Au 60–90% is comparable; however, the efficiency is relatively larger for more central events. This rise in the reconstruction efficiency for the central events is due to the fact

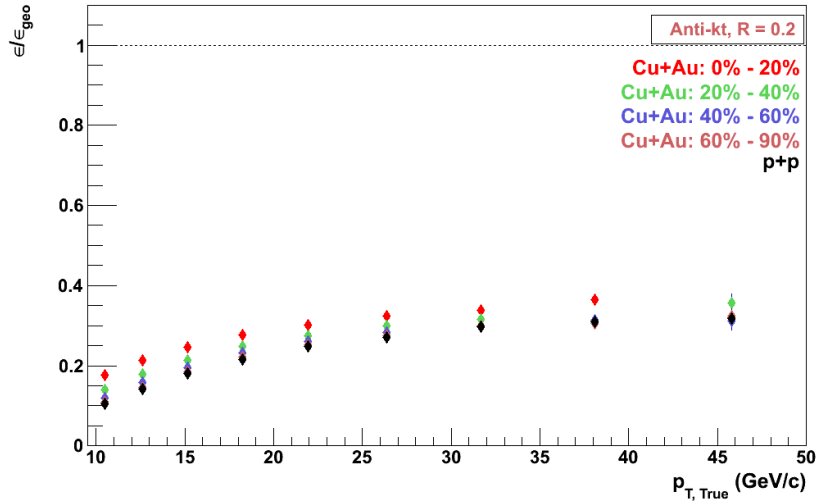


Figure 6.47: Jet reconstruction efficiency for the  $p+p$  and different centrality selections of the Cu+Au collisions.

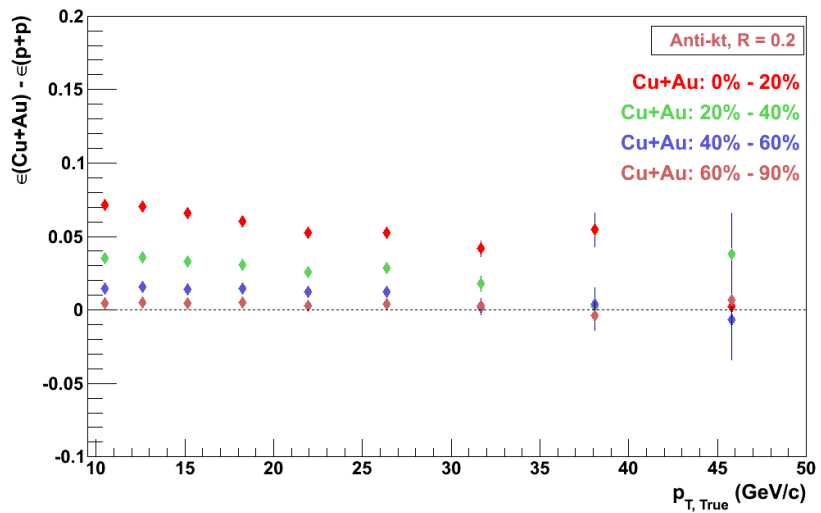


Figure 6.48: Jet reconstruction efficiency for the different centralities of the Cu+Au collisions subtracted from that of the  $p+p$  collisions.

that the underlying event can aid the reconstructed jet to pass the minimum  $p_{T,\text{Reco}}$  and  $n.c.$  requirements.

Figure 6.48 shows the jet reconstruction efficiency for the different centralities of the Cu+Au collisions subtracted from that of the  $p+p$  collisions. The centrality-dependent difference in the reconstruction efficiency is up to 7% at low- $p_T$ , but at high- $p_T$ , the difference decreases significantly.

### 6.5.2 Jet energy scale and jet energy resolution

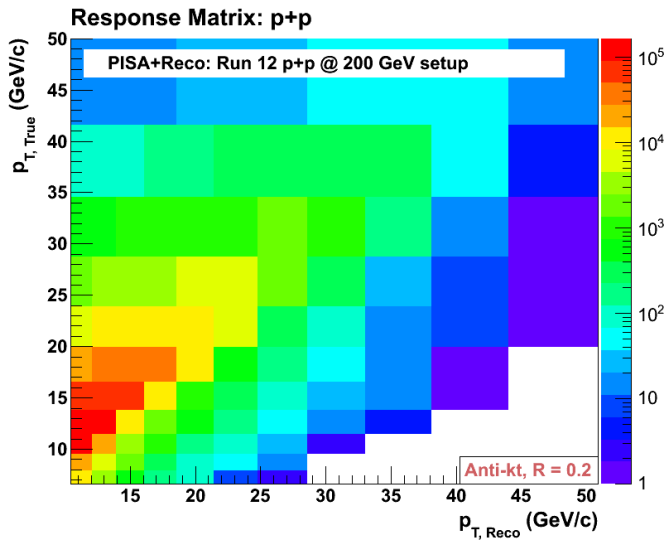


Figure 6.49: Response matrix for the  $p+p$  collisions.

Response matrix is formed from the matched pairs of  $(p_{T,\text{Reco}}, p_{T,\text{True}})$  jets. The centrality dependence of the  $p_T$  feeding (i.e., the energy scale of  $p_{T,\text{Reco}}$  becoming relatively higher due to the contribution from the underlying event) effect can be seen by comparing the response matrices for the  $p+p$  and different centralities of the Cu+Au collisions; Figure 6.49 and Figure 6.50 are the response matrices for the  $p+p$  and different centralities of the Cu+Au collisions, respectively. In Figure 6.50, the top-left plot is for the Cu+Au 0–20% centrality selection, top-right for 20–40%, bottom-left for 40–60%, and bottom-right for 60–90%.

The  $p_T$  feeding effect and the contribution from the underlying event becomes distinct while investigating the jet energy scale (JES) and the jet energy resolution (JER). The JES and JER

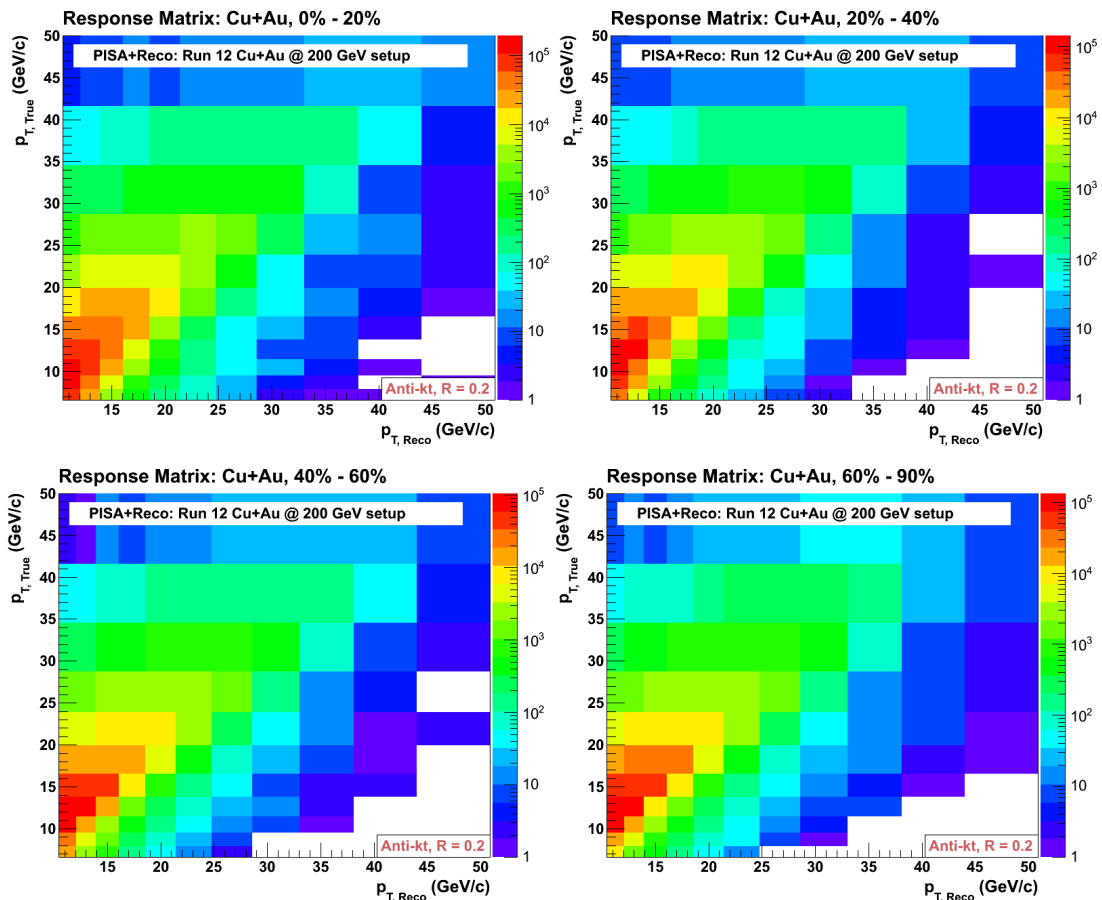


Figure 6.50: Response matrices for the different centralities of the Cu+Au collisions.

are determined by evaluating the distribution of  $p_{T, \text{Reco}}/p_{T, \text{True}}$  for the matched pairs of the truth and the reconstructed jets in the bins of  $p_{T, \text{True}}$ . Figure 6.51 and Figure 6.52 show such distribution for the Cu+Au 0–20% centrality selection. As the distributions are not Gaussian, the mean and standard deviation of the distribution are extracted without fitting.

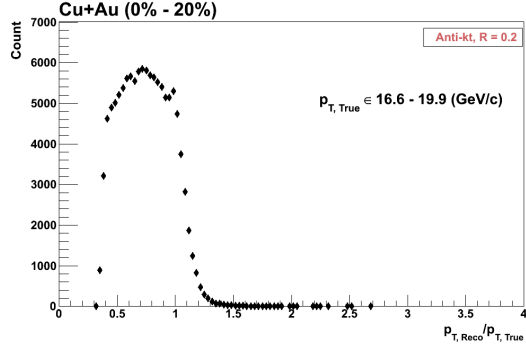


Figure 6.51:  $p_{T, \text{Reco}}/p_{T, \text{True}}$  distribution for  $p_{T, \text{True}} \in 16.6\text{--}19.9 \text{ GeV}/c$ .

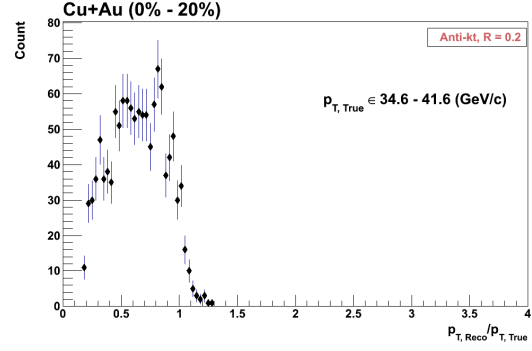


Figure 6.52:  $p_{T, \text{Reco}}/p_{T, \text{True}}$  distribution for  $p_{T, \text{True}} \in 34.6\text{--}41.6 \text{ GeV}/c$ .

Figure 6.53 shows the JES for the  $p+p$  and different centrality selections of the Cu+Au collisions. As the JES is the mean of the  $p_{T, \text{Reco}}/p_{T, \text{True}}$  distribution, from Figure 6.53, it can be deduced that, on average, PHENIX captures  $\approx 70\%$  of the jet energy.

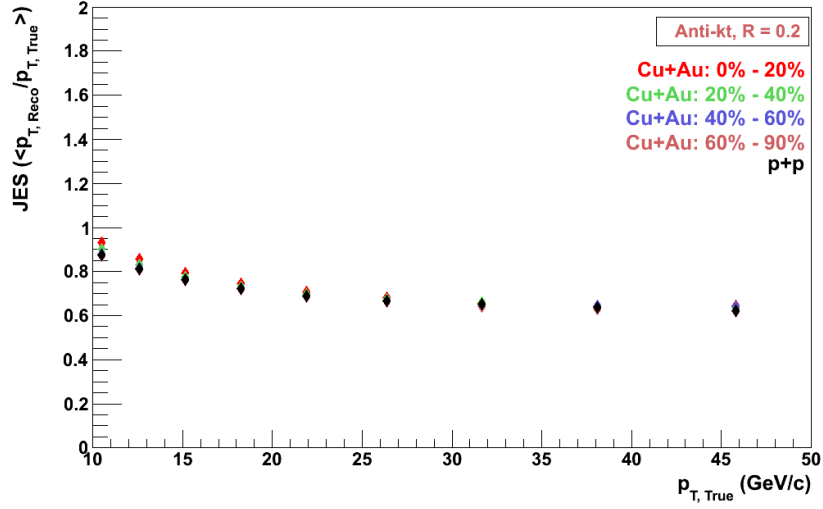


Figure 6.53: JES for the  $p+p$  and different centrality selections of the Cu+Au collisions.

Figure 6.54 is the JES for the different centralities of the Cu+Au collisions subtracted from that of the  $p+p$  collisions. The centrality-dependent difference in the JES is up to 6% at low- $p_T$ . The underlying event contribution is much stronger for the central collisions at low- $p_T$ , and the centrality dependence significantly decreases at high- $p_T$ .

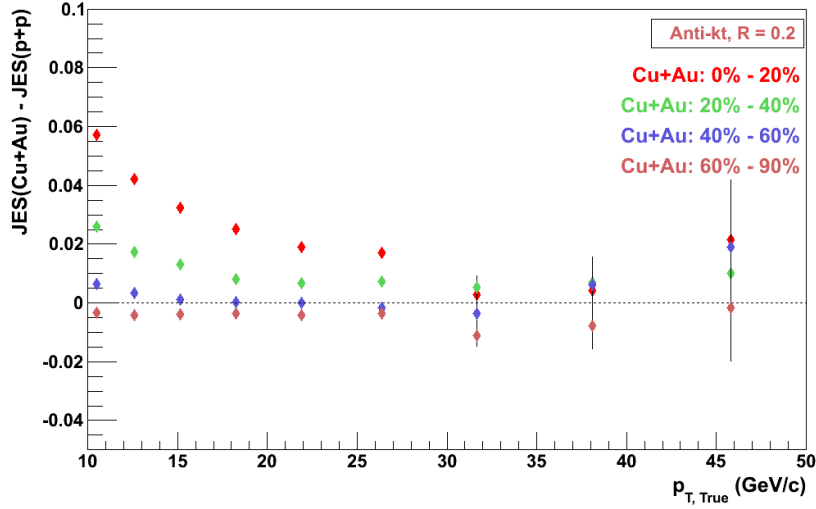


Figure 6.54: JES for the different centralities of the Cu+Au collisions subtracted from that of the  $p+p$  collisions.

Figure 6.55 shows the JER for the  $p+p$  and different centrality selections of the Cu+Au collisions, from which we can deduce that, on average, the JER is 14–23% for PHENIX.

Figure 6.56 is the JER for the different centralities of the Cu+Au collisions subtracted from that of the  $p+p$  collisions. The centrality-dependent difference in the JES is up to 5% at low- $p_T$ . Also, as with the JES, the underlying event contribution is much stronger for the central collisions at low- $p_T$ , and the centrality dependence significantly decreases at high- $p_T$ .

## 6.6 Fake jet simulation study

This section summarizes the fake jet simulation study using sHIJING. As no correction is derived or applied from this study, its sole purpose is to understand and benchmark the performance of the fake jet subtraction method.

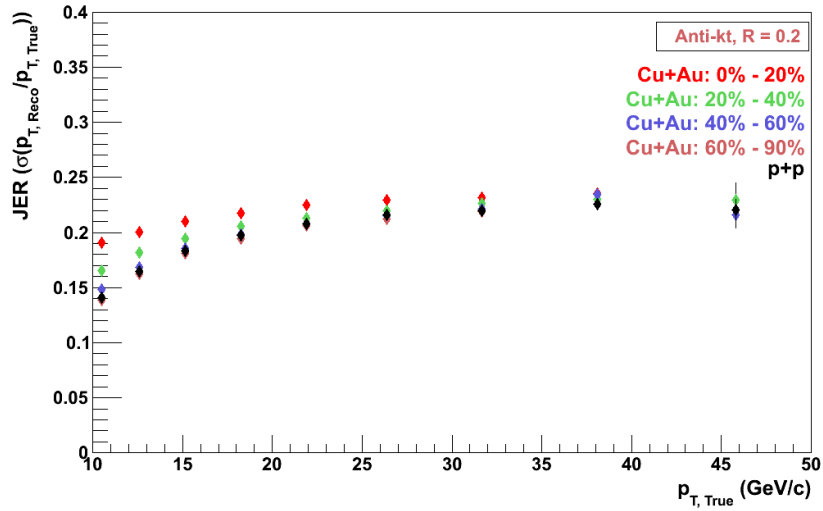


Figure 6.55: JER for the  $p+p$  and the different centrality selections of the Cu+Au collisions.

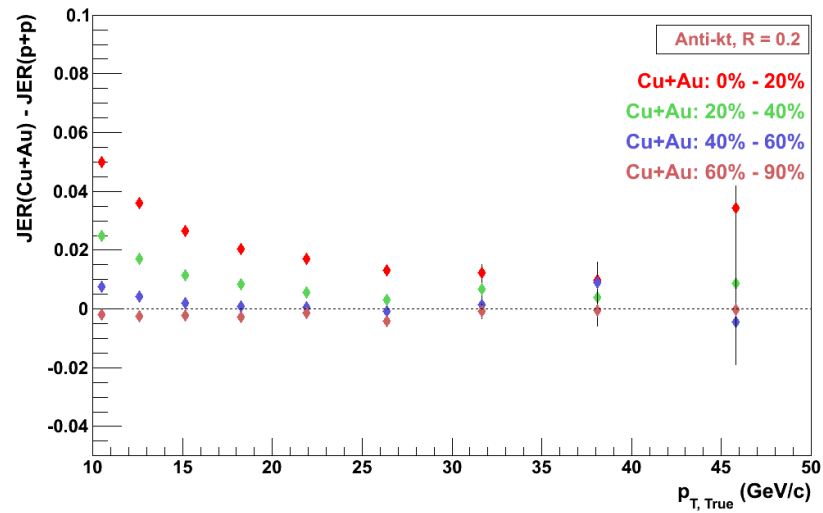


Figure 6.56: JER for the different centralities of the Cu+Au collisions subtracted from that of the  $p+p$  collisions.

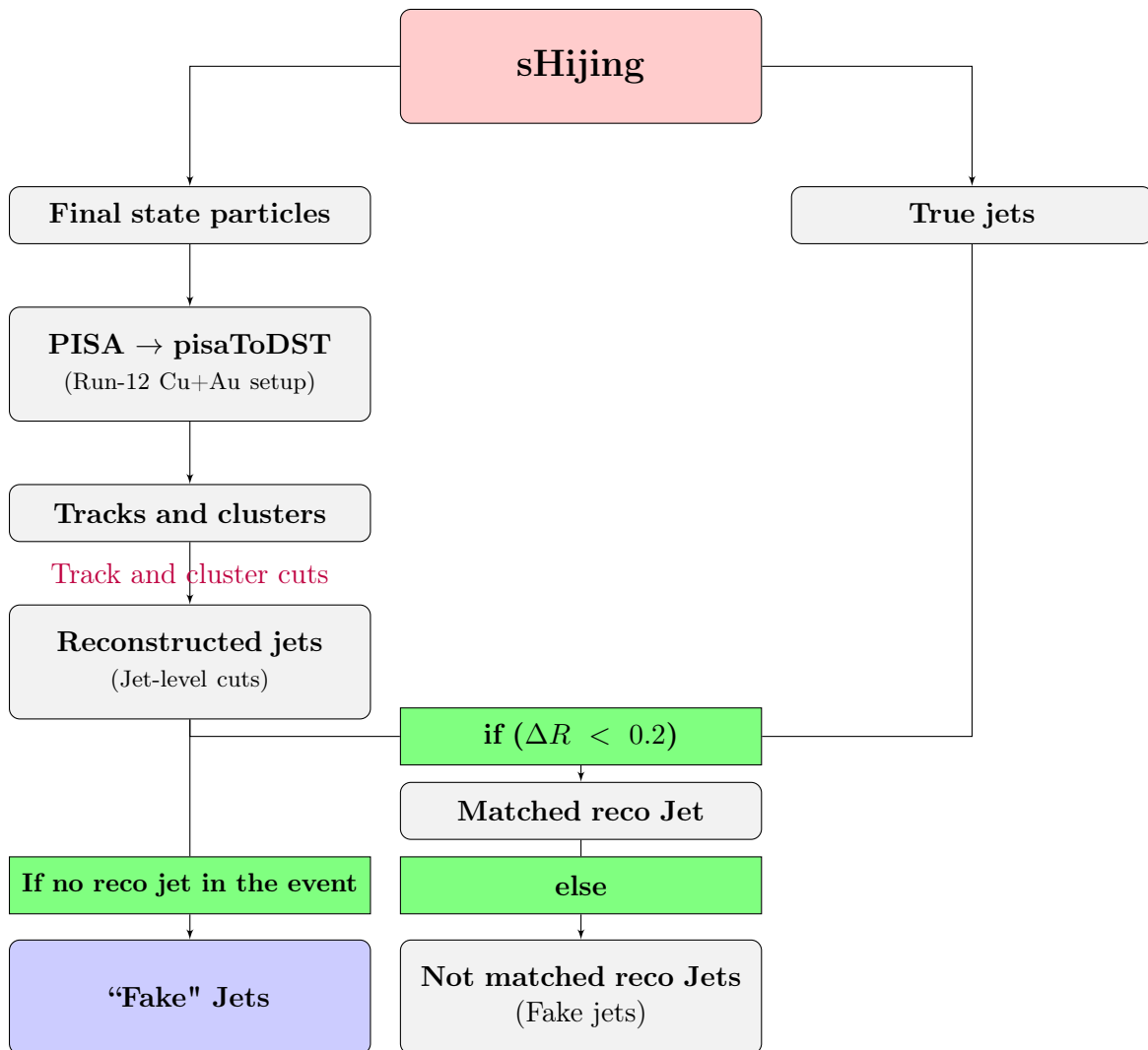


Figure 6.57: Simulation chain for the fake jet study.

Figure 6.57 summarizes the simulation chain for this study. In addition to the nominal settings mentioned in Section 4.2.2.2,  $R_{\text{Anti-}k_t} = 0.2$  is used to generate the sHIJING Cu+Au events. The final state particles of sHIJING are fed through PISA and then the output of PISA is passed through the pisaToDST macro. The reconstructed tracks and clusters are required to pass all the track and cluster cuts. The anti- $k_t$  algorithm is run on these tracks and clusters, and the reconstructed jets are then required to pass the jet-level cuts. If a reconstructed jet with  $p_{T,\text{Reco}} > 6.6 \text{ GeV}/c$  lies within the  $\Delta R < 0.2$  of the true jet axis (with  $p_{T,\text{True}} > 6.6 \text{ GeV}/c$ ), the jet is labeled as the matched jet, else it is labeled as the not-matched jet. For events without a reconstructed jet, the tracks and clusters go through the shuffling procedure as explained in Section 5.6.2.1, the jet reconstruction is performed on these shuffled tracks and clusters, and all the jet-level cuts are applied to the reconstructed jet. The resulting yield is labeled as the “fake” jet.

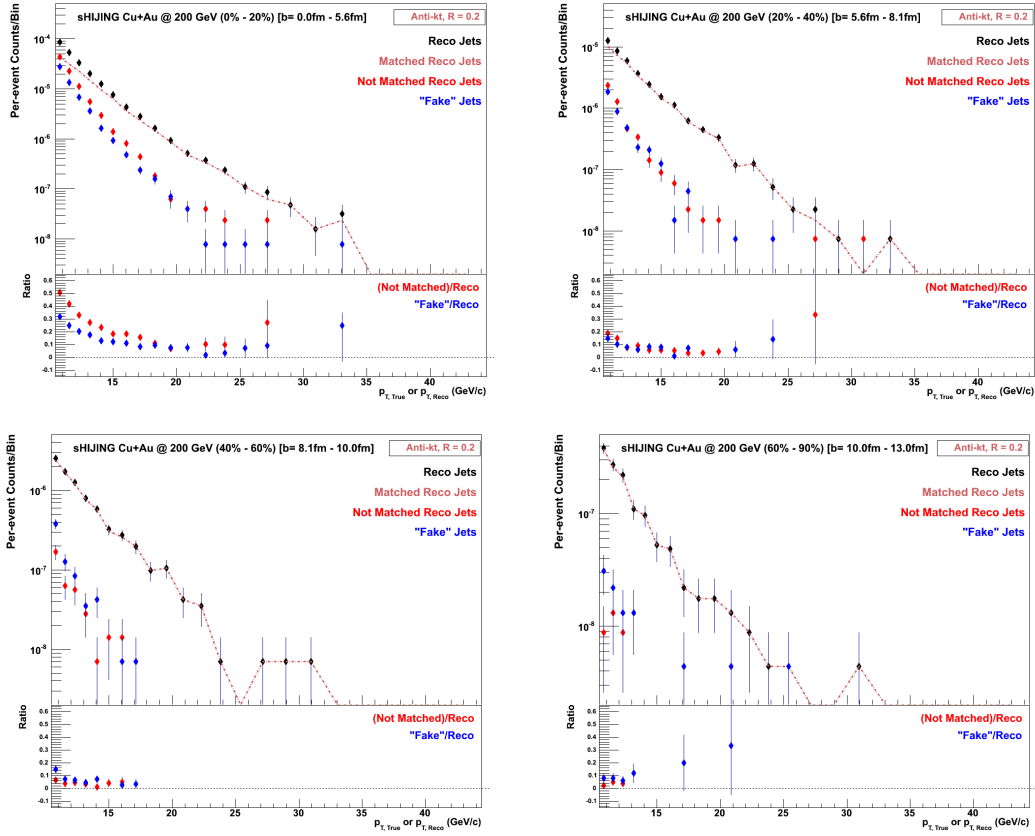


Figure 6.58: Fake jet simulation study for the different centralities of the Cu+Au collisions.

The fake jets are the jets that are not matched with the SHIJING true jets while the “fake” jets are the jets that the fake jet subtraction method estimates. Figure 6.58 shows the result of the study for the different centralities of the Cu+Au collisions; the top-left plot is for the Cu+Au 0–20% centrality selection, top-right for 20–40%, bottom-left for 40–60%, and bottom-right for 60–90%. Comparing the not-matched jet and “fake” jet yield, one can conclude that for the 0–20% and 20–40% selections, the “fake” jet yield is underestimated, whereas for the 40–60% and 60–90% centrality selections, the “fake” jet yield is overestimated. What this means is that when the fake jet subtraction is performed (as explained in Section 5.6.2.1), for the 0–20% and 20–40% centralities, the fake jet contribution is not fully subtracted, and for the 40–60% and 60–90% centralities, the fake jet contribution is little over subtracted (especially at low- $p_T$ ). It must be noted here that the fake jet contribution is also alternately analyzed later by re-running the analysis with higher minimum energy requirement on the tracks and clusters, and the uncertainty from this variation is included in the systematic uncertainty.

## CHAPTER 7. PATH TO FINAL RESULTS

### 7.1 Unfolding

Unfolding is a process of correcting the raw spectrum for the finite jet energy resolution introduced by underlying event fluctuations and detector effects. Response matrix  $A_{ij}$  is formed from the matched pairs of  $(p_T, \text{Reco}, p_T, \text{True})$  jets and gives the probability of an event generated in the true bin  $j$  to be found in the measured bin  $i$  such that

$$b_i^{\text{ini}} = \sum_j A_{ij} x_j^{\text{ini}}, \quad (7.1)$$

where  $b_i^{\text{ini}}$  is the histogram of Monte Carlo measured values and  $x_j^{\text{ini}}$  is the histogram of Monte Carlo true values.

The goal of the unfolding procedure is to find a meaningful way of solving the system of equations and determine the underlying real distribution  $x$  from a measured distribution  $b$  such that

$$b = Ax. \quad (7.2)$$

If the response matrix  $A$  can be inverted,  $x$  can be estimated as

$$x = A^{-1}b. \quad (7.3)$$

But even when the response matrix is invertible, an attempt to solve the problem directly by full inversion of the response matrix almost always leads to rapidly oscillating futile solutions. The singular value decomposition (SVD) method [119] will be used as the default method of unfolding in this analysis and the iterative Bayesian method [120] will be used as a cross-check. Both these methods require regularization to prevent statistical fluctuations and will be implemented by using RooUnfold<sup>i</sup> software package [121].

---

<sup>i</sup>RooUnfold-1.1.1.

### 7.1.1 Unfolding methods

#### 7.1.1.1 Singular value decomposition method

For a detailed description of the unfolding algorithm based on the singular value decomposition of a response matrix, see [119]. The singular value decomposition of a  $m \times n$  matrix  $A$  is its factorization of the form

$$A = USV^T, \quad (7.4)$$

where

- $U$  is a  $m \times m$  orthogonal matrix such that  $UU^T = U^TU = 1$ ,
- $V$  is a  $n \times n$  orthogonal matrix such that  $VV^T = V^TV = 1$ , and
- $S$  is a  $m \times n$  diagonal matrix with non-negative diagonal elements such that  $S_{ij} = 0$  for  $i \neq j$  and  $S_{ii} \equiv s_i \geq 0$

The numbers  $s_i$  are called singular values of the matrix  $A$ , and the columns of  $U$  and  $V$  are called the left and right singular vectors.

With the SVD method, the linear system  $Ax = b$  can be easily diagonalized by introducing rotated vectors  $z$  and  $d$  such that  $z \equiv V^T x$  and  $d \equiv U^T b$ . Equation 7.2 can be written in terms of Equation 7.4 as

$$b = USV^T x. \quad (7.5)$$

We can then simplify Equation 7.5 in terms of the rotated vectors  $z$  and  $d$  as

$$Sz = d \Rightarrow z = S^{-1}d. \quad (7.6)$$

Rewriting Equation 7.3, we get

$$\begin{aligned} x &= VS^{-1}U^T b \\ &= VS^{-1}d \\ &= Vz. \end{aligned} \quad (7.7)$$

Since the orthogonal matrices  $U$  and  $V$  are harmless, the SVD method reduces the problem of unfolding to individual  $s_i$  and  $d_i$ . However, determination of  $z_i = d_i/s_i$  can become complex for the following two reasons:

- Due to the errors in  $b$ , some  $d_i$  can become highly insignificant.
- Some  $s_i$  may be small (or even zero) and can exaggerate the contributions of poorly known coefficients.

It should be noted that if the measurement contains random statistical fluctuations, these fluctuations in the data get greatly magnified by the small singular values and can cause distortions in the unfolded distributions. The choice of reco-level binning in Section 6.1.3 is driven by the motivation to minimize these random statistical fluctuations, especially at high  $p_T$ .

SVD method solves the complexity of determining  $z_i$  by rescaling variables and equations, and achieves the suppression of spurious oscillatory component by adding the regularization term into the minimization condition. The new regularized  $z_i^{(\tau)}$  is written as

$$z_i^{(\tau)} = \frac{d_i}{s_i} \frac{s_i^2}{s_i^2 + \tau}. \quad (7.8)$$

For large  $s_i \gg \tau$ , the suppression factor  $\frac{s_i^2}{s_i^2 + \tau}$  is close to 1; but for smaller  $s_i$ , it works as a low pass filter.

Like mentioned earlier, the wildly oscillating contributions to the unfolded spectrum can be either from non-significant  $d_i$ 's (due to errors in the measured data) or from small  $s_i$ 's. To eliminate these wild oscillations smoothly, one should choose  $\tau \simeq s_k^2$ , where  $k$  is the index of the last significant  $d$ . Section 7 of [119] discusses a way to optimize the choice of regularization parameter: by plotting  $\log|d_i|$  vs.  $i$ . If the errors in the measured data are estimated correctly and the response matrix has been constructed ideally, the plot should show two distinct features; for small  $i$ ,  $d_i$  should be statistically significant ( $d_i \gg 1$ ) and for increasing  $i$ , it should fall exponentially. The critical value  $i = k$ , after which  $d_i$ 's are non-significant, is seen in the plot as the value of  $i$  where the behavior of  $d_i$  changes from exponentially falling to a constant (that oscillates around 1).

Figure 7.1 shows the distribution of  $d_i$  for the  $p+p$  and different centrality selections of the Cu+Au collisions. Red vertical lines show the choice of the regularization parameter. The optimal choice of the regularization parameter is very important for the SVD method. Choosing the regularization to be too small will over-regularize the result by removing relevant information from the unfolding procedure and bias the result towards the Monte Carlo truth

input, and choosing the regularization too large will under-regularize and the result becomes dominated by unphysical statistical fluctuations.

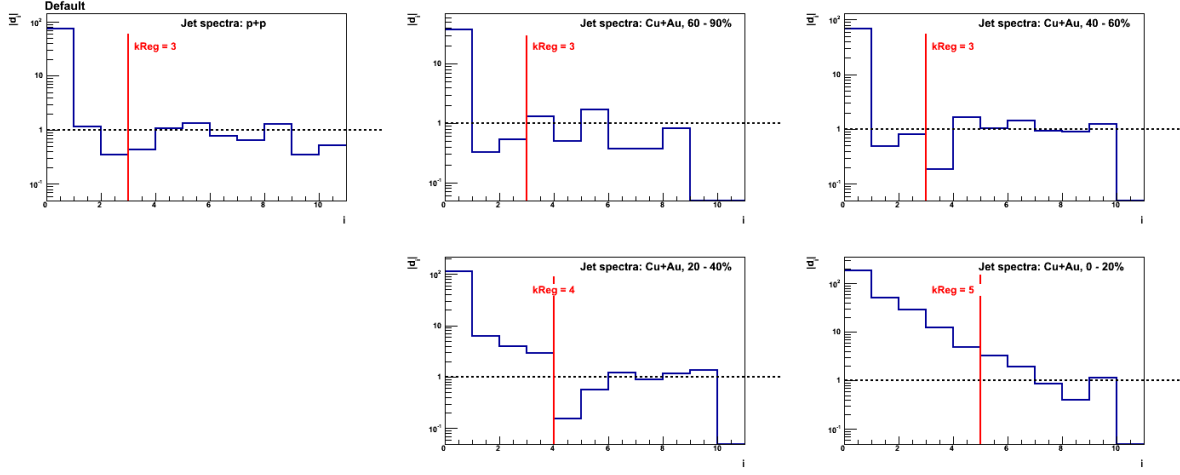


Figure 7.1: Distribution of  $d_i$  for the  $p+p$  and different centrality selections of the Cu+Au collisions. Red vertical lines show the choice of regularization parameter.

Table 7.1 summarizes the default regularization parameter selection for the SVD method for the  $p+p$  and different centralities of the Cu+Au collisions.

Table 7.1: Default regularization parameter selection for the SVD method.

Dataset	kReg
Cu+Au, 0–20%	5
Cu+Au, 20–40%	4
Cu+Au, 40–60%	3
Cu+Au, 60–90%	3
$p+p$	3

The sensitivity of results to the choice of the regularization parameter is investigated by varying the default regularization parameter by  $\pm 1$ . Other tests to the unfolding procedure are performed during the evaluation of the systematic uncertainty in Section 7.4. Figure 7.2 shows the  $p+p$  jet spectra for the default value of the regularization parameter and with variations

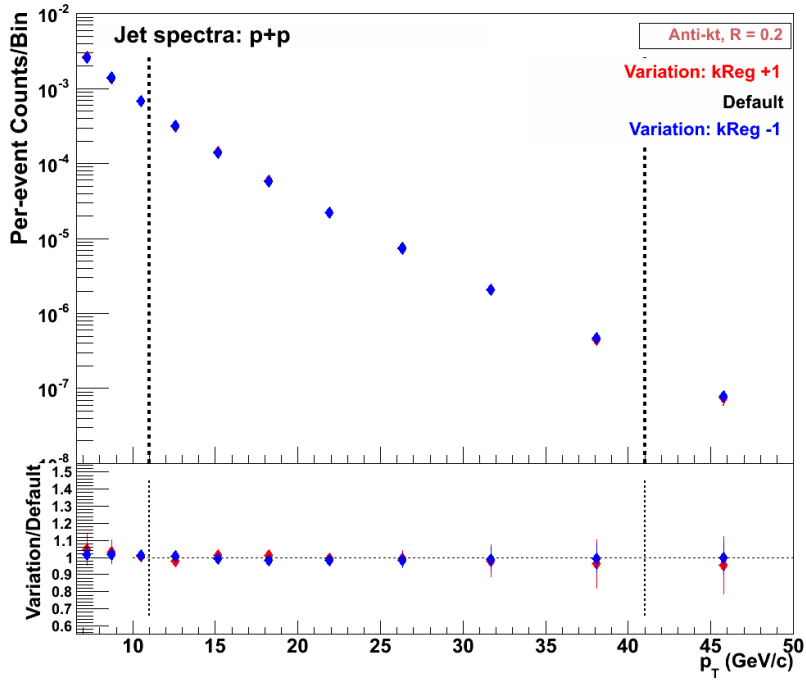


Figure 7.2:  $p+p$  jet spectra with the default value of the regularization parameter and with the variations  $\pm 1$ .

$kReg \pm 1$ . The bottom panel shows the variation/default ratio. The effect of the regularization parameter variation for the  $p+p$  jet spectra is minimal. Figure 7.3 shows the effect for the different centrality selections of the Cu+Au collisions. The effect is up to 25% for the 0–20% centrality but is less than 15% for other centralities.

### 7.1.1.2 Iterative Bayesian method

For a detailed description of the Bayesian method, see [120]. The Bayesian method iteratively applies Bayes' theorem to bring the raw distribution of data close to the true distribution of Monte Carlo. The raw distribution serves as an input to the first iteration and then the output of that iteration becomes input for the next iteration. The process continues until some specific number of iterations are reached. The number of iterations is usually set at the point where subsequent iterations do not significantly change the result, such that the  $\Delta\chi^2$  between the successive iterations becomes small.

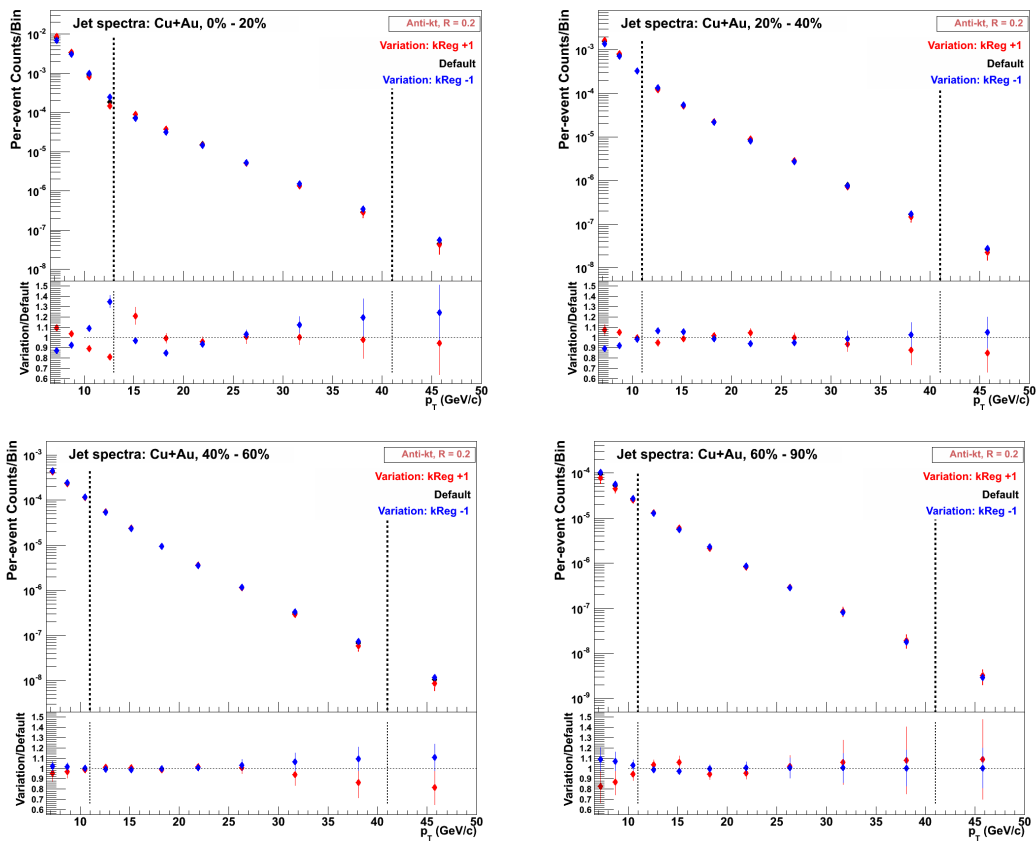


Figure 7.3: Different centrality selected Cu+Au jet spectra with the default value of the regularization parameter and with the variations  $\pm 1$ .

It was found that only 3 iterations were needed to obtain a reasonable performance without fine-tuning the regularization parameter for the Bayesian method. Hence, for the  $p+p$  and different centrality selections of the Cu+Au collisions 3 iterations were implemented for the Bayesian method.

### 7.1.2 Unfolded spectra

Statistical uncertainty on the unfolded spectrum was calculated by propagating the full covariance matrix through the unfolding. This error treatment was selected with the ‘RooUnfold::kCovariance’ option in the RooUnfold package. Also, the unfolded spectra were corrected for the reconstruction efficiency during the unfolding procedure. Hence, hereafter, the ‘unfolded’ spectrum will imply the ‘unfolded and reconstruction efficiency corrected’ spectrum.

Figure 7.4 and Figure 7.5 show the “fake” jet subtracted, the SVD method unfolded and the Bayesian method unfolded per-event jet yield for the  $p+p$  and different centralities of the Cu+Au collisions, respectively. Due to the residual presence of the fake jets even after the fake jet subtraction<sup>ii</sup>, there is a significant disagreement between the two methods for  $p_T < 15 \text{ GeV}/c$  in the Cu+Au 0–20% centrality selection. The systematic uncertainty due to the difference in the unfolding methods will be discussed and assigned in Section 7.4.

Truth-level bins near the reco-level bin edges where a good control of the unfolded spectrum cannot be achieved will not be included in the final results. The  $p_T$  range included in the final results will be denoted by the black vertical lines hereafter.

## 7.2 Trigger efficiencies, $\langle N_{\text{Coll}} \rangle$ , and $\langle T_{\text{AB}} \rangle$

### 7.2.1 BBC trigger efficiency

The BBC trigger cross-section derived through the Run-5 and the Run-6 vernier scan analysis is

$$\sigma_{\text{BBC}} = 23.0 \text{ mb} \pm 9.7\%[122],$$

---

<sup>ii</sup>The fake jet subtraction method underestimates for the central collisions; see Section 6.6

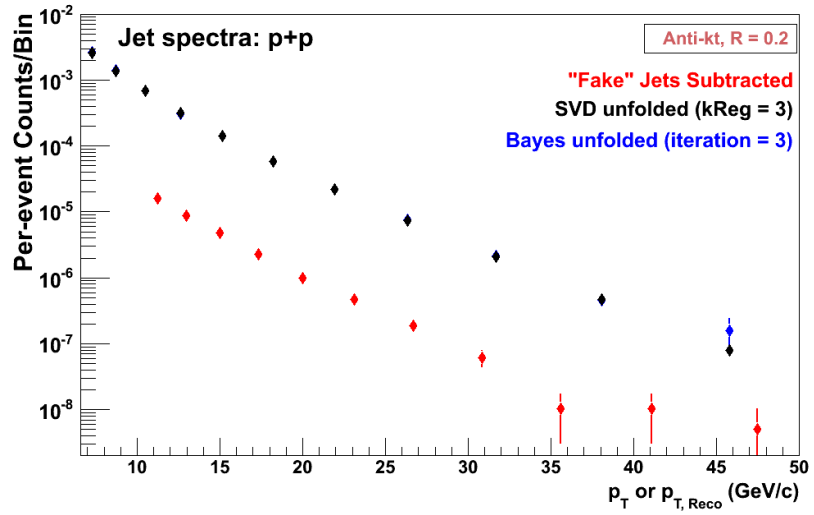


Figure 7.4: "Fake" jet subtracted, the SVD method unfolded and the Bayesian method unfolded per-event jet yield for the  $p+p$  collisions.

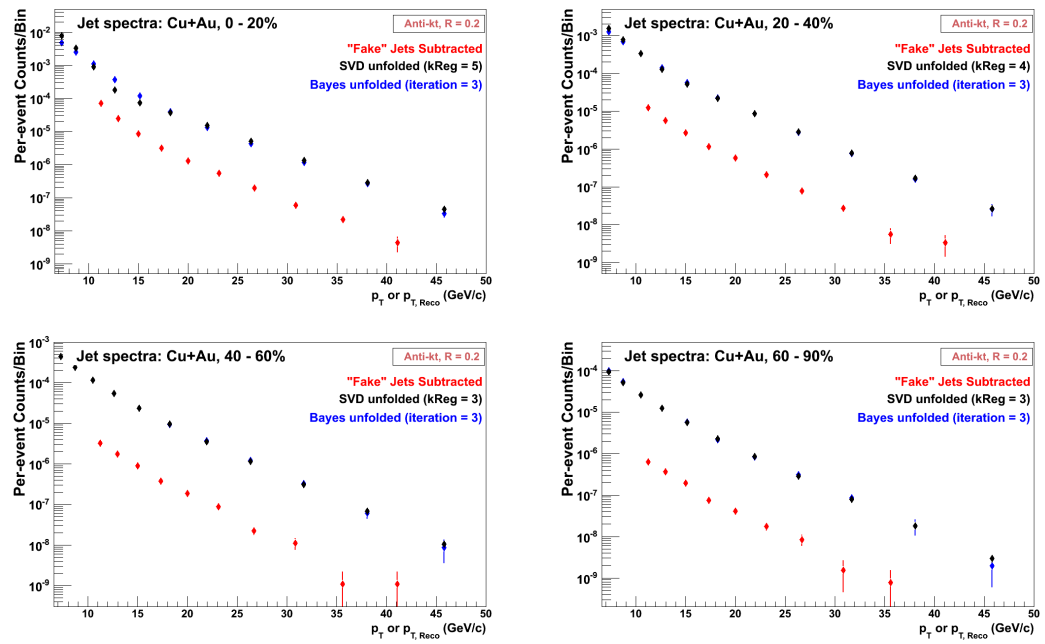


Figure 7.5: "Fake" jet subtracted, the SVD method unfolded and the Bayesian method unfolded per-event jet yield for the different centrality selections of the Cu+Au collisions.

and the world estimate for the  $p+p$  inelastic cross-section is

$$\sigma_{pp} = 42.2 \pm 1.9 \text{ mb}[123].$$

Thus, the BBC trigger efficiency ( $\epsilon_{BBC}^{MB}$ ) is 58%, which means that the BBC trigger normally fires on  $\sim 58\%$  of the  $p+p$  inelastic cross-section.

As jets are produced through the hard scattering processes, an event with a jet tends to have higher multiplicity, and the BBCs become susceptible to firing with an efficiency higher than the nominal. The BBC trigger efficiency for the hard scattering processes has been calculated from the yield of the high- $p_T$   $\pi^0$ 's with and without the BBC trigger in ERT events. It is determined to be

$$\epsilon_{BBC}^{\text{Hard}} = 79\% \pm 2\%[124].$$

### 7.2.2 ERT trigger efficiency

As mentioned in Section 3.2.4.2, the ERT triggers on the sum of the analog signals of the EMCAL towers, called the trigger tiles. The electronics is setup such that it allows to set three independent thresholds; 4x4a, 4x4b and 4x4c. For this analysis, the ERT 4x4c in coincidence with the BBCLL1 trigger, referred to as ERT\_4x4c&BBCLL1(narrow) trigger, is used for the  $p+p$  dataset. Threshold for the ERT\_4x4c for the Run-12 200 GeV  $p+p$  collisions was 1.4 GeV.

The ERT trigger efficiency is determined from the Minimum Bias dataset. Reconstructed jets are required to pass all the jet-level cuts as in the ERT triggered dataset. Then the ERT trigger efficiency is determined as

$$\text{Efficiency} = \frac{\text{no. of ERT triggered jets}}{\text{no. of inclusive jets}},$$

where the ERT triggered jet is a jet that includes at least one cluster as a constituent which lies in a Super Module with the ERT bit.

Figure 7.6 shows the ERT 4x4c trigger efficiency for the  $p+p$  collisions. The errors on the efficiency are the standard binomial errors. The distribution is fitted with the error function

$$erf(p_{T, \text{Reco}}) = a_0 + erf(a_1 + (a_2 \times p_{T, \text{Reco}})). \quad (7.9)$$

The error function plateaus at 91.2%.

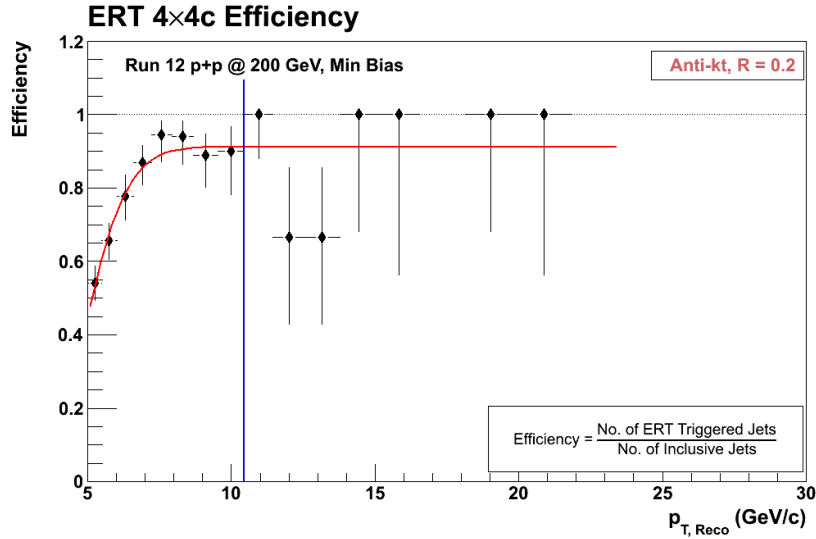


Figure 7.6: ERT 4x4c efficiency.

As the distribution quickly runs out of statistics to get a proper saturation at high- $p_T$  and as for this analysis only the  $p_{T, \text{Reco}} > 10.5 \text{ GeV}/c$  part of the spectrum is of interest, the efficiency and the error associated with it at high- $p_T$  is estimated by combining all the bins above  $p_{T, \text{Reco}} > 10.5 \text{ GeV}/c$ . The efficiency is calculated to be

$$\epsilon_{\text{ERT}} = 89\% \pm 7\%. \quad (7.10)$$

Hence, the ERT efficiency  $\epsilon_{\text{ERT}} = 0.89$  will be used for the  $p+p$  spectrum and a conservative systematic uncertainty of  $\pm 7\%$  will be assigned on the efficiency.

### 7.2.3 $\langle N_{\text{Coll}} \rangle$ and $\langle T_{\text{AB}} \rangle$ for Cu+Au

The mean values of the number of binary nucleon-nucleon collisions  $\langle N_{\text{Coll}} \rangle$  and of the nuclear thickness function  $\langle T_{\text{AB}} \rangle$  for the Cu+Au collisions are obtained from the PHENIX analysis note 1078 [104] and are summarized in Table 7.2. For the 60–90% centrality selection, both the  $\langle N_{\text{Coll}} \rangle$  and  $\langle T_{\text{AB}} \rangle$  are computed as an average of the 1% wide centrality bins from 60% to 90%.

Table 7.2:  $\langle N_{\text{Coll}} \rangle$  and  $\langle T_{\text{AB}} \rangle$  for the Cu+Au collisions.

Centrality	$\langle N_{\text{Coll}} \rangle$	$\langle T_{\text{AB}} \rangle$
0–20%	$313.8 \pm 28.39$	$7.471 \pm 0.4721$
20–40%	$129.3 \pm 12.36$	$3.079 \pm 0.2298$
40–60%	$41.84 \pm 5.313$	$0.9961 \pm 0.1195$
60–90%	$7.9405 \pm 0.3612$	$0.1886 \pm 0.0086$

### 7.3 Constructing the per-event jet yield

#### 7.3.1 Run scalers

There are three main types of PHENIX run scalers: the raw, the live, and the scaled. The raw scaler counts the number of times a trigger fire, the liver scaler counts the number of times a trigger fire when the DAQ is not busy, and the scaled trigger counts the number of times a trigger fire when the DAQ is not busy and after the pre-scale is applied. If the scaledown is  $s$ , the scaled trigger rate = (live trigger rate)/(1+s); hence, 1 out of every (1+s) live trigger is sent to the GTMs.

#### 7.3.2 Per-event jet yield for a triggered dataset

In this section, the construction of per-event jet yield for a non-specific triggered dataset is discussed. Later, the same procedure is followed to construct the yield for the Minimum Bias and ERT triggered datasets.

If  $N_{\text{run}}^{\text{jet, trig}}$  is the total number of jets reconstructed in a run for triggered events, then

$$N_{\text{run}}^{\text{jet, trig}} \times (1 + s_{\text{trig}})$$

is the pre-scale corrected effective number of reconstructed jets in the run (where  $s_{\text{trig}}$  is the scaledown for a specific trigger). If  $N_{\text{run}}^{\text{ana, MB}}$  is the total number of MB events that pass the offline vertex cut, then

$$N_{\text{run}}^{\text{ana, MB}} \times (1 + s_{\text{MB}})$$

is the total number of events sampled by the DAQ for the Minimum Bias trigger (where  $s_{MB}$  is the scaledown for the Minimum Bias trigger).

Hence, for a triggered dataset, the per-event jet yield for a run is

$$\begin{aligned} \frac{1}{N_{\text{evts}}} \frac{dN}{dp_T} &= \frac{1}{N_{\text{run}}^{\text{ana, MB}}} \times \frac{1}{(1+s_{MB})} \times \frac{dN_{\text{run}}^{\text{jet, trig}}}{dp_T} \times (1+s_{\text{trig}}) \\ &= \frac{1}{N_{\text{run}}^{\text{ana, MB}} \times \frac{(1+s_{MB})}{(1+s_{\text{trig}})}} \times \frac{dN_{\text{run}}^{\text{jet, trig}}}{dp_T}. \end{aligned} \quad (7.11)$$

These can be combined from all the good runs to get the total per-event jet yield as

$$\frac{1}{N_{\text{evts}}} \frac{dN}{dp_T} = \frac{1}{\sum_{\text{run}} N_{\text{run}}^{\text{ana, MB}} \times \frac{(1+s_{MB})}{(1+s_{\text{trig}})}} \times \sum_{\text{run}} \frac{dN_{\text{run}}^{\text{jet, trig}}}{dp_T}. \quad (7.12)$$

### 7.3.3 Per-event jet yield for the Minimum Bias dataset

As  $s_{\text{trig}} = s_{MB}$  for the Minimum Bias dataset, Equation 7.12 becomes

$$\frac{1}{N_{\text{evts}}} \frac{dN}{dp_T} = \frac{1}{\sum_{\text{run}} N_{\text{run}}^{\text{ana, MB}}} \times \sum_{\text{run}} \frac{dN_{\text{run}}^{\text{jet, MB}}}{dp_T}, \quad (7.13)$$

where  $\sum_{\text{run}} N_{\text{run}}^{\text{ana, MB}}$  is the total number of Minimum Bias events analyzed (that pass the offline vertex cut) and  $\sum_{\text{run}} \frac{dN_{\text{run}}^{\text{jet, MB}}}{dp_T}$  is the total number of jets reconstructed in those events within the given  $p_T$  bin. For different centrality selections, the jet yield ( $N_{\text{run}}^{\text{jet, MB}}$ ) and the  $N_{\text{run}}^{\text{ana, MB}}$  are restricted to events within the given centrality.

### 7.3.4 Per-event jet yield for the ERT dataset

For the ERT dataset, equation 7.12 becomes

$$\frac{1}{N_{\text{evts}}} \frac{dN}{dp_T} = \frac{1}{\sum_{\text{run}} N_{\text{run}}^{\text{ana, MB}} \times \frac{(1+s_{MB})}{(1+s_{\text{ERT}})}} \times \sum_{\text{run}} \frac{dN_{\text{run}}^{\text{jet, ERT}}}{dp_T}. \quad (7.14)$$

This yield is further corrected for  $\epsilon_{\text{BBC}}^{\text{Hard}}$  and  $\epsilon_{\text{ERT}}$  as

$$\frac{1}{N_{\text{evts}}} \frac{dN}{dp_T} = \frac{1}{\epsilon_{\text{ERT}}} \times \frac{1}{\epsilon_{\text{BBC}}^{\text{Hard}}} \times \frac{1}{\sum_{\text{run}} N_{\text{run}}^{\text{ana, MB}} \times \frac{(1+s_{MB})}{(1+s_{\text{ERT}})}} \times \sum_{\text{run}} \frac{dN_{\text{run}}^{\text{jet, ERT}}}{dp_T}, \quad (7.15)$$

where  $\sum_{\text{run}} N_{\text{run}}^{\text{ana, MB}} \times \frac{(1+s_{MB})}{(1+s_{\text{ERT}})}$  is obtained from the Minimum Bias datastream.

## 7.4 Evaluation of the systematic uncertainty

### 7.4.1 Unfolding procedure

#### 7.4.1.1 Shape of the input spectrum

Compared to other methods (for e.g., bin-by-bin unfolding), the results of the SVD method are less sensitive to the choice of the input spectrum. By default, the input spectrum for the unfolding procedure is the PYTHIA truth spectrum. To test the sensitivity of the results to the shape of the input spectrum, the power of the truth spectrum is varied by  $\pm 0.5$ . The default data is then unfolded with this variation in the procedure. Figure 7.7 and Figure 7.8 show the effect for the  $p+p$  spectrum and the different centrality selected Cu+Au spectrum, respectively. The upper panel shows the jet spectrum in consideration and the lower panel shows the ratio of the variation to the default spectrum. The effect is few percentage at low- $p_T$  and up to 12% at high- $p_T$ .

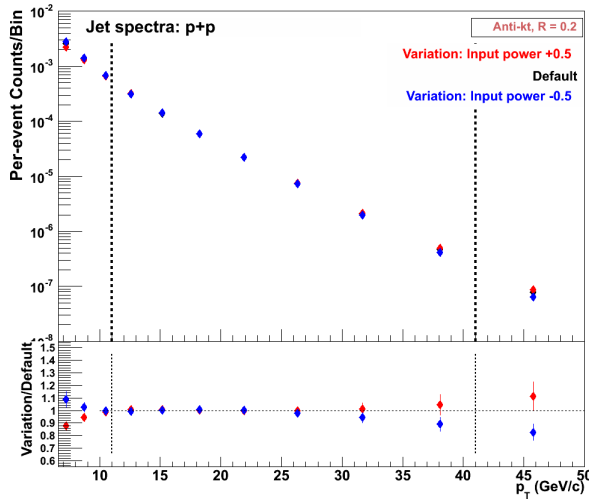


Figure 7.7: Effect for the  $p+p$  spectrum due to the variation in the shape of the input spectrum.

Figure 7.9 shows the effect for the ratios of the spectra. The variations cancel for some ratios but not for all. Overall, the effect is less than 12%. The symmetric systematic uncertainty is set by taking the bracketed values of the positive and negative results and dividing by two.

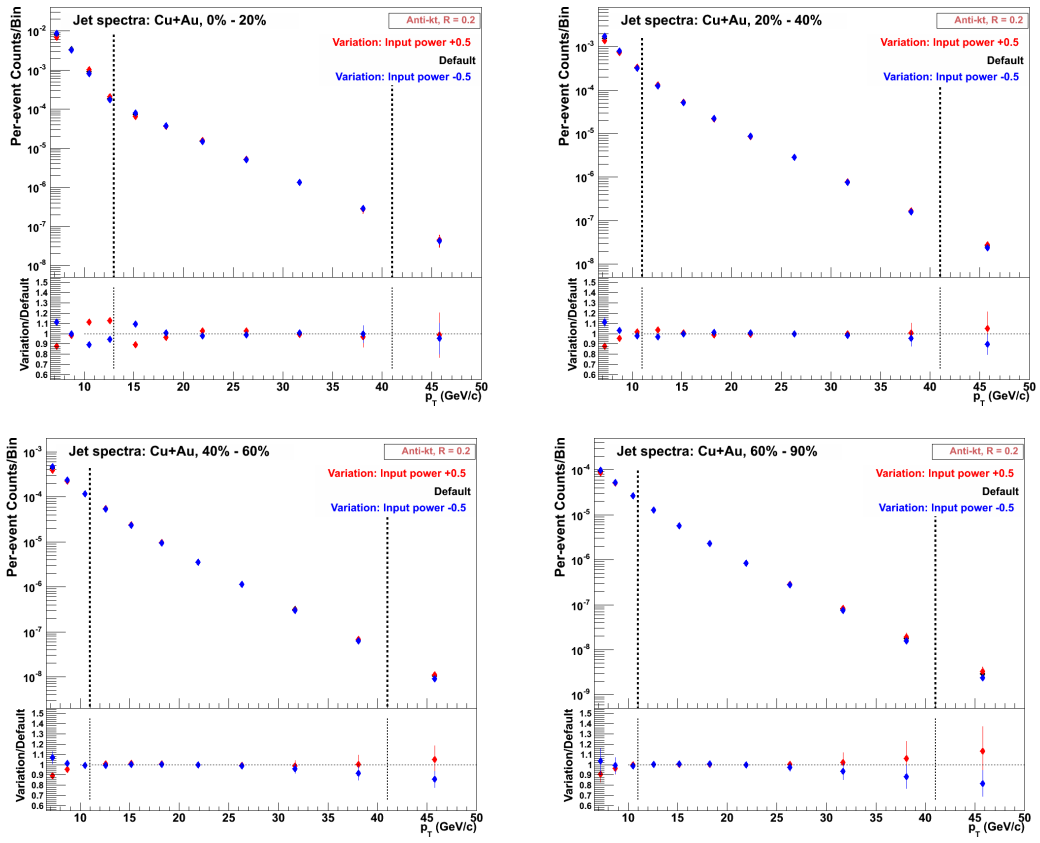


Figure 7.8: Effect for the different centrality selected Cu+Au spectrum due to the variation in the shape of the input spectrum.

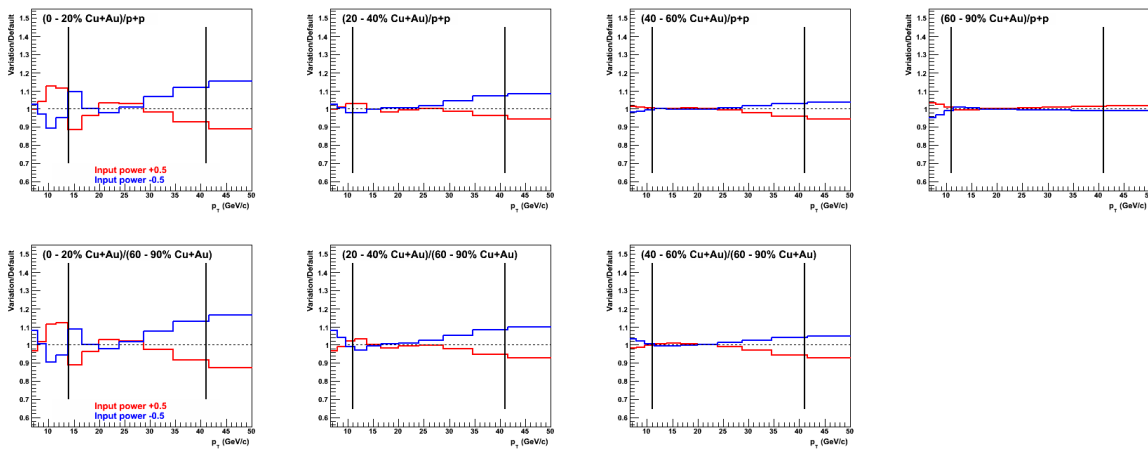


Figure 7.9: Double ratio for the variation in the shape of the input spectrum.

#### 7.4.1.2 Unfolding method

Checking the sensitivity of the results to the choice of unfolding method is very important.

Like mentioned earlier in Section 7.1.1, the SVD method is the default method and the Bayesian method is used as the variation. Figure 7.10 and Figure 7.11 show the effect for the  $p+p$  spectrum and the different centrality selected Cu+Au spectrum, respectively. Although the effect is moderate (less than 10%) for the  $p+p$  and Cu+Au 20–40%, 40–60%, and 60–90% spectra, the effect is up to 60% at  $p_T$  range 13.8–16.6 GeV/c for the 0–20% spectrum (the marker point is out of default bound in the variation/default panel).

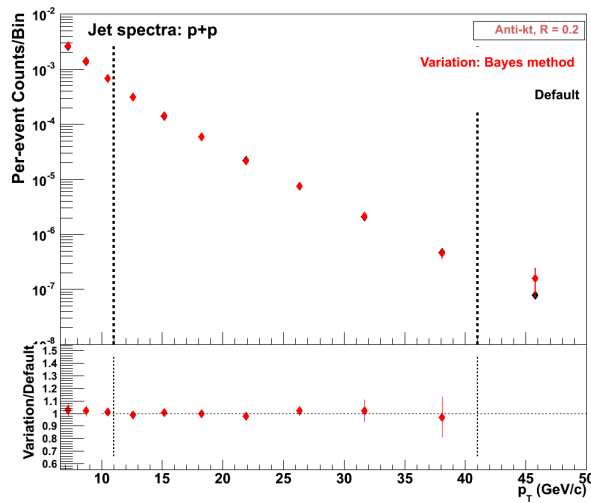


Figure 7.10: Effect for the  $p+p$  spectrum due to the variation in the unfolding method.

Figure 7.12 shows the effect for the ratios of the spectra. The variations cancel for some ratios but not for all. Overall, the effect is less than 20%, except for the ratios with the 0–20% centrality spectrum. The symmetric systematic uncertainty is set by taking the absolute value of the variation.

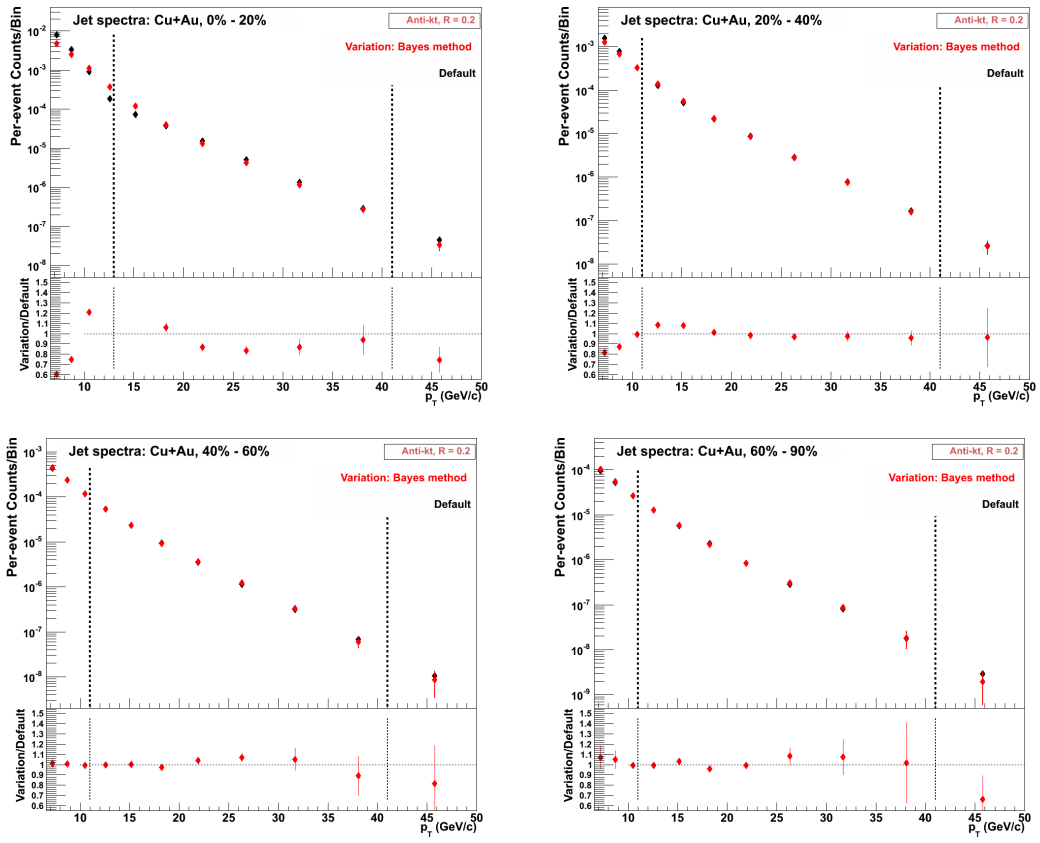


Figure 7.11: Effect for the different centrality selected Cu+Au spectrum due to the variation in the unfolding method

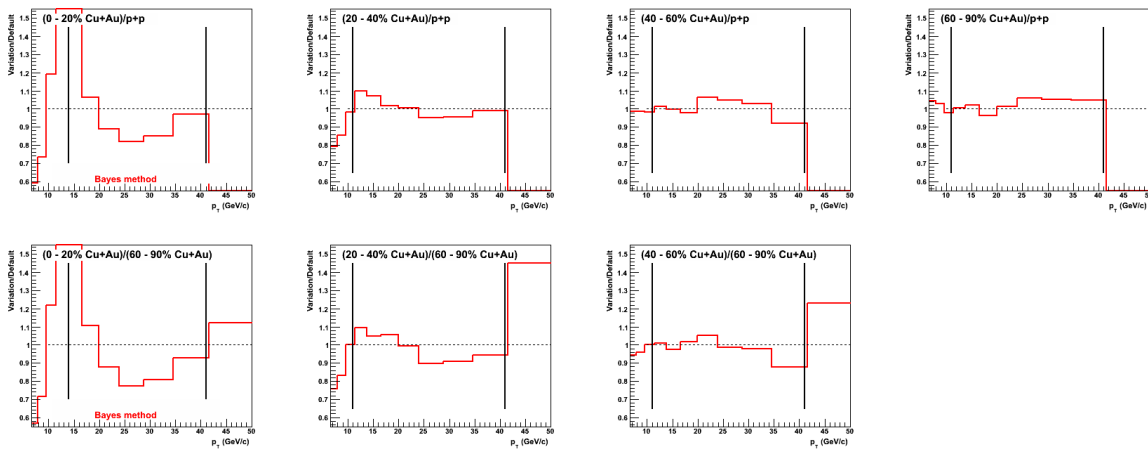


Figure 7.12: Double ratio for the variation in the unfolding method.

## 7.4.2 Energy scale

### 7.4.2.1 DC $p_T$ scale

The uncertainty in the DC  $p_T$  scale is estimated by varying the  $p_T$  of tracks in  $p_T$  dependent way in the simulation: 2% for  $p_T < 10 \text{ GeV}/c$  and increased linearly such that it is 4% at  $30 \text{ GeV}/c$ . The default data is then unfolded with the modified response matrix. Figure 7.13 and Figure 7.14 show the effect for the  $p+p$  spectrum and the different centrality selected Cu+Au spectrum, respectively. Overall, the effect is 4–13%.

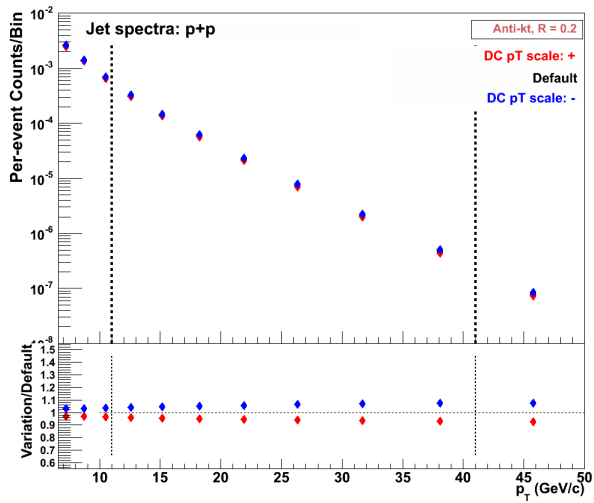


Figure 7.13: Effect for the  $p+p$  spectrum due to the variation in the DC  $p_T$  scale.

Figure 7.15 shows the effect for the ratios of the spectra. The variations cancel almost completely for the most ratios. The symmetric systematic uncertainty is set by taking the bracketed values of the positive and negative results and dividing by two.

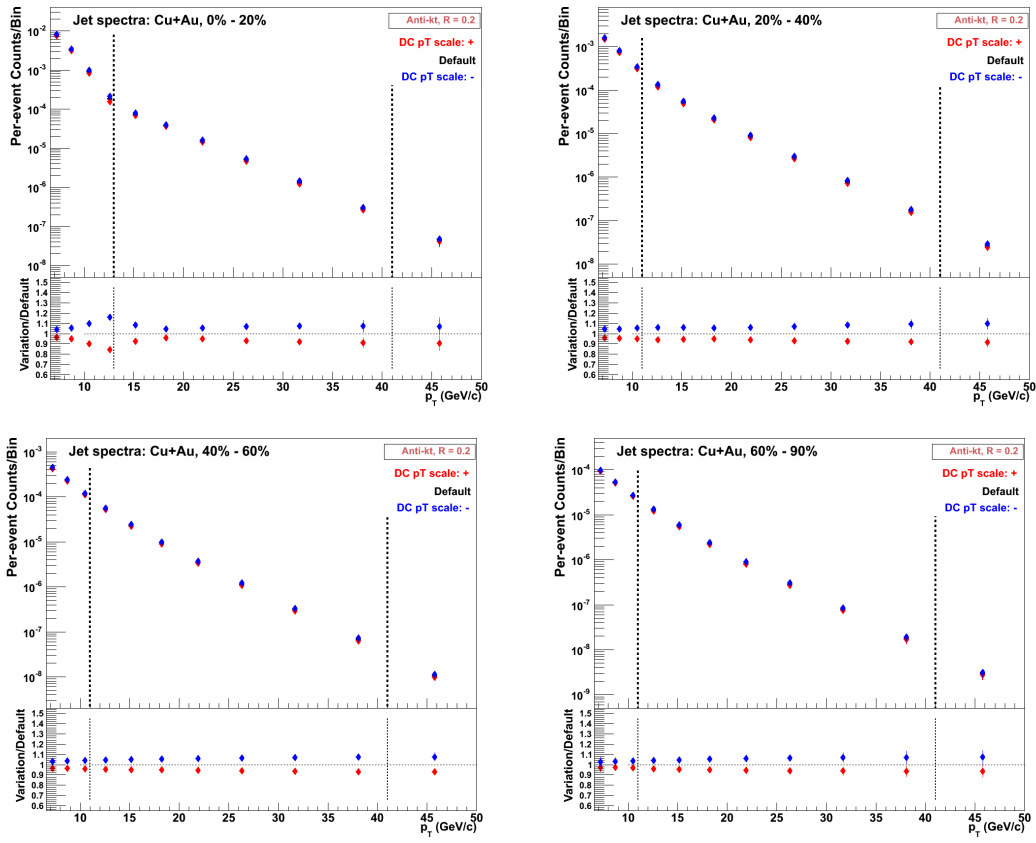


Figure 7.14: Effect for the different centrality selected Cu+Au spectrum due to the variation in the DC  $p_T$  scale.

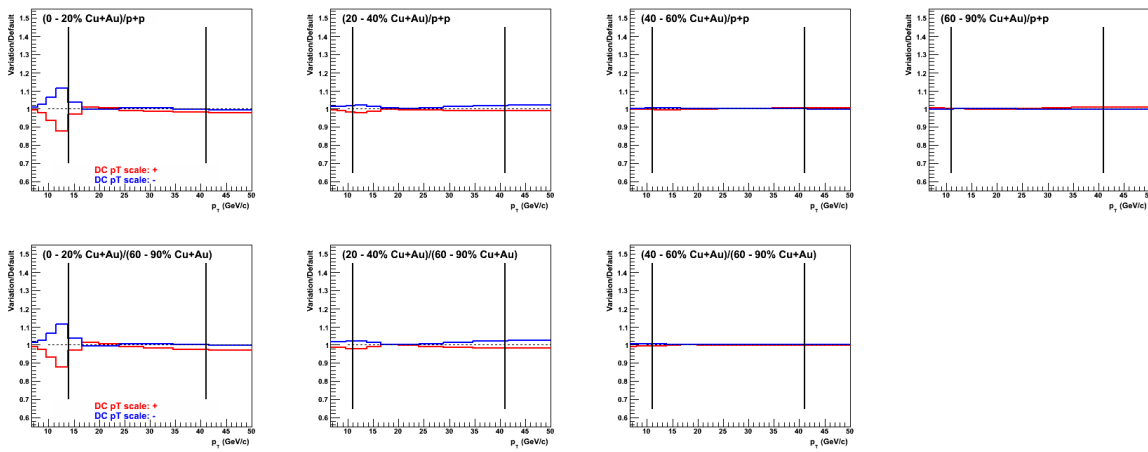


Figure 7.15: Double ratio for the variation in the DC  $p_T$  scale.

#### 7.4.2.2 EMCAL energy scale

The uncertainty in the EMCAL response is estimated by varying the energy of the clusters by  $\pm 3\%$ . The default data is then unfolded with the modified response matrix. Figure 7.16 and Figure 7.17 show the effect for the  $p+p$  spectrum and the different centrality selected Cu+Au spectrum, respectively. Overall, the effect is 9–25%.

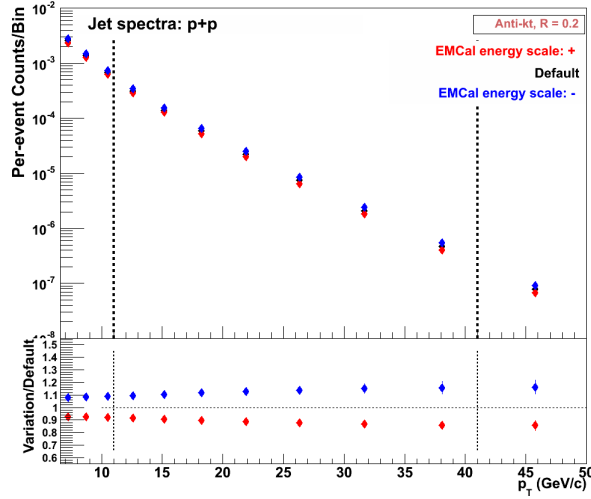


Figure 7.16: Effect for the  $p+p$  spectrum due to the variation in the EMCAL energy scale.

Figure 7.18 shows the effect for the ratios of the spectra. The variations cancel almost completely for the most ratios. The symmetric systematic uncertainty is set by taking the bracketed values of the positive and negative results and dividing by two.

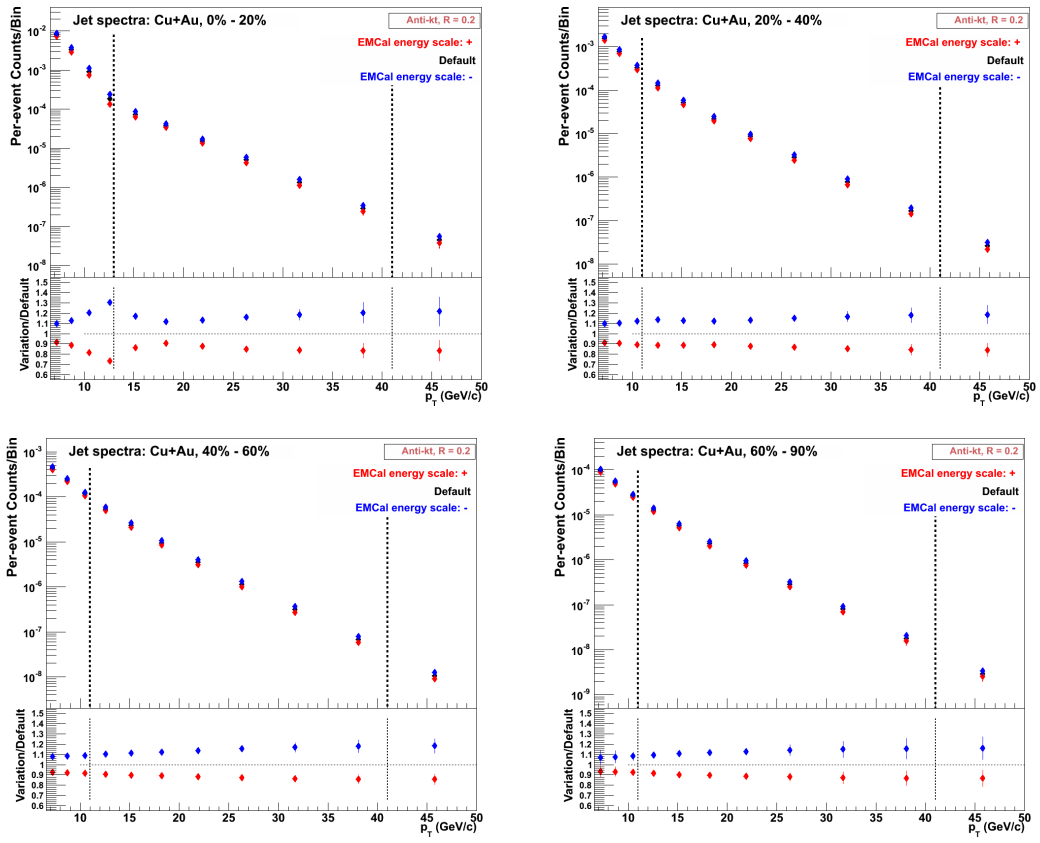


Figure 7.17: Effect for the different centrality selected Cu+Au spectrum due to the variation in the EMCAL energy scale.

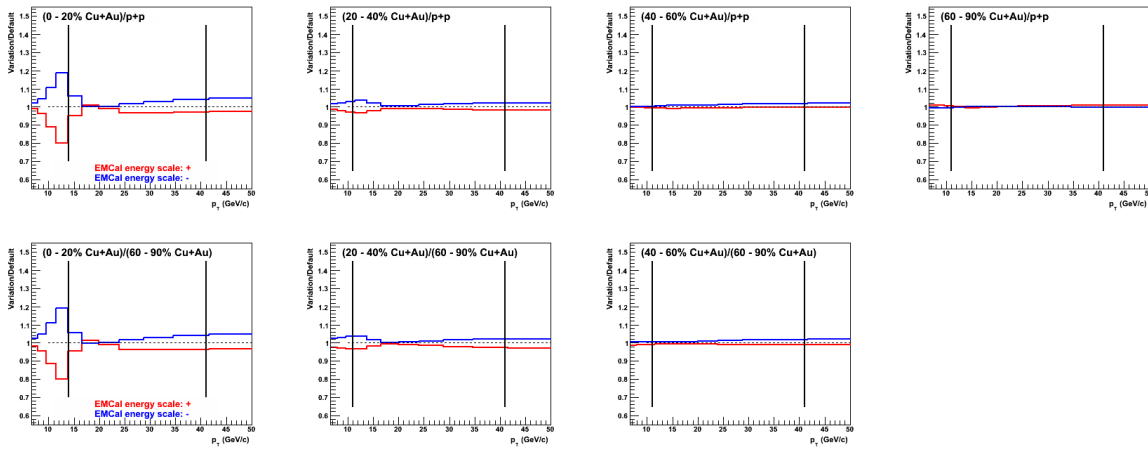


Figure 7.18: Double ratio for the variation in the EMCAL energy scale.

### 7.4.3 Jet-level cuts

#### 7.4.3.1 Number of constituents

The data and the MC simulation are re-run with the  $n.c. \geq 5$  jet-level selection (the default selection is  $n.c. \geq 3$ ). The modified data is then unfolded with the modified response matrix. Figure 7.19 and Figure 7.20 show the effect for the  $p+p$  spectrum and the different centrality selected Cu+Au spectrum, respectively.

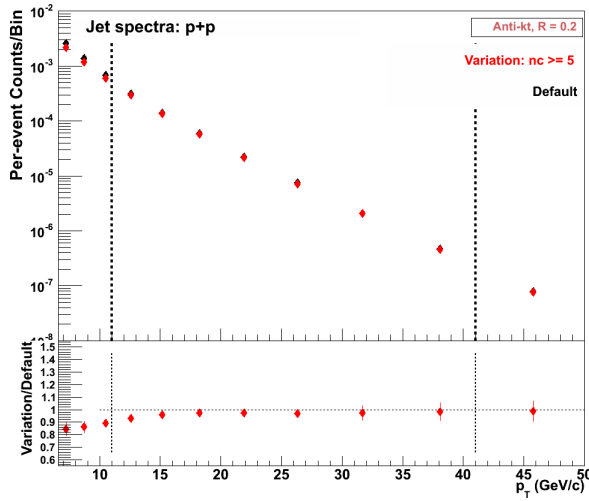


Figure 7.19: Effect for the  $p+p$  spectrum due to the variation in the  $n.c.$  selection.

#### 7.4.3.2 Charged fraction

The data and the MC simulation are re-run with the  $c.f. > 0.2$  and  $c.f. < 0.6$  selection (the default selection is  $c.f. > 0.2$  and  $c.f. < 0.7$ ). The modified data is then unfolded with the modified response matrix. Figure 7.21 and Figure 7.22 show the effect for the  $p+p$  spectrum and the different centrality selected Cu+Au spectrum, respectively.

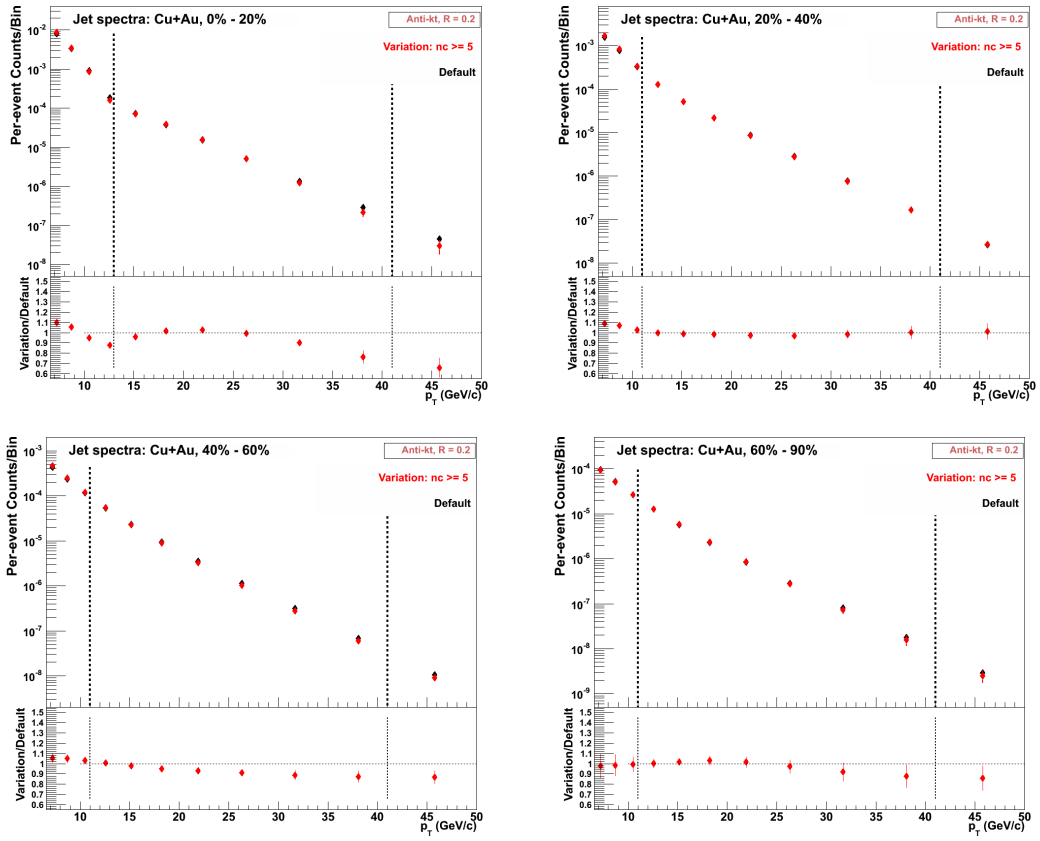


Figure 7.20: Effect for the different centrality selected Cu+Au spectrum due to the variation in the  $n.c.$  selection.

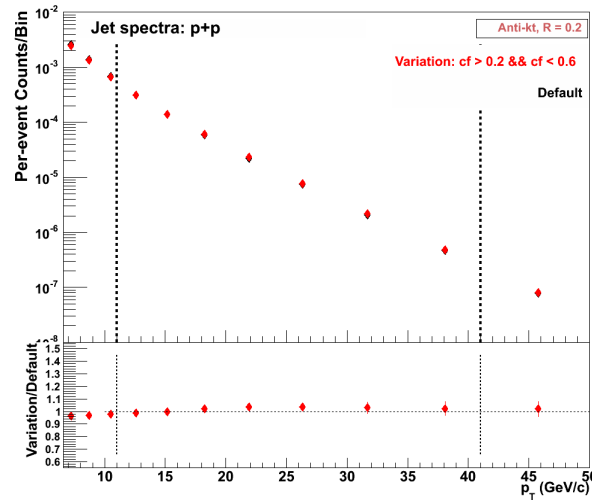


Figure 7.21: Effect for the  $p+p$  spectrum due to the variation in the  $c.f.$  selection.

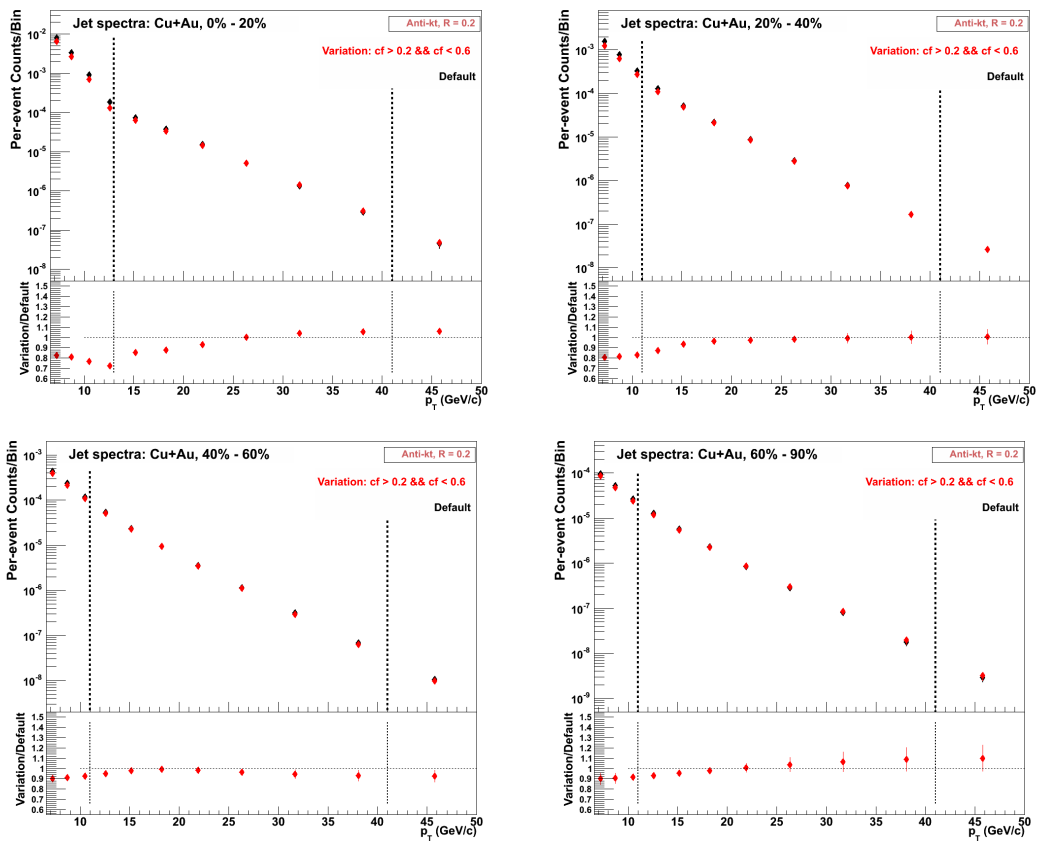


Figure 7.22: Effect for the different centrality selected Cu+Au spectrum due to the variation in the *c.f.* selection.

### 7.4.3.3 *n.c.* and *c.f.* combined

As considering multiple variations in the jet-level cuts separately is likely to include correlated effects, the data and MC simulation are re-run with the  $n.c. \geq 5$  and  $c.f. > 0.2$  and  $c.f. < 0.6$  selection. The modified data is then unfolded with the modified response matrix. Figure 7.23 and Figure 7.24 show the effect for the  $p+p$  spectrum and the different centrality selected Cu+Au spectrum, respectively. The black line show the relative uncertainty when *n.c.* and *c.f.* variations are added in quadrature. For the final result, this combined jet-level variation will be used for the total systematic uncertainty (not *c.f.* and *c.f.* variations added in quadrature).

The effect is 3–6% for the  $p+p$  spectrum, up to 17% for the Cu+Au 0–20% spectrum, up to 11% for the 20–40% and 60–90% spectra. For the Cu+Au 40–60% spectrum, the effect increases towards high- $p_T$  and reaches up to 25%. As this effect is not solely due to the variation in the jet-level cut but also due to the sensitive behavior of the unfolding towards the choice of regularization, for the 40–60% spectrum, variation/default ratio is taken as an average of the 20–40% and 60–90% spectra.

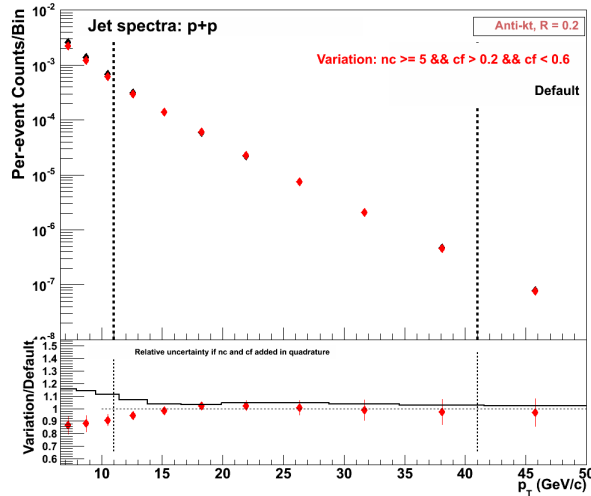


Figure 7.23: Effect for the  $p+p$  spectrum due to the variation in *n.c.* and *c.f.* combined selection.

Figure 7.25 shows the effect for the ratios of the spectra. Overall, the effect is up to 16%. The symmetric systematic uncertainty is set by taking the absolute value of the variation.

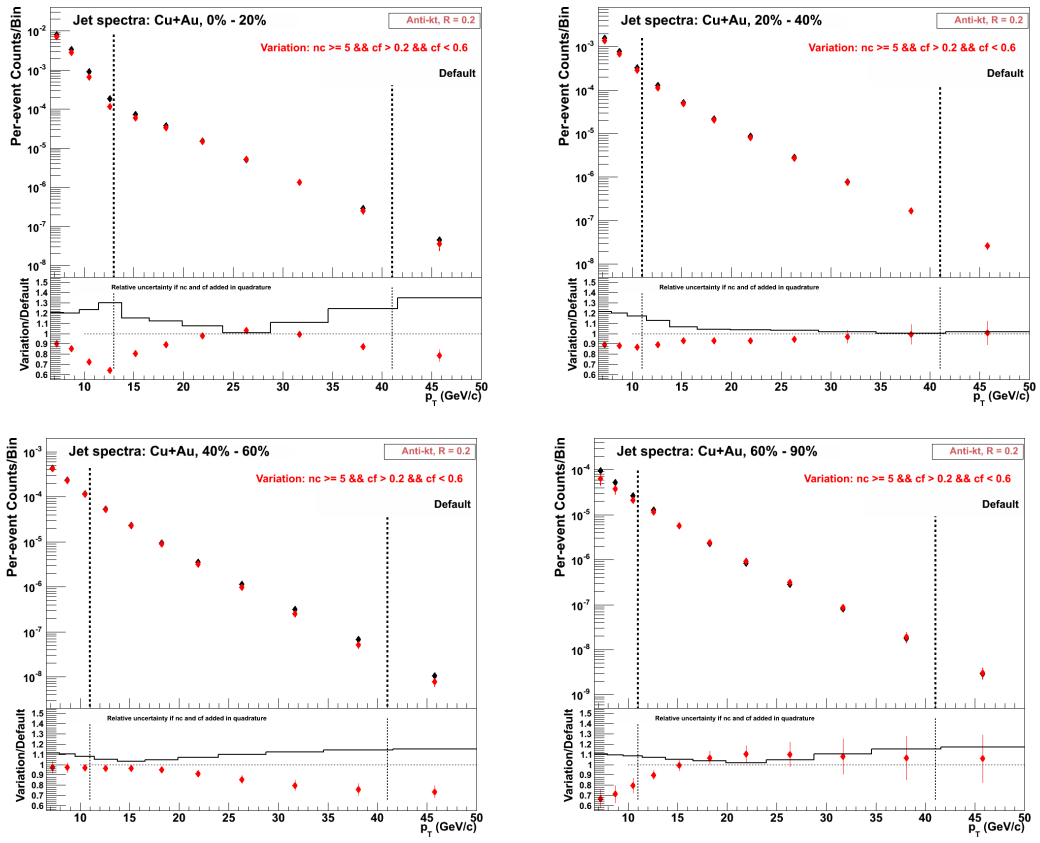


Figure 7.24: Effect for the different centrality selected Cu+Au spectrum due to the variation in the *n.c.* and *c.f.* combined selection.

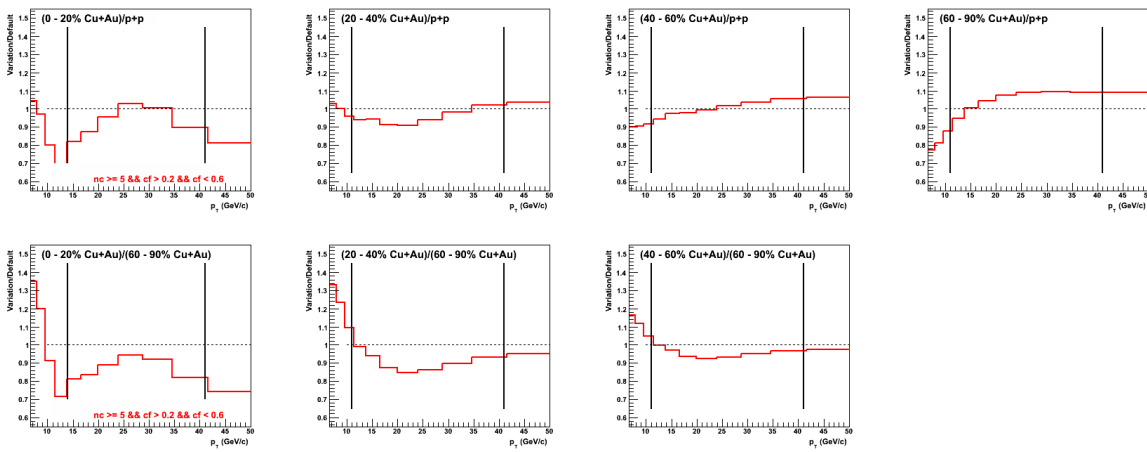


Figure 7.25: Double ratio for the variation in the *n.c.* and *c.f.* combined selection.

#### 7.4.4 Acceptance

##### 7.4.4.1 Tight fiducial cut

The data and the MC simulation are re-run by requiring the reconstructed jets to lie within a tighter phase space. The modified data is then unfolded with the modified response matrix. Figure 7.26 and Figure 7.27 show the effect for the  $p+p$  spectrum and the different centrality selected Cu+Au spectrum, respectively. Overall, the effect is less than 10%, except for the  $p+p$  spectrum where it goes up to 15% at high- $p_T$ .

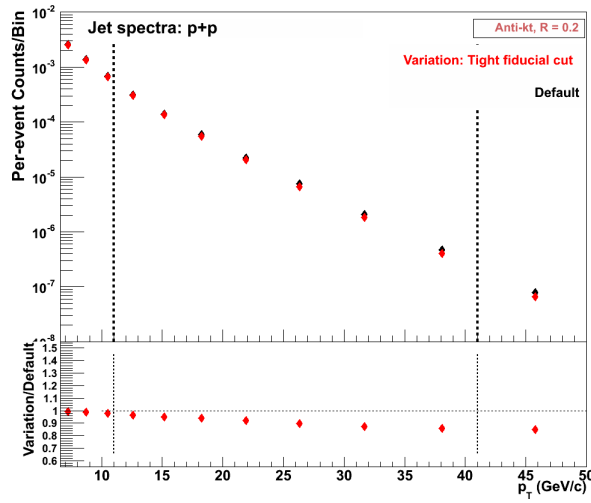


Figure 7.26: Effect for the  $p+p$  spectrum due to the variation in the fiducial requirement.

Figure 7.28 shows the effect for the ratios of the spectra. The effect reaches up to 25% at high- $p_T$  for some ratios. The symmetric systematic uncertainty is set by taking the absolute value of the variation.

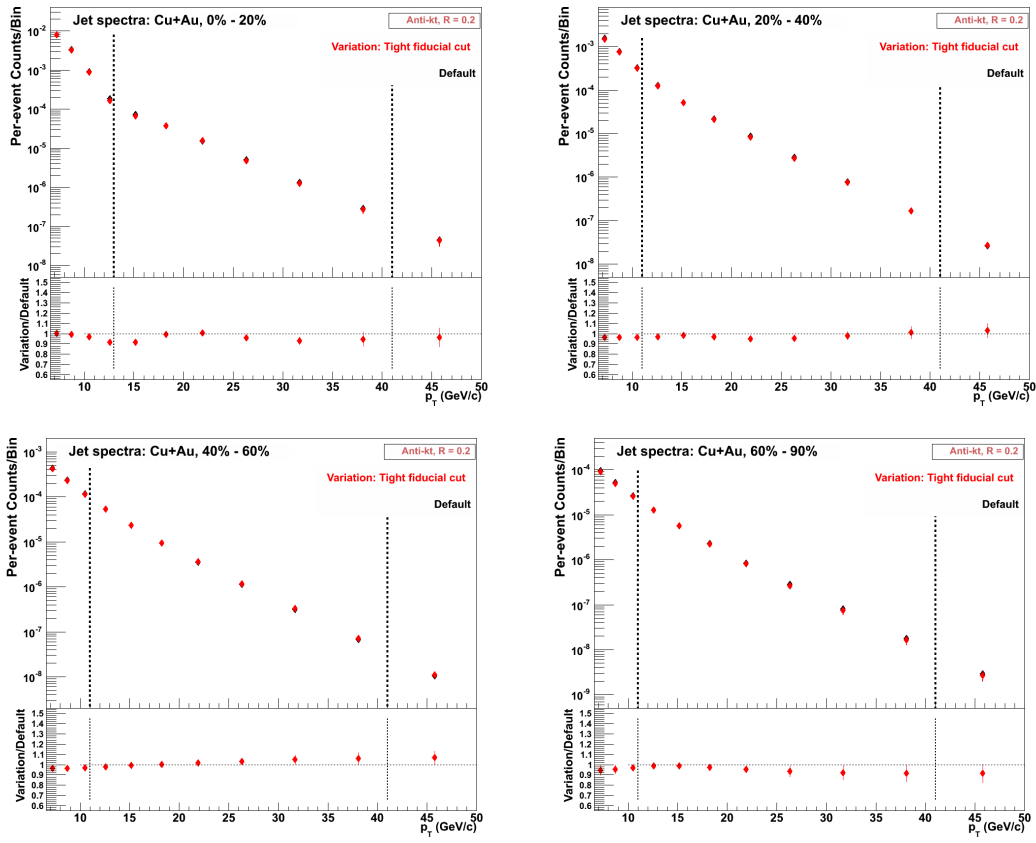


Figure 7.27: Effect for the different centrality selected Cu+Au spectrum due to the variation in the fiducial requirement.

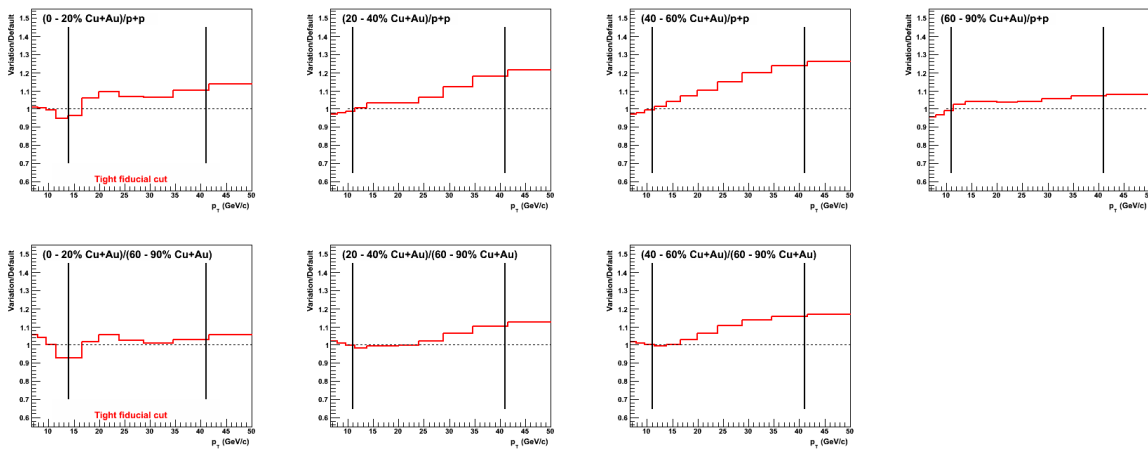


Figure 7.28: Double ratio for the variation in the fiducial requirement.

#### 7.4.4.2 Arm

The east arm yield is unfolded with the response matrix for the east arm and the west arm yield is unfolded with the response matrix for the west arm. Figure 7.29 and Figure 7.30 show the effect for the  $p+p$  spectrum and the different centrality selected Cu+Au spectrum, respectively. Overall, the effect is up to 20%, except for the Cu+Au 60–90% spectrum where it reaches up to 34%. As this effect is not solely due to the variations but also due to the sensitive behavior of the unfolding procedure towards the choice of the regularization parameter, for the 60–90% spectrum, the variation/default ratio is taken as an average of the 20–40% and 40–60% spectra.

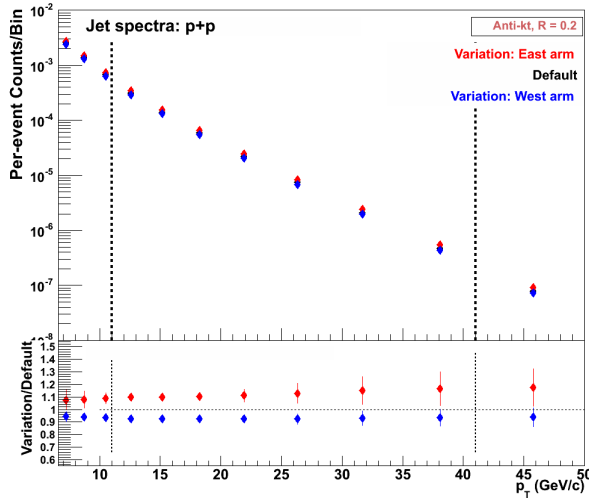


Figure 7.29: Effect for the  $p+p$  spectrum when the east and the west arm yield are unfolded separately.

Figure 7.31 shows the effect for the ratios of the spectra. The variations cancel for the some ratios but not for all. The effect reaches maximum of 23% at high- $p_T$ . The symmetric systematic uncertainty is set by taking the bracketed values of the positive and negative results and dividing by two.

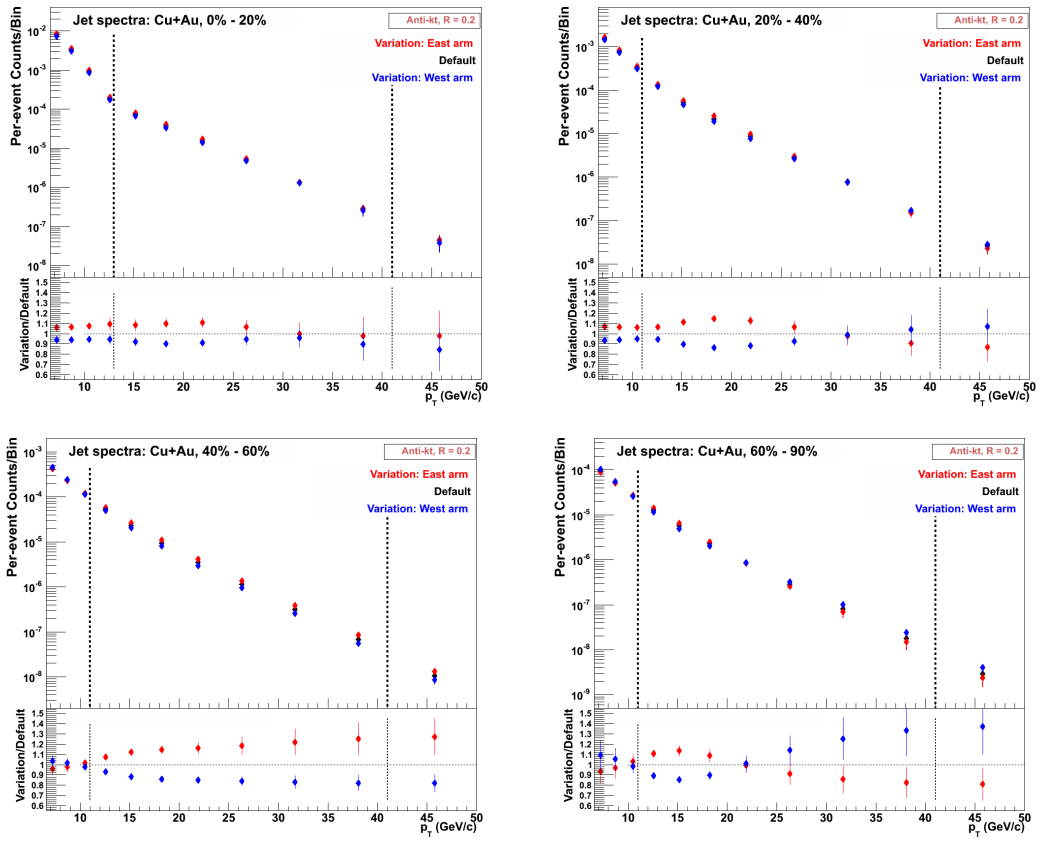


Figure 7.30: Effect for the different centrality selected Cu+Au spectrum when the east and the west arm yield are unfolded separately.

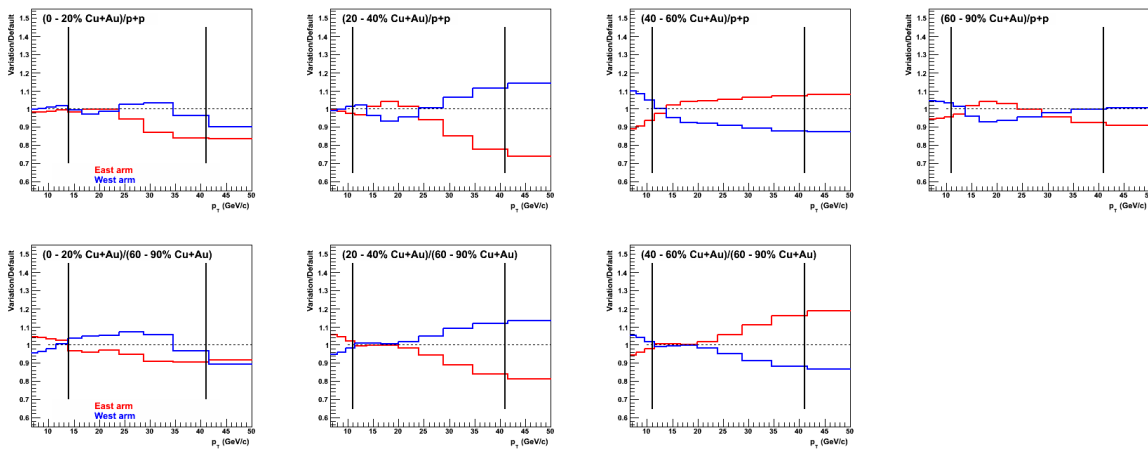


Figure 7.31: Double ratio for the east and the west arm yield unfolded separately.

### 7.4.5 Fake jet

The data and the MC simulation are re-run by requiring the cluster energy to be greater than 2.0 GeV and the track  $p_T$  to be greater than 2.0 GeV/c (the default requirement is cluster energy  $> 0.5$  GeV and track  $p_T > 0.5$  GeV/c). The modified data is then unfolded with the modified response matrix. No “fake” jet subtraction is performed in the data. Figure 7.32 and Figure 7.33 show the effect for the  $p+p$  spectrum and the different centrality selected Cu+Au spectrum, respectively. Overall, the effect is less than 12% except for the Cu+Au 60–90% spectrum where it reaches up to 26%.

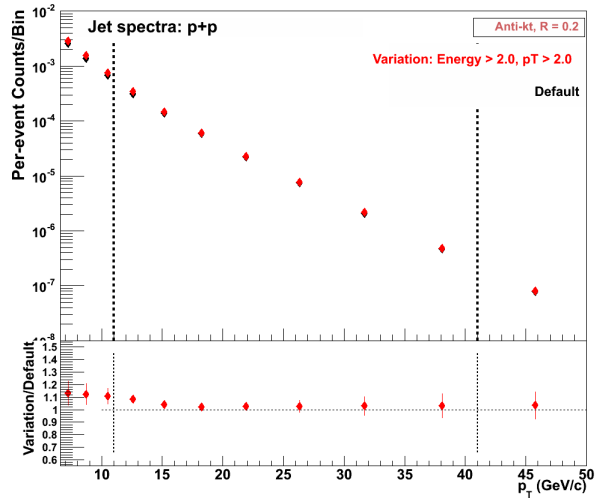


Figure 7.32: Effect for the  $p+p$  spectrum due to the variation in the minimum cluster energy and track  $p_T$  requirements.

Figure 7.34 shows the effect for the ratios of the spectra. The effect is up to 20% at high- $p_T$ . The symmetric systematic uncertainty is set by taking the absolute value of the variation.

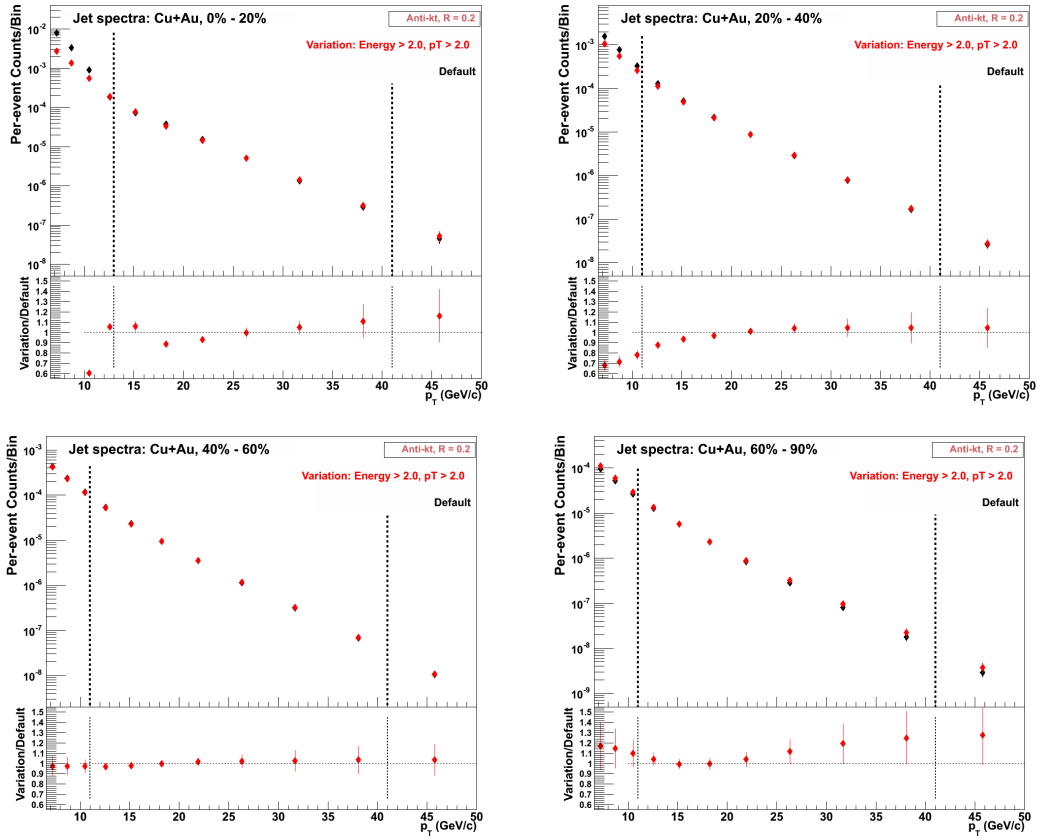


Figure 7.33: Effect for the different centrality selected Cu+Au spectrum due to the variation in the minimum cluster energy and track  $p_T$  requirements.

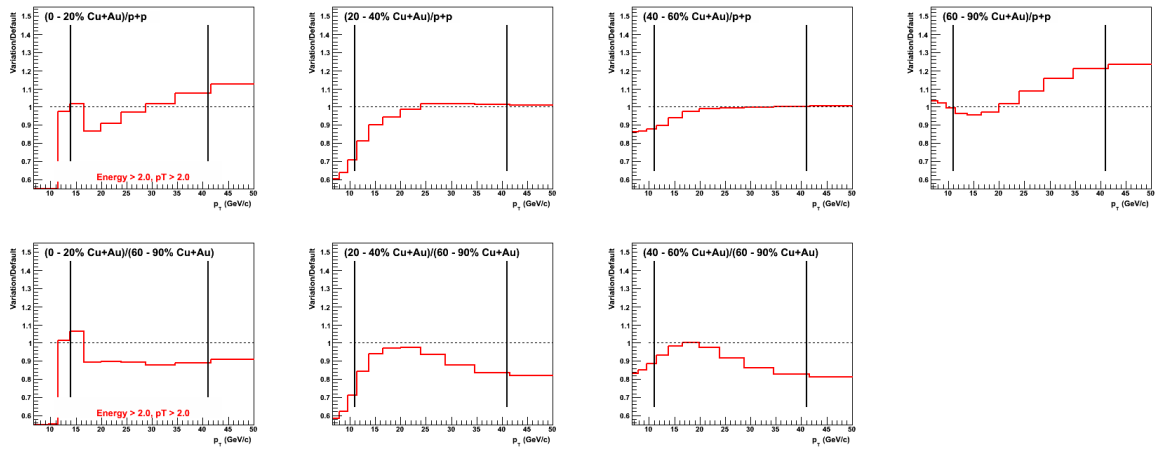


Figure 7.34: Double ratio for the variation in the minimum cluster energy and track  $p_T$  requirements.

## CHAPTER 8. FINAL RESULTS

### 8.1 $p+p$ cross-section

Figure 8.1 shows the per-event jet yields for the  $p+p$  and different centrality selections of the Cu+Au collisions with an arbitrary normalization. The vertical bars in the measurement indicate the statistical uncertainties and the shaded bands indicate the total systematic uncertainties. The  $p+p$  per-event jet yield is then converted into the  $p+p$  cross-section as

$$\frac{d\sigma}{dp_T} = \sigma_{pp} \times \frac{1}{N_{evts}} \frac{dN}{dp_T}, \quad (8.1)$$

where  $\sigma_{pp} = 23.0 \times 10^6$  nb is the Minimum Bias cross-section.

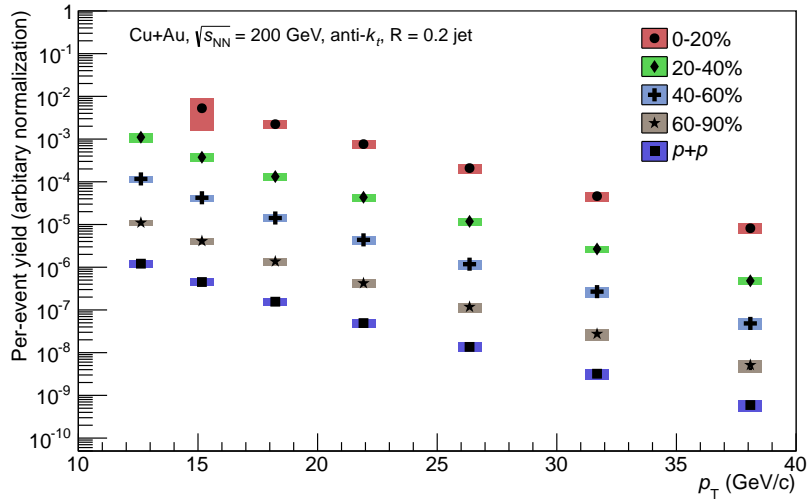


Figure 8.1: Measured anti- $k_t$ ,  $R=0.2$  jet yield in the  $p+p$  and Cu+Au collisions with an arbitrary normalization. The vertical bars in the measurement indicate the statistical uncertainties and the shaded bands indicate the total systematic uncertainties.

Perturbative theory calculation for the NLO jet cross-section and the hadronization corrections was performed by Gregory Soyez [125]. Events were generated using the NLOJet++

program [126, 127] with central value for the CTEQ6.6 [128], and the jets were reconstructed using FastJet. The total theoretical uncertainty was obtained by applying the 7-point rule; i.e., by taking the envelope of results obtained by varying the renormalization and factorization scale as

$$\left(\frac{\mu_R}{p_T}, \frac{\mu_F}{p_T}\right) = (1, 1), (1/2, 1), (2, 1), (1, 1/2), (1, 2), (1/2, 1/2) \text{ and } (2, 2).$$

Details of the hadronization correction can be found in [129], from which few key points are summarized below:

- The effect of the hadronization correction is to shift the  $p_T$  of the jet by an average amount.
- The uncertainty on the hadronization correction is estimated by varying Milan factor by 20%.
- Because of the  $1/R$  behavior of the correction, sizable correction is expected at small  $R$ .

Theory calculations are fitted with a fit function of the form

$$c_0 \times p_T^{-c_1 - (c_2 \times p_T^{c_3})},$$

by making sure that the variation in the fit is less than 2%. Figure 8.2 shows the measured jet cross-section compared to the NLO calculations. The vertical bars in the measurement indicate the statistical uncertainties and the shaded bands indicate the total systematic uncertainties, which includes the overall normalization uncertainties. The lines are the theoretical values and the bands are the theoretical scale uncertainty; the green color lines and bands are NLO calculations, and the red color lines and bands are NLO calculations corrected for the hadronization. The lower panel shows the ratio of NLO + Hadronization calculation to data. Both NLO and NLO+Hadronization calculations over-predict the jet cross-section at all  $p_T$  range. In order to properly compare the measured cross-section to theoretical QCD calculations, one must properly account for the fragmentation of partons into hadrons. This hadronization correction is especially significant for small radii jets and the comparison in Figure 8.2 establishes the necessity for more sophisticated hadronization calculations. As the effect of hadronization in the calculation done here is to simply shift the  $p_T$  of the jet by an average amount, the hadronization correction values should be perceived, at most, as an indication of the effect one should

expect. With an implementation of complete hadronization model, we expect larger hadronization contribution and a better agreement between data and theoretical calculation over the full  $p_T$  range.

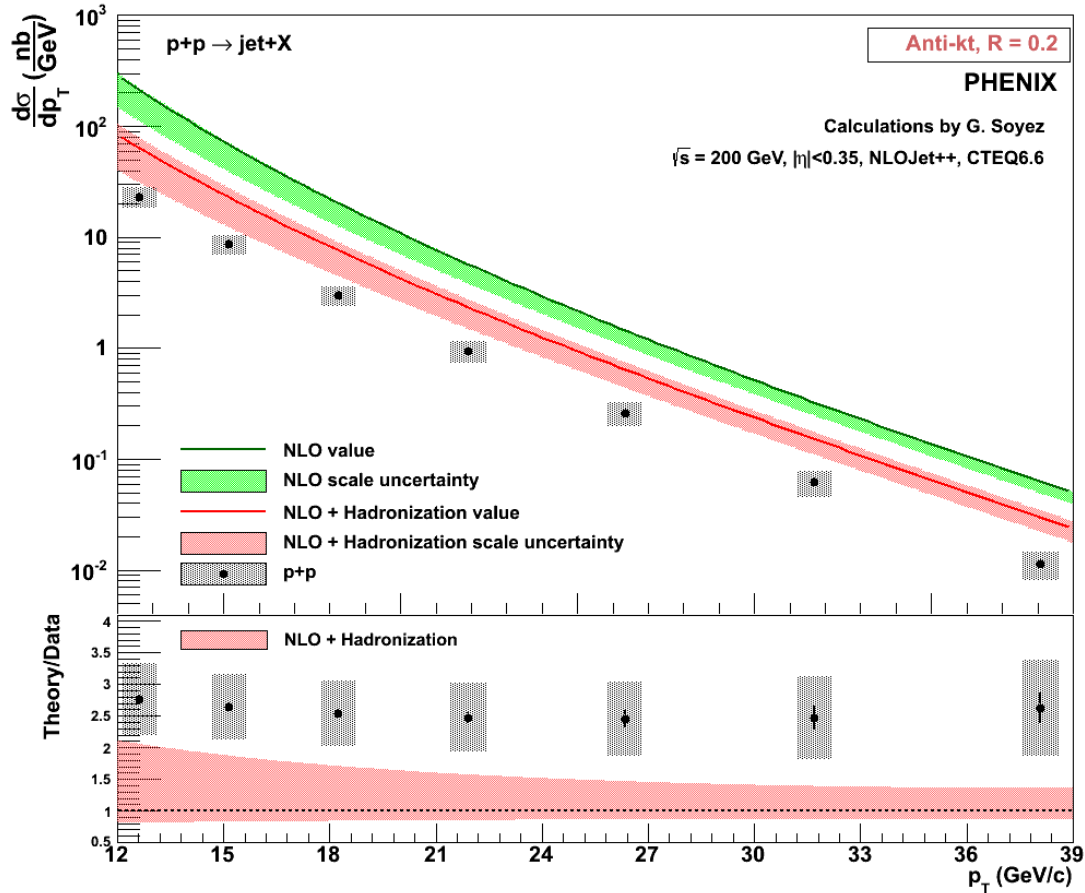


Figure 8.2: Measured and calculated anti- $k_t$ ,  $R=0.2$  jet cross-section in the  $p+p$  collisions. The vertical bars in the measurement indicate the statistical uncertainties and the shaded bands indicate the total systematic uncertainties(which includes the overall normalization uncertainties). The lines are the theoretical values and the bands are the theoretical scale uncertainty; the green color lines and bands are NLO calculations and the red color lines and bands are NLO calculations corrected for hadronization. The lower panel shows the ratio of NLO + Hadronization calculation to data.

## 8.2 $R_{\text{AA}}$ and $R_{\text{CP}}$

The nuclear modification factor  $R_{\text{AA}}$  for a given centrality is calculated as

$$R_{\text{AA}}^{\text{cent}} = \frac{\left( \frac{1}{N_{\text{evts}}^{\text{cent}}} \frac{dN}{dp_{\text{T}}}^{\text{cent}} \right)_{\text{CuAu}}}{T_{\text{AB}}^{\text{cent}} \times \frac{d\sigma^{\text{MB}}}{dp_{\text{T}}}}, \quad (8.2)$$

where  $T_{\text{AB}} = N_{\text{Coll}}/\sigma_{\text{pp}}^{\text{inel}}$ . Figure 8.3 shows the  $R_{\text{AA}}$  for four different centrality selections of the Cu+Au collisions as a function of jet transverse momentum. The vertical bars indicate the statistical uncertainties and the shaded bands indicate the systematic uncertainties. The overall normalization uncertainties are shown as the vertical bands on the left side at  $R_{\text{AA}} = 1$  mark. The jet suppression shows centrality dependence but no  $p_{\text{T}}$  dependence. Also, for the most central collisions (0–20%), jets are suppressed by approximately a factor of two.

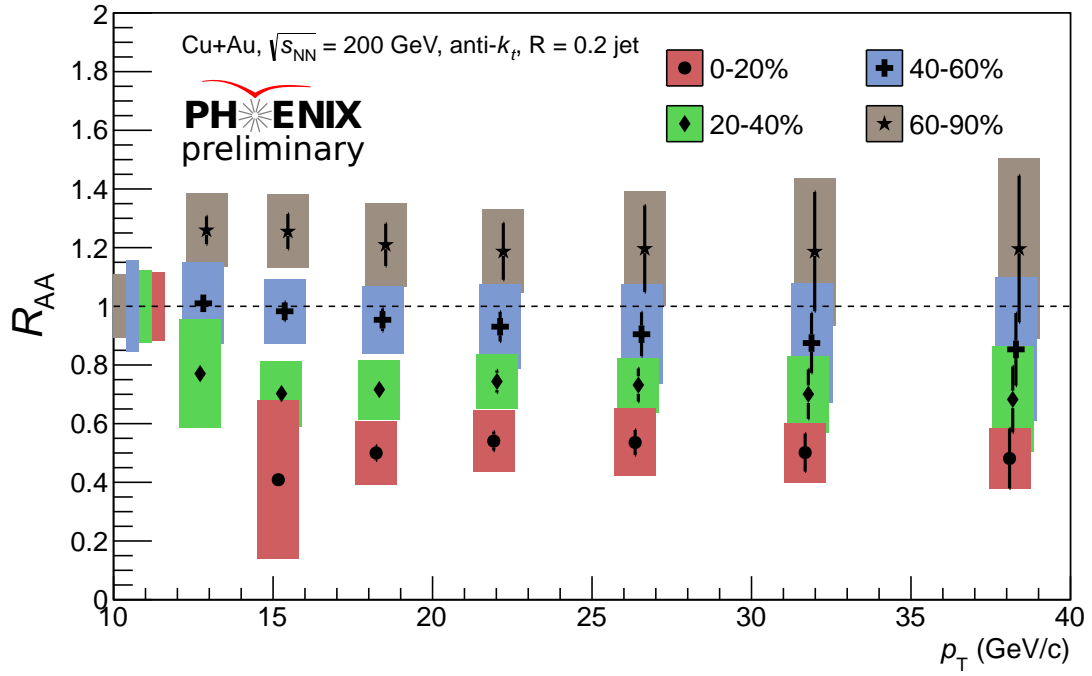


Figure 8.3:  $R_{\text{AA}}$  for four different centrality selections of the Cu+Au collisions a function of jet transverse momentum  $p_{\text{T}}$ . The vertical bars indicate the statistical uncertainties and the shaded bands indicate the systematic uncertainties. The overall normalization uncertainties are shown as the vertical bands on the left side at  $R_{\text{AA}} = 1$  mark.

Figure 8.4 shows the  $R_{AA}$  as a function of the number of participating nucleons  $N_{\text{Part}}$  of the Cu+Au collisions for two different  $p_T$  ranges: 17–20 GeV/c and 29–35 GeV/c. Again, the vertical bars indicate the statistical uncertainties and the shaded bands indicate the systematic uncertainties. The jet suppression shows strong centrality dependence but no  $p_T$  dependence.

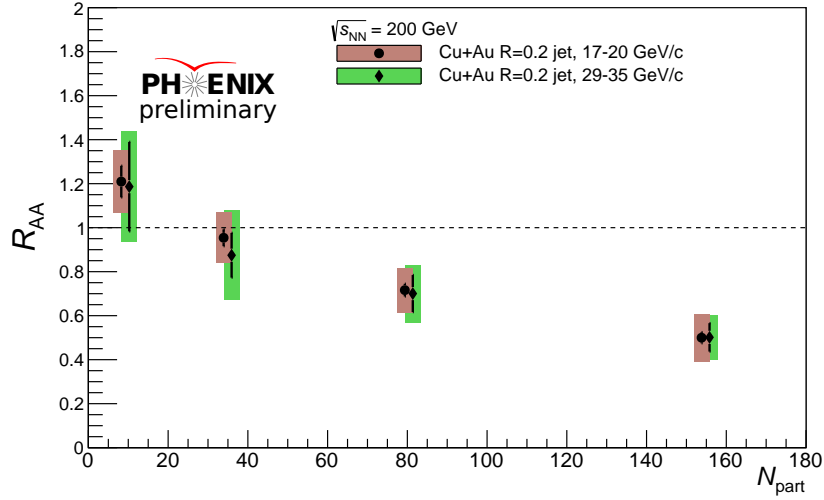


Figure 8.4:  $R_{AA}$  as a function of the number of participating nucleons  $N_{\text{Part}}$  for two different  $p_T$  ranges: 17–20 GeV/c and 29–35 GeV/c.

Figure 8.5 shows the theory calculations for two different couplings between the jet and the QGP medium:  $g = 2.0$  and  $g = 2.2$ . The calculations are done for small cold nuclear matter (CNM) effect; and are based on Soft Collinear Effective Theory with Glauber Gluons as in [130] and the baseline partonic calculation with cold nuclear matter effects as in [131]. The calculations give a comparable description of the experimental data and recount the  $p_T$  dependence of the jet suppression well.

The central to peripheral ratio  $R_{CP}$  relative to the most peripheral centrality (60–90%) is calculated as

$$R_{CP}^{\text{cent}} = \frac{\left( \frac{1}{N_{\text{coll}}^{\text{cent}}} \right) \left( \frac{1}{N_{\text{evts}}^{\text{cent}}} \frac{dN}{dp_T}^{\text{cent}} \right)_{\text{CuAu}}}{\left( \frac{1}{N_{\text{coll}}^{60-90\%}} \right) \left( \frac{1}{N_{\text{evts}}^{60-90\%}} \frac{dN}{dp_T}^{60-90\%} \right)_{\text{CuAu}}}. \quad (8.3)$$

Figure 8.6 shows the  $R_{CP}$  for three different centrality selections of the Cu+Au collisions as a function of jet transverse momentum  $p_T$ . The vertical bars indicate the statistical uncertainties and the shaded bands indicate the systematic uncertainties. The overall normalization uncer-

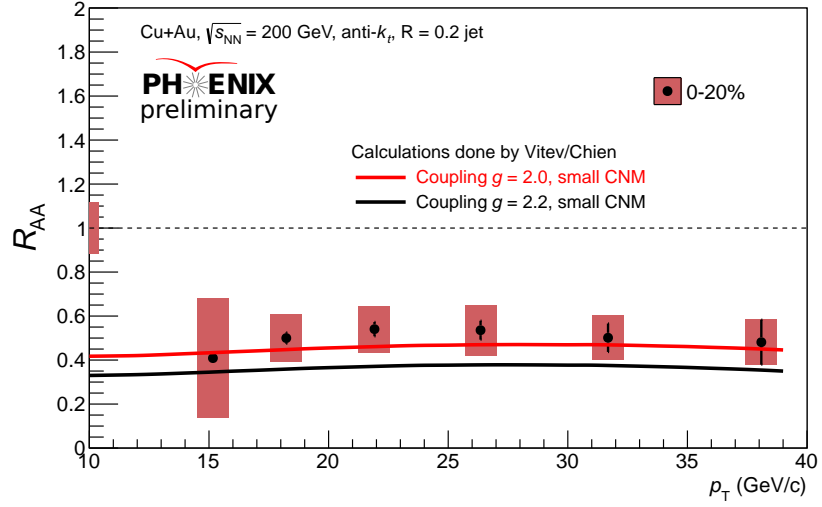


Figure 8.5: Jet  $R_{AA}$  for the most central case compared to theory calculations for two different couplings between the jet and the QGP medium:  $g = 2.0$  and  $g = 2.2$ . The calculations are done for small cold nuclear matter (CNM) effect.

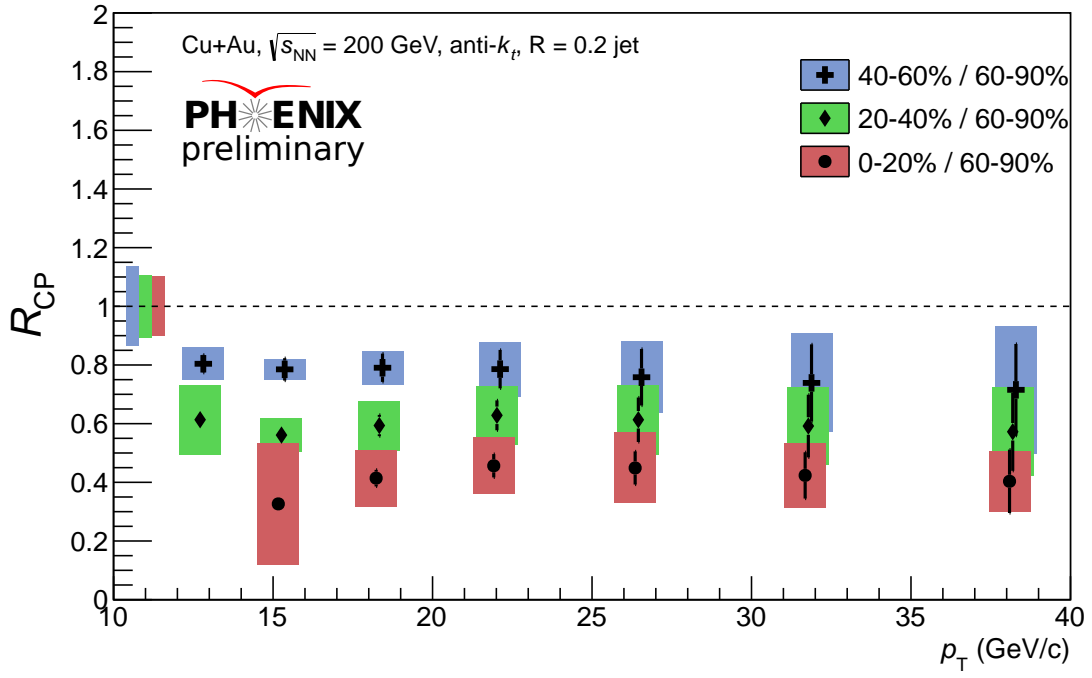


Figure 8.6:  $R_{CP}$  for three different centrality selections of the Cu+Au collisions as a function of jet transverse momentum  $p_T$ . The vertical bars indicate the statistical uncertainties and the shaded bands indicate the systematic uncertainties. The overall normalization uncertainties are shown as vertical band on the left side at  $R_{CP} = 1$  mark.

tainties are shown as the vertical bands on the left side at  $R_{\text{CP}} = 1$  mark. The  $R_{\text{CP}}$  shows similar jet suppression as the  $R_{\text{AA}}$  but with relatively reduced systematics. Appendix C shows the comparison of  $R_{\text{AA}}$  and  $R_{\text{CP}}$  constructed from the uncorrected reco-level, the SVD method unfolded, and the Bayes method unfolded yields.

### 8.3 Tabulation of the final results

Table 8.1 shows the overall normalization uncertainties for the observables in this analysis. Table 8.2 and Table 8.3 show the final  $R_{\text{AA}}$  and  $R_{\text{CP}}$  values with the statistical and systematic uncertainties.

Table 8.1: Tabulation of the overall normalization uncertainties for the observables in this analysis. The uncertainties are added in quadrature to obtain the total.

Observable	$N_{\text{Coll}}$	$T_{\text{AB}}$	$\sigma_{\text{BBC}}$	$\epsilon_{\text{BBC}}^{\text{Hard}}$	Total
$p+p$	-	-	9.7%	2%	9.9%
Cu+Au 0-20% / $p+p$	-	6.3%	9.7%	2%	11.7%
Cu+Au 20-40% / $p+p$	-	7.5%	9.7%	2%	12.4%
Cu+Au 40-60% / $p+p$	-	12.0%	9.7%	2%	15.6%
Cu+Au 60-90% / $p+p$	-	4.6%	9.7%	2%	10.96%
Cu+Au 0-20% / Cu+Au 60-90%	10.1%	-	-	-	10.1%
Cu+Au 20-40% / Cu+Au 60-90%	10.6%	-	-	-	10.6%
Cu+Au 40-60% / Cu+Au 60-90%	13.5%	-	-	-	13.5%

Table 8.2: Tabulation of the  $R_{AA}$  results. The quantities in parentheses are the absolute statistical and systematic uncertainties. The normalization uncertainties from Table 8.1 are not shown here.

$p_T$ range (GeV/c)	0-20%	20-40%	40-60%	60-90%
11.5-13.8	-	0.77(0.02)(0.18)	1.01(0.02)(0.14)	1.26(0.05)(0.13)
13.8-16.6	0.41(0.02)(0.27)	0.70(0.03)(0.11)	0.98(0.03)(0.11)	1.26(0.06)(0.13)
16.6-19.9	0.50(0.03)(0.11)	0.72(0.03)(0.10)	0.95(0.04)(0.12)	1.21(0.07)(0.14)
19.9-23.9	0.54(0.03)(0.11)	0.74(0.04)(0.09)	0.93(0.05)(0.14)	1.19(0.10)(0.14)
23.9-28.8	0.54(0.04)(0.11)	0.73(0.06)(0.09)	0.90(0.07)(0.17)	1.20(0.15)(0.19)
28.8-34.6	0.50(0.06)(0.10)	0.70(0.08)(0.13)	0.87(0.10)(0.20)	1.19(0.20)(0.25)
34.6-41.6	0.48(0.10)(0.10)	0.68(0.11)(0.18)	0.85(0.12)(0.24)	1.20(0.25)(0.31)

Table 8.3: Tabulation of  $R_{CP}$  results. The quantities in parentheses are the absolute statistical and systematic uncertainties. The normalization uncertainties from Table 8.1 are not shown here.

$p_T$ range (GeV/c)	0-20% / 60-90%	20-40% / 60-90%	40-60% / 60-90%
11.5-13.8	-	0.61(0.03)(0.12)	0.80(0.03)(0.06)
13.8-16.6	0.33(0.02)(0.21)	0.56(0.03)(0.06)	0.79(0.04)(0.04)
16.6-19.9	0.41(0.03)(0.10)	0.59(0.04)(0.08)	0.79(0.05)(0.06)
19.9-23.9	0.46(0.04)(0.10)	0.63(0.05)(0.10)	0.79(0.07)(0.09)
23.9-28.8	0.45(0.06)(0.12)	0.61(0.08)(0.12)	0.76(0.10)(0.12)
28.8-34.6	0.42(0.08)(0.11)	0.59(0.11)(0.13)	0.74(0.13)(0.17)
34.6-41.6	0.40(0.11)(0.10)	0.57(0.13)(0.15)	0.72(0.16)(0.22)

## 8.4 Conclusion

This dissertation has presented results for the jet cross-section in the  $p+p$  collisions and the jet  $R_{AA}$  and  $R_{CP}$  in the Cu+Au collisions. The  $R_{AA}$  and  $R_{CP}$  results presented here from different centrality selections of the Cu+Au collisions show a strong modification of jet production at all  $p_T$ . Jets are found to be suppressed by approximately a factor of two in the central Cu+Au collisions as compared to the  $p+p$  collisions, and the suppression shows no  $p_T$  dependence. The theory calculation for small CNM effect for the most central case gives a comparable description of the experimental data and recount the  $p_T$  dependence of the jet suppression well.

This work is the first measurement of the centrality-dependent yields of fully reconstructed jets in Cu+Au collisions at RHIC. The measurements presented here are intended to be only the beginning of a detailed study of the fundamental nature of the strongly coupled QGP and how the hard processes are affected by the QGP medium. The PHENIX collaboration has proposed a major upgrade to the PHENIX detector at RHIC [132]. This upgrade, known as sPHENIX, will enable an extremely rich jet physics program and will be able to advance our understanding of the QGP and the energy loss mechanism. With the fully reconstructed jet, dijet,  $\gamma$ -jet, and fragmentation function observables at the RHIC energies, sPHENIX will be able to probe the QGP medium over a variety of length scales. Also, by comparing these measurements with the ones from the LHC, variety of questions regarding size, shape, and temperature dependence of the medium can be answered.

## BIBLIOGRAPHY

- [1] James K. Laylin. *Nobel Laureates in Chemistry*. Chemical Heritage Foundation (June 1, 1993), 1901-1992.
- [2] E. Rutherford. The scattering of alpha and beta particles by matter and the structure of the atom. *Phil. Mag.*, 21:669–688, 1911.
- [3] Hideki Yukawa. On the Interaction of Elementary Particles. I. *Proc. Phys.-Math. Soc. Japan*, 17:48–57, 1935.
- [4] Seth H. Neddermeyer and Carl D. Anderson. Note on the nature of cosmic-ray particles. *Phys. Rev.*, 51:884–886, May 1937.
- [5] J. C. Street and E. C. Stevenson. New evidence for the existence of a particle of mass intermediate between the proton and electron. *Phys. Rev.*, 52:1003–1004, Nov 1937.
- [6] C. M. G. Lattes, H. Muirhead, G. P. S. Occhialini, and C. F. Powell. Processes Involving Charged Mesons. *Nature*, 159:694–697, 1947.
- [7] G.D. Rochester and C.C. Butler. Evidence for the Existence of New Unstable Elementary Particles. *Nature*, 160:855–857, 1947.
- [8] Murray Gell-Mann. A Schematic Model of Baryons and Mesons. *Phys.Lett.*, 8:214–215, 1964.
- [9] J. D. Bjorken and S. L. Glashow. Elementary Particles and SU(4). *Phys. Lett.*, 11:255–257, 1964.
- [10] Martin L. Perl et al. Evidence for Anomalous Lepton Production in e+ - e- Annihilation. *Phys. Rev. Lett.*, 35:1489–1492, 1975.

- [11] S. W. Herb et al. Observation of a Dimuon Resonance at 9.5-GeV in 400-GeV Proton-Nucleus Collisions. *Phys. Rev. Lett.*, 39:252–255, 1977.
- [12] F. Abe et al. Observation of top quark production in  $\bar{p}p$  collisions. *Phys. Rev. Lett.*, 74:2626–2631, 1995.
- [13] V. V. Ezhela, S. B. Lugovsky, and O. V. Zenin. Hadronic part of the muon g-2 estimated on the sigma\*\*2003(tot)(e+ e- → hadrons) evaluated data compilation. 2003.
- [14] Richard E. Taylor. Deep inelastic scattering: The Early years. *Rev. Mod. Phys.*, 63:573–595, 1991.
- [15] Henry W. Kendall. Deep inelastic scattering: Experiments on the proton and the observation. *Rev. Mod. Phys.*, 63:597–614, 1991.
- [16] Jerome I. Friedman. Deep inelastic scattering: Comparisons with the quark model. *Rev. Mod. Phys.*, 63:615–629, 1991.
- [17] J. D. Bjorken. Asymptotic Sum Rules at Infinite Momentum. *Phys. Rev.*, 179:1547–1553, 1969.
- [18] R. Keith Ellis, W. James Stirling, and B. R. Webber. QCD and collider physics. *Camb. Monogr. Part. Phys. Nucl. Phys. Cosmol.*, 8:1–435, 1996.
- [19] Curtis G. Callan, Jr. and David J. Gross. High-energy electroproduction and the constitution of the electric current. *Phys. Rev. Lett.*, 22:156–159, 1969.
- [20] David Griffiths. *Introduction to elementary particles*. Weinheim, Germany: Wiley-VCH (2008) 454 p, 2008.
- [21] H. Fritzsch, Murray Gell-Mann, and H. Leutwyler. Advantages of the Color Octet Gluon Picture. *Phys. Lett.*, B47:365–368, 1973.
- [22] L.D. Faddeev and V.N. Popov. Feynman diagrams for the yang-mills field. *Physics Letters B*, 25(1):29 – 30, 1967.

- [23] Siegfried Bethke. Experimental tests of asymptotic freedom. *Prog. Part. Nucl. Phys.*, 58:351–386, 2007.
- [24] David J. Gross and Frank Wilczek. Ultraviolet Behavior of Nonabelian Gauge Theories. *Phys. Rev. Lett.*, 30:1343–1346, 1973.
- [25] H. David Politzer. Reliable Perturbative Results for Strong Interactions? *Phys. Rev. Lett.*, 30:1346–1349, 1973.
- [26] J. Beringer et al. Review of Particle Physics (RPP). *Phys. Rev.*, D86:010001, 2012.
- [27] Howard Georgi and H. David Politzer. Electroproduction scaling in an asymptotically free theory of strong interactions. *Phys. Rev.*, D9:416–420, 1974.
- [28] Guido Altarelli. Experimental Tests of Perturbative QCD. *Ann. Rev. Nucl. Part. Sci.*, 39:357–406, 1989.
- [29] G. Hanson et al. Evidence for Jet Structure in Hadron Production by e+ e- Annihilation. *Phys. Rev. Lett.*, 35:1609–1612, 1975.
- [30] R. Schwitters et al. Azimuthal Asymmetry in Inclusive Hadron Production by e+ e- Annihilation. *Phys. Rev. Lett.*, 35:1320, 1975.
- [31] Go on a particle quest at the first cern hackfest. <https://scienzenode.org/spotlight/go-particle-quest-first-cern-hackfest.php>. Accessed: 2015-09-12.
- [32] Kenneth G. Wilson. Confinement of Quarks. *Phys. Rev.*, D10:2445–2459, 1974.
- [33] John C. Collins and M. J. Perry. Superdense Matter: Neutrons Or Asymptotically Free Quarks? *Phys. Rev. Lett.*, 34:1353, 1975.
- [34] G. Baym and S. A. Chin. Can a Neutron Star Be a Giant MIT Bag? *Phys. Lett.*, B62:241–244, 1976.
- [35] George Chapline and Michael Nauenberg. Asymptotic Freedom and the Baryon-Quark Phase Transition. *Phys. Rev.*, D16:450, 1977.

- [36] Edward V. Shuryak. Quark-Gluon Plasma and Hadronic Production of Leptons, Photons and Psions. *Phys. Lett.*, B78:150, 1978. [Yad. Fiz.28,796(1978)].
- [37] O. K. Kalashnikov and V. V. Klimov. Phase Transition in Quark - Gluon Plasma. *Phys. Lett.*, B88:328, 1979.
- [38] F. Karsch. Lattice QCD at high temperature and density. *Lect. Notes Phys.*, 583:209–249, 2002.
- [39] Zoltan Fodor. Lattice QCD results at finite temperature and density. *Nucl. Phys.*, A715:319–328, 2003.
- [40] Ludmila Levkova. QCD at nonzero temperature and density. *PoS*, LATTICE2011:011, 2011.
- [41] J. D. Bjorken. Highly Relativistic Nucleus-Nucleus Collisions: The Central Rapidity Region. *Phys. Rev.*, D27:140–151, 1983.
- [42] K. Adcox et al. Measurement of the mid-rapidity transverse energy distribution from  $s(\text{NN})^{**}(1/2) = 130\text{-GeV}$  Au + Au collisions at RHIC. *Phys. Rev. Lett.*, 87:052301, 2001.
- [43] Tapan K. Nayak. Heavy Ions: Results from the Large Hadron Collider. *Pramana*, 79:719–735, 2012.
- [44] Michael Patrick McCumber. *Measurement of Fast Parton Interactions with Hot Dense Nuclear Matter via Two-Particle Correlations at PHENIX*. PhD thesis, SUNY, Stony Brook, 2009.
- [45] R. Baier, Alfred H. Mueller, D. Schiff, and D. T. Son. 'Bottom up' thermalization in heavy ion collisions. *Phys. Lett.*, B502:51–58, 2001.
- [46] Peter Brockway Arnold, Jonathan Lenaghan, Guy D. Moore, and Laurence G. Yaffe. Apparent thermalization due to plasma instabilities in quark-gluon plasma. *Phys. Rev. Lett.*, 94:072302, 2005.

- [47] R. J. Fries, Berndt Muller, C. Nonaka, and S. A. Bass. Hadron production in heavy ion collisions: Fragmentation and recombination from a dense parton phase. *Phys. Rev.*, C68:044902, 2003.
- [48] R. J. Fries. Recombination models. *J. Phys.*, G30:S853–S860, 2004.
- [49] Anne Marie Sickles. *Azimuthal correlation and conditional yield measurements at  $\sqrt{s_{NN}} = 200$  GeV in Au + Au, d + Au and p + p collisions at RHIC*. PhD thesis, SUNY, Stony Brook, 2005.
- [50] Berndt Muller. Physics and signatures of the quark - gluon plasma. *Rept. Prog. Phys.*, 58:611–636, 1995.
- [51] A. Adare et al.  $J/\psi$  suppression at forward rapidity in Au+Au collisions at  $\sqrt{s_{NN}} = 200$  GeV. *Phys. Rev.*, C84:054912, 2011.
- [52] A. Andronic, P. Braun-Munzinger, K. Redlich, and J. Stachel. Statistical hadronization of charm in heavy ion collisions at SPS, RHIC and LHC. *Phys. Lett.*, B571:36–44, 2003.
- [53] Berndt Muller, Jurgen Schukraft, and Boleslaw Wyslouch. First Results from Pb+Pb collisions at the LHC. *Ann. Rev. Nucl. Part. Sci.*, 62:361–386, 2012.
- [54] Prashant Shukla. Overview of quarkonia and heavy flavour measurements by CMS. *Proc. Indian Natl. Sci. Acad.*, 81(1):199–206, 2015.
- [55] T. Matsui and H. Satz.  $J/\psi$  Suppression by Quark-Gluon Plasma Formation. *Phys. Lett.*, B178:416, 1986.
- [56] Xiao-Ming Xu, D. Kharzeev, H. Satz, and Xin-Nian Wang.  $J/\psi$  suppression in an equilibrating parton plasma. *Phys. Rev.*, C53:3051–3056, 1996.
- [57] Xin-Nian Wang and Miklos Gyulassy. Gluon shadowing and jet quenching in A + A collisions at  $s^{**}(1/2) = 200$ -GeV. *Phys. Rev. Lett.*, 68:1480–1483, 1992.
- [58] M. Djordjevic. Heavy quark energy loss: Collisional vs radiative. *Nucl. Phys.*, A783:197–204, 2007.

- [59] R. Baier, D. Schiff, and B. G. Zakharov. Energy loss in perturbative QCD. *Ann. Rev. Nucl. Part. Sci.*, 50:37–69, 2000.
- [60] M. Gyulassy, P. Levai, and I. Vitev. Jet tomography of Au+Au reactions including multigluon fluctuations. *Phys. Lett.*, B538:282–288, 2002.
- [61] John E. Huth et al. Toward a standardization of jet definitions. In *1990 DPF Summer Study on High-energy Physics: Research Directions for the Decade (Snowmass 90) Snowmass, Colorado, June 25-July 13, 1990*, 1990.
- [62] Gregory Soyez. Recent progress in defining jets. *Nucl. Phys. Proc. Suppl.*, 191:131–140, 2009.
- [63] Gavin P. Salam and Gregory Soyez. A Practical Seedless Infrared-Safe Cone jet algorithm. *JHEP*, 05:086, 2007.
- [64] Matteo Cacciari, Gavin P. Salam, and Gregory Soyez. FastJet User Manual. *Eur. Phys. J.*, C72:1896, 2012.
- [65] Matteo Cacciari, Gavin P. Salam, and Gregory Soyez. The Anti-k(t) jet clustering algorithm. *JHEP*, 04:063, 2008.
- [66] Yue-Shi Lai and Brian A. Cole. Jet reconstruction in hadronic collisions by Gaussian filtering. 2008.
- [67] Yue Shi Lai. *Direct Jet Reconstruction in Proton-Proton and Copper-Copper at  $\sqrt{s_{NN}} = 200$  GeV*. PhD thesis, Nevis Labs, Columbia U., 2012.
- [68] Dennis Perepelitsa. *Inclusive jet production in ultrarelativistic proton-nucleus collisions*. PhD thesis, Columbia U., 2013.
- [69] John C. Collins, Davison E. Soper, and George F. Sterman. Factorization of Hard Processes in QCD. *Adv. Ser. Direct. High Energy Phys.*, 5:1–91, 1989.

- [70] B. Jager, A. Schafer, M. Stratmann, and W. Vogelsang. Next-to-leading order QCD corrections to high  $p(T)$  pion production in longitudinally polarized pp collisions. *Phys. Rev.*, D67:054005, 2003.
- [71] A. Adare et al. Inclusive cross-section and double helicity asymmetry for pi0 production in p + p collisions at  $s^{**}(1/2) = 200$ -GeV: Implications for the polarized gluon distribution in the proton. *Phys. Rev.*, D76:051106, 2007.
- [72] K. J. Eskola, H. Paukkunen, and C. A. Salgado. EPS09: A New Generation of NLO and LO Nuclear Parton Distribution Functions. *JHEP*, 04:065, 2009.
- [73] Michael J. Tannenbaum. Hard and Soft Physics at RHIC with implications for LHC. *PoS*, High-pT physics09:004, 2009.
- [74] K. Adcox et al. Suppression of hadrons with large transverse momentum in central Au+Au collisions at  $\sqrt{s_{NN}} = 130$ -GeV. *Phys. Rev. Lett.*, 88:022301, 2002.
- [75] C. Adler et al. Centrality dependence of high  $p_T$  hadron suppression in Au+Au collisions at  $\sqrt{s_{NN}} = 130$ -GeV. *Phys. Rev. Lett.*, 89:202301, 2002.
- [76] Georges Aad et al. Measurements of the Nuclear Modification Factor for Jets in Pb+Pb Collisions at  $\sqrt{s_{NN}} = 2.76$  TeV with the ATLAS Detector. *Phys. Rev. Lett.*, 114(7):072302, 2015.
- [77] B. Abelev et al. Measurement of charged jet suppression in Pb-Pb collisions at  $\sqrt{s_{NN}} = 2.76$  TeV. *JHEP*, 03:013, 2014.
- [78] Jaroslav Adam et al. Measurement of jet suppression in central Pb-Pb collisions at  $\sqrt{s_{NN}} = 2.76$  TeV. *Phys. Lett.*, B746:1–14, 2015.
- [79] A. Adare et al. Centrality-dependent modification of jet-production rates in deuteron-gold collisions at  $\sqrt{s_{NN}}=200$  GeV. 2015.
- [80] M. Harrison, T. Ludlam, and S. Ozaki. RHIC project overview. *Nucl. Instrum. Meth.*, A499:235–244, 2003.

- [81] H. Hahn et al. The RHIC design overview. *Nucl. Instrum. Meth.*, A499:245–263, 2003.
- [82] Wolfram Fischer and John M. Jowett. Ion Colliders. *Rev. Accel. Sci. Tech.*, 7:49–76, 2014.
- [83] I. Alekseev et al. Polarized proton collider at RHIC. *Nucl. Instrum. Meth.*, A499:392–414, 2003.
- [84] K. H. Ackermann et al. STAR detector overview. *Nucl. Instrum. Meth.*, A499:624–632, 2003.
- [85] I. Arsene et al. Quark gluon plasma and color glass condensate at RHIC? The Perspective from the BRAHMS experiment. *Nucl. Phys.*, A757:1–27, 2005.
- [86] K. Adcox et al. Formation of dense partonic matter in relativistic nucleus-nucleus collisions at RHIC: Experimental evaluation by the PHENIX collaboration. *Nucl. Phys.*, A757:184–283, 2005.
- [87] B. B. Back et al. The PHOBOS perspective on discoveries at RHIC. *Nucl. Phys.*, A757:28–101, 2005.
- [88] John Adams et al. Experimental and theoretical challenges in the search for the quark gluon plasma: The STAR Collaboration’s critical assessment of the evidence from RHIC collisions. *Nucl. Phys.*, A757:102–183, 2005.
- [89] J. G. Alessi et al. Performance of the New EBIS Preinjector. *Conf. Proc.*, C110328:1966–1968, 2011.
- [90] K. Adcox et al. PHENIX detector overview. *Nucl. Instrum. Meth.*, A499:469–479, 2003.
- [91] Yoshinori Fukao. Forward upgrade for W physics at the RHIC-PHENIX experiment. *J. Phys. Conf. Ser.*, 295:012165, 2011.
- [92] C. Aidala et al. The PHENIX Forward Silicon Vertex Detector. *Nucl. Instrum. Meth.*, A755:44–61, 2014.
- [93] M. Allen et al. PHENIX inner detectors. *Nucl. Instrum. Meth.*, A499:549–559, 2003.

- [94] Clemens Adler, Alexei Denisov, Edmundo Garcia, Michael J. Murray, Herbert Strobele, and Sebastian N. White. The RHIC zero degree calorimeter. *Nucl. Instrum. Meth.*, A470:488–499, 2001.
- [95] S. H. Aronson et al. PHENIX magnet system. *Nucl. Instrum. Meth.*, A499:480–488, 2003.
- [96] V. G. Ryabov. Drift chambers for the PHENIX central tracking system. *Nucl. Instrum. Meth.*, A419:363–369, 1998.
- [97] K. Adcox et al. PHENIX central arm tracking detectors. *Nucl. Instrum. Meth.*, A499:489–507, 2003.
- [98] K. Adcox et al. Construction and performance of the PHENIX pad chambers. *Nucl. Instrum. Meth.*, A497:263–293, 2003.
- [99] S. S. Adler et al. High  $p_T$  charged hadron suppression in Au + Au collisions at  $\sqrt{s}_{NN} = 200$  GeV. *Phys. Rev.*, C69:034910, 2004.
- [100] M. Aizawa et al. PHENIX central arm particle ID detectors. *Nucl. Instrum. Meth.*, A499:508–520, 2003.
- [101] L. Aphecetche et al. PHENIX calorimeter. *Nucl. Instrum. Meth.*, A499:521–536, 2003.
- [102] Kenichi Karatsu. *Measurement of Cross Section and Single Spin Asymmetries of  $W^\pm$ -Boson Production in Polarized pp Collisions at  $\sqrt{s} = 500$  GeV*. PhD thesis, Kyoto U., 2011.
- [103] R. J. Glauber and G. Matthiae. High-energy scattering of protons by nuclei. *Nucl. Phys.*, B21:135–157, 1970.
- [104] J.T. Mitchell, Mike Dai, Mingxiu Sun. PHENIX Analysis Note 1078: Centrality Calibration and Glauber Model Calculations for the Run-12 200 GeV Cu+Au Dataset.
- [105] Michael H. Seymour and Marilyn Marx. Monte Carlo Event Generators. In *Proceedings, 69th Scottish Universities Summer School in Physics : LHC Phenomenology (SUSSP69)*, pages 287–319, 2013.

- [106] Torbjorn Sjostrand, Stephen Mrenna, and Peter Z. Skands. PYTHIA 6.4 Physics and Manual. *JHEP*, 05:026, 2006.
- [107] Miklos Gyulassy and Xin-Nian Wang. HIJING 1.0: A Monte Carlo program for parton and particle production in high-energy hadronic and nuclear collisions. *Comput. Phys. Commun.*, 83:307, 1994.
- [108] J. A. Hanks et al. Method for separating jets and the underlying event in heavy ion collisions at the BNL Relativistic Heavy Ion Collider. *Phys. Rev.*, C86:024908, 2012.
- [109] Matteo Cacciari, Juan Rojo, Gavin P. Salam, and Gregory Soyez. Jet Reconstruction in Heavy Ion Collisions. *Eur. Phys. J.*, C71:1539, 2011.
- [110] PHENIX Luminosity Accumulation - Run12 200 GeV Cu+Au. [http://logbook.phenix.bnl.gov/Run8/Run12\\_cuau/run12.html](http://logbook.phenix.bnl.gov/Run8/Run12_cuau/run12.html).
- [111] PHENIX Luminosity Accumulation - Run12 200 GeV p+p. [http://logbook.phenix.bnl.gov/Run8/Run12\\_200pp/run12.html](http://logbook.phenix.bnl.gov/Run8/Run12_200pp/run12.html).
- [112] Dch quality bits. <https://www.phenix.bnl.gov/phenix/WWW/p/lists/phenix-off-l/msg07182.html>.
- [113] Datta, Amaresh. PHENIX Analysis Note 689: Drift Chamber QA.
- [114] Schaefer, Brennan and Huang, Shengli. PHENIX Analysis Note 1074: Identified Particle Spectra Measurements from Cu+Au 200GeV Collisions of PHENIX Run12.
- [115] Timilsina, Arbin and Lajoie, John. PHENIX Analysis Note 1105: Recalibration of EMCAL Track Matching Variables in Run-12 Cu+Au Collisions.
- [116] Perry, Josh. PHENIX Analysis Note 1117: PC3 and EMC Charged Tracking Recalibration for theRun12pp200 Dataset.
- [117] Joshua Paul Perry. *A Novel Approach to Central-Jet Forward-Hadron Correlations in Proton-Proton Collisions at 200 GeV at the PHENIX Experiment.* PhD thesis, Iowa State University, 2014.

- [118] R. Brun, R. Hagelberg, M. Hansroul, and J. C. Lassalle. Geant: Simulation Program for Particle Physics Experiments. User Guide and Reference Manual. *CERN-DD.*, 1978.
- [119] Andreas Hocker and Vakhtang Kartvelishvili. SVD approach to data unfolding. *Nucl. Instrum. Meth.*, A372:469–481, 1996.
- [120] G. D’Agostini. A Multidimensional unfolding method based on Bayes’ theorem. *Nucl. Instrum. Meth.*, A362:487–498, 1995.
- [121] RooUnfold: ROOT Unfolding Framework. <http://hepunx.rl.ac.uk/~adye/software/unfold/RooUnfold.html>.
- [122] S. S. Adler et al. Centrality dependence of pi0 and eta production at large transverse momentum in  $s(\text{NN})^{**}(1/2) = 200\text{-GeV}$  d+Au collisions. *Phys. Rev. Lett.*, 98:172302, 2007.
- [123] Sergey Belikov, Gerry Bunce, Mickey Chiu, Angelika Drees, Brendan Fox, Yuji Goto, Takahiro Kawabata, Naohito Saito, Hiroki Sato, Mike Tannenbaum. PHENIX Analysis Note 184: Determination of the Absolute Luminosity for the Proton-Proton Data at  $\sqrt{s}=200$  GeV Recorded by PHENIX during RHIC Run-02.
- [124] Stefan Bathe, Alexander Bazilevsky, Henner Buesching. PHENIX Analysis Note 470: Neutral Pion Spectra measured with the EMCAL in  $\sqrt{s}=200$  GeV p+p Collisions PHENIX-Run3 Preliminary result.
- [125] Gregory Soyez. Private communication.
- [126] Zoltan Nagy. Three jet cross-sections in hadron hadron collisions at next-to-leading order. *Phys. Rev. Lett.*, 88:122003, 2002.
- [127] Zoltan Nagy. Next-to-leading order calculation of three jet observables in hadron hadron collision. *Phys. Rev.*, D68:094002, 2003.
- [128] Pavel M. Nadolsky, Hung-Liang Lai, Qing-Hong Cao, Joey Huston, Jon Pumplin, Daniel Stump, Wu-Ki Tung, and C. P. Yuan. Implications of CTEQ global analysis for collider observables. *Phys. Rev.*, D78:013004, 2008.

- [129] Gregory Soyez. A Simple description of jet cross-section ratios. *Phys. Lett.*, B698:59–62, 2011.
- [130] Yang-Ting Chien and Ivan Vitev. Towards the Understanding of Jet Shapes and Cross Sections in Heavy Ion Collisions Using Soft-Collinear Effective Theory. 2015.
- [131] Yang-Ting Chien, Alexander Emerman, Zhong-Bo Kang, Grigory Ovanesyan, and Ivan Vitev. Jet Quenching from QCD Evolution. 2015.
- [132] A. Adare et al. An Upgrade Proposal from the PHENIX Collaboration. 2015.

## APPENDIX A. FAST FILTER CLASS

A fast filter class called TAcceptParticle was developed at ISU to simulate the acceptance of the PHENIX detector in a given magnetic field configuration.

Given the  $\theta$  of a track and the  $z_{\text{vertex}}$  of the collision, the  $zed^{\text{i}}$  of the track can be calculated as

$$zed = z_{\text{vertex}} - R_{\text{DC}} \tan(\theta - \frac{\pi}{2}), \quad (\text{A.1})$$

where  $R_{\text{DC}} = 224.0$  cm.

For the Run-12 ++ magnetic field configuration, the  $\alpha^{\text{ii}}$  of a track is related to the  $p_{\text{T}}$  and  $zed$  as:

$$\alpha = -\text{charge} \frac{0.1015 - (1.452 \times 10^{-6} zed) + (2.356 \times 10^{-6} zed^2)}{p_{\text{T}}} \quad (\text{A.2})$$

The track's (new) phi coordinate in the Run-12 magnetic field at which it crosses the drift chamber reference radius is then calculated from the alpha. A track passes the acceptance if

- it falls inside this new phi, and
- if  $|zed_{\text{DC, track}}| < 90.0$  cm

---

<sup>i</sup>zed is the  $z$ -coordinate at which the track crosses the PC1

<sup>ii</sup> $\alpha$  is the inclination of the track with respect to an infinite momentum track

## APPENDIX B. MATCHING

Even when we know all the information about the true jet, there might be an arbitrariness when the inclusive jets are matched to it. To minimize the arbitrariness, we implement the one-to-one matching between the true jets and the inclusive jets as described below:

1. Each true jet is paired with each inclusive jet. The true jet information, the inclusive jet information, and the  $\Delta R$  between them is stored in a paired list.  $\Delta R$  is calculated as:

$$\Delta R = \sqrt{\Delta\eta^2 + \Delta\phi^2} \quad (\text{B.1})$$

2. The paired list is sorted by the  $\Delta R$  in an ascending order.
3. To ensure the one-to-one matching, the front of the paired list is saved as a unique pair (in a unique pair list) and other elements in the paired list that contain either that particular true or inclusive jet is removed. The process is repeated until the paired list is empty, and the unique pair list contains unique pairs of the true and inclusive jets.
4. Only pairs with  $\Delta R < \Delta R_{\min}$  are considered to be matched.

### APPENDIX C. CROSS-CHECKS: $R_{AA}$ and $R_{CP}$

Figure C.1 and Figure C.2 show the comparison of  $R_{AA}$  and  $R_{CP}$  constructed from the uncorrected reco-level, the SVD method unfolded, and the Bayes method unfolded yields, respectively.

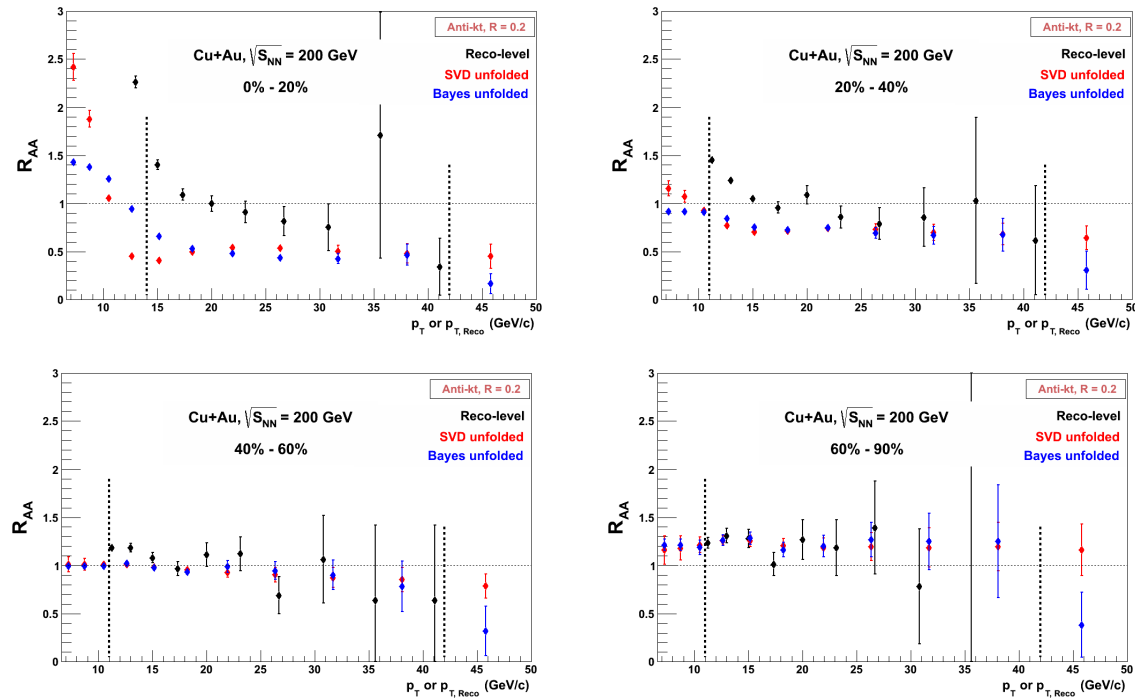


Figure C.1: Comparison of  $R_{AA}$  constructed from the uncorrected reco-level, the SVD method unfolded and the Bayes method unfolded yields.

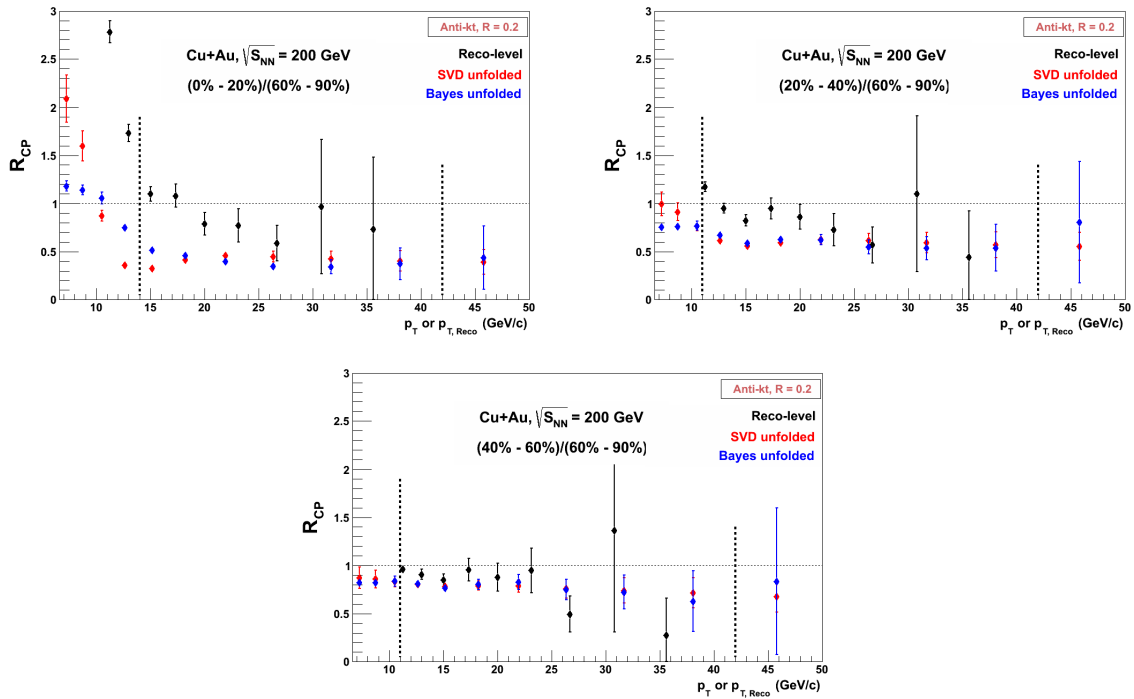


Figure C.2: Comparison of  $R_{CP}$  for uncorrected reco-level yield and SVD and Bayes method unfolded yield.